Elastic properties of carbonates

Dissertation
zur Erlangung des Doktorgrades
der Naturwissenschaften

vorgelegt beim Fachbereich Geowissenschaften/Geographie
der Johann Wolfgang Goethe-Universität
Frankfurt am Main

von
Pennacchioni Lea
aus Padova, Italy

Frankfurt 2022
(D30)

vom Fachbereich Geowissenschaften/Geographie der Johann Wolfgang Goethe-Universität als Dissertation angenommen.

Dekan: Prof. Dr. Jürgen Runge

1. Gutachter: Prof. Björn Winkler

2. Gutachter: Dr. Eiken Haussühl

Datum der Disputation: 17.10.2022

Contents

List of Figures

List of Tables

Zusammenfassung

Diese Arbeit ist Teil des Projekts 9 innerhalb der von der DFG geförderten Forschergruppe CarboPaT (FOR2125), die sich mit den physikalischen Eigenschaften und der Phasenstabilität von Karbonaten beschäftigt. Der allgemeine Rahmen dieser Arbeit ist die Untersuchung der elastischen Eigenschaften von Karbonaten in Abhängigkeit von ihrer chemischen Zusammensetzung. Das Interesse an der Untersuchung von Karbonaten ist im Rahmen des tiefen Kohlenstoffkreislaufs gerechtfertigt. Kohlenstoff ist ein grundlegendes Element für die Bewohnbarkeit des Planeten und das Leben auf der Erde, und 99% des Kohlenstoffs können in der Tiefe der Erde gespeichert sein. An der Erdoberfläche sind 60-70 % des Kohlenstoffs in Karbonatmineralien [90] eingelagert, die dann durch Subduktion der ozeanischen Lithosphäre ins Erdinnere transportiert werden, hauptsächlich in Form von Sedimenten. Obwohl subduzierende Platten einer Dekarbonisierung, Dehydrierung und Schmelze mit Freisetzung von CO_2 durch Suprasubduktionsvulkanismus unterworfen sind, kann ein Teil der subduzierten Karbonate überleben und weiter in den tiefen Erdmantel transportiert werden. Direkte Beweise für das Vorhandensein von Karbonaten im Erdinneren, die möglicherweise bis in den unteren Erdmantel reichen, liefern syngenetische Einschlüsse von Karbonaten in Diamanten [242, 226, 119, 27, 102, 264] und Mantelxenolithen [263]. Das Vorhandensein von Karbonaten in der tiefen Erde hat einen entscheidenden Einfluss auf die physikalischen Eigenschaften des Erdmantels. Insbesondere das Schmelzen und die chemische Speziation der Elemente im Erdmantel werden stark von der Form des C und der Stabilität der Karbonate beeinflusst [58, 59]. Daher ist die Untersuchung der Stabilität und der physikalischen Eigenschaften von Karbonaten bei hohen Drücken und Temperaturen von grundlegender Bedeutung, da das Verständnis der am tiefen Kohlenstoffkreislauf beteiligten Prozesse dazu beiträgt, unser Bild des gesamten Mantels zu verbessern.
Die systematische Charakterisierung der elastischen Eigenschaften von Karbonaten in Abhängigkeit von ihrer Struktur und chemischen Zusammensetzung ist von großer Bedeutung, da sie es ermöglichen kann, ihr Vorhanden-

sein und ihre Verteilung durch Seismologie zu identifizieren. Die Umkehrung seismischer Beobachtungen, um die chemische Zusammensetzung und Mineralogie des Erdinneren erfolgreich einzugrenzen, erfordert die Kenntnis der physikalischen Eigenschaften aller möglichen Erdmaterialien bei den im Erdinneren herrschenden Drücken und Temperaturen. Bisher hat sich eine Vielzahl von Studien auf die Erstellung von Phasendiagrammen und strukturellen Übergängen mit Hilfe von Röntgenbeugungs- und Schwingungsspektroskopieexperimenten konzentriert [86]. Es gibt nur wenige Studien über den vollständigen elastischen Tensor von Karbonaten, aber die meisten Datensätze werden nicht von einer genauen Charakterisierung der Proben begleitet, bei denen es sich oft um feste Lösungen handelt und die genaue chemische Zusammensetzung, die Dichte oder die Details über die verwendeten experimentellen Methoden nicht dargestellt werden. Ziel dieser Arbeit ist es, die Auswirkung der chemischen Zusammensetzung auf die elastischen Eigenschaften von Karbonaten zu untersuchen und zuverlässige Datensätze zur Elastizität der wichtigsten Karbonate und ihrer festen Lösungen zu liefern. Die Messungen wurden sowohl an kristallinen (natürlichen und synthetischen) als auch amorphen Verbindungen durchgeführt. Untersucht wurden die elastischen Eigenschaften von natürlichen kristallinen Aragonit-, Fe-Dolomit- und Ankeritproben mit unterschiedlichen chemischen Zusammensetzungen. Die neuen, qualitativ hochwertigen Ergebnisse stellen die Referenz für die Elastizität von Aragonit, Fe-Dolomit und Ankerit dar.
Drei gut charakterisierte Proben von natürlichem Aragonit, $CaCO_3$, mit Sr-Gehalten von 0.1, 0.3 und 1.5 mol% wurden bei Umgebungsbedingungen durch Brillouin-Spektroskopie untersucht. Diese Proben decken zusammen mit den Ergebnissen einer früheren Brillouin-Spektroskopie-Studie an einem Aragonit mit 2.4 mol% Sr den gesamten Bereich der Zusammensetzung natürlicher Aragonite ab. Das Vorhandensein von Sr führt zu einer Erweichung des Materials und einer Verringerung der elastischen Aggregateigenschaften von Aragonit. Insbesondere zeigen die in dieser Arbeit vorgestellten Ergebnisse einen Zusammensetzungstrend im isothermen Volumenmodul, der qualitativ mit den Ergebnissen einer früheren Studie übereinstimmt, in der die Wirkung von Sr auf den Volumenmodul von synthetischen aragonitstrukturierten $Sr_xCa_{1-x}CO_3$-Mischkristallen mit $x = 0,2, 0,5, 0,8$ mittels DFT und Hochdruck-Röntgenbeugung untersucht wurde. Die in einem so engen Zusammensetzungsbereich beobachteten Effekte liegen jedoch an der Grenze der experimentellen Auflösung der Brillouin-Streuung. Der Unterschied zwischen den aggregierten elastischen Eigenschaften von Calcit und Aragonit wird in dieser Arbeit ebenfalls diskutiert. Im Allgemeinen wird erwartet, dass ein Hochdruckpolymorph wie Aragonit einen größeren Volumenmodul hat als ein Niederdruckpolymorph (Calcit). Die unterschiedliche

Struktur der beiden $CaCO_3$-Polymorphe führt jedoch dazu, dass Aragonit einen um 9.7 % niedrigeren Volumenmodul als Calcit aufweist. Dieses scheinbar anomale Verhalten ist auf die unterschiedliche Anordnung der Ca- und C-Koordinationsumgebungen zurückzuführen, den Bausteinen, aus denen die jeweiligen Strukturen von Calcit und Aragonit bestehen. Karbonatgruppen CO_3 sind bei niedrigem Druck steifer, daher wird die Kompression in $CaCO_3$ durch geometrische Veränderungen in den Ca-O-Polyedern kompensiert. In Aragonit sind die Ca-O-Polyeder gegenüber der Calcitstruktur geneigt, so dass die CO_3-Gruppen in verschiedenen Ebenen angeordnet sind, was dazu führt, dass Aragonit eine geringere Kompressibilität entlang der c-Achse, aber eine höhere Kompressibilität entlang der a- und b-Achse aufweist.
Die elastischen Eigenschaften von Fe-Dolomit und Ankerit $(CaMgFe)(CO_3)_2$ wurden in dieser Arbeit erstmals analysiert. $CaMg(CO_3)_2$-$CaFe(CO_3)_2$ Mischkristalle mit höherem $CaMg(CO_3)_2$-Gehalt sind ferroanische Dolomite (Fe-Dolomit), während der Begriff "Ankerit" für Mischkristalle mit höherem $CaFe(CO_3)_2$-Gehalt verwendet wird. Frühere Untersuchungen von reinem Dolomit, $CaMg(CO_3)_2$ und Fe-Dolomit zeigen, dass Dolomit im $P-T$-Bereich zwischen 5-7 GPa und 800-1300 K zu Magnesit $MgCO_3$ und Aragonit zerfällt, während Fe-Dolomit bei hohem Druck und hohen Temperaturen stabiler sein könnte als Karbonate mit einzelnen Kationen. Daher wird Fe-Dolomit als ein brauchbarer Kandidat für die Darstellung von Kohlenstoffreservoiren in der Erde angesehen. Drei gut charakterisierte Proben von Fe-Dolomit mit einem Gehalt an $CaFe(CO_3)$, x, von 0.05 (Ank-1), 0.29 (Ank-4) und 0.40 (Ank-2) sowie eine Ankeritprobe mit $x = 0.63$ (Ank-5) wurden untersucht. Die Proben Ank-1, Ank-2 und Ank-5 wurden bei Umgebungsbedingungen mittels Brillouin-Spektroskopie untersucht. Die Proben Ank-2, Ank-4 und Ank-5 wurden mit Hochdruck-Sychrotron-Pulver-XRD-Experimenten untersucht. Die Kombination von Brillouin-Spektroskopie und Hochdruck-Pulver-Röntgendetektion zeigt eine deutliche Abhängigkeit der elastischen Eigenschaften von der chemischen Zusammensetzung. Das Vorhandensein von $CaFe(CO_3)_2$ hat einen bemerkenswerten Einfluss auf die elastischen Tensorkoeffizienten: C_{11}, C_{33} und C_{44} zeigen eine Abnahme von 17% (für C_{11} und C_{33}) und 13% (C_{44}) mit zunehmendem $CaFe(CO_3)_2$-Gehalt; C_{12} und C_{15} zeigen eine Zunahme von 9% und 20% mit zunehmendem $CaFe(CO_3)_2$-Gehalt. Frühere Studien zu den elastischen Eigenschaften von $MgCO_3$-$FeCO_3$-Mischkristallen zeigten ein ähnliches Verhalten der elastischen Tensorkoeffizienten in Abhängigkeit vom $FeCO_3$-Gehalt. Der Effekt der Mg-Substitution durch Fe, der zu einer Verringerung des Schermoduls und der Schallgeschwindigkeiten führte, hatte jedoch keine Auswirkungen auf den Volumenmodul der $MgCO_3$-$FeCO_3$-Mischkristalle. Die Ergebnisse meiner Studie über $CaMg(CO_3)_2$-$CaFe(CO_3)_2$-Mischkristalle zeigen, dass das Vorhan-

densein von Fe in der Struktur zu einer Senkung sowohl des Schütt- und Scheraggregatmoduls als auch der Schallgeschwindigkeiten führt. Insbesondere die Abhängigkeit des Schüttgutmoduls vom $CaFe(CO_3)_2$-Gehalt zeigt ein nichtlineares Verhalten mit einem Minimum um 40 mol%.
Neben der Untersuchung der elastischen Eigenschaften von kristallinen Karbonaten in Abhängigkeit von ihrer Zusammensetzung wurde die Bedeutung der kationischen Substitution für die Struktur und das Hochdruckverhalten von Karbonaten durch die Untersuchung eines synthetischen $SrCO_3$-$CaCO_3$-Mischkristalls untersucht. Die Probe wurde bei 2 GPa und 1300 K in einer Multianvil-Apparatur synthetisiert, um einen $Sr_xCa_{1-x}CO_3$-Mischkristall mit Calcit-Struktur und $x = 18$ mol% zu erhalten. Ich untersuchte die Auswirkungen von Sr auf die Struktur und das Phasenverhalten bei Umgebungsbedingungen und bei hohem Druck (bis zu 9 GPa), indem ich Synchrotron-basierte Einkristall-Röntgenbeugungsexperimente durchführte. Bei Umgebungsbedingungen führt das Vorhandensein von 18 mol% Sr zu einer strukturellen Veränderung im Vergleich zu reinem Calcit, und $Sr_{0.18}Ca_{0.82}CO_3$ kristallisiert in einer monoklinen Struktur, Raumgruppe $P2_1/c$ und $Z = 4$, einer neuen Struktur, die zum ersten Mal im System $SrCO_3$-$CaCO_3$ beobachtet wurde, ähnlich der Calcit-II-Struktur, genannt Sr-Calcit-II (Sr-CC-II). Die Parameter der Einheitszelle sind $a = 6,4237(7)$ Å, $b = 5,0176(1)$ Å, $c = 8,1129(1)$, $\beta = 108,064(1)^\circ$ und $V = 248,60(1)$Å^3. Die Transmissionselektronenmikroskopie-Analyse wurde auch an mehreren Proben aus derselben Synthesecharge wie die mittels XRD untersuchten Proben durchgeführt und zeigte das Vorhandensein komplexer Zwillings- und Antiphasendomänen, Sie zeigten das Vorhandensein komplexer Zwillings- und Antiphasendomänen, die auf eine Umlagerung von Atomen aus einer anfänglich ungeordneten calcitartigen Phase ($CaCO_3$-IV oder $CaCO_3$-V, beschrieben durch Orientierungsstörungen der CO_3-Gruppen) unter den Synthesebedingungen hinweisen, die sich während des schnellen Abschreckens auf Umgebungsbedingungen geordnet und in die Sr-CC-II-Phase umgewandelt hat. Bei 1.7 GPa verwandelt sich Sr-CC-II in ein neues Polymorph, Sr-CC-III (monoklin, Raumgruppe $P2_1/m$, $Z = 8$). Sr-CC-III unterscheidet sich von allen bekannten Polymorphen von reinem $CaCO_3$, weist jedoch einige Gemeinsamkeiten mit den metastabilen Hochdruck-Polymorphen von Calcit $CaCO_3$-III und $CaCO_3$-IIIb auf, wie z. B. die nichtkoplanaren CO_3-Gruppen und das Vorhandensein von kationischen Stellen mit unterschiedlicher Koordinationsgeometrie. Sr-CC-III wird bis zu einem maximalen experimentellen Druck von etwa 9 GPa beobachtet. Die Anpassung einer Birch-Murnaghan-Zustandsgleichung zweiter Ordnung an die experimentellen Volumina für die Sr-CC-III-Phase ergibt extrapolierte Werte für das Volumen und den Volumenmodul von $V_0 = 474(1)$ Å^3 und $K_0 = 69(2)$ GPa.

In dieser Arbeit wurde die Untersuchung der elastischen Eigenschaften von Carbonaten nicht nur auf kristalline Materialien beschränkt, sondern auch auf amorphes Calciumcarbonat (ACC) ausgedehnt. ACC ist die am wenigsten stabile polymorphe Form von $CaCO_3$ und ist eine Verbindung, die mehr als einen amorphen Zustand (Polyamorphie) aufweist, wobei jede Form eine unterschiedliche Kurzstreckenordnung hat. ACC ist ein Material von großem Interesse, da es der Vorläufer für kristalline $CaCO_3$-Polymorphe ist, die an der Erdoberfläche vorkommen. Darüber hinaus wurde in einer neueren Studie erörtert, dass ACC auch für die Erforschung der Erdtiefe von Interesse sein könnte, da der temperaturbedingte Phasenübergang von Aragonit zu ACC im Bereich des Phasendiagramms von $CaCO_3$ oberhalb von 3 GPa und 1000 K beobachtet wurde. In dieser Arbeit wurden die Schallgeschwindigkeiten und elastischen Eigenschaften von drei synthetischen ACC-Proben mit unterschiedlichen Wassergehalten bis zu 18 Gew.% durch Brillouin-Spektroskopie bis zu 20 GPa bestimmt. Die Ergebnisse dieser Studie zeigen eine gleichmäßige Druckabhängigkeit der akustischen Geschwindigkeiten mit dem Druck während der Kompression und Dekompression. Es wurden keine Anomalien bei 10 GPa beobachtet, einem Druck, bei dem zuvor in einer XRD-Hochdruckstudie ein struktureller Phasenübergang für wasserhaltiges ACC festgestellt worden war. Der Unterschied zwischen dem isothermen und dem isentropen Volumenmodul, der mit zunehmendem Druck zunimmt, scheint jedoch auf eine kontinuierliche Entwicklung der lokalen Struktur von ACC bei der Kompression hinzudeuten. Diese Studie zeigt, dass die Zugabe von 18 Gew.% H_2O zu einer Erweichung von 38% des Volumenmoduls und 36% des Schermoduls von ACC führt. Der Vergleich zwischen den elastischen Eigenschaften von wasserfreiem ACC und Aragonit zeigt, dass ACC im Druckbereich zwischen 0 und 20 GPa stärker komprimierbar ist als Aragonit. Der Temperatureffekt wurde nicht berücksichtigt, da der Einfluss des Drucks auf die elastischen Eigenschaften von Karbonaten viel größer ist. Die Ergebnisse unserer Studie zeigen, dass eine Amorphisierung von Aragonit im $P-T$-Bereich zwischen 4.8 und 8 GPa zu einer Erweichung dieses Karbonats (Senkung des Volumenmoduls um -25% und des Schermoduls um -40%) und zu einer Veränderung der mechanischen Eigenschaften von Kalziumkarbonat und der Schallgeschwindigkeiten (-7.3% der longitudinalen und -15% der transversalen Schallgeschwindigkeiten) führen würde. Dies könnte wichtige Auswirkungen auf die Charakterisierung von Prozessen haben, die mit dem Metling und der Dekarbonisierung der subduzierenden Platten und dem Recycling von Kohlenstoff in den Subduktionszonen zusammenhängen. Darüber hinaus wurde die Untersuchung der Auswirkung der Zusammensetzung auf die elastischen Eigenschaften von Familien isostruktureller Festkörper auch auf eine andere Klasse von Materialien ausgedehnt, die Metall-

Guanidinium-Formiate (MGF), $C(NH_2)_3M^{II}(HCOO)_3$, mit M^{II} =Mn, Zn, Cu, Co, Cd und Ca. Diese Materialien kristallisieren in orthorhombischer Symmetrie. MnGF, ZnGF und CoGF sind isostrukturell mit der Raumgruppe $Pnna$. CuGF hat eine ähnliche Kristallstruktur, weist aber als Cu^{2+} ein Jahn-Teller-Ion eine stärkere Verzerrung der konstituierenden Polyeder auf und kristallisiert in der Raumgruppe $Pn2_1a$. In dieser Studie wurden synthetische Kristalle jeder Zusammensetzung durch eine Kombination aus Brillouin-Spektroskopie (BS), plattenparalleler ebener Wellentechnik (PPPW), Resonanz-Ultraschallspektroskopie (RUS), Dichtefunktionaltheorie (DFT) und thermisch diffuser Streuungsanalyse (TDSA) untersucht. Insbesondere wurden die elastischen Eigenschaften von (i) MnGF mittels BS, DFT und TDSA untersucht; (ii) ZnGF durch BS, PPPW, RUS und DFT; (iii) CuGF durch PPPW, RUS und DFT und (iv) CoGF durch DFT. Die mit den verschiedenen Techniken erzielten Ergebnisse stimmen perfekt überein, mit Ausnahme des C_{33}-Koeffizienten von MnGF und ZnGF, der durch DFT-Berechnungen erhalten wurde und der viel größer (15%) als die experimentell ermittelten Werte ist. Unsere Ergebnisse zeigen, dass die elastischen Eigenschaften der Aggregate und die Koeffizienten der elastischen Tensoren stark von der Größe des M^{II}-Kations abhängen. Größere M^{II}-Kationen führen zu weicheren Verbindungen. Die kationische Substitution mit Cu, einem Jahn-Teller-Ion, verursacht eine strukturelle Verzerrung, die zu einer drastischen Erweichung des Materials führt, verglichen mit ZnGF und CoGF. Unsere Ergebnisse bestätigen auch die in früheren XRD- und Neutronenbeugungsstudien an Einkristallen beobachtete axiale Komprimierbarkeit von MnGF und ZnGF entlang der c-Achse, die nahezu null beträgt.

Summary of the thesis

Carbon is an element that controls planetary habitability, and is fundamental for life on Earth. Its behaviour has important consequences for the global climate system, the origin and evolution of life on Earth. While the biosphere and atmosphere's carbon cycle only accounts for less than 1% of the global carbon budget, hidden reservoirs of deep carbon in the Earth's interior comprise the predominant storage of carbon on the planet [218]. At the Earth's surface, 60-70 % of carbon is hosted by carbonate minerals [90], which are then transported to the Earth's interior, mainly in the form of sediments, by subduction of the oceanic lithosphere. Subducting plates are subjected to decarbonation, dehydration, and melting with CO_2 release via supra-subduction volcanism. Nevertheless, part of the subducted carbonates' may survive and be further transported to the deep mantle [108, 185]. Direct evidence of the existence of carbonates in the Earth's interior, possibly reaching down to the lower mantle, comes from the finding of syngenetic inclusions of carbonates in diamonds [242, 226, 119, 27, 102, 264] and mantle xenoliths [263]. The presence of carbonates in the deep Earth has a critical effect on the physical properties of the mantle. Melting and chemical speciation of the mantle are strongly affected by the form of C and carbonate stability [58, 59]. Therefore, the study of the stability and physical properties of carbonates at high pressures and temperatures is fundamental, because understanding the processes involved in the deep carbon cycle helps to improve our picture of the whole mantle.
The systematic characterization of the elastic properties of carbonates as a function of their structure and chemical composition is of great importance because it may allow to identify their presence and distribution by seismology. Inverting seismic observations to successfully constrain the chemical composition and mineralogy of the Earth's interior requires knowledge of the physical properties of all possible Earth's materials at pressures and temperatures applicable to the Earth's interior. Up to now, a multitude of studies has focused on the construction of phase diagrams and structural transitions by means of X-ray diffraction and vibrational spectroscopy experiments [86].

Few studies are available on the complete elastic tensor of carbonates, however most of the datasets are not accompanied by an accurate characterization of the samples, which are often solid solutions and the exact chemical composition, density or the details about the experimental methods used are not presented. The aim of this thesis is to study the effect of chemical composition on the elastic properties of carbonates, providing a reliable dataset on the elasticity of the main carbonates. In particular, the elastic properties of crystalline aragonite, $CaCO_3$, and Fe-dolomite, $(Ca, Mg, Fe)(CO_3)_2$, with different compositions were studied by Brillouin spectroscopy at ambient conditions. Brillouin spectroscopy was also used to investigate the elastic behaviour of amorphous calcium carbonate samples with different water contents (up to 18 wt%) at high pressures, up to 20 GPa.
Furthermore, the importance of cationic substitution on the structure and high pressure behaviour of carbonates was investigated by studying a synthetic $CaCO_3$-$SrCO_3$ solid solution at ambient conditions and at high pressures, up to 10 GPa, by single crystal X-ray diffraction. Finally, the study of the effect of composition on the elastic properties of families of isostructural solids was also extended to a different class of materials, the metal guanidinium formates. The elasticity of a family of perovskite metal organic frameworks, metal guanidinium formates $C(NH_2)_3M^{II}(HCOO)_3$, with M^{II} =Mn, Zn, Cu, Co, Cd and Ca was investigated by combining Brillouin spectroscopy, resonant ultrasound spectroscopy, density functional theory and thermal diffuse scattering analysis.

Chapter 1

Introduction

> If you thought science was certain-well, that is just an error on your part.
>
> Richard Feynman

1.1 Motivation

Carbon is one of the most important elements on Earth. It is fundamental for the global climate system, the origin and evolution of life, carbon-based energy resources, and for a vast array of materials that are central to our daily lives [172]. Carbon moves through the surface and the Earth's interior in what is called the deep carbon cycle. In fact, most of C on Earth is stored in the core and the mantle and only 1 % of the global carbon contributes to the well-known surface carbon cycle between the atmosphere and biosphere [219].
Carbon from the oceanic lithosphere (sediments, crust and lithospheric mantle) is carried into the deep Earth, mainly in the form of carbonates, by subduction of the oceanic lithosphere [185]. The amount of carbon that is subducted into the mantle varies from trench to trench, however estimates are in the order of megatons per year, 61-114 Mt C/y [59], 40-66 Mt C/y [108]. Depending on the slab temperature and redox conditions, the sedimentary carbon budget (seawater-precipitated and organic carbon) is subjected to decarbonation, dehydration and melting and is released on the mantle wedge and recycled back into the surface by volcanism [59, 108, 51, 204, 185]. In warmer slabs, carbonate in metasedimentary rocks will be lost generating carbonated melts and recycled back to the surface of the Earth. The flux of

carbon that is recycled to the surface via volcanism, although not well constrained, is estimated in the order of megatons per year (31-127 Mt C/y [59], 26-85 Mt C/y [108]), about 40-70% of the subducted C budget [59]. Colder slabs, however, are not predicted to form carbonate melts at any depth above the lower mantle and can transport carbon into the deep Earth [216]. Despite the many studies on C fluxes, accurate estimates of carbon abundances in the Earth's interior are challenging, as they take into account the unknown primordial C budget [146] and the low solubility of carbon in mantle silicates [109, 197, 210], the low modal abundance of accessory C-bearing minerals and graphite/diamond in mantle xenoliths [172]. The estimated amount of C overall inventory in the Earth is in the range between 370(150) and 740(370) ppm [72].

Carbon on Earth can be found in different forms, depending on the redox and hydration states and pressure-temperature conditions. In particular, about 60-70% of the Earth's surface C budget is hosted by carbonate minerals [90]. Solid carbonates can be found as stable phases in the deep Earth, up to at least the transition zone, as evidenced by inclusions in diamonds [242, 226, 119, 27, 102, 264] and mantle xenoliths [263, 134]. In some shallow parts of the oceanic mantle temperatures are too high for the crystalline carbonate forms to be stable and C is generally dissolved in melts or fluids. On the other hand, the deeper part of the mantle can be too reduced to favor stable carbonates and C is hosted in reduced carbon phases such as diamond and graphite [59]. Additionally, C can be found in the form of Fe carbides in the Earth's mantle, depending on the metallic Fe and C ratios [59]. Fig. 1.1 represents a summary of the distribution of the different C species inside the Earth focusing on the asthenospheric mantle, continental lithosphere and the subducted slabs [172].

The presence of carbonates in the deep Earth has a tremendous influence on the partial melting of mantle lithologies, which leads to chemical differentiation of the mantle [58, 57, 59]. The occurrence of partial melting could be the reason for some low velocity zones in the upper mantle [59]. Furthermore, carbonate melts in the deep Earth have important implications for the origin deep focus earthquakes (occurring below 300 km) [216, 265]. Earthquakes at depths greater than 70 km are limited to a few regions associated with current or recent subduction. Intermediate depth earthquakes (70-300 km) result from the dehydration of minerals in the subduction slab, however deep seismicity (300-690 km) is not yet fully understood [253]. Mechanisms for earthquakes happening at depths lower than 70 km, according to modern theories, are associated to three different non-mutually exclusive causes: (i) phase transformations which cause volume decreases and nanocrystalline reaction products, thus leading to seismic events (i.e. phase transformation

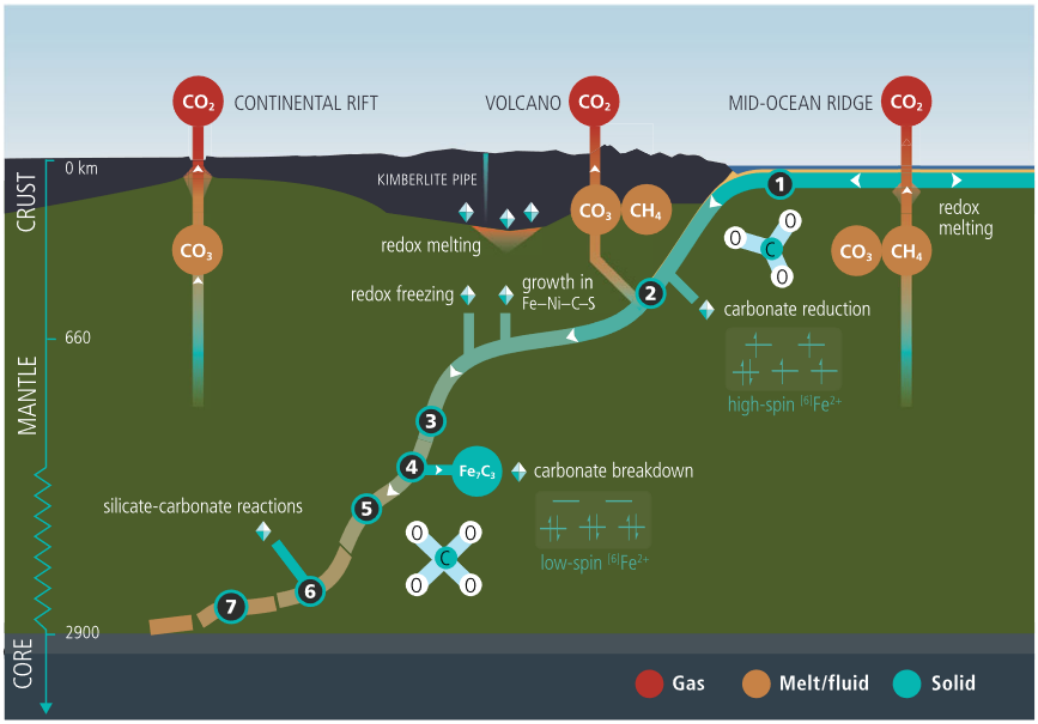

Figure 1.1: Cartoon of distribution and forms of C inside the Earth. Red circles: gas form of C; Orange circles are fluid or molten forms of C; green circles represent accessory solid phases of C, while the octahedra are diamond phases. The numbers indicate the important phase transitions in carbonates: (1) calcite to aragonite; (2) dolomite to dolomite-II, (3) aragonite to postaragonite; (4) dolomite-II to dolomite-III; (5) Fe sp^2-carbonate to Fe sp^3-carbonate, (6) postaragonite to sp^3-carbonate; (7) magnesite to magnesite-II. Figure from Orcutt et al. (2019) [172].

from olivine to wadsleyite and ringwoodite); (ii) shear heating and thermal run-away mechanisms that enable significant fault ruptures due to the high temperatures generated along a propagating fault tip; (iii) the formation of thin melt layers along the fault zones. In a recent study, Shirey et al. (2021) [216] discuss phase relationships for carbonate-bearing altered ocean crust suggesting that carbonate is retained in old, cold subduction zones to transition zone depths, where it will form carbonated melt. The presence of carbonate melt at transition zone conditions, provides a viable explanation for deep earthquakes [216, 249].

The study of deep carbon has attracted a lot of interest from the twenty-first century, aiming at understanding the C amount, distribution, form and stability in the Earth. For this purpose the Deep Carbon Observatory was es-

tablished (DCO; http:// deepcarbon.net) in 2009. Furthermore, in 2015 a research group funded by the Deutschen Forschungsgesellschaft (DFG) named CarboPaT was also established aiming to understand the physical properties and phase stability of carbonates at high pressure and temperature conditions (https://www.goethe-universityfrankfurt.de/48626215/for2125). This work of thesis is part of Project 9 within the CarboPaT research group and focuses on the creation of an accurate database of the elastic properties of the main carbonates.

The systematic characterization of the elastic properties of carbonates as a function of their structure and chemical composition is of great importance to identify their presence and distribution by seismology. Elasticity is a property fundamental for understanding the structure and properties of the Earth as seismic waves provide the most important information on the Earth's interior. Seismic waves are elastic waves traveling through the Earth, whose velocity can be calculated based on the knowledge of the elastic properties of the minerals and rocks they travel through. Seismological observations allowed to identify several features in the Earth's structure, such as large low shear velocity provinces, anomalies in the velocities across the transition zone and pervasive scatterers throughout the mantle [142]. Most of these features are still poorly understood. Inverting seismic observations to successfully constrain the chemical composition and mineralogy of the Earth's interior requires knowledge of the physical properties of all possible Earth's materials at pressures and temperatures relevant for the Earth's interior. Phase transitions, chemical reactions, texturing and deformation, which affect the elastic properties of the rocks of the mantle are known to influence, and sometimes dominate, seismic velocities [142, 106].

Reliable datasets of the elastic properties of carbonates as a function of their structure, composition and pressure-temperature conditions are fundamental to determine if carbonates could be viable candidates to explain the anisotropic anomalies observed in the mantle and possibly quantify the amount of C in the mantle. Up to now, a large number of studies have focused on the construction of phase diagrams by means of X-ray diffraction and vibrational spectroscopy experiments [86]. Few studies are available on the complete elastic tensor of carbonates, however most of the available datasets are on insufficiently characterized samples, whose exact chemical composition and density are not presented or clearly documented.

Experimental determination of the elastic properties of carbonates is also necessary as a benchmark for computational calculations [255]. *Ab initio* methods can predict the elastic properties of phases across the entire range of pressure and temperature conditions of the Earth's mantle with uncertainties smaller than 2-5%. Uncertainties associated with computational techniques

derive from the approximations used in the calculations, accurate experimental measurements are necessary to improve these approximations [142].
Carbonates were initially not considered to explain seismic discontinuities due the low abundance of C within the Earth and lack of knowledge on the elasticity of these minerals at pressure temperature conditions relevant to the mantle. However, the presence of carbonates at different depths, proved by direct observation of inclusions in deep diamonds [27], has the potential to alter the elastic properties of mantle rocks, making carbonates potentially seismically detectable. In the following, a description of carbonates and the state of the art on the main carbonates stability and elastic properties will be provided.

1.2 Carbonates

Carbonates are by far the most abundant carbon bearing compounds on Earth. Solid carbonates exist both in amorphous and crystalline form, with more than 300 different mineral species that have received IMA approval (http://rruff.info/ima/) [86].
Carbonates can be grouped with respect to their crystal structure. The most common carbonates in the Earth's crust belong to three structure groups: calcite, aragonite and dolomite, shown in Fig. 1.2. Carbonates of alkaline earth or transition metal cations with atomic radii smaller or equal to Ca^{2+} belong in the calcite-type structure. Calcite-type carbonates crystallize in the trigonal symmetry and space group $R\bar{3}c$. Common examples of calcite-type minerals are calcite ($CaCO_3$), magnesite ($MgCO_3$), siderite ($FeCO_3$) and rhodocrosite ($MnCO_3$). Carbonates of metal cations with atomic radii of the same size or bigger than Ca^{2+} crystallize in the aragonite-type structure, with orthorhombic symmetry with space group $Pmcn$. Examples of aragonite-type carbonates are aragonite ($CaCO_3$), strontianite ($SrCO_3$), witherite ($BaCO_3$) and cerussite ($PbCO_3$). The dolomite-type structure group is topologically similar to the calcite-type and is commonly observed for double carbonates. The alternate layered structure, perpendicular to c, occupied by different cations causes the loss of a glide plane, resulting in the space group $R\bar{3}$. Examples of carbonates belonging to this structure group include dolomite $CaMg(CO_3)_2$, ankerite $CaFe(CO_3)_2$ and kutnohorite $CaMn(CO_3)_2$. In addition to the above mentioned carbonate groups, more than 90 species have been described, which crystallize in different structures (e.g. vaterite ($CaCO_3$) and huntite $CaMg_3(CO_3)_4$) but only a handful are common [86].
In addition to anhydrous carbonates, such as the ones mentioned above, hy-

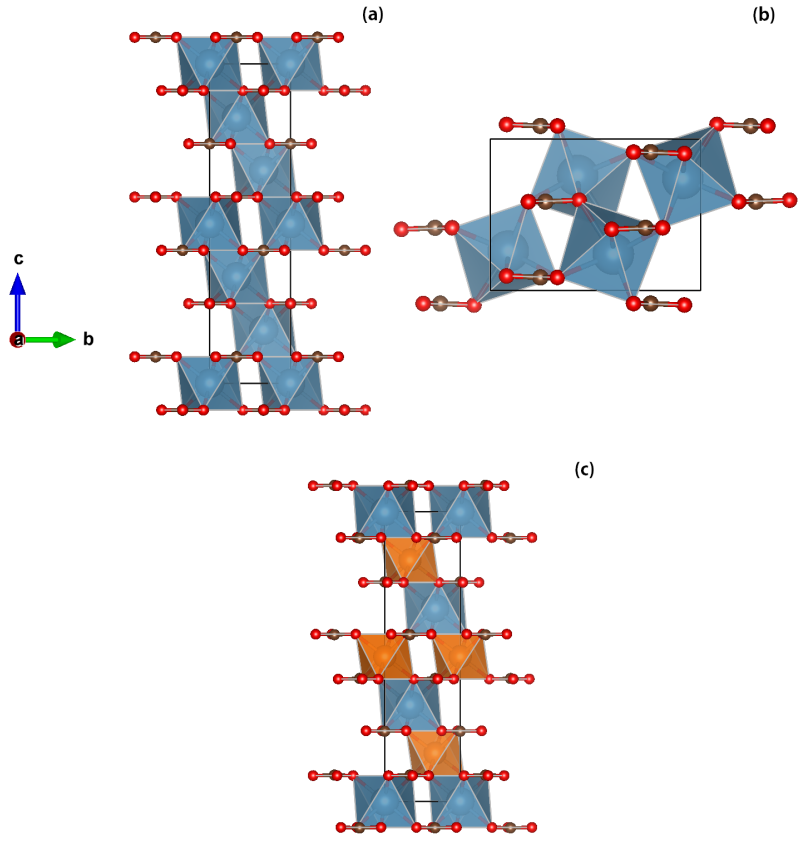

Figure 1.2: Crystal structures of calcite (space group $R\bar{3}c$) (a), aragonite (space group $Pmcn$)(b) and dolomite (space group $R\bar{3}$) (c). In blue are the Ca-O coordination polyhedra, in orange the Mg-O coodrination polyhedra. The red atoms are O, while brown atoms are C. Visualization from VESTA [161].

drous carbonate minerals are also found in nature. In the following the phase diagram and elastic properties of the main carbonates will be described.

1.2.1 Calcium carbonate, $CaCO_3$

Calcium carbonate, $CaCO_3$, is among the most abundant carbonates in crustal materials. At ambient conditions calcium carbonate exhibits three crystalline anhydrous polymorphs: calcite, vaterite, aragonite, and three hydrous forms: amorphous calcium carbonate (ACC), calcium carbonate monohydrate (monohydrocalcite, $CaCO_3{\cdot}H_2O$), and calcium carbonate hexahydrate (ikaite, $CaCO_3{\cdot}6\,H_2O$) [31]. Calcite is the thermodynamically stable phase at ambient conditions, and it has a trigonal structure and crystallizes

in the $R\bar{3}c$ space group with 6 formula units (Z); Ca is surrounded by 6 oxygens, while C is coordinates 3 oxygens. Aragonite is a high pressure polymorph but is metastably present at ambient conditions, especially as a product of biomineralization and precipitation processes. It has an orthorhombic structure and crystallizes in the $Pmcn$ space group with $Z = 4$, and unit cell parameters $a = 4.961(1)$ Å, $b = 7.970(2)$ Å, $c = 5.742(1)$ Å; Ca coordinates 9 oxygens. Vaterite is a metastable phase across the whole P-T range and its structure is composed of at least two different crystallographic structures that coexist within a pseudo-single crystal, with the major structure exhibiting hexagonal symmetry (space group $P6_3/mmc$, $Z = 6$ for the main structure and space group $Ama2$, $Z = 4$ for the secondary structure) [100, 47]. In the following, the phase diagram and elastic properties of $CaCO_3$ will be discussed.

The phase diagram of $CaCO_3$ is shown in Fig. 1.3, where the thermodynamically stable phases are represented by different colors. Upon temperature increase, calcite transforms to calcite-IV (at about 980 K) and calcite-V (at about 1200 K). The structure of calcite-IV belongs to the $R\bar{3}c$ space group, as calcite, but is characterized by orientational disorder of the CO_3 groups where the O atoms at Wyckoff position 18e can have different, but finite, arrangements around the C atom [97]. At higher temperatures, approximately at 1240 K, calcite-IV transforms to calcite-V. The space group of calcite-V is $R\bar{3}m$ and the c-length is halved compared to the calcite phase [10, 97, 96]. In calcite-V, the oxygen atoms exist with equal probability along the undulated circular orbital around the central carbon. The structures of calcite-I, calcite-IV and calcite-V are shown in Fig. 1.4.

Upon pressure increase, calcite transforms to aragonite, which is the thermodynamically stable phase up to 30 GPa. At higher pressures aragonite transforms to a new polymorph, $CaCO_3$-VII. $CaCO_3$-VII crystallizes in the monoclinic symmetry with space group $P2_1/c$ and with $Z = 4$ [13, 220, 120]. $CaCO_3$-VII was shown to have the same structure of the $P2_1/c - l$ polymorph, which had been previously predicted using *ab initio* random structure searching technique [182, 13, 75]. At pressures between 50 GPa and 90 GPa and temperatures in the range between 1500 and 2500 K, calcium carbonate crystallizes in the post-aragonite structure (space group $Pmmn$, $Z = 2$, $a = 4.101(1)$ Å, $b = 4.561(1)$ Å, and $c = 3.964(1)$ Å, at 66.4 GPa) [168].

Despite the numerous studies on $CaCO_3$ at high pressures and temperatures, there is still an area of the phase diagram, ranging from 3 to 11 GPa and 800 to 1600 K, that is still controversial (part of the phase diagram overlaid with line-shades Fig. 1.3). Suito et al. (2001) [230] suggested it might be a disordered crystalline phase, Litasov et al. (2017) [126] proposed a new phase to exist at these P-T conditions. Neither study, however, provided de-

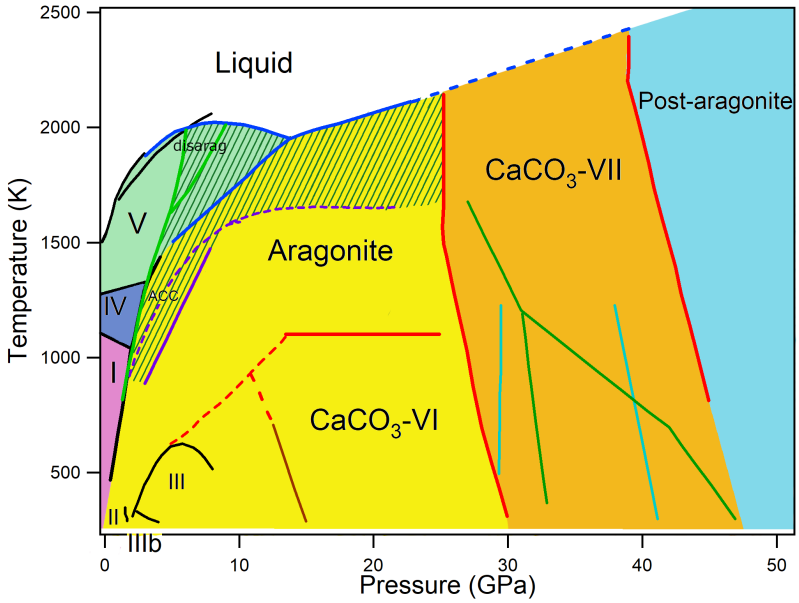

Figure 1.3: Phase diagram of $CaCO_3$. Different colors represent the thermodynamically stable phases. Black lines: phase boudaries from Suito et al. (2001) [230], Ter Heege and Renner (2007) [232]. Blue lines from show the melting curves from conductivity experiments [121], dashed line represents the extrapolated melting curve [129]. Red lines show the phase boundaries from Bayarjargal et al. (2018) [13]. Brown curve shows the phase transition from $CaCO_3$-III and $CaCO_3$-VI from Koch-Müller et al. (2016) [113]. The green lines show the phase boundaries between $CaCO_3$-V and aragonite and the disordered aragonite phase (disarag) from DFT calculations by Gavryshkin et al. (2020) [76] (the part of the diagram overlaid by lines-shade shows the disordered/amorphous aragonite phase). The purple curve show the phase boundary between aragonite and amorphous $CaCO_3$ from Hou et al. (2019) [92] (solid curve) and Litasov et al. (2017) [126] (dashed curve). The light blue lines represent the calculated phase boundary of $P2_1/c-l$ phase [220]. The dark green lines shows the calculated stability field of phase $CaCO_3$-VII [75]. The phase boundaries of metastable phases ($CaCO_3$-II, $CaCO_3$-III, $CaCO_3$-IIIb and $CaCO_3$-VI). Figure modified after Bayarjargal et al. (2018) [13].

tailed structural information on this phase. Hou et al. (2019) [92] observed a temperature-induced amorphization of aragonite at these P-T conditions, by performing energy-dispersive X-ray diffraction (EDXRD) experiments in a Paris-Edinburgh press. At about 5 GPa and 1470 K the XRD diffraction patterns are consistent with an amorphous phase, but at lower temperatures the presence of sharp peaks suggests the presence of a disordered crystalline

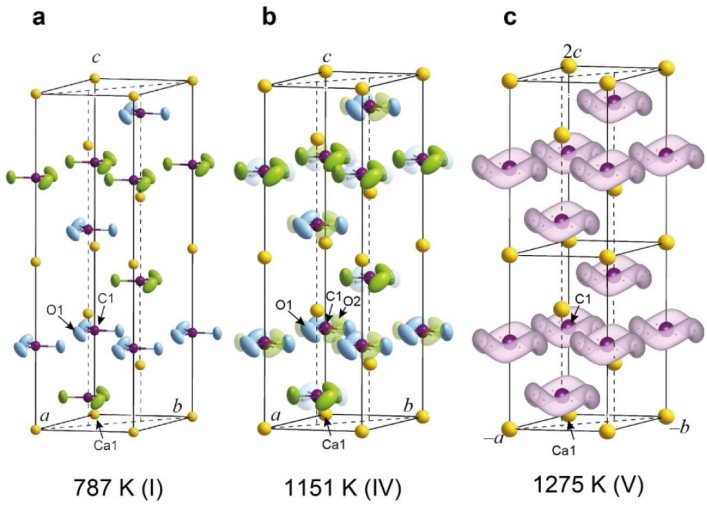

Figure 1.4: Structures of calcite (a), calcite-IV (b) and calcite-V (c). Figure from Ishizawa et al. (2013) [97].

phase [92]. Gavryushkin et al. (2020) [76] performed *ab initio* molecular dynamics (MD) calculations on calcite and aragonite, and observed a disordered phase of aragonite, disarag, to be stable at pressures between 3 and 10 GPa and temperatures between 1600 and 2000 K. Disarag is simiar to $CaCO_3$-V phase, with freely rotating CO_3 groups.

Calcite The behaviour of $CaCO_3$ upon compression, using calcite as starting mateiral, has been extensively studied to high pressures and temperatures [156, 150, 152, 184, 113, 13]. These studies reported that, at $T \sim$300 K, calcite undergoes a series of metastable phase trasformations. At 1.7 GPa calcite transforms to a new polymorph, $CaCO_3$-II [156]. $CaCO_3$-II has a monoclinic symmetry with space group $P21/c$ and $Z = 4$. Its structure can be described as a distortion of calcite. The phase transition from calcite to $CaCO_3$-II is a displacive transformation, and as such, $CaCO_3$-II is not quenchable to ambient pressure [156, 83]. The essential structural features of $CaCO_3$-II with respect to calcite are represented by a rotation of the CO_3 groups around the calcite trigonal axis and a displacement of the Ca atoms from the calcite $\bar{3}$ trigonal site Fig. 1.5a.
At 2.5 GPa, $CaCO_3$-II transforms to another phase, originally named $CaCO_3$-III, observed up to 15 GPa. However, further studies demonstrated that two different polymorphs can be observed in this pressure range, $CaCO_3$-III and $CaCO_3$-IIIb [150, 152, 184, 113]. Both $CaCO_3$-III and $CaCO_3$-IIIb (Fig. 1.5) are triclinic and crystallize in the space group $P\bar{1}$ with $Z = 10$ and $Z = 4$ re-

spectively [150]. The main crystallographic feature of $CaCO_3$-III and $CaCO_3$-IIIb, compared to calcite and $CaCO_3$-II, is the different arrangement of CO_3^{2-} carbonate units, which are no longer parallel to one another [150, 152, 184]. Furthermore, both $CaCO_3$-III and $CaCO_3$-IIIb contain non-equivalent Ca polyhedra in their structures, with coordination number varying from 7 to 9. There are five different cationic sites in $CaCO_3$-III and two sites (7 and 9 coordinated) in $CaCO_3$-IIIb [150].

At about 15 GPa $CaCO_3$-IIIb transforms to $CaCO_3$-VI [150, 113, 13].

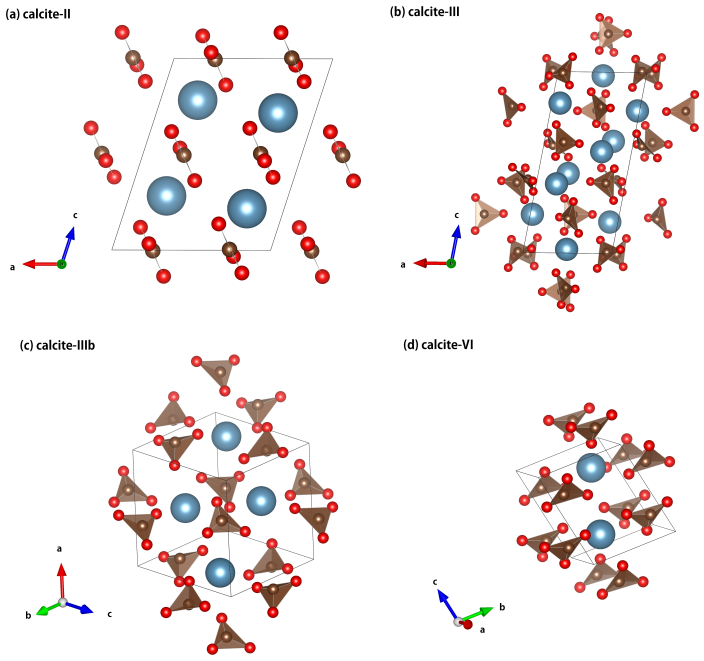

Figure 1.5: Structures of high pressure polymorphs of $CaCO_3$. Structural models drawn using VESTA [161].

$CaCO_3$-IV has triclinic structure with space group $P\bar{1}$. In this structure, the CO_3 groups are once again parallel, but the structure is no longer layered as in calcite. Furthermore, the Ca site has irregular coordination (7+2) with seven shorter Ca-O distances (2.1−2.3 Å) and two longer ones (2.5−2.6 Å) [150]. $CaCO_3$-II, $CaCO_3$-III and $CaCO_3$-IIIb, $CaCO_3$-VI are metastable phases and transform to aragonite upon heating.

At higher pressures (> 30 GPa) and temperatures (> 500 K) both aragonite and $CaCO_3$-VI transform to $CaCO_3$-VII [13]. In this thesis we focused on the pressure range betwen 0 to 20 GPa. Fig. 1.5 shows the structures of $CaCO_3$ high pressure polymorphs in this pressure range.

Aragonite The high pressures behaviour of $CaCO_3$ using aragonite as starting material, has also been reported in previous studies [126, 13]. Aragonite is stable upon compression up to about 25 GPa, pressure at which aragonite transforms to $CaCO_3$-VII. $CaCO_3$-VII transforms to post-aragonite at about 40 GPa [13, 120].
Differently from calcite, the compression of aragonite does not lead to the formation of metastable phases. Aragonite is stable in a wide range of pressures and temperatures. However, the phase diagram between 3 and 10 GPa and 1000 K is controversial. Some studies suggested the presence of a new disordered phase of aragonite, named disarag, similar to the high-temperature polymorph of calcite, $CaCO_3$-V [76, 126], while Hou et al. (2019) [92] suggested a temperature-induced amorphization of aragonite at these $P-T$ conditions.

Vaterite The behaviour of vaterite upon compression was studied by Maruyama et al. (2017) [147] who performed Raman spectroscopy and X-ray diffraction experiments on a synthetic vaterite sample up to 14 GPa. They observed two phase transitions at 4.3 GPa and 13.1 GPa to vaterite-II and vaterite-III. However, not all sample material transformed to the high pressure polymorphs of vaterite. Instead part of the sample transformed to $CaCO_3$-III.

Hydrous $CaCO_3$ phases Calcium carbonate has two known hydrous phases: ikaite, $CaCO_3{\cdot}6\,H_2O$, and monohydrocalcite $CaCO_3{\cdot}H_2O$ [37]. Ikaite is thermodynamically metastable at atmospheric pressure, but is stable at room temperature above 0.5 GPa. It crystallizes in the monoclinic system and belongs to the $C2/c$ space group and $Z = 4$. Monohydrocalcite crystallizes in the hexagonal system (space group $P3_1$, $Z = 9$).
Amorphous calcium carbonate (ACC) is the least stable non crystalline $CaCO_3$ polymorph and it possesses more than one amorphous state with calcite-like, vaterite-like and aragonite-like local structures [33]. High pressures studies on ACC reported a phase transition at about 10 GPa [70, 73].

Elasticity of $CaCO_3$

Calcite The full elastic tensor of calcite at ambient conditions has been determined in several studies (here the most recent studies only are reported) [45, 55, 56, 88, 239, 123]. Calcite has a trigonal symmetry with space group $R\bar{3}c$, as such elastic stiffness tensor is completely described by 6 different elastic tensor coefficients (see Ch. 1): C_{11}, C_{12}, C_{13}, C_{14}, C_{33} and C_{44}. The C_{66} coefficient is given by $C_{66} = (C_{11} - C_{12})/2$.

Dandekar et al. (1968a,1968b) [55, 56] determined the elastic tensor of calcite by ultrasonic pulse-echo experiments. Chen et al. (2001) [45] and Lin et al. (2013) [123] performed Brillouin spectroscopy experiments on natural calcite samples. The individual elastic tensor coefficients obtained from the different studies agree within 5%. In addition to the ambient conditions experiments, the high temperature behaviour of the elastic constants of calcite were investigated up to 900 K [56, 123]. Studies on the C_{ij} dependence on pressure were also performed [55, 239]. Finally, a high pressure Brillouin spectroscopy study was performed up to ∼10 GPa [266]. The results from the study however show a sudden lowering of the acoustic velocities at the transition from calcite to $CaCO_3$-II [266].

Table 1.1: Elastic tensor coefficients of calcite from the different literature studies: Chen et al. (2001)-Chen [45], Dandekar (1968)- Dandekar-a [55], Dandekar (1968)- Dandekar-b [56], Lin et al. (2013) [123].

C_{ij}	Chen [45]	Dandekar-a[55]	Dandekar-b[56]	Lin[123]
C_{11} (GPa)	149.4(7)	148.0(2)	146.3(5)	149.9(5)
C_{12} (GPa)	57.9(11)	55.4(9)	60(1)	59.5(2)
C_{13} (GPa)	53.5(9)	54.5 (9)	51(3)	57.3(3)
C_{14} (GPa)	-20.0(2)	-20.8(6)	-20.8(6)	-17.9(2)
C_{33} (GPa)	85.2(18)	85.7(1)	85.3(5)	87.0(4)
C_{44}(GPa)	34.1(5)	32.7(1)	34(2)	32.2(2)
C_{66}(GPa)	46(1)	46.3(4)	43.3(7)	45.2(5)

Aragonite Aragonite crystallizes in the orthorhombic symmetry with space group $Pmcn$ and $Z = 4$. The elastic tensor is completely described by 9 independent elastic tensor coefficients: C_{11}, C_{12}, C_{13}, C_{22}, C_{23}, C_{33}, C_{44}, C_{55} and C_{66} (see Ch. 1). The elastic tensor of aragonite has been determined in two experimental studies [240, 133]. The results of the two studies, shown in Tab. 1.2, differ substantially (up to more than 100% for the off-diagonal coefficients C_{13} and C_{23}). The elastic tensor of aragonite has also been determined by DFT calculations [166, 94]. Huang et al. (2017) [94] described the stability and elastic properties of aragonite and its high pressure polymorphs (post-aragonite and $P2_1/c - h$ phases) up to 150 GPa, showing the pressure behaviour of the elastic constants, velocities, elastic moduli and velocity anisotropies. Additional experiments are necessary to establish a consistent dataset. In this work of thesis, Brillouin spectroscopy (BS) experiments were performed on three, well characterized, natural aragonite samples at ambient conditions. The results are discussed in Ch. 3.

Table 1.2: Elastic tensor coefficients of aragonite from different experimental studies by Voigt (1910) [240] and Liu et al. (2005) [133] and DFT studies by Huang et al. (2017) [94] and Nguyen-Thanh et al. (2016) [166].

C_{ij}	Voigt [240]	Liu [133]	Huang [94]	Nguyen-Thanh [166]
C_{11}(GPa)	156.9	171(1)	162	172(4)
C_{12}(GPa)	36.6	60(1)	53.65	55(6)
C_{13}(GPa)	2	28(2)	26.42	33.4(8)
C_{22}(GPa)	87	110.1(9)	107.81	113(7)
C_{23}(GPa)	15.9	42(2)	42.77	46.4(9)
C_{33}(GPa)	85	98(1)	96.48	100.2(4)
C_{44}(GPa)	41.3	39.3(6)	41.91	37.2(1)
C_{55}(GPa)	25.6	24.2(4)	36.44	21(1)
C_{66}(GPa)	42.7	40.2(6)	19.59	41(3)

Vaterite and hydrated $CaCO_3$ phases No complete elastic tensor has been measured to this day for vaterite. It was, however, obtained in a computational study by Xiao et al. (2011) [259] (Tab. 1.3).
Recent studies [207, 37, 271] investigated the elastic and structural properties of $CaCO_3$ hydrated phases by first-principle calculations based on using standard (DFT-PBE) and dispersion corrected (DFT-D2) DFT. The complete elastic tensor for ikaite and monohydrocalcite is reported in two studies [207, 37] (Tab. 1.4).
The elastic properties of ACC were reported in a high pressure XRD study [70] (isothermal bulk modulus) and a Brillouin spectroscopy study [67]. ACC is an isotropic material, and as such, its elastic stiffness tensor is completely described by two independent C_{ij} (see Ch. 1): C_{11} and C_{12} (Tab. 1.4).

Table 1.3: Elastic tensor coefficients of vaterite from Xiao et al. (2011) [259].

C_{ij}	Xiao [259]
C_{11} (GPa)	86.6
C_{12} (GPa)	40.6
C_{13} (GPa)	61.2
C_{23} (GPa)	15.9
C_{33} (GPa)	170.6
C_{44} (GPa)	9.9
C_{66} (GPa)	23.0

Table 1.4: Elastic tensor coefficients of ikaite and monohydrocalcite from Chahi et al. (2020) [37] and ACC from Faatz et al. (2005) [67].

	Ikaite		Monohydrocalcite		ACC
C_{ij}	DFT-PBE [37]	DFT-D2 [37]	DFT-PBE [37]	DFT-D2 [37]	BS
C_{11} (GPa)	46.19	62.71	83.33	89.25	60
C_{12} (GPa)	18.05	23.64	22.54	24.35	32
C_{13} (GPa)	14.36	22.20	27.54	30.72	-
C_{15} (GPa)	-1.2	2.52	-	-	-
C_{22} (GPa)	75.57	93.13	-	-	-
C_{23} (GPa)	18.93	24.45	-	-	-
C_{25} (GPa)	-0.52	-0.77	-	-	-
C_{33} (GPa)	64.73	76.66	76.63	78.53	-
C_{35} (GPa)	-5.79	-8.10	-	-	-
C_{44} (GPa)	12.97	13.74	25.67	27.41	-
C_{46} (GPa)	-1.43	-0.78	-	-	-
C_{55} (GPa)	11.38	12.31	-	-	-
C_{66} (GPa)	17.24	19.83	30.39	32.46	-

1.2.2 Magnesite, $MgCO_3$

Magnesite, $MgCO_3$, has been observed in diamond inclusions that likely originated from the Earth's lower mantle and is considered to be the dominant carbonate in the mantle [103, 82]. $MgCO_3$ crystallizes in the trigonal structure with space group $R\bar{3}c$, as calcite. Studies have shown that magnesite is stable at pressure-temperature (P-T) conditions of the Earth's mantle [98, 169, 221, 139, 17]. The phase diagram of $MgCO_3$, shown in Fig. 1.6, has been the subject of several studies [107, 71, 98, 24, 221, 139]. In particular, it has been recently extended up to ∼148 GPa and ∼3600 K by Binck et al. (2020) [17] who combined Raman spectroscopy in the laser-heated DAC with DFT calculations. At high pressure and temperatures, magnesite transforms to a new polymorph, $MgCO_3$-II. $MgCO_3$-II is a carbonate with tetrahedrally coordinated carbon. It has a monoclinic symmetry and space group $C2/m$, and is stable over the entire P-T range of the Earth's lowermost mantle geotherm [17].

Elasticity of $MgCO_3$ Several studies reported the complete sets of elastic tensor coefficients for magnesite measured at ambient conditions [46, 202, 261, 95, 87]. Unfortunately, no error bar was provided in the study by Hear-

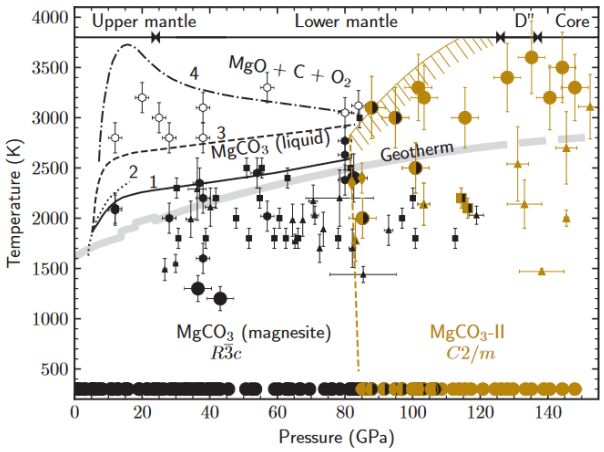

Figure 1.6: Phase diagram of $MgCO_3$. Figure from Binck et al. (2020) [17].

mon (1979) [87]. The results are shown in Tab. 1.5. The agreement between the individual coefficients is better than 5% except for C_{12}, C_{14} and C_{44}. However, it is important to stress that the sample by Chen et al.(2006) [46] for which the highest disagreement (10% in C_{12}) is reported does not present a chemical analysis of the material. Yang et al. (2014) [261] investigated the elastic tensor coefficients behaviour at high pressures (up to 14 GPa) and high temperatures up to 750 K. DFT calculations on the pressure dependence of the C_{ij} of $MgCO_3$ [227] showed perfect agreement, with the exception of C_{12}, with the data by Yang et al. [261]. $MgCO_3$, magnesite forms a complete solid solution with siderite ($FeCO_3$). $MgCO_3$-$FeCO_3$ solid solutions will be discussed in the next section.

Table 1.5: Elastic tensor coefficients of $MgCO_3$ from the different literature studies: Chen et al. (2006)[46], Yang et al. (2014) [261], Sanchez-Valle et al. (2011)-SV [202], Humbert and Plicque (1972)-HP[95], Hearmon (1979)-H [87]

C_{ij}	Chen [46]	Yang [261]	SV [202]	HP [95]	H [87]
C_{11} (GPa)	260(3)	261(1)	262(2)	258.7(2)	259
C_{12} (GPa)	83(5)	74(2)	76(2)	76(2)	75.6
C_{13} (GPa)	60(3)	60(2)	61(1)	58.8(6)	58.5
C_{14} (GPa)	-21(1)	19.7(2)	19.8(3)	19.0(1)	19.0
C_{33} (GPa)	154(4)	158(3)	157(2)	155.5(5)	156
C_{44} (GPa)	60(1)	57.8(4)	58.4(5)	54.8(5)	54.8
C_{66} (GPa)	88(6)	93(2)	93(3)	91(2)	91.7

1.2.3 Siderite, $FeCO_3$

Siderite, $FeCO_3$, is isostructural to calcite and magnesite, crystallizing in the trigonal symmetry with space group $R\bar{3}c$, with $Z = 6$. The phase diagram of $FeCO_3$, shown in Fig. 1.7, and its equation of state have been studied both experimentally and computationally [23, 132, 127, 36, 163]. At about 40 GPa, Fe in siderite undergoes a spin transition from a high spin state (HS) to a low spin state (LS) [131]. The HS-LS transition in $FeCO_3$ leads to a volume reduction (6-10%) making the LS state denser and more incompressible than the HS state [131]. This has important implications for carbonates seismic detectability. At high pressure and temperatures conditions siderite decom-

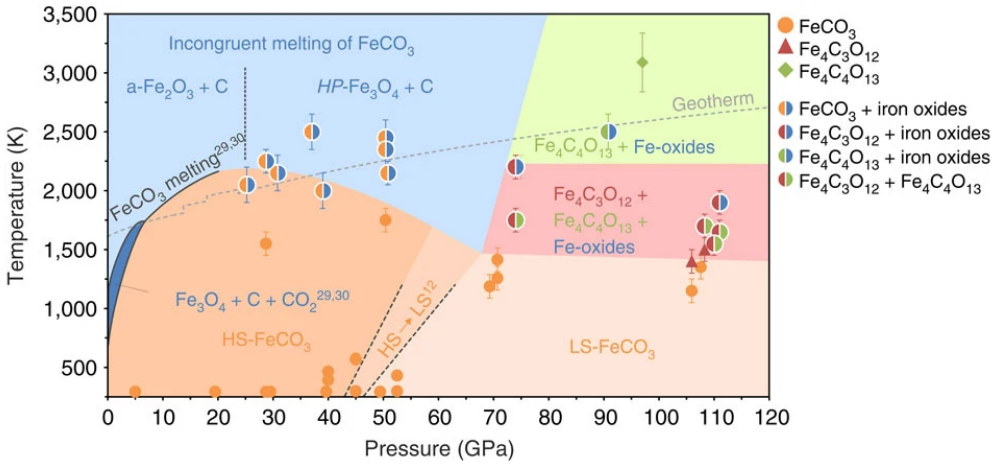

Figure 1.7: Phase diagram of $FeCO_3$. Figure from Cerantola et al. (2017) [36].

poses into several oxides (i.e. Fe_2O_3, Fe_3O_4, Fe_5O_7 and Fe_4O_5) or transforms to tetrahedrally coordinated carbonate [36, 118].
Siderite is partially soluble in calcite, but forms a complete solid solution with $MgCO_3$. Solid solutions with a Mg-rich part are named ferromagnesites, while solid solutions with a Fe-rich part are called magnesiosiderites. The effect of composition on the spin transition has been investigated in several high pressure studies [74, 124]. The high pressure behaviour of $FeCO_3$-$MgCO_3$ solid solutions has been the object of several studies [26, 249, 155, 43].

Elasticity of $FeCO_3$ The complete elastic tensor of end-member siderite at ambient conditions is reported in only one experimental study, in which the elastic properties of $MgCO_3$, $FeCO_3$ and $MgCO_3$-$FeCO_3$ solid solutions were

investigated by Brillouin spectroscopy [202]. The results of this study, in combination with high pressure DFT and experimental studies on $MgCO_3$-$FeCO_3$ solid solutions investigated the effect of the Fe content on the elastic properties of solid solutions [227, 74]. In particular, Stekiel et al. (2017) [227] combined inelastic X-ray scattering experiments and DFT calculations to investigate the high pressure dependence of the elastic tensor coefficients of $MgCO_3$-$FeCO_3$ solid soltions with different compositions. Fu et al. (2017) [74] performed high pressure Brillouin spectroscopy experiments up to 70 GPa. Fig. 1.8 shows the results of these studies. It is evident that the presence of Fe has a strong effect on the individual elastic tensor coefficients, leading to variations up to 30%. These results confirm the importance of chemical composition on the evaluation of the elastic properties of the studied materials.

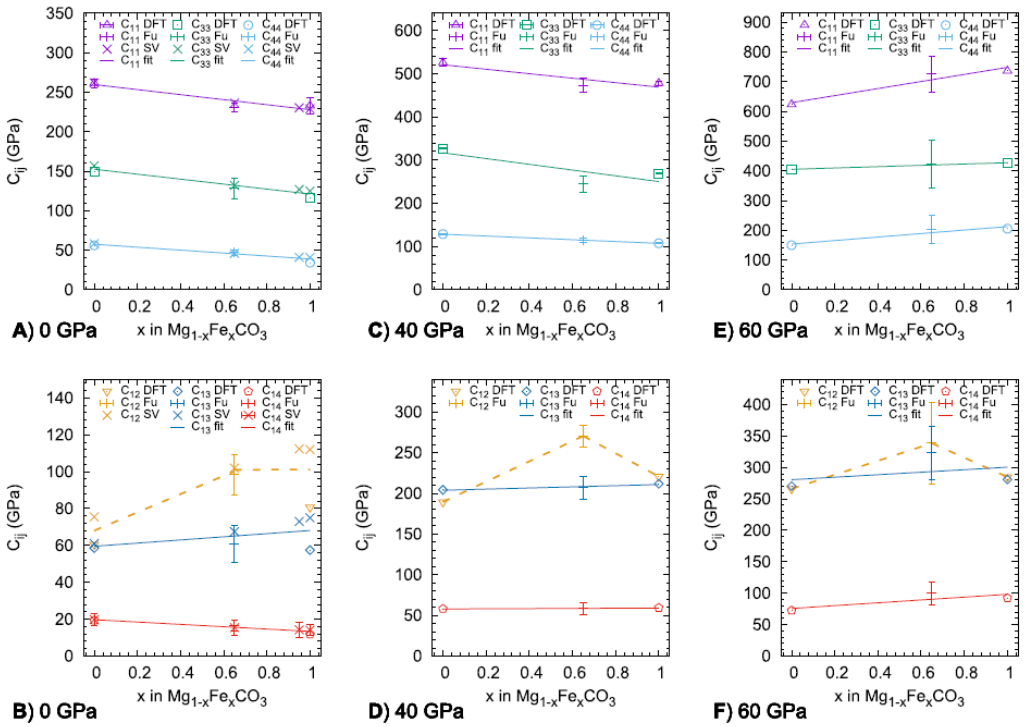

Figure 1.8: Elastic tensor coefficients from DFT [227] and BS experiments ([202, 74]) as function of composition for pressures of 0 GPa (A,B), 40 GPa (C,D) and 60 GPa (E,F). Figure from Stekiel et al. (2017) [227].

In addition to the studies on the elastic tensor coefficients, a study on the single crystal X-ray diffraction and nuclear inelastic scattering of two synthetic samples of siderite and magnesiosiderite (with composition $Fe_{0.26}Mg_{0.74}CO_3$) reported the high pressure dependence on the acoustic wave velocities [44].

Table 1.6: Elastic tensor coefficients of $FeCO_3$ from Sanchez-Valle et al. (2011)-SV [202] and Stekiel et al. (2017) [227].

C_{ij}	SV [202]	Stekiel (DFT) [227]
C_{11} (GPa)	229(2)	227.9
C_{12} (GPa)	112(2)	105.2
C_{13} (GPa)	75(3)	68.1
C_{14} (GPa)	14.0(3)	13.4
C_{33} (GPa)	125(2)	121.2
C_{44} (GPa)	41(1)	39
C_{66} (GPa)	59(3)	61.4

1.2.4 Rhodocrosite, $MnCO_3$

Rhodocrosite, $MnCO_3$, is a calcite-type carbonate and crystallizes in the trigonal symmetry with space group $R\bar{3}c$ and $Z = 6$. Compared to $CaCO_3$, $MgCO_3$ and $FeCO_3$, rhodocrosite is not a significant constituent of rock assemblages in subduction zones, but $MnCO_3$ commonly found as a minor component in other carbonates, such as calcite and dolomite. The high pressure stability, equation of state and vibrational properties of $MnCO_3$ have been studied at high pressures by XRD and spectroscopy experiments [170, 25, 130, 268]. At about 44 GPa [130, 154] $MnCO_3$ transforms to a new polymorph, $MnCO_3$-II, isostructural to $CaCO_3$-VI [154]. Shi et al. (2012) [213] studied $CaCO_3$-$MnCO_3$ solid solutions to investigate the effect of Mn incorporation on the phase stability and elastic properties of $CaCO_3$.

Elasticity of $MnCO_3$ The complete elastic tensor of rhodocrosite $MnCO_3$ was studied by Brillouin spectroscopy at ambient conditions by Chen et al. (2001) [45]. Furthermore, a BS study on the high pressure behaviour of the elastic properties of rhodocrosite at pressures up to 10 GPa was also conducted by Zhao et al. (2018) [267].

Table 1.7: Elastic tensor coefficients of $MnCO_3$ from Chen et al. (2001) [45].

C_{ij}	Chen [45]
C_{11} (GPa)	224(2)
C_{12} (GPa)	93(2)
C_{13} (GPa)	76(2)
C_{14} (GPa)	-17.3(6)
C_{33} (GPa)	133(4)
C_{44} (GPa)	44.5(9)
C_{66} (GPa)	66(3)

1.2.5 Dolomite, $CaMg(CO_3)_2$ and Ankerite, $Ca(Fe, Mg)(CO_3)_2$

Dolomite, $CaMg(CO_3)_2$, is a common carbonate on the Earth's surface and is considered one of the possible constituents of the Earth's carbon reservoirs [153, 236]. It is the stoichiometric calcium and magnesium double carbonate stable at ambient conditions. Dolomite crystallizes in the trigonal symmetry in the $R\bar{3}$ space group and $Z = 6$. In this structure Ca and Mg coordinate six oxygen atoms. The structure differs from that of calcite by the loss of a c glide plane due to the layered ordering of the Ca, Mg cations (Fig. 1.2c). The degree of cationic ordering is temperature-dependent. The structure becomes progressively disordered at 1300 K, and disordering is complete at temperatures below 1500 K and pressures in the range between 3-4 GPa [272]. A single crystal study on ordered and disordered dolomite by Zucchini et al. (2014) [273] showed that ordered dolomite is denser than the disordered one and that pressure stabilizes the ordered phase [273].
Ankerite is the Fe-rich double carbonate, isostructural to dolomite. The term ankerite was originally used to describe $Ca(Fe, Mg)(CO_3)_2$ carbonates independently from the Fe content. Nowadays, the term ferroan dolomite (Fe-dolomite) is used to describe $CaMg(CO_3)_2$-$CaFe(CO_3)_2$ solid solutions with higher $CaMg(CO_3)_2$ component, while the term ankerite describes solid solutions with higher $CaFe(CO_3)_2$ component.
Endmember $CaFe(CO_3)_2$ compositions have not been yet observed in natural samples, but have been synthesized in laboratory [60, 39]. In nature, dolomite-ankerite solid solutions reaching approximately 70 mol % of the $CaFe(CO_3)_2$ component can be found [193].
Several studies have been performed on the phase stability and behavior of dolomite and ankerite (up to 65% Fe) at high pressure and temperatures [141, 153, 65, 18, 236]. At pressures of about 5-7 GPa and in the temperature range of about 800-1300 K end-member dolomite, $CaMg(CO_3)_2$

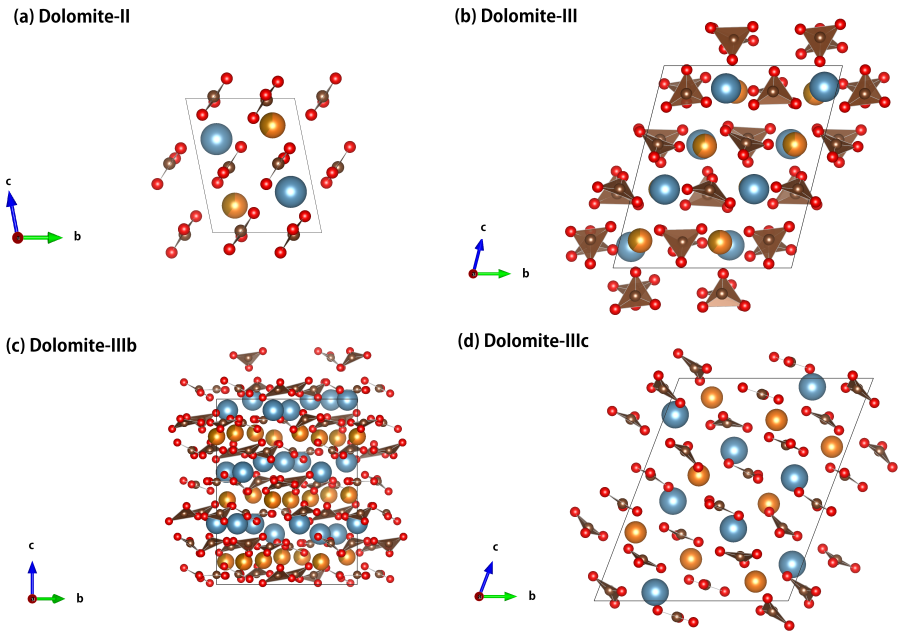

Figure 1.9: Structures of high pressure dolomite-phases. Dol-II (a), Dol-III (b), Dol-IIIb (c) and Dol-IIIc (d). Blue atoms are Ca, orange atoms are Mg, red atoms are O and the brown ones are C. The brown triangles represent the CO_3 groups. Structural models drawn using VESTA [161].

was observed to decompose into aragonite and magnesite [215]. However, it undergoes a series of phase transformations, without decomposing, upon compression at ambient temperatures.

At pressures of ∼11 GPa, vibrational spectroscopy studies reported the presence of a local distortion in the dolomite (Dol-I) structure, the Dol-Ib phase, however this phase was not observed in any XRD experiment [65, 18]. At about 14 to 17 GPa dolomite trasforms to a new polymorph, dolomite-II (Dol-II). Dol-II is triclinic with space group $P\bar{1}$ and $Z = 4$ and is topologically similar to $CaCO_3$-II (Fig. 1.9a). Dolomite-II contains two independent divalent cation sites with different coordination (8 and 6 respectively) [153]. Dol-II is observed up to 36-40 GPa (depending on the Fe content in the samples) and undergoes a first-order phase transition at higher pressures.

Three different high-pressure structures have been proposed for dolomite and Fe-dolomites at pressures higher than 40 GPa, shown in Fig. 1.9b-d. All three structures are topologically similar. For pure $CaMg(CO_3)_2$ dolomite, the Dol-IIIc structure is reported [151, 18].

Dol-IIIc crystallizes in the triclinic symmetry with space group $P\bar{1}$ and

$Z = 8$. In Dol-IIIc the planar CO_3 groups are no longer coplanar to each other and the structure is characterized by alternating distorted MgO_6 octahedra and CaO_n polyhedra with Ca coordination with O ranging from 7 to 9 (Fig. 1.9d) [18]. Dol-IIIc was observed to transform to a new polymorph, Dolomite-V, upon heating to 1800 K [18]. Dolomite-V crystallizes in the space group $C2/c$ with $Z = 4$. The structure is ordered and consists of CO_3 groups tilted against each other, distorted MgO_6 octahedra and CaO_8 square antiprisms arranged in alternating layers along the a-axis [18]. The phase diagram of end-member dolomite is shown in Fig. 1.10 [18].
Introducing Fe into the structure leads to the formation of different high pressure polymorphs at about 36 GPa, i.e. Dol-III and Dol-IIIb shown in Fig. 1.9 (rather than the Dol-IIIc polymorph observed in pure $CaMg(CO_3)_2$) and stabilizes the high pressure structures [153]. Dol-III is triclinic with space group $P\bar{1}$ and $Z = 8$. Similar to Dol-IIIc the CO_3 groups are no longer co-planar to one another and some of them share the edges with the CaO_n polyhedra (n ranging from 7 to 9) (Fig. 1.9b) [153]. Dol-IIIb crystallizes in the trigonal symmetry with space group $R3$ and $Z = 42$. Similarly to Dol-III and Dol-IIIc, carbonate groups are no longer coplanar in this structure [151]. Heating experiments showed that Dol-III and Dol-IIIb are stable phases at high P-T conditions, making Fe-dolomite a possible carbon repository at Earth's lower mantle conditions [141, 151].
At pressure of 115 GPa and temperatures of 2500 K Fe-dolomite transforms to a new polymorph, dolomite-IV (Dol-IV). Dol-IV crystallizes in the orthorhombic symmetry with space group $Pnma$ and $Z = 12$ [151]. It is a ring carbonate with tetrahedrally coordinated carbon.

Elasticity of $CaMg(CO_3)_2$ The complete elastic tensor of dolomite was determined in several experimental and computational studies (see Tab. 1.8). However, the chemical composition of the samples used in the studies has not been reported and the results are in partial disagreement (48% for C_{15}, 14% for C_{33}, 25% for C_{13} and 14% for C_{14} coefficients)[95, 46]. An additional BS study was performed on a well characterized [272] dolomite sample [223]. The results have not been published yet, however the elastic tensor coefficients from this study were communicated at the 54^{th} annual meeting of the European High Pressure Research Group and at the 2^{nd} European Mineralogical Conference [223].

No data has been provided to this day on the elastic tensor of ankerite-rich carbonates. Ch. 6 reports a BS study on the elastic properties of dolomite and ankerite samples (up to 63 mol% of $CaFe(CO_3)_2$ component). The complete elastic tensor is reported for both samples as well as the structural evolution,

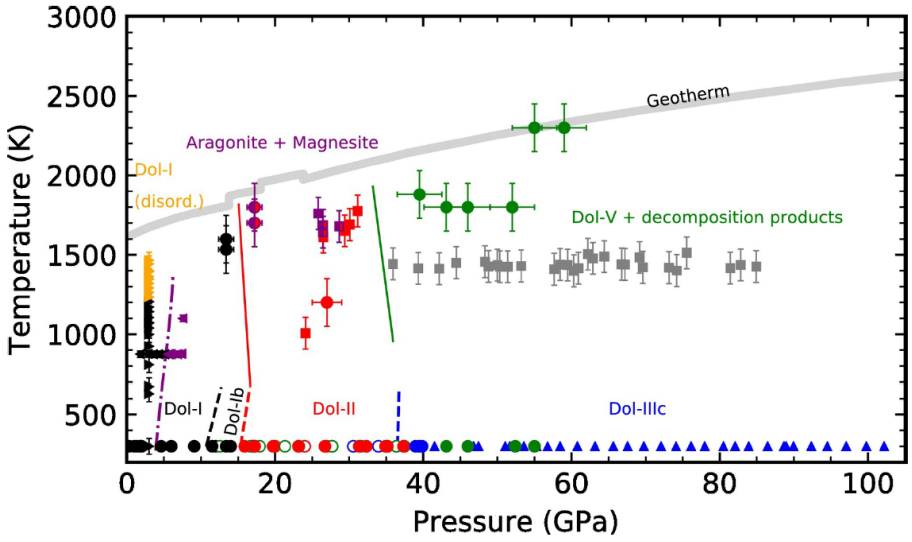

Figure 1.10: Phase diagram of $CaMg(CO_3)_2$. Figure from Binck et al. (2020) [18].

monitored by powder XRD.

Table 1.8: Elastic tensor coefficients of $CaMg(CO_3)_2$ from Humbert and Plicque (1972)-HP [95], Chen et al. (2006) [46], Speziale et al. [223], Bakri and Zaoui (2011) [12] and Titiloye et al. (1998) [233]. The different sign of the C_{14} coefficient is related to the different convention used to tranfor the crystallographic coordinate system to the cartesian one used to describe the sample's orientation.

C_{ij}	Speziale [223]	Chen [46]	Humbert [95]	Bakri [12]	Titiloye [233]
C_{11} (GPa)	206(1)	204(2)	205	196.6	201.6
C_{12} (GPa)	69(2)	69(3)	71	64.6	71.0
C_{13} (GPa)	59(2)	46(4)	57.4	54.71	57.4
C_{14} (GPa)	-21(2)	20(1)	-19.5	22.45	-19.5
C_{15} (GPa)	10(3)	7(2)	13.7	-1.35	13.7
C_{33} (GPa)	115(1)	97(5)	112.8	110.01	113.0
C_{44} (GPa)	40.5(4)	39(2)	39.8	41.57	39.8

1.2.6 Strontianite, $SrCO_3$

Strontianite, $SrCO_3$, is isostructural to aragonite, crystallizing in the orthorhombic symmetry with space-group $Pmcn$ and $Z = 4$ (unit cell pa-

rameters at ambient conditions are $a = 5.126(1)$ Å, $b = 8.472(2)$ Å, and $c = 6.061(1)$ Å) [14]. $SrCO_3$ has a similar phase diagram to that of aragonite, but the phase transitions take place at lower pressures due to the larger cation size (Sr^{2+} has radius of 1.31 Å, in comparison with that of Ca^{2+} 1.18 Å [209]). At ambient temperature and pressures between 22 and 28 GPa $SrCO_3$ transforms to post-aragonite $SrCO_3$-II (space group $Pmmm$, $Z = 2$, $a = 4.521(1)$ Å, $b = 4.918(1)$ Åand $c = 4.219(1)$ Å, at 28 GPa) [14].

Elasticity of $SrCO_3$ The complete elastic tensor of a synthetic $SrCO_3$ sample was measured by Brillouin spectroscopy complemented by DFT calculations in one study [16]. The results of the study show perfect agreement between the calculated and measured tensor coefficients (see Tab. 1.9).

Table 1.9: Elastic tensor coefficients of $SrCO_3$ from Biedermann et al. (2017) [16, 166].

C_{ij}	Biedermann et al. [16, 166]	
	BS	DFT
C_{11} (GPa)	153(1)	152(1)
C_{12} (GPa)	52(1)	54(1)
C_{13} (GPa)	38(11)	33(1)
C_{22} (GPa)	109.6(8)	109(1)
C_{23} (GPa)	43(15)	43(1)
C_{33} (GPa)	75(1)	74(1)
C_{44} (GPa)	28.0(5)	34(1)
C_{55} (GPa)	28.6(4)	26(1)
C_{66} (GPa)	33.2(5)	38(1)

1.3 Scope of the thesis

Knowing the physical and chemical behaviour of carbonate minerals as a function of their structure and chemical composition high pressure and temperature conditions is crucial for understanding the deep carbon cycle in our planet. However, the current knowledge of the elastic properties of carbonates and their dependence on their structure and composition is still far from being complete.

This work of thesis is the result of several projects. The main part of my PhD project has been focused on the study of the full elastic tensor of carbonates and its relationship with the compositional and structural parameters of the

studied samples. Chapter 1 reports the study of the single crystal elasticity of natural aragonites $CaCO_3$ at ambient conditions. Three, well characterized, aragonite samples were studied by Brillouin spectroscopy, showing good reproducibility of the results.
Chapter 2 describes the effect of Sr incorporation in a $CaCO_3$ sample, synthesized at high pressure and temperatures. This study mainly focuses on the effect of Sr on the structure and structural evolution with pressure, rather than the elastic properties of said samples.
Chapter 3 describes the mechanical behaviour of a synthetic sample of amorphous calcium cabonate at high pressures, investigated by Brillouin spectroscopy.
Chapter 4 is a study on natural ankerite samples with different chemical compositions, combining high pressure synchrotron X-ray diffraction with Brillouin spectroscopy experiments.
In addition to the study of carbonates, the effect of structural and compositional differences on the elasticity a material was also investigated by studying metal-organic framework compounds with different compositions, as described in Chapter 5.

Chapter 2

Methods

Different techniques were used in this work of thesis to investigate specific aspects of the samples of interest. Basics of the physical principles and technical aspects of each technique are summarized in this chapter.
In the first section the techniques used for sample characterization will be described. The second section of this chapter will describe specifics on high pressure experiments. The third section will focus on X-ray diffraction. Section four will be dedicated to the techniques used to study the elastic properties of samples. Elasticity is the central topic of this thesis, therefore, a theoretical background will be provided in addition to the description of the methods used. Among the different techniques to study the elastic properties of our samples we will focus mainly on Brillouin spectroscopy.

2.1 Sample's characterization

2.1.1 Electron Microprobe Analysis

Electron microprobe (EMP) is an analytical technique that employs an electron beam to induce the emission of characteristic X-rays from a sample, which are then used to constrain the chemical composition the sample. An introduction to the basic principles of EMP together with quantitative analytical corrections and applications to the Geosciences can be found in Reed (2005)[192]. In an electron microprobe experiment, an electron beam is accelerated under vacuum using high voltages (5-20 kV) and focused on the sample material. Typical currents used to operate the electron beam are 5 to 50 nA. In this high voltage-low current conditions it is possible to focus the beam diameter in the nm range (up to a maximum of 20 μm). The electron bombardment produces two major interaction mechanisms: (i) the ioniza-

tion of the sample where electrons are removed from the sample material; (ii) the primary electron from the beam decelerates due to the Coulomb field associated with the atoms of the sample, creating a continuous X-ray spectrum (Bremsstrahlung). The ionization of the sample generates X-rays that are characteristic for different elements (characteristic X-rays) and whose intensities are measured with wavelength (WDS) or energy dispersive spectrometers (EDS). Using the intensities of the characteristic X-rays' spectra of standard materials it is possible to quantitatively analyze the chemical composition of the samples. The detection limits are usually between 5 and 800 μg/g, depending on the concentrations differences between the standard and the sample material. Further effects like the production of secondary and backscattered electrons as well as cathodoluminescence can be used for imaging purposes. All EMP measurements described in this thesis were performed at the German Research Centre for Geosciences (GFZ) (Helmholtz Center Potsdam, Germany) using a JEOL thermal field emission instrument JXA-8500F (HYPERPROBE). Prior to being analyzed, selcted grains of sample materials were embedded in epoxy resin and polished with 0.25 μm diamond paste.

2.1.2 Focused Ion Beam

Focused ion beam (FIB) is an instrument that allows for the sample's morphological modification by means of a process known as 'sputtering'. The target is bombarded by heavy ions allowing for material to be removed from the sample with nanometer-scale precision. Currently, the major application of FIB in experimental Geosciences is site-specific preparation of lamellae for transmission electron microscopy (TEM) [256]. A detailed description of this technique is beyond the scope of this thesis and can be found elsewhere [78, 256]. In this work of thesis FIB milling was used to prepare Sr-calcite samples for TEM analysis (Ch. 4) using a HELIOS system operated at an accelerating voltage of 30 kV and a current of 2.2 nA.

2.1.3 Transmission Electron Microscopy

Transmission Electron Microscopy (TEM) is a technique that allows to completely characterize solid-state samples on the nanometer scale [256], providing information on the chemical composition and the structure of the studied materials. TEM operates by accelerating a monochromatic beam of electrons under vacuum at high voltages (300 kV) and transmitting it through a very thin electron-transparent sample, less than 200 nm depending on the acceleration voltage of the microscope. Chemical information about solid-state

samples are obtained with TEM by means of three different analytical techniques: energy dispersive X-ray analysis (EDX); electron energy-loss spectroscopy (EELS) and high-angle annular dark field imaging (HAADF).
EDX analysis provides chemical information from characteristic X-rays of the sample. EELS allows for elemental identification at the nanoscale by measuring the energy loss of the incident electrons that pass through the sample. Compared to EDX, EELS has higher signal to noise ratios, spatial resolution ($\sim$1 nm), energy resolution ($<$1 eV) and sensitivity to elements with lower atomic numbers. HAADF is an imaging technique that provides atomic-resolution images that are sensitive to the atomic number (Z). The basic idea behind HAADF imaging is the angular selection of the scattered signal by collecting inchoerently scattered electrons (Rutherford scattering from the nucleus of the atoms) at very large angles.
A detailed introduction to TEM is beyond the scope of this thesis and can be found in Williams and Carter (1996) [254]. The TEM mesurements reported in this thesis were performed by Prof. Wirth on a FEI Tecnai G2 F20-X-Twin microscope at the German Research Centre for Geosciences (GFZ), Potsdam.

2.1.4 Thermogravimetry and Differential thermal analysis

Thermogravimetry (TG) is a technique in which the mass of a sample is monitored as a function of time and temperature. The sample is heated in a controlled atmosphere while the temperature of the sample, in a specific atmosphere, is programmed. TG is generally used to detect evaporation, decomposition, crystallization, oxidation and other processes that cause mass changes as a result of temperature changes.
Differential thermal analysis (DTA) is a technique that monitors the difference in temperature between the sample and a reference material against time or temperature while the temperature of the sample, in a specific atmosphere, is programmed. It is common to measure TG and DTA simultaneously in a single apparatus.
In this work of thesis simultaneous TGA/DTA measurements were performed on amorphous calcium carbonate (ACC) samples using a NETZSCH TG 209F1 Libra equipment (Netzsch, Selb, Germany). All measurements were performed by Matthias Schneider, of the Chemistry department, at the University of Potsdam, Germany.

2.2 High pressure experiments

2.2.1 Diamond anvil cell

A diamond anvil cell (DAC) is a tool that was developed to perform experiments at extreme conditions. Its operating principle consists in the uniaxial compression of a sample between two flat-top parallel diamond-anvils. The transparency of the diamonds to a wide range of electromagnetic radiations allows for in-situ optical and spectroscopic measurements of the sample material. Fig. 2.1 shows a schematic representation of a DAC. Many types of DAC designs exist to this day [105, 21], however they share the same basic components. The main body of the cell consists of two gem quality dia-

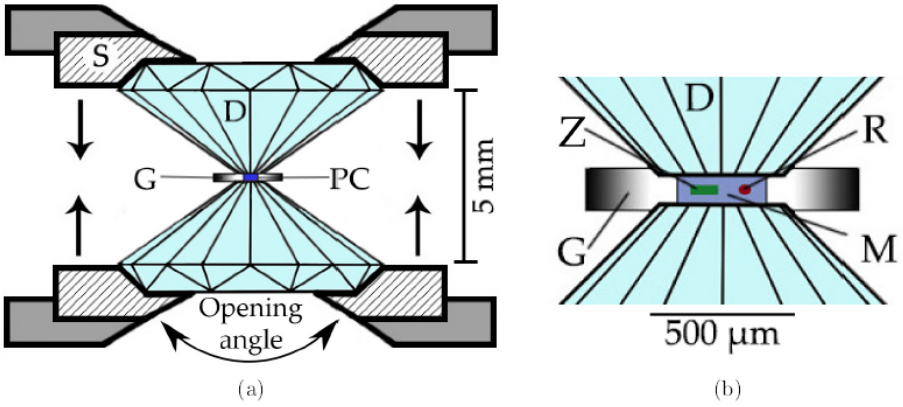

Figure 2.1: Schematic representation of a DAC. Each component of the DAC is marked by a letter. S is the seat, D are the diamonds, G is the gasket, PC is the pressure chamber, Z is the sample, M is the pressure transmitting medium and R is the ruby.

mond with flat tips (culets) glued to two hard (e.g. tugsten carbide) seats. In a high pressure experiment, the two diamond anvils are driven against each other to increase pressure on the studied sample placed in a sample chamber. Depending on the culet's size, different pressures can be achieved: the smaller the culet the higher the pressure. In this thesis, diamonds with flat culets with diameter of 300 μ were used for experiments with Bohler Almax [21] and symmetric DACs to perform experiments in the pressure range between 0 and 45 GPa. The sample chamber consists of a hole drilled (usually by using either laser-drilling or electric discharge machines) on a metal plate, named gasket. Different materials can be used as gaskets, however the most commonly employed material is Re as it behaves exceptionally

well at high pressures. The sample chamber is drilled after the gasket has been indented by pressing it between the two aligned anvils, compressing it down to 15-45 μm. The indentation thickness is dependent on the diamond culet: smaller culets require thinner indentation thicknesses [64]. The sample is usually loaded in the sample chamber together with chips of materials that show an accurately calibrated correlation between pressure and a change in their physical properties (easily measurable in a DAC), acting as pressure-temperature indicators. Ruby (Al_2O_3:Cr) and Sm:YAG are commonly used as pressure gauges in optical/spectroscopic DAC high pressure experiments. In this work of thesis ruby will be used as pressure indicator in all the high pressure experiments. The pressure determination for ruby relies on the pressure-induced frequency shift of the R1 fluorescence line (Fig. 2.2). This pressure-related shift has been calibrated at room temperature up to

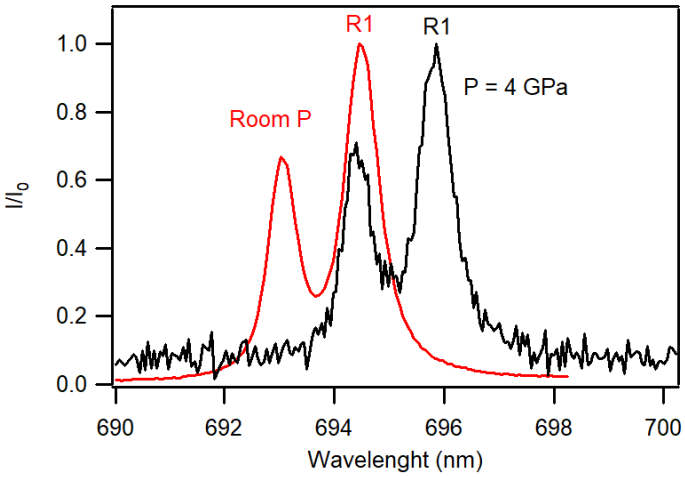

Figure 2.2: Ruby fluorescence spectra at ambient conditions (red curve) and at 4 GPa (black curve). The arrow shows the R1 peak in the fluorescence spectrum of ruby.

[212]. The pressure inside the sample chamber is determined following the pressure-frequency relation described by [212]:

$$P = 1.87 \times 10^3 \frac{\Delta\lambda}{\lambda_0} \left[1 + 5.63 \left(\frac{\Delta\lambda}{\lambda_0} \right) \right] \tag{2.1}$$

High-pressure experiments can be performed with or without pressure transmitting medium (PTM). Since DACs generate uniaxial stresses, using a PTM allows for homogeneous stress distribution in the chamber. Different compounds can be used as PTMs, such as noble gases, halides, oil, salts, alcohol

mixtures and even the sample itself in powder form. In this work of thesis argon and neon were employed as PTM. Using Ne as PTM ensured quasi-hydrostatic conditions in the pressure range of interest of the experiments conducted here [112].
High pressure and high temperature experiments are also possible to perform in DACs, however no heating experiments were used in this thesis, therefore heating in DACs will not be discussed here.

2.3 X-ray diffraction

X-ray diffraction (XRD) is a powerful non-destructive analytical technique used to reveal information about the crystal structure, chemical composition and physical properties of crystalline materials. When light encounters an obstacle of size comparable with the wavelength of the radiation diffraction occurs. A crystalline material is an object with a 3D periodic structure. If exposed to X-rays with wavelengths close to the interatomic distances that causes diffraction of the X-rays (Bragg diffraction):

$$2d \sin\theta = n\lambda \tag{2.2}$$

where d is the distance between a family of hkl crystallographic planes, θ is the angle of incidence of the X-rays, λ is the wavelength of the X-rays, n is the order of the reflection and is an integer number. In a X-ray diffraction (XRD) experiment monochromatic radiation coming from a radiation source, filtered by a monochromator is directed to a sample on a holder, after having passed through a series of slits used to adjust the shape of the beam. The diffracted radiation is then collected by a detector. Different configurations control the wavelength/energy and size of the incident beam, the sample's movement geometry and the detector type. A diffraction pattern, produced in a diffraction process, is given by the intensity of the scattered waves as a function of the scattering angles. Intense peaks, known as Bragg reflections are present on the diffraction pattern at values of 2θ for which the Bragg condition is fulfilled (Eq. 2.2).
X-ray diffraction experiments can be performed both on powder samples and single crystal samples. The information obtained from powder X-ray diffraction (PXRD) and single crystal X-ray diffraction (SC-XRD) is different.
The position of the peaks (as 2θ-angles or d-spacing) allow for phase identification as every compound has a unique set of d-spacing.
The diffraction pattern in a SC-XRD experiment consists in diffraction spots, at certain 2θ angles defined by the Bragg's law Eq. 2.2. The XRD diffractometer geometry is usually different for PXRD and SC-XRD experiments [30].

2.3.1 Powder X-ray diffraction

Powder X-ray diffraction (PXRD) is an analytical technique primarily used for phase identification of crystalline materials and can provide information on unit cell dimensions. Ambient conditions PXRD patterns were recorded in transmission mode using a fully automated STOE STADI P diffractometer with monochromated $K\alpha 1$ of Cu radiation ($\lambda = 1.5406$ Å) equipped with a Germanium (111) monochromator and a MYTHEN detector operating at 40 kV and 40 mA. The diffractometer had a Bragg-Brentano geometry (shown in Fig. 2.3). The samples were pounded and finely ground (to μm-grain size) using a mortar and the powdered sample was distributed on a flat disk made of amorphous material. The disk was placed on a holder that was rotated during data collection while the arm where the detector was mounted also rotated of an angle 2θ. Patterns were recorded in the range of $2\theta = 5° - 125°$ using a step interval of 0.05°. The peaks positions were calibrated externally using a NBS standard.

As part of the work presented in this thesis, high pressure PXRD experi-

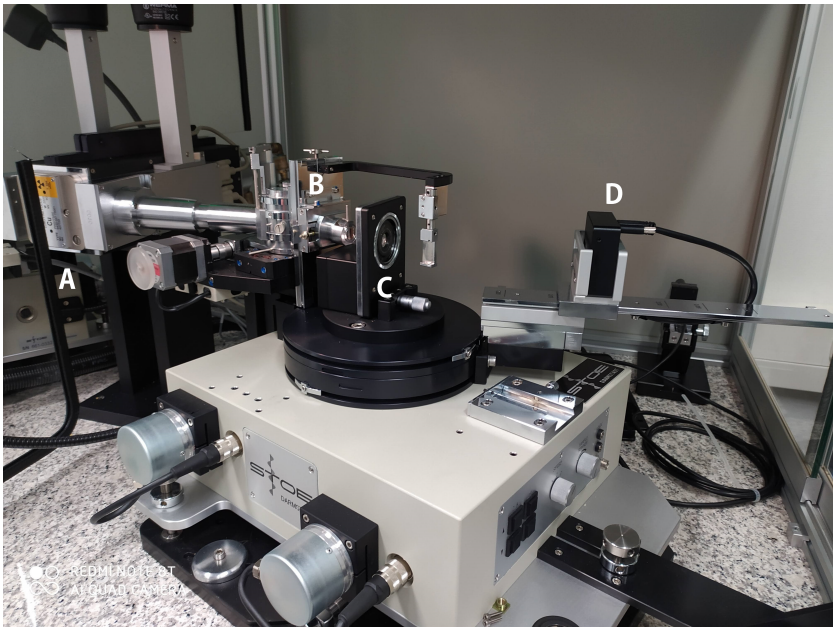

Figure 2.3: STOE STADI P, Bragg-Brentano diffractometer. (A) Radiation source (B) Ge monochromator, (C) sample and (D) MYTHEN detector.

ments were performed on ankerite samples (Ch. 6) at the diffraction beamline dedicated to extreme conditions P02.2 at PETRA-III (Hamburg, Germany) using radiation of 42 keV of energy, $\lambda = 0.29$ Å, focused down to 2 x 2 μm^2 by

a Kirkpatrick-Baez (KB) mirror system (Liermann et al. 2015 [122]) and a PerkinElmer XRD 1621 flat-panel detector. Prior to data collection, calibration files were created using a CeO_2 standard. The diffraction images of the studied samples were integrated using the DIOPTAS software [187], which allows for background subtraction and creates 2-D diffraction patterns. For processing of the powder patterns, GSAS-II software package [117, 235] was used. Once the diffraction pattern of a sample has been collected, it can be processed using several methods: the Rietveld method, Le Bail method, Pawley method. In a PXRD diffractogram the intensity $I(\theta)$ at the scattering angle 2θ is the sum of all the (hkl) reflections and the background function $B_i(\theta)$. The integrated intensitiy of the peaks I_{hkl} is given by:

$$I_{hkl} = M_{hkl} P_{hkl} L_{hkl} F_{hkl}^2 \tag{2.3}$$

where M_{hkl} is the multiplicity, P_{hkl} is the preferred orientation factor, L_{hkl} is the Lorentz polarization factor and F_{hkl} is the structure factor defined by:

$$F_{hkl} = \sum_{n=1}^{N} f_n \exp 2\pi i(hx_n + ky_n + lz_n) \tag{2.4}$$

where f_n is the atomic scattering factor of the n-th atom at coordinate (x_n, y_n, z_n). In Rietveld refinement the structure factor F_{hkl} is computed according to Eq. 2.4 and as such the atomic coordinates and their temperature factor can be refined during the procedure. In a Pawley refinement, on the other hand, the intensities I_{hkl} themselves are considered refinable parameters. In both Rietveld and Pawley algorithms, the refined parameters are optimized in order to minimize the weighted R factor R_{wp}:

$$R_{wp} = \frac{\sqrt{\sum_i w_i |I_{obs} - I_{cal}|^2}}{\sqrt{\sum_i w_i |I_{obs}|^2}} \tag{2.5}$$

with $w_i = 1/I_{obs}$.
In this work of thesis, PXRD patterns collected at ambient conditions were fitted using the Rietveld refinement, while high pressure data was fitted using the Pawley refinement.

2.3.2 Single crystal X-ray diffraction

Single crystal X-ray diffraction (SC-XRD) allows for absolute structure determination. In a SC-XRD experiment, the experimental setup is more complex compared to a powder diffractometer, as the sample is rotated along multiple

directions during the data collection. Typically four or three-cyrcle diffractometers are employed for SC-XRD experiments. In this work of thesis an in-house four-cyrcle diffractometer XCalibur3 (Rigaku Oxford Diffraction) with monochromatic Mo-K_α (λ=0.7104 Å) radiation was used to determine the orientation of the single crystals studied in the Brillouin spectroscopy experiments.

High pressure SC-XRD measurements were performed on synthetic Sr-calcite samples compressed in a DAC (Ch. 4) at the X-ray diffraction beamline dedicated to extreme conditions P02.2 at Petra-III, Hamburg, Germany. Here, we will describe the general procedure and principles of SC-XRD, a more detailed and extensive description of the experimental protocol for high pressure single crystal experiments can be found in Bykova (2015) [30]. Prior to data collection, calibration files were produced using a well characterized enstatite ($MgSiO_3$) single crystal. Once the calibration files have been created, the data collection can start. The first step consists in placing the sample on the X-ray beam. The alignment is performed by scanning along the y-, z- and ω-axes (the x-axis is defined as the direction of the incident X-ray beam), the difference in absorbance between gasket material, sample and sample chamber allows to position of the sample with respect to the X-ray beam. It is important to place the sample at the center of rotation of the system so that it will not move out of the beam during data collection. Data collection can be performed using three types of scans: (i) still-scans, during which the DAC remains stationary while being exposed to the X-ray beam for a time t; (ii) wide-scans, during which the DAC is rotated around the ω-axis while exposed to the beam for a few seconds; (iii) step-scans, during which the DAC is rotated around the ω-axis by an angle ω (dependent on the DAC opening angle) and is exposed to the beam every step $\delta\omega$ for a few seconds. Still-scans and wide-scans are generally used to check the sample quality and the phases present. Step-scans are used for data collection in a SC-XRD experiment. Data integration and absorption corrections were performed using the CrysAlis^{PRO} software [53]. The first step of the data analysis performed with the CrysAlis software consists in the selection of the diffraction peaks of the sample. Diamond, pressure transmitting medium, gasket etc. also produce peaks that need to be filtered out, this can be achieved exploring the Ewald sphere and manually selecting the peaks that belong to the sample. Finally, one can perform data reduction procedures during which the program extracts the reflection intensities and produces a file, with extension .hkl, containing all the *hkl* reflections and their intensities, used in the structure solution procedure. Structure solution and refinement were performed using JANA crystallographic software [181].

Structure solution is a process that allows to calculate the position of atoms and the thermal parameters using a set of experimental structural amplitudes F_{hkl} obtained from the measured intensities of the reflections I_{hkl}:

$$F_{hkl}^2 = \frac{I_{hkl}}{k \cdot L_p \cdot A} \tag{2.6}$$

where k is the scale factor, L_p is the Lorentz-polarization correction, A is the transmission factor. A generic wave diffracted by a lattice plane of a crystal is described by the structure factor given by:

$$\mathbf{F}_{hkl} = F_{hkl} \exp(i\alpha_{hkl}) = \sum_j f_j \exp(2\pi i(hx_j + ky_j + lz_j)) \tag{2.7}$$

where f_j is the scattering factor and x_j, y_j, z_j are the coordinates of the j^{th} atom and α_{hkl} is the phase of the diffracted beam. While the amplitude F_{hkl} of the structure factor can be derived from the diffraction experiments the phases are unknown. This creates the so-called phase problem, which is the main issue in a structure solution procedure. Different techniques are available nowadays for phases elaboration: direct methods, Patternson methods, heavy atoms methods etc. Once the phases have been derived, it is possible to calculate the atomic positions as the electron density is related to the structure factors with an inverse Fourier transform:

$$\rho_{xyz} = \frac{1}{V} \sum_{hkl} F_{hkl} \exp[-2\pi i(hx + ky + lz)] \tag{2.8}$$

with V unit cell volume.
After an initial structural model has been obtained it is refined against the experimental data using a least-squares minimization of adjustable parameters. Model and experimental data agreement is defined by R-factors, which represent the quality of the structural model used:

$$R_1 = \frac{\sum ||F_{obs}| - |F_{calc}||}{\sum |F_{obs}|} \tag{2.9}$$

$$wR_2 = \left[\frac{\sum w|F_{obs}^2 - F_{calc}^2|}{\sum wF_{obs}^2} \right]^{1/2} \tag{2.10}$$

where w is a weighing factor individually derived for each measured reflection based on the standard uncertainty and F are structure factor amplitudes (*obs*-observed, *calc*-calculated from the model.)

2.4 Elasticity

The elastic properties of a material define how it deforms (strains) as a result of the forces (stresses) applied on a body made up of the material. Specifically, elasticity refers to instantaneous changes in the sample and does not include time-dependent deformations or permanent irreversible changes. The elastic properties of a material, therefore, relate stresses and the resulting strains. The relationship between stress and strain in linear elasticity can be generally expressed by the Hooke's law. Stress, denoted as σ_{ij} with $i, j = 1, 2, 3$ is a second rank tensor and represents the force applied to a body. Strain, denoted ϵ_{ij} is also a second rank tensor and follows the same conventions used for stress. Because stress and strain are tensor properties, each with $3 \times 3 = 9$ components, the elastic properties of a material are described by a tensor with $9 \times 9 = 81$ components. This tensor is either the compliance tensor s_{ijkl}, which specifies the strains resulting from an applied stress from $\epsilon_{ij} = s_{ijkl}\sigma_{ij}$; or the stiffness tensor c_{ijkl} which expresses the stresses as a function of the strains $\sigma_{ij} = c_{ijkl}\epsilon_{ij}$ (note: Einstein summation is assumed). Although the elasticity tensor has 81 components, they are not independent and can be reduced to 21 independent elastic coefficients by considering symmetry arguments based on the definition of stress and strain (symmetric tensors, reduction of the independent coefficients from 81 to 36) and the second law of thermodynamics, implying that work must be done to create a state of strain from a relative minimum of energy [165]. In addition to that, depending on the symmetry of the material the number of independent components can be further reduced, as shown in Tab. 2.1. Fig. 2.4 shows the independent elastic tensor coefficients and the relationship between them for different crystal systems:

Table 2.1: Number of independent tensor components (N. ic) for each Laue class.

Crystal system	Laue class	N. ic
Cubic	m3,m3m	3
Hexagonal	6/m,6/mmm	5
Tetragonal	4/mmm	6
Trigonal	3m	6
Tetragonal	4/m	7
Trigonal	-3	7
Orthorhombic	mmm	9
Monoclinic	2/m	13
Triclinic	-1	21

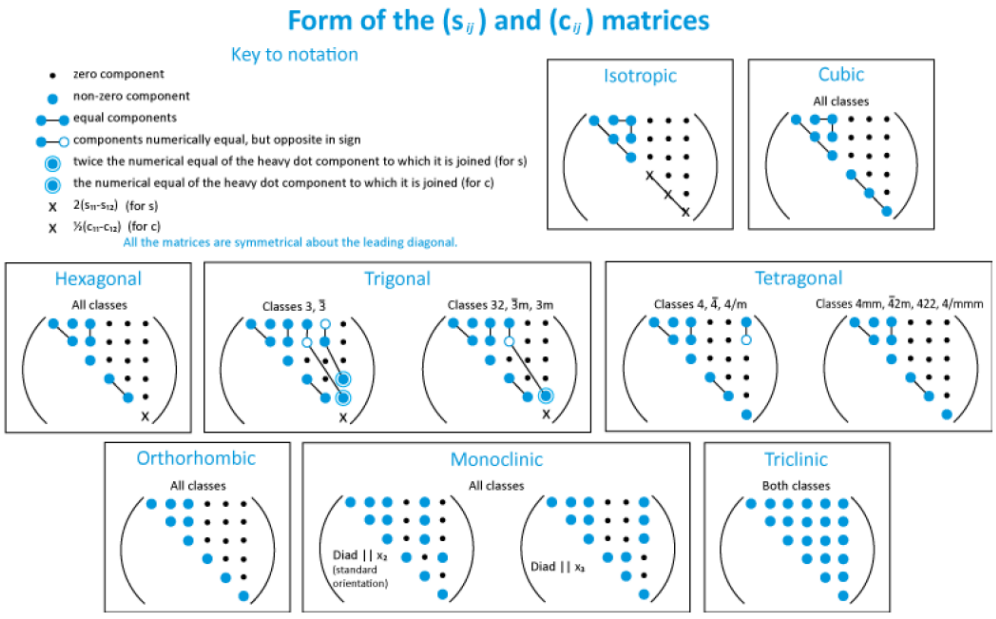

Figure 2.4: Elastic stiffness and compliance tensor coefficents in the Voigt notation and their relations between them for different crystal systems. Figure from [167].

Stress and strain tensors can be reduced to 6-vectors and are related to one another by 6×6 matrices to reduce the full-tensor expressions, this representation is referred to as Voigt notation, where: $\sigma_{11} \rightarrow \sigma_1$, $\sigma_{22} \rightarrow \sigma_2$, $\sigma_{33} \rightarrow \sigma_3$, $\sigma_{23} \rightarrow \sigma_4$, $\sigma_{13} \rightarrow \sigma_5$ and $\sigma_{12} \rightarrow \sigma_6$. A similar transformation can be applied to the components of the strain tensor ϵ_{ij}. This helps reducing the tensor equation $\sigma_{ij} = C_{ijkl}\epsilon_{ij}$ to a simple matrix equation $\sigma_i = C_{ij}\epsilon_j$, with [165]:

$$\sigma_i{}^T = [\sigma_{11}, \sigma_{22}, \sigma_{33}, \sigma_{23}, \sigma_{13}, \sigma_{12}] \tag{2.11}$$

$$\epsilon_i{}^T = [\epsilon_{11}, \epsilon_{22}, \epsilon_{33}, 2\epsilon_{23}, 2\epsilon_{13}, 2\epsilon_{12}] \tag{2.12}$$

All the physical properties reported in the following articles are reffered to a Cartesian set of reference axes. For cubic, tetragonal and orthorhombic crystal symmetries X, Y, Z are parallel to the *a, b, c*- axes of the crystal. In the trigonal and hexagonal systems, Z is normally chosen parallel to the *c* axis while X and Y lie on the (001) plane. For monoclinic and triclinic systems, it is necessary to determine which convention to use before interpreting published values of the coefficients as it is not possible to put all the Cartesian axes parallel to crystal axes.
In the study of the Earth's interior, the Earth's mantle and crust are com-

posed of multi-phase assemblages. It is, therefore, important to study the elastic behaviour of aggregates. The elastic properties (bulk and shear moduli) of polycrystalline materials can be determined by measuring single crystals samples of the same material and calculating an aggregate average (weighed on the distribution of the grains' orientations) over the single crystal elastic constants. The most commonly used averages, in the case of aggregates with randomly oriented grains, are the Voigt and the Reuss averages.
The Voigt (V) bound assumes that strain is uniform throughout the aggregate and the isotropic stiffnesses are obtained by averaging the single crystal elastic stiffnesses over all possible orientations. The Voigt bulk and shear moduli are given by:

$$K_V = \frac{1}{3}(A + 2B) \tag{2.13}$$

$$G_V = \frac{1}{5}(A - B + 3C) \tag{2.14}$$

where $A = \frac{1}{3}(C_{11}+C_{22}+C_{33})$, $B = \frac{1}{3}(C_{12}+C_{13}+C_{23})$ and $C = \frac{1}{3}(C_{44}+C_{55}+C_{66})$. The Reuss bound (R) assumes uniform stress throughout the sample and derived the effective isotropic compliances in terms of the single-crystal compliances averaged over all orientations:

$$K_R = [3(a + 2b)]^{-1} \tag{2.15}$$

$$G_R = 5/(4a - 4b + 3c) \tag{2.16}$$

with $a = \frac{1}{3}(s_{11} + s_{22} + s_{33})$, $b = \frac{1}{3}(s_{12} + s_{13} + s_{23})$ and $c = \frac{1}{3}(s_{44} + s_{55} + s_{66})$. The arithmetic mean of the Voigt and Reuss bounds, the Voight-Hill-Reuss (VHR) average, is generally used describe the elastic properties of randomly oriented poly-crystals (isotropic materials) [89]:

$$K_{VHR} = (K_V + K_R)/2 \tag{2.17}$$

$$G_{VHR} = (G_V + G_R)/2 \tag{2.18}$$

In geophysics we are interested in measuring the acoustic wave velocities that propagate in a material, which are directly related to the elastic properties of the material. Let us consider a material point located with respect to a cartesian coordinate system, and denote its position as X. If stress is applied the final position of the particle is x:

$$x_i = X_i + u_i \tag{2.19}$$

where u_i is the particle displacement. For small vibrations of the first order in the displacement, the equation of motion is expressed as:

$$\rho \frac{\partial^2 u_i}{\partial t^2} = C_{ijkl} \frac{\partial^2 u_k}{\partial x_j \partial x_l} \tag{2.20}$$

where ρ is the density, C_{ijkl} is the elastic tensor. Assuming a plane wave solution for Eq. 2.20 we obtain the Christoffel equation:

$$|C_{ijkl}n_j n_l - \rho v^2 \delta_{ik}| = 0 \tag{2.21}$$

where v is the phase velocity, n_i is a unit vector defining a given propagation direction. The solutions to Eq. 2.21 are either a quasi-longitudinal (P-wave) wave with polarization parallel to the direction of propagation and two quasi-shear (S-waves) waves with polarization perpendicular to n_i. Longitudinal waves propagate faster than shear waves. Pure longitudinal and shear polarizations are found only isotropic materials or along special high symmetry direction for anisotropic materials. Wave velocities are related to the elastic bulk and shear moduli in an isotropic homogeneous material by:

$$v_P = \sqrt{\frac{K + 4/3G}{\rho}} \tag{2.22}$$

$$v_S = \sqrt{\frac{G}{\rho}} \tag{2.23}$$

Single crystals are generally elastically anisotropic regardless of the symmetry, consequently elastic wave velocities depend on the direction of propagation. In particular, the single crystal azymuthal anisotropy for acoustic waves is given by [140]:

$$A_P = \frac{v_{P,max} - v_{P,min}}{v_P} \tag{2.24}$$

$$A_S = \frac{v_{S,max} - v_{S,min}}{v_S} \tag{2.25}$$

where v_P and v_S are the isotropic velocities.
Elastic anisotropy is crucial for diverse applications such as phase transformations, dislocation dynamics and many others. However, most of the definitions of elastic anisotropy, such as the ones reported above, lack universality. The universal anisotropy index, A^U, defined as [189]:

$$A^U = 5\frac{G_V}{G_R} + \frac{K_V}{K_R} - 6 \tag{2.26}$$

takes into account all the tensorial nature of the elastic stiffness and overcomes the dilemma of the non-uniqueness of the anisotropy definitions. In this formulation A^U is zero for locally isotropic single crystals and the departure of A^U from zero defines the extent of the single crystal anisotropy.

The elastic properties of a material can be experimentally measured using different methods. In the following the methods used in this work of thesis to measure elasticity will be described. The main focus will be on Brillouin spectroscopy, as it is the main technique exploited in this study. A review of the methods available to study the elastic properties of a material is given by [8].

2.4.1 Brillouin spectroscopy

Lattice dynamics Before describing Brillouin spectroscopy (BS) it is important to introduce a few concepts, such as dispersion curves and phonons, that will be fundamental for understanding the theory behind BS.
In a crystal at temperatures above 0 K, atoms vibrate around their equilibrium positions (thermal fluctuations). In the following, a basic description of lattice dynamics will be provided, a more complete description can be found elsewhere [111, 54, 22, 62].
Let us consider an infinite crystalline lattice formed by N unit cells, with S atoms per unit cell with positions $\mathbf{R}$, which are displaced from the equilibrium due to the thermal agitation. The first step of the analysis of the lattice dynamics consists in the construction of a potential energy function expressed as a power series of the displacement of the nuclei from their equilibrium positions, based on an an harmonic approximation (in which only quadratic terms in the potential energy are considered). The energy H of the system is then:

$$H = \sum_{ls} \frac{p_{ls}^2}{2M} + \frac{1}{2} \sum_{lsl's'} \mathbf{u}_{ls}^T \Phi_{lsl's'} \mathbf{u}_{l's'} \tag{2.27}$$

where $\sum_{ls} \frac{p_{ls}^2}{2M}$ is the kinetic energy and $\Phi_{lsl's'} = \frac{\partial^2 E}{\partial u_{ls} \partial u_{l's'}}$ is the force constant matrix (quadratic term of the Taylor expansion of the potential energy), where the summation is on the s-atom of the l^{th} unit cell and $\mathbf{u}_{ls}(t)$ is the displacement vector. In the harmonic approximation, we therefore get a set of $3sN$ equations of motion, that separate into N uncoupled sets of equations, each set of $3s$ corresponding to a particular value of $\mathbf{q}$ with solutions in the form:

$$u_{ls} = \frac{1}{\sqrt{N m_s}} \sum_{q,j} Re\{a_j(\mathbf{q}) \epsilon_{js}(\mathbf{q}) e^{i(\mathbf{q}\cdot(\mathbf{R}_l + \mathbf{r}_s) + \omega_j(\mathbf{q})t)}\} \tag{2.28}$$

Where m_s is the mass of the sth atom, $a_j(\mathbf{q})$ is the normal coordinate of the vibrational mode, $\epsilon_{js}(\mathbf{q})$ is the normalized displacement pattern, $\omega_j(\mathbf{q})$ the frequency of the vibrational mode, j runs over the S possible solutions, S being the number of atoms in the unit cell, and $\mathbf{q}$ is a vector in the

first Brillouin zone. This solutions corresponds to the decomposition of the displacement $\mathbf{u}_{ls}$ into normal modes, allowing to consider the lattice vibration as a collective motion of all the atoms in the crystal. The total energy of the system is that of the harmonic oscillator and is obtained by summing over the kinetic and vibrational energy. If we consider the quantum mechanical description, in which the particles are non-interacting we obtain:

$$E = \sum_{\mathbf{q}j} \hbar\omega_j(\mathbf{q}) \left(n_{\mathbf{q},j} + \frac{1}{2} \right) \tag{2.29}$$

where n is the occupation number, an integer denoting the number of phonons in a state defined by the quantum numbers $\mathbf{q}, j$. From Eq. 2.29 it is evident that the total energy of the system is described by discrete energy levels. A crystal can, therefore, be considered a gas of non-interacting quasi-particles with discrete energy and frequency. These quasi-particles are called *phonons*. When the equations of motion are solved for different values of $\mathbf{q}$ one obtains a series of dispersion curves (ω as a function of $\mathbf{q}$). There are always $3s$ branches but in particular cases some branches might not be distinct due to the degeneracy of the equations of motion. Three out of the $3s$ branches are correspondent to all atoms moving in unison (in the $\mathbf{q} \to 0$ limit), these branches always exhibit $\omega \to 0$ behavior. These $\mathbf{q} \to 0$ modes are identical to macroscopic sound waves and are called acoustic modes. The remaining $3s - 3$ branches have non-zero intercepts and correspond to relative motions of the atoms within a unit cell. These branches are called optical modes as they are related to molecular vibrations and are responsible for infrared absorption by the crystal.

Brillouin spectroscopy Brillouin spectroscopy (BS) is an optical technique used to determine the directional dependence of acoustic phonons in a material. BS experiments can be performed on crystalline materials, glasses and liquids. The potential of BS in geosciences was recognized by Anderson et al. (1969) [3], while the first experiment was performed by Weidner et al. (1975) [247]. Nowadays BS is commonly employed to investigate the elastic properties of minerals from ambient conditions to pressure and temperature conditions of the mantle.
In a BS experiment a monochromatic radiation is focused on the sample and the scattered light is collected by a detector. The kinematics of light scattering can be derived either from a classical point of view considering the perturbation of the dielectric tensor by lattice vibrations ($\mathbf{q}$, ω); or from a quantum mechanics point of view considering the second-quantized theory of lattice dynamics. In the following we will use the quantum mechanical

approach. Each normal mode of the lattice vibration $\{\mathbf{q}, \omega\}$ is described in terms of phonons of energy $\hbar\omega$ and momentum $\hbar\mathbf{q}$. In a light scattering event a phonon is created or annihilated as shown in Fig. 2.5. The conservation of energy and momentum between the photon and the phonon are described by:

$$\mathbf{k}_s = \mathbf{k}_i \pm \mathbf{q} \tag{2.30}$$

$$\omega_s = \omega_i \pm \Omega \tag{2.31}$$

where k_i, ω_i, k_s and ω_s are the incident and scattered light wavevector and frequency and Ω are the 3s frequencies of the three acoustic branches at $|\mathbf{q}| = |k_s - k_i| \approx 2|k_i|\sin(\theta/2)$. The + sign in Eq. 2.30-2.31 is related to the Stokes event, in which a phonon is created, while the − sign is due to the phonon annihilation or Anti-Stokes event.

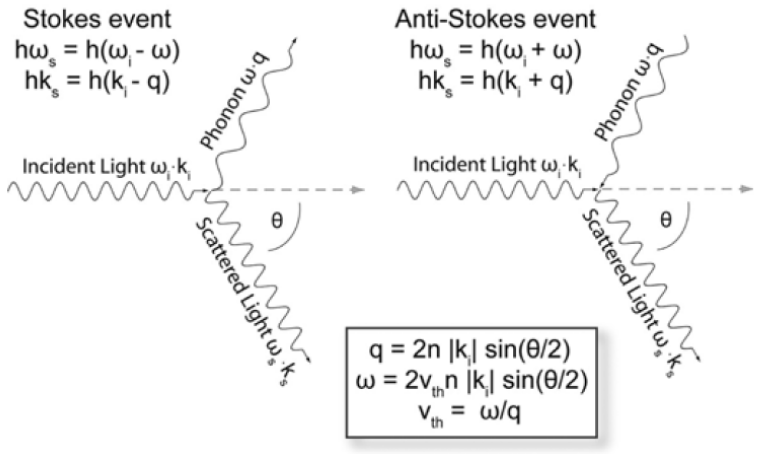

Figure 2.5: Stokes and Antistokes events. Figure from [8].

Brillouin scattering is due to the inelastic scattering of light by acoustic phonons. Acoustic phonons' q values are very small, the components of scattering due to acoustic modes occur at frequencies Ω that are much smaller (in the range between 0.01 cm^{-1} and 10 cm^{-1}) compared to those of optical modes (range 100 cm^{-1} – 1000 cm^{-1}). The resulting Brillouin shift in frequency $\Delta\omega_B$ is given by:

$$\Delta\omega_B = 2vn|k_i|\sin(\theta/2) \tag{2.32}$$

where n is the refraction index, k_i is the wavevector of the incident light, v is the acoustic wave velocity and θ is the scattering angle. A representative

Brillouin spectrum is shown in Fig. 2.6 and is characterized by a main central peak related to the elastic scattering of light (Rayleigh scattering) and three pair of peaks symmetrically placed on the sides of the Rayleigh peak that correspond to the three mutually perpendicular polarizations of the acoustic waves.

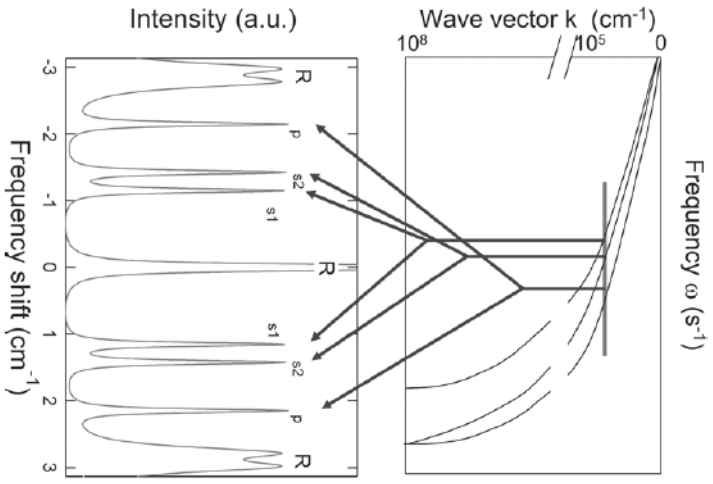

Figure 2.6: Dispersion curves and Brillouin spectrum. Figure from [8].

A more thorough description of Brillouin spectroscopy and its applications in geosciences can be found in [54, 224]. Brillouin scattering experiments are performed in a range of different setups and scattering geometries. The basic features, common to all the setups consist in a monochromatic light source (laser) which is focused on the sample, a spectrometer and a detector. Due to the λ^{-4} dependence on the intensity of the scattered light, blue and green lasers are the most commonly adopted as light sources in BS experiments.
In a BS experiment, very small frequency shifts are measured ($10^{-2} < \Delta\omega_B < 10$ cm^{-1}), therefore, Fabry-Perot interferometers (FPI) are used to separate the spectral components of the light. A complete description of the Fabry-Pérot interferometer can be found in Jacquinot (1960) [99]. The general idea behind FPI will be briefly described in the following. A FPI consists of two flat mirror plates with faces parallel to each other separated by a distance L (mirror spacing). The incident beam is subjected to multiple reflections on the opposing mirrors' surfaces. The transmitted wavelength must satisfy the interference condition:

$$m\lambda = 2nL\cos\alpha \tag{2.33}$$

where m is an integer, n the refractive index of the medium between the

mirrors, L the mirror spacing and α the incidence angle. Another important parameter is the free spectral range Δk of the interferometer, defined as the frequency interval (in wavenumbers) given by the difference between two wavelengths simultaneously transmitted by adjacent interference orders. For a single FPI the minimum achievable Δk (controlled by the geometrical parameters of the external optical system) is 0.5×10^{-2} cm^{-1}. In a BS experiment the FPI is used as a variable narrow band-pass filter by scanning the selected free spectral range by moving the mirrors using piezoelectric transducers and achieving rapid and linear scan rates. Single FPI as BS spectrometers have limitations, the biggest one is the low spectral contrast by overlapping of transmission from different interference orders. In order to solve this problem, multiple interferometers operated in series are used (multi-passing interferometers). By using multipassing interferometry the free spectral range can be expanded by combining interferometers of different mirror spacings L_i. In particular a 'tandem' design is defined by transmission of light only when $\lambda_1 = \frac{2nL_1}{m_1} = \lambda_2 = \frac{2nL_2}{m_2}$. This condition increases the free spectral range by a factor of few tens. To use in an efficient manner such a combination of interferometers, they need to be precisely synchronized so that increments of the mirror distances, δL_i (where the index i refers to the i^{th} interferometer of the series) satisfy:

$$\frac{\delta L_1}{\delta L_2} = \frac{L_1}{L_2} \tag{2.34}$$

In particular, the most common design of tandem multi-pass interferometers used in BS experiments was developed by Sandercock (1978) [203]. In this setup, two FPI are positioned so that the second FPI is oriented at an angle β with respect to the first one. The mirror distance is such that $L_2 = L_1 \cos\beta$ and the condition of Eq. 2.34 is satisfied at all times during the operation of the interferometer. Detectors used in BS experiments must represent a compromise between high energy efficiency in the range of interest and high signal to noise ratio.

Brillouin spectroscopy is highly sensible to the scattering geometry used. The scattering geometry used in a BS experiment is fundamental in order to accurately select the scattering wavevector and angle, which are needed to obtain the acoustic velocities. In order to define the angle of scattering of the incident light in the sample it is necessary to know the characteristics of the sample and the sample container. The scattering angle is then obtained applying Snell's law. The geometry of the light path outside the sample can be set with an accuracy of 10^{-2} degrees. The final accuracy for the internal scattering geometry is constrained by the uncertainty in the refractive indices of sample (and sample container in certain experiments, e.g. high pressure

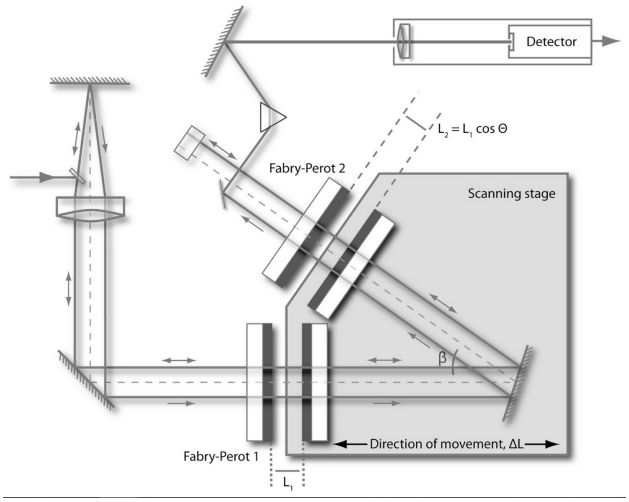

Figure 2.7: Multipass FPI in the tandem implementation by Sandercock. Figure from [224].

experiments in which the sample is inside a DAC, see Fig. 2.8).

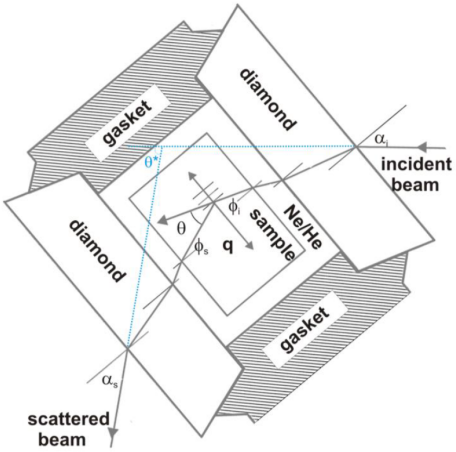

Figure 2.8: Scattering in a DAC. Figure from [224].

In order to simplify the determination of the internal scattering angle several geometries are used in BS experiments, as shown in Fig. 2.9. The most commonly used geometry, in particular for high pressure applications, is the forward symmetric geometry or platelet geometry, in which the incident and scattered sample interfaces are parallel to each other and perpendicular to the bisector of the external scattering angle set by the optics arrangement (see Fig. 2.9a). In this geometry the refractive index of the sample is not needed and the wavevector is $q = 2sin(\theta^*/2)/\lambda_0$, where θ^* is the external scattering

angle and λ_0 is the incident light wavelength in air. Another commonly used geometry is the 90° normal geometry, where the sample incidence and scattering faces are 90° from each other and perpendicular to the incident and scattered light paths respectively (see Fig. 2.9b). In this geometry the effect of the refraction at the sample's surface is removed by symmetry and the wavevector of the scattering vibration is at 45° from both the incident and scattered wavevectors. The magnitude of the scattering wavevector in this geometry is $q = n\sqrt{2}/\lambda_0$, where n is the refractive index of the sample. Further scattering geometries are the backscattering geometry (Fig. 2.9c) and the tilted backscattered geometry (Fig. 2.9d). The backscattering geometry only gives information on the quasi-longitudinal mode, and the magnitude of the scattering wavevector is given by $q = 2n/\lambda_0$. This geometry, when combined with the symmetric forward scattering can give information on the refractive index of an isotropic material at the wavelength of the laser source. Finally the tilted backscattering geometry is used to measure surface Brillouin scattering of opaque materials. In this case the scattering wavevector is $q = 2\sin\phi/\lambda_0$, where ϕ is the angle between incident/scattered wavevector and the surface normal.

All the BS experiments presented in this thesis were performed at the

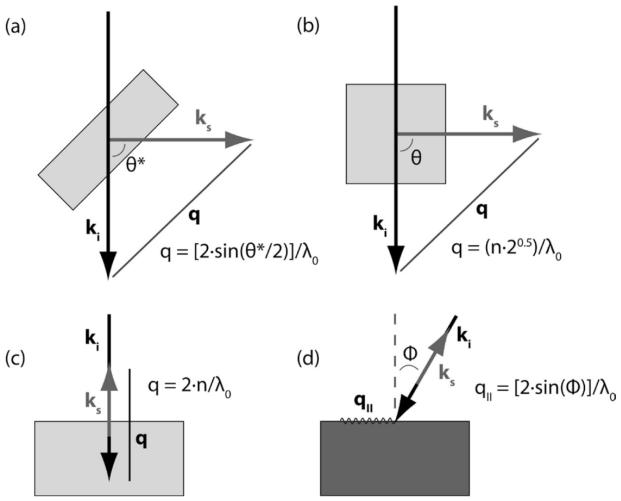

Figure 2.9: Schematic diagram of the different scattering geometries used in BS experiments: (a) forward symmetric geometry; (b) normal geometry; (c) backscattering geometry; (d) tilted backscattering geometry. Figure from [224].

Brillouin spectroscopy laboratory at the German Research Center for Geosciences, GFZ, (Helmholtz Centre, Potsdam). The setup used in our BS ex-

periments is shown in Fig. 2.10. A Coherent VERDI V2 solid state Nd:YVO_4 green laser ($\lambda = 532$ nm) was used as light source. The heart of the setup consists of a six-pass Sandercock-type tandem Fabry-Pérot interferometer equipped with a single photon counting module detector (COUNT® BLUE). A second HeNe red laser is used for the sample alignement.

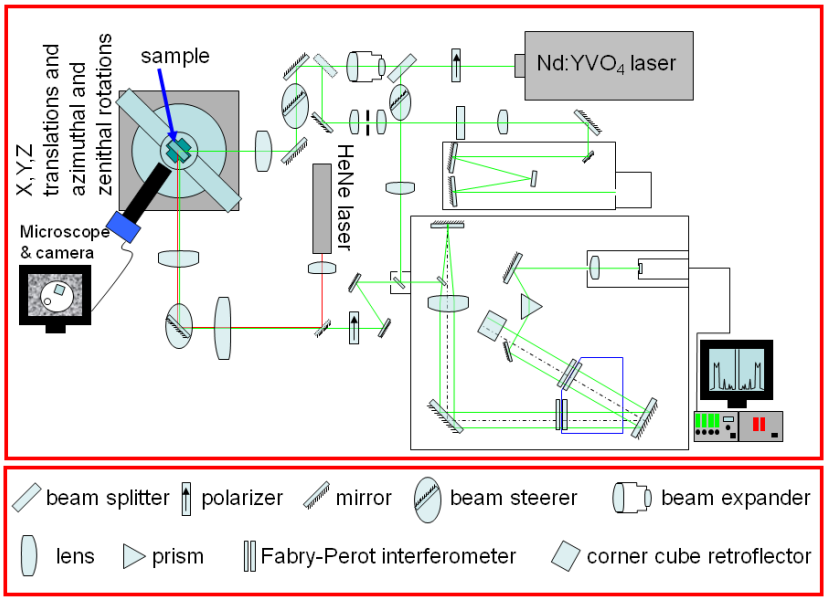

Figure 2.10: Brillouin and Raman setup of the Brillouin spectroscopy laboratory at the German Research Center for Geosciences (GFZ), Potsdam.

The measurements are performed in a forward symmetry geometry with an external angle $\theta = 60°$ between incident and scattered beams. In this geometry, the velocities of the acoustic waves that propagate through the sample are obtained from the Brillouin frequency shifts $\Delta\omega_B$ as:

$$v = \frac{\Delta\omega_B \lambda}{2sin(\theta/2)} \tag{2.35}$$

From the velocities v determined by BS measurements along different directions on single crystals of known density, ρ, it is possible to determine the elastic tensor C_{ijkl} by inversion of the set of Christoffel's equations corresponding to the set of individual probed modes (Eq. 2.21), using a least-square fit. In general, in each Brillouin spectrum, the fastest velocity is associated with the quasi-longitudinal mode and the slower velocities are associated to the quasi-transverse modes with the help of symmetry considerations. The orientation of the sample can be pre-determined by in-situ XRD. If the orientation of the sample is not well defined, for high symmetry single crystals measured in

platelet geometry it is possible to refine both elastic tensor coefficients and sample orientation, simultaneously. Except for directions with degeneracies of the acoustic phonon branches or directions following certain selection rules, it is possible to observe all acoustic modes for each direction. This leads to a large redundancy of measured phase velocities with respect to the number of independent coefficients to be determined, that would, in principle, allow for the determination of the full elastic tensor of crystals of any symmetry with a relatively small number of measurements performed in general directions. However, subsets of moduli are strongly correlated and limited datasets can strongly decrease our abililty to recover the full elastic tensor [35].

2.4.2 Equations of state

The thermodynamic state of a system is usually defined by pressure P, temperature T and specific volume V. The variation of the unit cell volume V of a material as a function of P and T is described by its equation of state (EoS). Measured EoS are generally parameterized in terms of bulk modulus, K:

$$K = -V \left(\frac{\partial P}{\partial V} \right)_T \tag{2.36}$$

and its pressure derivatives $K' = (\partial K/\partial P)_{P=0}$ and $K'' = (\partial^2 K/\partial P^2)_{P=0}$, evaluated at P=0. The bulk modulus obtained from XRD experiments is obtained from experiments performed at constant temperaure, and is called isothermal bulk modulus K_T. The isothermal bulk modulus is different from the value obtained from elasticity measurements (e.g. Brillouin spectroscopy, ultrasonic measurements), which measure adiabatic (at constant entropy, S) bulk moduli, K_S. The two values of the bulk moduli are related by:

$$\frac{K_S}{K_T} = 1 + \gamma_{th} \alpha T \tag{2.37}$$

where γ_{th} is the thermodynamic Grüneisen parameter and α is the volumetric thermal expansion of the material [186]. At room temperature, the difference between the isothermal and adiabatic bulk moduli is typically a few percent for the vast majority of minerals.

A number of EoS have been derived [269, 19, 6, 4], in particular we will focus on finite strain EoS, which are based on the assumption that the strain energy of a solid undergoing a compression is expressed as a Taylor series in terms of finte strain, f. Finite strain f can be defined in a number of ways,

in this work we will use the Eulerian strain:

$$f = \frac{1}{2}\left[\left(\frac{V_0}{V}\right)^{2/3} - 1\right] \tag{2.38}$$

The most common EoS used in geosciences is based on the Eulerian strain and is the Birch-Murnaghan (BM) equation, which is derived from the expansion of the Helmholtz free energy in the Eulerian strain [19]. Expansion of the BM equation to the fourth order in the strains yields:

$$P = 3K_0 f(1+2f)^{5/2}\left(1 + \frac{3}{2}(K_0' - 4)f + \frac{3}{2}\left(K_0 K_0'' + (K_0' - 4)(K_0' - 3) + \frac{35}{9}\right)f^2\right) \tag{2.39}$$

A tool that provides a direct indication of the compressional behaviour of a material and a useful visual evaluation od the quality of an EoS fit is given by the so called $F - f$ plot [6]. For the BM EoS, the normalized stress F is defined as:

$$F = \frac{P}{3f(1+2f)^{5/2}} \tag{2.40}$$

where f is the Eulerian finite strain 2.38. If the data points lie on a horizontal line of constant $F = K_0$, then $K_0' = 4$ and a second order truncation (order at which the expansion of the Helmholtz free energy in Eulerian strain is truncated) of the BM EoS can be used to fit the data. If the data lie on an inclined straight line, the slope is equal to $3K_0(K_0' - 4)/2$ and the data can be fitted with a third order truncation of the EoS.

2.4.3 Density functional theory

Density functional theory (DFT) is a successful theory, originally developed by Hohenberg and Kohn [91], that allows to calculate the electronic structure-property relations of crystalline compounds [106, 255]. Traditional electronic structure methods consist of using the Schrödinger equation of N interacting electrons moving in an external electrostatic potential, however this problem is non trivial even for low N and the computational effort grows rapidly with increasing N. DFT uses a different approach where, instead of a many-body wave function, the energy of electrons moving in an external potential is a unique functional of the electron density $\rho(\mathbf{r})$, making a computationally feasible model even for large systems. A practical scheme for DFT calculations is given by the so-called Kohn-Sham equations [115] (expressed in atomic units where $\hbar = e = m_e = 4\pi\epsilon_0 = 1$):

$$\left[-\frac{1}{2}\nabla^2 + V_{ext} + \int \frac{\rho(\mathbf{r}')}{|\mathbf{r} - \mathbf{r}'|}d\mathbf{r}' + V_{xc}(\mathbf{r})\right]\psi_i(\mathbf{r}) = \epsilon_i\psi_i(\mathbf{r}) \tag{2.41}$$

$$\rho(\mathbf{r}) = \sum_{i}^{n} |\psi_i(\mathbf{r})|^2 \tag{2.42}$$

$$V_{xc} = \frac{\delta E_{xc}\left[\rho(\mathbf{r})\right]}{\delta n(\mathbf{r})} \tag{2.43}$$

Where ψ_i are the single-electronic wave functions, $-\frac{1}{2}\nabla^2\psi_i(\mathbf{r})$ in Eq. 2.41 represents the kinetic energy of the electrons, V_{ext} is the external potential, $\int \frac{\rho(\mathbf{r}')}{|\mathbf{r}-\mathbf{r}'|} d\mathbf{r}'$ is the Hartree potential which describes the interaction of the i-th electron with the average electron density and V_{xc} is the exchange-correlation potential and contains all the inter-electronic interactions that are not included in the previous terms (this term is an approximation).
Several DFT-based codes are available nowadays, in particular, "planewave" codes such as CASTEP [49] or VASP [116] (and many others such as Quantum Espresso, ABINIT) are computationally efficient as the electron states in the ionic core are not computed explicitly, but solved using pseudopotentials or the projector augumented method (PAW) [20]. Pseudopotentials are effective potentials designed to reproduce the scattering of electrons by the atoms in such a way that only valence electrons become relevant. The accuracy of the pseudopotential based calculations depends on the quality of the pseudopotential itself. For the above mentioned DFT codes the convergence behaviour is typically controlled by only a few parameters, such as the kinetic cut-off energy and the k-space sampling, making it straightforward to ensure the convergence of the results. As mentioned above, current DFT calculations require an approximate description of the exchange-correlation interaction, V_{xc}. A commonly used functional is the local density approximation, LDA, however calculations using LDA binding energies might predict incorrect ground state structures, leading to small lattice parameters. A second common choice is the generalized gradient approximation, GGA, of which several variants have been proposed, such as the Perdew-Burke-Ernzerhof (PBE) [177], PBE-SOL [179] and many others. GGA calculations are known to result in larger lattice constants ('underbinding') but the binding energies are improved compared to LDA. DFT calculations are commonly employed to predict structural parameters and physical properties of crystalline materials, in particular, in this work of thesis, DFT calculations were performed by Prof. Björn Winkler and Dr. Johannes Wagner to obtain the elastic stiffness coefficients of aragonite (Ch. 3), dolomite (Ch. 6) and metal organic frameworks with different compositions (Ch. 7) at P=0 GPa. The approach used to obtain elastic stiffness coefficients is typically from stress-strain relations. The results of the calculations are greatly influenced by the choice of the exchange-correlation functional: LDA results in an upper bound to the elastic stiffness coefficients, while GGA provides a lower bound. Comparison of

the elastic stiffness coefficients computed using LDA, GGA-PBE, PBESOL and WC-xc functionals showed that PBESOL and WC-xc outperform LDA and GGA-PBE approximations [255]. The accuracy of DFT-based calculations for elastic stiffness coefficients is about 5% for the diagonal coefficients and about 10% for off-diagonal coefficients [255].

2.4.4 Other techniques

In addition to Brillouin spectroscopy measurements, complementary techniques such as plane parallel plate ultrasound technique, resonant ultrasound spectroscopy and thermal diffuse scattering analysis were used to determine the elastic tensor coefficients of metal organic frameworks (Ch. 7).

Plane parallel plate ultrasonic technique

In a plate ultrasonic technique the sample is connected to a transducer by means of a suitable transmission medium. The transducer (piezoelectric crystal) excites mechanical oscillations through a sample (which is typically a parallel platelet), generating ultrasonic waves. The ultrasonic wave generated at the face of the plate which is in contact with the transducer travels through the crystal and is reflected at the upper face of the plate. The state of resonance is detected by the change of impedance in the transducer-sample system, or by diffraction of light on the ultrasonic grating. Resonance frequencies can be detected by measuring the phase angle between the current and the voltage. The difference between the m^{th} and the n^{th} frequencies, f_m and f_n, and the thickness of the sample parallel to the propagation direction d are related to the velocity of the ultrasonic wave of a certain mode v by:

$$v = 2d\left(\frac{f_m - f_n}{m - n}\right) \tag{2.44}$$

By measuring the acousic velocities that propagate through the sample, for given known directions and the density of the studied samples it is possible to obtain information on the elastic tensor parameters. In this thesis, ultrasonic measurements were performed by Dr. Eiken Haussühl at the Institut für Geowissenschaften, Goethe Universität, Frankfurt.

Resonant ultrasound spectroscopy

Resonant ultrasound spectroscopy (RUS) is a technique based on the fact that solid objects have natural frequencies at which they vibrate when mechanically excited. These natural frequencies are related to the elastic properties,

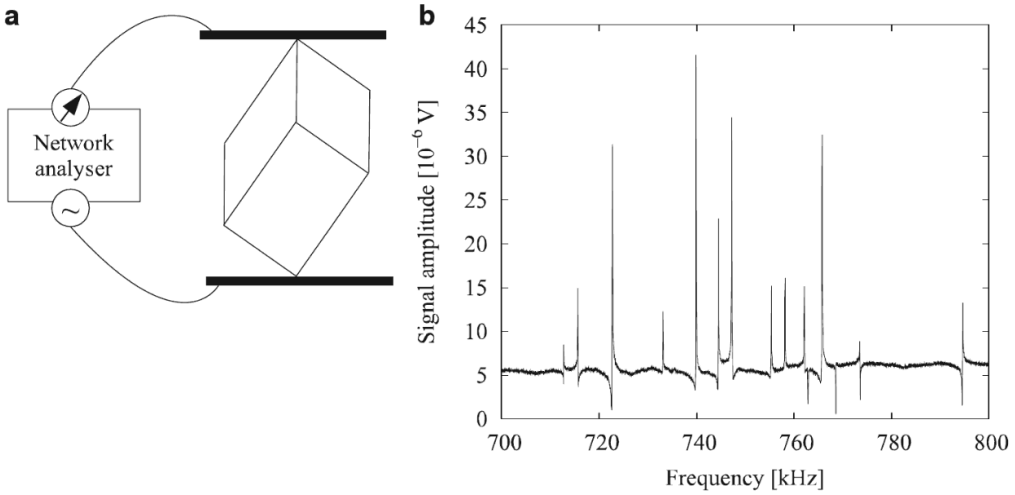

Figure 2.11: (a) Schematic of a RUS set-up. (b) RUS sprectrum of tormaline. Figure from Schreuer et al. (2005) [206].

size and shape of the material. The sample can be either a single crystal or a compressed polycrystalline aggregate, and can range in size between 1 mm and 1 cm (for elasticity measurements). In a RUS experiment the sample is lightly clamped between two transducers, the force acting on the sample is selected so that the sample will be in a freely vibrating body condition. A sinusoidal signal is applied to one of the transducers and analysed by the second one. The advantage of RUS is the possibility to obtain all independent elastic tensor coefficients of a crystal at ambient conditions on a single sample with high accuracy and internal consistency regardless of the symmetry. RUS can also be applied to a broad range of temperatures but is challenging at high pressures. The principles of RUS analysis are laid out in [157, 206]. Here, a quick overview of RUS technique is presented. Fig. 2.11 shows the schematic of a RUS setup and an example of RUS spectrum. In a RUS experiment frequencies between 50 kHz and 20 MHz are employed (with a frequency resolution of 0.003 kHz). The elastic tensor coefficients are derived from the resonance spectrum using the frequencies of m observed eigenmodes, m being dependent on the sample symmetry (e.g. for cubic crystal at least 100 eigenmodes are needed). The C_{ij} evaluation is carried out by a least-squares procedure in which the observed resonance frequencies are compared to calculated ones. The calculated frequencies are obtained from sample dimensions, experimental density, dielectric permittivity and a trial set of elastic coefficients and piezoelectric stress coefficients by solving a general eigenvalue problem, the rank of which is equivalent to the number of

basis functions used for the components and displacement vector expansion. The least square refinement consists in the minimization of the quantity:

$$\chi = \sum_{i=1}^{n} w_i(\omega_i^2(calc) - \omega_i^2(obs)) \tag{2.45}$$

for n circular eigenmodes with resonance frequencies $f_i = \omega_i/2\pi$.

In this work of thesis, RUS measurements were performed by Dr. Eiken Haussühl using a custom-built RUS-device [85] at the Institut für Geowissenschaften, Goethe Universität, Frankfurt.

Thermal diffuse scattering

Thermal diffuse scattering (TDS) refers to scattering caused by lattice thermal vibrations (phonons). Diffuse scattering can be due to either thermally excited elastic waves or to particular features of the static arrangement of atoms in a crystal and produces a background darkening on X-ray diffractograms around the Bragg reflections. As a physical phenomenon, the diminution of the intensity of X-ray reflections due to the thermal vibration of atoms, had been noticed already in 1920, however, it is only with the currently available high-flux brilliant synchrotron facilities, used in combination with bidimensional single-photon counting X-ray detectors with good quantum efficiencies that TDS was rediscovered [245]. TDS allows to determine phonon dispersions, similarly to neutron scattering and inelastic X-ray scattering. In particular, thermal diffuse scattering, has high data-acquisition rate and a simple experimental setup compared to other techniques and allows to obtain the full elastic tensor of a material from a single diffraction experiment for arbitrary crystal symmetries. A previous study by Wehinger et al. (2017) [245] on calcite and magnesium oxide showed it is possible to obtain the complete elasticity tensor by measuring TDS at two close temperatures (multi-temperature approach). The results from the study displayed remarkable agreement with literature data, showing that TDS can compare to standard methods (i.e., BS, RUS) with the advantage of applicability to very small, opaque materials of arbitrary shape [245].
The analysis of TDS data is based on the fitting of the elastic stiffness coefficients C_{ijkl} to the TDS intensities close to Bragg reflections in 'regions of interest' (ROIs) in the reciprocal space. The ROIs are chosen in order to be close enough to the reciprocal lattice points as to include diffuse scattering due to acoustic phonons, but far enough to exclude Bragg scattering. Typical distances from the nearest Bragg spot are 0.05-0.15 $Å^{-1}$. The intensity of TDS is given by [245]:

$$I = N I_0 Q^T \frac{k_B T}{q^2 \Lambda(q)} Q \Big| \sum_s \frac{f_s}{\sqrt{m_s}} e^{-M_s} \Big|^2 \tag{2.46}$$

with

$$\Lambda_{jm}(q) = \frac{1}{\rho q^2}(C_{ijlm} q_i q_l), \tag{2.47}$$

where N is the number of unit cells, I_0 the incident beam intensity, Q the total scattering vector, k_B the Boltzmann constant, T the temperature, q the momentum transfer, f the atomic scattering factor of ion s with mass m and Debye-Waller factor M and ρ is the density of the material. A detailed explanation of the formalism can be found in [258, 244, 245, 29].
By measuring TDS at two different temperatures, it is possible to isolate the component of the diffuse scattering due to the static disorder, air scattering and fluorescence, as they show a much smaller temperature dependence than TDS. The scattering intensities can then be calculated by summing over the three phonon branches using Eq. 2.46. The calculated intensities are then renormalized by an array $g(Q)$, which takes into account absorption, polarization and geometric factors. A second array $b(Q)$ is also added, for the background. The elastic tensor C is determined by solving the optimization problem

$$C, b_2, b_1, g = \mathrm{argmin}_{C', b_2', b_1', g'} \left(\sum_Q \left(\left[I^{calc}_{Q,T_2}(C', b_2', g') - I^{calc}_{Q,T_1}(C', b_1', g') \right] - \left[I^{exp}_{Q,T_2} I^{exp}_{Q,T_1} \right] \right)^2 \right) \tag{2.48}$$

where C is constrained by the crystal symmetry, and b and g are kept in the vicinity of the individual Bragg reflections [245, 29]. A more detailed description on the TDS analysis is beyond the scope of this thesis and can be found in [245, 29, 159, 244, 258]. In this thesis TDS experiments were performed at the P21.1 beamline at PETRA-III, DESY, Hamburg, Germany (the results of the study are reported in Ch. 7, where a combination of different techniques was used to study the elasticity of metal organic framework compounds). Photons with energy of 100 keV were used in order to avoid sample damage. A CdTe PILATUS 1M detector with pixel size of 0.172×0.172 μm was used, which provides a dynamic range and allows near noiseless measurements. At 100 keV, the detector had a quantum efficiency of 56%. The analysis of TDS data was performed by Julia Büscher.

Chapter 3

Elasticity of natural aragonite, a Brillouin spectroscopy study

The elastic stiffness tensor of aragonite ($CaCO_3$, orthorhombic with space group *Pmcn*) has only been reported in two experimental studies and the results of these studies differ strongly from one another (up to more than 100% for off-diagonal coefficients C_{13} and C_{23}). Voigt (1910) [240] performed torsion experiments and, from the elastic response of the crystal, determined the elastic tensor coefficients of aragonite. However, no information was provided on the chemical composition of the samples used in that study and the method used to determine the elastic properties of this material is likely to be affected by significantly large measurement errors. Liu *et al.* (2005) [133] performed Brillouin spectroscopy experiments on a natural aragonite sample with 2.5 wt% of $SrCO_3$ (i.e. 1.7 mol%), which is the maximum amount of Sr observed in natural samples.
That means that, to this date, there is no univocally experimentally determined elastic tensor for end-member aragonite available. Natural carbonates are known to incorporate trace elements, in particular Sr is commonly present in natural aragonites up to 2 mol% [34, 158]. Several studies have been performed on the influence of Sr on the elastic properties and phase stabilities of $CaCO_3$ [222, 34, 32]. Brillouin spectroscopy and SC-XRD studies performed on synthetic strontianite $SrCO_3$, showed that $SrCO_3$ is much softer than aragonite $CaCO_3$ (the bulk modulus of $SrCO_3$ is 16% lower than that of aragonite) [16, 14]. Finally, Spahr et al. (2021) [222] investigated the effect of Sr on the bulk modulus of synthetic $Sr_xCa_{1-x}CO_3$ solid solutions with aragonite structure ($x = 0.2, 0.5, 0.8$), by high pressure (up to 40 GPa) synchrotron powder XRD and DFT calculations, showing that the presence of Sr leads to a non-linear lowering of the bulk modulus, with a minimum at $x = 0.5$.

Additionally, the elastic properties of aragonite were also studied in several computational studies [175, 94, 166]. However, additional experimental studies are fundamental to establish a reliable reference set of elastic coefficients for end-member aragonite and determine its dependence on Sr-Ca substitution in the Sr-poor range proper of natural materials.
Here, we report a Brillouin spectroscopy study on natural aragonite samples. In order to verify the reproducibility of the results, three different, well characterized samples were used. The different chemical compositions of the samples studied cover most of the compositional range of natural aragonites with Sr contents ranging from 0.1 to 1.5 mol%.

3.1 Samples and methodology

The single crystals used in this study are natural samples: two samples from Bilina in Czech Republic (Arag-T, Arag-NT) and one from Sicily, Italy (Arag-S). The samples were optically clear and free of twins. The chemical composition of each sample was obtained by electron microprobe analysis (EMPA) using a JEOL thermal field emission instrument JXA-8500F (HYPERPROBE) at the German Research Centre for Geosciences (GFZ) (Helmholtz Center Potsdam, Germany), using an acceleration voltage of 15 kV, a beam current of 5 nA, and a spot size of 8 μm (See Appendix A). The results are shown in Tab.3.1.

The unit cell parameters for each sample were obtained by powder X-ray

Table 3.1: Chemical composition (expressed as mole fractions of the endmembers) of the samples used in this study from the EMPA. (bdl= below detection limit)

Sample	$CaCO_3$	$SrCO_3$	$BaCO_3$	$MgCO_3$	$MnCO_3$	$FeCO_3$
Arag-T	0.9986(7)	0.0012(5)	bdl	bdl	bdl	bdl
Arag-NT	0.996(1)	0.003(1)	bdl	bdl	bdl	bdl
Arag-S	0.985(1)	0.015(1)	bdl	bdl	bdl	bdl

diffraction at ambient conditions, using a STOE Stadi P diffractrometer with a Bragg-Brentano geometry, a Ge(111) monochromator and a 7° wide position sensitive detector. Standard operating conditions (CuKα1-radiation, 40 kV and 40 mA) were used to collect data in the 2θ range 5-125° with a step size of 0.1°. The structure refinement Rietveld analyses were performed using the GSAS software package [235] (Fig. A.2).

Table 3.2: Unit cell parameters, volume and densities from Rietveld refinement of the powder diffraction experiments performed on the samples in this study and in the study by [133].

Sample	a (Å)	b (Å)	c (Å)	V (Å^3)	ρ (g/cm^3)
Arag-T	4.9617(7)	7.969(1)	5.7423(8)	227.05(6)	2.9280(7)
Arag-NT	4.9593(8)	7.965(1)	5.734(1)	226.73(7)	2.9321(9)
Arag-S	4.9631(2)	7.9695(4)	5.7444(3)	227.21(2)	2.9394(3)
Liu et al. (2005)	4.96183(1)	7.96914(2)	5.74285(2)	227.081(1)	2.9513(1)

The obtained values of the unit cell parameters are in reasonably good agreement with the reference values found in ICDS-16682076 [9]. The unit cell parameters and densities are reported in Tab. 3.2, together with the literature values of the sample studied by Liu et al. (2005) [133]. The samples thickness varied from 1 mm to a few μm and they were finely polished to obtain transparent samples with parallel faces. Brillouin spectroscopy (BS) measurements were performed at the Brillouin laboratory at the German Research Centre for Geosciences, GFZ, in Potsdam.
The elastic stiffness tensor for end-member aragonite $CaCO_3$ was also obtained, for comparison, by Dr. Johannes Wagner from *ab initio* DFT calculations using the projector augmented wave approach (PAW) [20]. The general gradient approximation (GGA) in the revised Perdow-Burke-Ernzerhof (PBE-sol) [178] formalism was used for the exchange correlation energy as implemented in the VASP code. A set of $7 \times 4 \times 6$ k-points was used to sample the Brillouin zone. The cutoff energy was set to 600 eV.

3.2 Results

Aragonite is orthorhombic with a space group *Pmcn*, hence the elastic stiffness tensor C_{ij} has 9 independent non-zero coefficients: C_{11}, C_{12}, C_{13}, C_{22}, C_{23}, C_{33}, C_{44}, C_{55} and C_{66} in contracted Voigt notation. In platelet-geometry, for non-cubic crystals it is necessary to collect data in at least two orthogonal planes to minimize the covariance between the values of the elastic tensor coefficients and provide a more accurate set of elastic constants. In this work at least three approximately orthogonal planes per sample were measured by BS:

Arag-T For sample Arag-T three orthogonal planes were cut. Two of the three planes were then oriented by single crystal XRD, showing a cut perpendicular to the [001], [0.67, -1, 0] axes and the orientation of the third platelet is constrained to be perpendicular to the others, obtaining the crystallographic plane (-1, 0.67, 0). More than 300 acoustic velocity data were collected for this sample along a total of 108 distinct directions.

Arag-NT For sample Aragonite-NT six different orientations were studied: the sample was first cut in three orthogonal planes, two of which were oriented by SC-XRD, showing a cut perpendicular to [001] and [110] the orientation of the other slices was determined geometrically, finding the crystallographic planes: (-110), (1, 0.26, 0), (100) and (010). 550 velocity data were collected for this sample along a total of 198 distinct crystallographic directions.

Arag-S For sample Aragonite-S four different crystallographic orientations were studied but none of them were oriented by SC-XRD. The orientation of the platelets was determined from the acoustic velocities dispersion curves, and using the elastic tensor coefficients obtained for sample Arag-T as a starting model. This allowed to determine a possible orientation of the sample, which was then refined in combination with the elastic tensor coefficients C_{ij}. The refinement of the Eulerian angles show that the crystallographic planes studied were (001), (1, -0.2, 0), (-0.08, -0.15, 1) and (0.32, -1, 0). More than 400 velocity data were collected for this sample along 144 distinct directions.

Fig. 3.1 shows a representative Brillouin spectrum for Arag-T. Most of the Brillouin spectra show strong intensities for the wave velocities (v_p and v_s) with high signal to noise ratios. The complete velocities dataset was used to determine the elastic tensor coefficients, by fixing the Eulerian angles of the platelets oriented by SC-XRD and refining the Eurlerian angles of the remaining platelets.
Using the normal vectors obtained by the single crystal diffraction study and the literature values from Liu et al. (2005) [133] as an initial set of estimated elastic constants, it was possible to obtain the elastic tensor coefficients by least-square fitting of the full sets of Christoffel's equations (one per each individual acoustic mode). Fig. 3.2 shows the acoustic velocities as a function of the rotational angle for the sample Arag-T and Arag-S. The elastic tensor coefficients, C_{ij}, experimentally obtained for natural aragonites in this BS study together with the literature data [133, 240] are listed in Tab. 3.3. Tab. 3.3 also shows the elasticity values for end-member strontianite $SrCO_3$[16]. Additionally, Tab. 3.3 also lists the aggregate elastic bulk

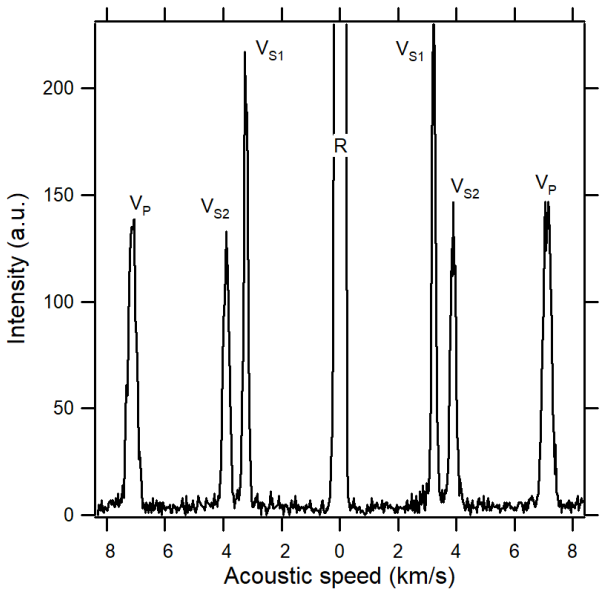

Figure 3.1: Representative spectrum of Arag-T showing the frequency shift from the elastically scattered central Rayleigh peak (labeled R) and the peaks corresponding to the longitudinal and transverse mode (v_p and v_s).

(K_H) and shear moduli (G_H) calculated using the Voigt-Reuss-Hill (H) averaging scheme and the axial compressibilities β_i, together with literature data for comparison. The axial compressibilities, β_i, represent the change in lenght along the orthorhombic axes under hydrostatic pressure and are related to the elastic compliances s_{ij} by [167]:

$$\beta_a = s_{11} + s_{12} + s_{13} \tag{3.1}$$

$$\beta_b = s_{21} + s_{22} + s_{23} \tag{3.2}$$

$$\beta_c = s_{31} + s_{32} + s_{33} \tag{3.3}$$

In addition to the elastic properties, it is possible to obtain information on the acoustic velocity anisotropy values for aragonite. The anisotropy of the longitudinal velocity v_p can be obtained using the anisotropy factor A_p [140]:

$$A_p[\%] = \frac{(v_{p,Max} - v_{p,min})}{(v_{p,Max} + v_{p,min})} \cdot 200 \tag{3.4}$$

where $v_{p,Max} = \sqrt{\frac{C11}{\rho}}$ and $v_{p,min} = \sqrt{\frac{C33}{\rho}}$ represent the maximum and minimum compressional wave velocities respectively. For aragonite, P-waves

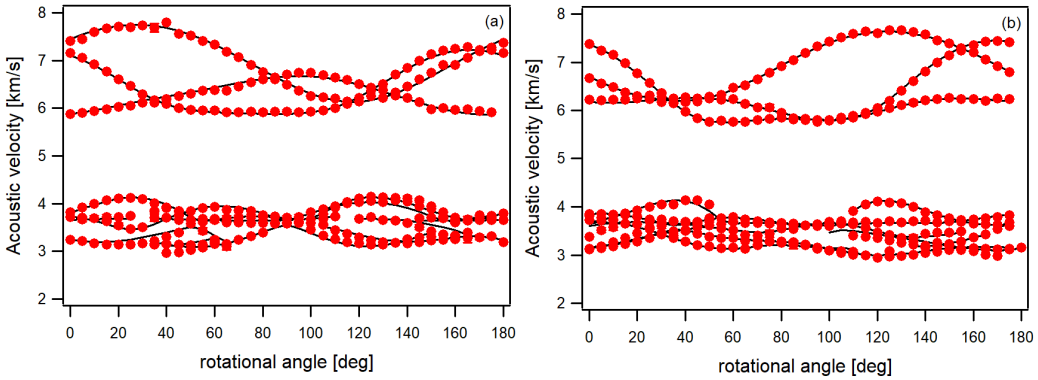

Figure 3.2: Longitudinal and transverse acoustic velocities for the three platelets of Arag-T (a) and Arag-S (b) as a function of the rotational angle. The solid lines are calculated from the fit of the Christoffel's equation.

Table 3.3: Elastic tensor coefficients, elastic parameters and axial compressibilities β for aragonite (this study and Liu et al. 2005 [133] and Voigt (1910) [240]) and $SrCO_3$ [16].

	This study				Lit. data		
					$CaCO_3$		$SrCO_3$
Elastic	DFT	Arag-T	Arag-NT	Arag-S	Liu [133]	Voigt[240]	Bied.[16]
C_{11} (GPa)	178(1)	176.0(5)	176.2(6)	173.8(5)	171(1)	159.6	153(1)
C_{12} (GPa)	61.9(8)	60.1(5)	63(1)	62.5(5)	60(1)	36.6	52(1)
C_{13} (GPa)	29.7(7)	29.8(6)	25.5(8)	27.2(6)	28(2)	2.0	38(11)
C_{22} (GPa)	113(2)	110.1(4)	111.6(4)	111.4(4)	110.1(9)	87.0	109.6(8)
C_{23} (GPa)	47.7(7)	45.2(7)	43.4(7)	43.2(5)	42(2)	15.9	43(15)
C_{33} (GPa)	102(1)	101.4(3)	103.7(2)	99.8(2)	98(1)	85.0	75(1)
C_{44} (GPa)	40.2(3)	40.9(5)	40.0(3)	39.7(3)	39.3(6)	41.3	28.0(5)
C_{55} (GPa)	22.26(3)	27.5(4)	26.6(3)	25.9(6)	24.2(4)	25.6	28.6(4)
C_{66} (GPa)	40.8(5)	39.8(5)	39.4(4)	39.6(3)	40.2(6)	42.7	33.2(5)
K_H (GPa)	72.5(4)	71.0(3)	70.7(3)	70.1(2)	69(1)		64(4)
G_H (GPa)	36.9(3)	37.1(2)	36.9(2)	36.4(1)	35.8(2)		31(1)
β_a(TPa^{-1})	2.97(1)	2.92(1)	2.9(2)	3.0(2)	3.0(2)		3(2)
β_b(TPa^{-1})	4.23(4)	4.6(2)	4.7(8)	4.6(5)	4.6(2)		4(6)
β_c(TPa^{-1})	6.9(3)	6.9(2)	6.9(5)	7.3(5)	7.3(6)		10(8)

propagate fastest along the [100] direction and slowest in the [001] direction [94].
The polarization anisotropy factor for the transverse velocities v_S defines the

difference in percentage between the two orthogonally polarized v_s in a given direction normalized to the average shear wave velocity, v_s. It is given by:

$$A_{pol-S}[\%] = \frac{v_{s1} - v_{s2}}{v_s} \cdot 100 \tag{3.5}$$

where $v_s = \sqrt{\frac{G}{\rho}}$. For aragonite, the largest S-wave splitting (dVs) is observed for the [010] and [111] directions [94]. A better quantification for anisotropy is given by the universal anisotropy index, A^u (Eq. 2.26). The values for azimuthal, splitting and universal anisotropy of the samples measured in this study, together with the literature values for aragonite [133] and strontianite [16] are listed in Tab. 3.4.

Table 3.4: Acustic velocity anisotropy of aragonite (this study and Liu et al. 2005 [133]) and $SrCO_3$ (Biedermann et al. (2017) [16]).

	This study			Lit. data	
				$CaCO_3$	$SrCO_3$
Anisotropy	Arag-T	Arag-NT	Arag-S	Liu [133]	Bied. [16]
A^u	0.463(6)	0.506(6)	0.504(4)	0.53(1)	0.5(2)
$A_P[\%]$	27.4	26.4	27.6	27.7	35.3
$A_{pol-S}[\%]$	33.83	35.1	33.8	34.9	18.2

3.3 Discussion

Our data show good agreement (within 3% for the individual tensor coefficients C_{ij}) with the values obtained from the DFT calculations (this study and the study by Nguyen-Than et al. (2016) [166], for which a discrepancy of 12% along the C_{12} is observed) and with the previously measured elastic tensor coefficients from Liu et al. (2005) [133], as shown in Fig. 3.3. The results of this study provide the most complete available data-set for aragonite at ambient conditions, covering the compositional range of natural aragonites. The measured elastic stiffness coefficients values vary slightly among the samples, in particular the C_{11} and C_{33} coefficients shows a 3% lowering from the Sr-free aragonite and to the sample with the highest Sr content from Liu et al. (2005) [133]. Fig. 3.4 shows the dependence of $r_{ij} = \sqrt{\frac{C_{ij}}{\rho}}$ as a function of the composition. The value of the isentropic bulk modulus K_S obtained from the elastic tensor coefficients decreases with increasing Sr content from Arag-T to Arag-S. The trend is confirmed by the results relative to Sr-richer

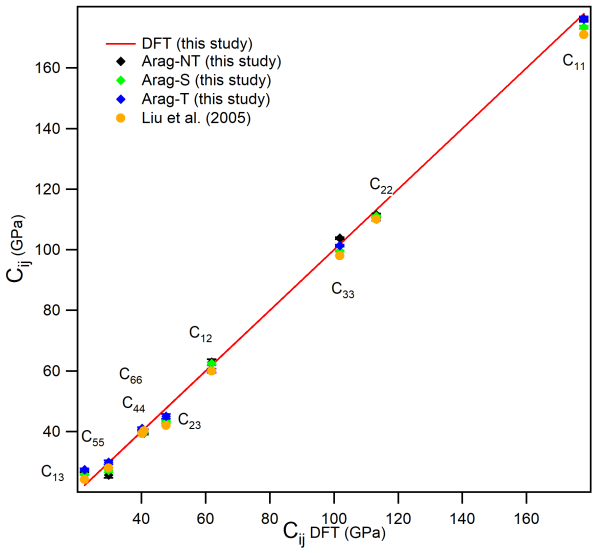

Figure 3.3: Comparison between the elastic tensor coefficients of aragonite measured in this study and the coefficients obtained from DFT calculations (also this study). The data from Liu et al. (2005) [133] are also shown.

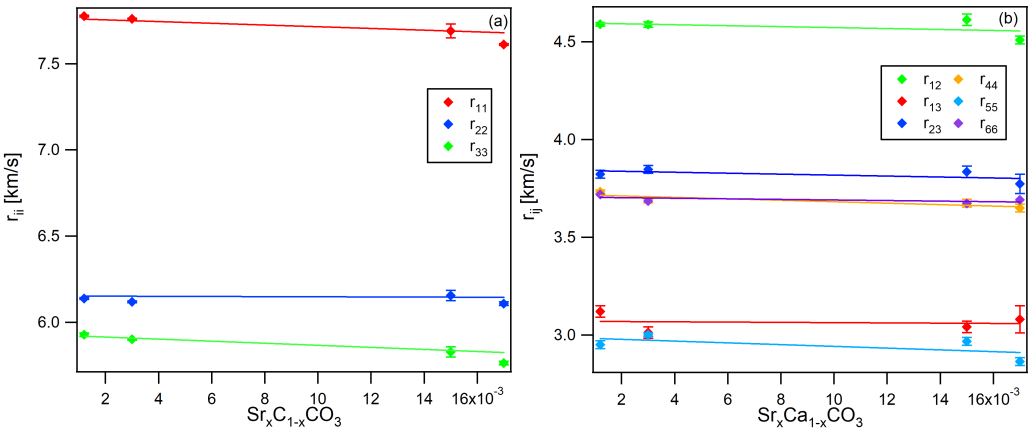

Figure 3.4: Square root of the normalized elastic coefficients $\sqrt{\frac{C_{ij}}{\rho}}$ as a function of composition for the samples measured in this study and in the study by Liu et al. [133].

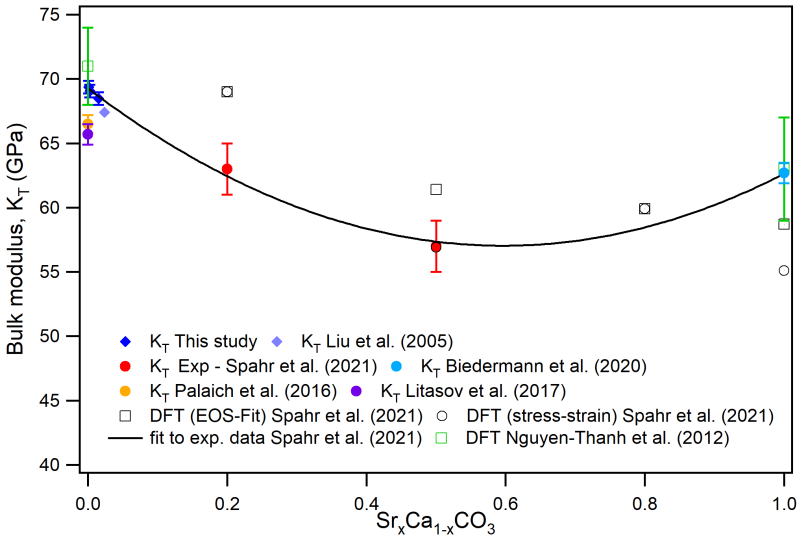

Figure 3.5: Isothermal bulk modulus for $Sr_xCa_{1-x}CO_3$ solid solutions. Modified after Spahr et al. (2021) [222]. Diamonds represent the values obtained from Brillouin spectroscopy (this study and Liu et al. [133]). Values for end-member $CaCO_3$ and $SrCO_3$ are from Nguyen-Thanh et al. (2012) [166] and Biedermann et al. [14]. Experimental values from PXRD experiments are from Palaich et al. (2016) [173] and Litasov et al. (2017) [126].

sample analyzed by Liu et al. [133]. We compared our results with the values relative to the isothermal bulk modulus obtained from a series of synthetic compositions in the system $CaCO_3$-$SrCO_3$ [222]. In order to compare the results we converted K_S in K_T using the thermodynamic identity of Eq. 2.37, assuming the the Grüneisen parameter and the thermal expansion coefficient are constant across the SrO compositional range between 0 and 2.5 wt%. In particular, we used the values of the thermal expansion α=5.8×10^{-5} K^{-1} and Grüneisen parameter γ = 1.39 determined for synthetic aragonite by Litasov et al. (2017) [126]. The difference in the elastic tensor coefficients and aggregate elastic moduli is consistent with an effect of Sr on the elastic parameters from aragonite $CaCO_3$ to strontianite $SrCO_3$ [16]. However, the variation is too small to ascertain the effect of a few mol % of Sr on the elasticity of aragonite.

Another issue to be addressed is the comparison between the elastic bulk modulus of aragonite with respect to that of calcite. It is generally expected, for a high pressure polymorph to have a greater bulk modulus compared to the low-pressure polymorph. For $CaCO_3$, aragonite is denser than calcite, as expected, however the different structure makes aragonite more compressible, with a bulk modulus 9.7 % lower than that of calcite (K_{VHR} =

78.6(4) GPa [123]) at ambient conditions. The comparison between elastic moduli and axial compressibilities of aragonite (sample Arag-T) and calcite (from Lin et al. (2013) [123]) is reported in Tab. 3.5. From the results re-

Table 3.5: Elastic parameters of aragonite (Arag-T) and calcite (from Lin et al. (2013) [123]).

Elastic	Arag-T this study	Calcite Lin et al. [123])
K_H (GPa)	71.0(3)	78.6(4)
G_H (GPa)	37.1(2)	32.1(2)
β_a (TPa^{-1})	2.92(1)	2.55
β_b (TPa^{-1})	4.6(2)	2.55
β_c (TPa^{-1})	6.9(2)	8.14
v_P (km/s)	6.64(3)	6.68(2)
v_S (km/s)	3.68(1)	3.43(1)

ported in Tab. 3.5, it is evident that aragonite has a lower value (-9.7 %) of bulk modulus, K, but a higher (+13 %) shear modulus, G, and, while calcite is more compressible than aragonite along the c-axis, the axial compressibility along the a- and b-axes is higher in aragonite. The difference in structure between calcite and aragonite can be used to explain the apparently anomalous behaviour of the aggregate elastic moduli of $CaCO_3$. The axial compressibility of calcite and aragonite is directly related to the orientation and compressibility of the constituing polyhedra that make their respective structures [198]. Carbonate groups CO_3 are stiff at low pressures, and compression in calcite and aragonite is accommodated by geometric changes in the Ca-O polyhedra. In both calcite and aragonite, the plane created by the a- and b-axes is parallel to the carbonate groups, and the c-axis is perpendicular to them, as shown in Fig. 1.2. Thus resulting in a higher compressibility along the c-axis for both structures. Calcite is trigonal with space group $R\bar{3}c$. In calcite, the CO_3 groups are arranged into planes (see Fig. 1.2a), whose distance is 2.85 Å, from one another along the c-axis. Aragonite is orthorhombic with space group $Pmcn$. In aragonite the Ca-O polyhedra are tilted with respect to the calcite structure; as a consequence, the CO_3 groups are arranged in different levels (Fig. 1.2b), distanced 1.88 Å, along the c-axis. This different arrangement of the polyhedra causes aragonite to have smaller compressibility along the c-axis compared to calcite. However, the distance between the stiff CO_3 groups in the layers perpendicular to c in the aragonite structure is larger than in those of calcite, which leads to higher axial

compressibilities along the a- and b-axes, and an overall lower bulk modulus of aragonite.

3.4 Conclusions

The elastic tensor coefficients and aggregate elastic moduli of aragonite were obtained by Brillouin spectroscopy for three well-characterized natural aragonite samples. The results of our study provide the best available experimental dataset for the elastic properties of aragonite. The data are in good agreement with the values obtained by Lin et al. (2013) [123] and were confirmed by DFT calculations.
The results of this study also show that low amount of Sr in the samples (up to a maximum of 1.5 mol%) does not have a significant effect on the elastic properties of aragonite. By including the results for 2.5 wt% $SrCO_3$, we can determine a compositional trend, which qualitatively confirms the XRD studies performed on a wider compositional range. However, the effects we observe across such a narrow compositional range are at the limit of the experimental resolution of Brillouin scattering.

Chapter 4

Crystal structure and phase behavior of a $CaCO_3$-$SrCO_3$ solid solution up to 10 GPa

In addition to the unary calcium carbonate system, binary carbonate systems are of wide interest as they dominate in nature. Key questions are how cation substitution modifies the $CaCO_3$ phase diagram and what controls order-disorder processes [237, 28]. Recently, the presence of calcium carbonate inclusions with high Sr and Ba contents in diamonds from the transition zones was reported [136, 135]. The reported concentrations of Sr in calcium carbonate vary from a few hundreds of mole percent (0.06-0.7 mol%) [101] to 5-18 mol% in highly enriched varieties [136, 137]. The high content of Ba and Sr in carbonates was suggested to be indicative of deep metasomatic processes related to carbonatites [136, 137, 135]. Carbonatites possess high abundances of Sr and Ba, which can be found as main component in carbonates (e.g. witherite, barytocalcite, carbocernaite, olekminskite etc.) or as impurities in other minerals [241, 69, 196]. The Sr content in calcite in carbonatites reaches, in general, a maximum of 2 mol% [40], but few occurrences of Sr-enriched calcites with up to 9 mol% of Sr were also reported [241]. Given the significant role of carbonates in the mantle processes related to melting [58, 110], metasomatism [263, 110] and diamond formation [174, 225], the diversity of the compositions found in natural samples should be addressed. Cationic substitutions can have an important impact on the phase diagrams, physical properties and melting temperatures of the studied materials and should be considered in the modeling of the processes that involve carbonate minerals. Here, we will focus on Ca-Sr substitution. Experimental studies have shown that $SrCO_3$-$CaCO_3$ solid solutions crystallize in the orthorhombic aragonite structure [34, 138], and a quan-

tum chemical calculation study revealed that the incorporation of large ions (e.g., Sr^{2+}, Ba^{2+}) is energetically incompatible with calcite [149]. Nevertheless, several high pressure-high temperature studies on the $SrCO_3$-$CaCO_3$ and $BaCO_3$-$CaCO_3$ systems have been performed, showing that the miscibility of Sr in the calcite structure, although limited to few mol% at ambient conditions, increases with increasing pressure and temperature [41, 42, 32]. Additionally, it was clarified that calcite-incompatible ions (Sr^{2+}, Ba^{2+}) can be structurally incorporated into calcite through crystallization from amorphous calcium carbonate [148, 128, 200, 252]. A sample with stoichiometry of $Ca_{0.82}Sr_{0.18}CO_3$ was recently synthesized at high pressure and high temperatures, quenched at high pressure and recovered to ambient conditions by Martirosyan et al. (2021) [145]. The authors studied the recovered sample by Raman and Fourier transform infrared (FTIR) spectroscopy at high pressures and high temperatures, revealing several phase transitions. In addition to that, the characterization of the recovered sample by powder X-ray diffraction at ambient conditions showed that, despite the fact that most of the reflections in the XRD pattern could be indexed in the calcite structure, several low intensity peaks exhibited a splitting incompatible with calcite, but indicative of a structure with lower symmetry. These results, in particular the controversial structural characterization of the sample material, motivate further investigation of this system, especially, in order to determine the structure at ambient conditions and the relationships between the high-pressure phases of $CaCO_3$-$SrCO_3$ and pure $CaCO_3$. Here, we use a combination of transmission electron microscopy (TEM) and synchrotron-based single crystal X-ray diffraction (XRD) to characterize the microstructures of the sample material synthesized by Martirosyan et al (2021) [145], determine its crystal structure and explore its structural evolution under pressure to 9 GPa.

4.1 Experimental methods

4.1.1 Sample synthesis and characterization

A $CaCO_3$-$SrCO_3$ solid solution with stoichiometry of $Ca_{0.82}Sr_{0.18}CO_3$ was synthesized at 2 GPa and 1273 K in a Walker-type multi-anvil apparatus at German Research Centre for Geosciences GFZ Potsdam. The chemical composition of the sample was determined by electron microprobe analysis (EMPA). Details of the sample's synthesis and characterization are described in Martirosyan et al. (2021) [145].

4.1.2 High pressure experiments

Four different single crystals, ranging from $40\times40\times20$ μm^3 to $40\times70\times20$ μm^3 in size, were handpicked from the synthesis product were studied by single crystal XRD. Two samples were analyzed at ambient conditions and two at high pressures (see Table 4.1 for experimental details).

Sample	**MNAC**	**MNHP**	**BJAC**	**BJHP**
Max. Pressure (GPa)	0	13	0	9
Ω range/step scan (°)	32/0.5	32/0.5	20/0.5	30/0.5
Acq. Time (s)	1	1	15	15
Presure medium	-	Argon	-	Neon
Detector dist. (mm)	404.4303	404.4303	404.2289	404.2289
Wavelegth (Å)	0.2892	0.2892	0.2905	0.2905

Table 4.1: Experimental details for the different experiments.

The first crystal (MNHP) was studied using a symmetric diamond anvil cell (DAC), with diamond culets of 250 μm in diameter. A sample chamber of 120 μm in diameter was obtained by pre-indenting the central part of a 250 μm-thick Re-foil to 35 μm and drilling a hole in it with an electric discharge machine (EDM). Argon was used as pressure-transmitting medium and a ruby sphere was loaded in the sample chamber for pressure determination. The second crystal (BJHP) was studied using a Boehler-Almax DAC [21], equipped with Boehler-Almax-designed diamonds/seats and culets with a diameter of 300 μm. The sample chamber was obtained by pre-indenting the central part of a 250 μm-thick Re-foil to 40 μm and laser-drilling it to obtain a sample chamber with a diameter of 150 μm. Neon was used as pressure transmitting medium [112] and a ruby sphere as pressure calibrant. For both experiments after each pressure increase we waited for at least 4 hours (to stabilize the pressure) before collecting X-ray diffraction data. The fluorescence of the ruby was measured immediately after each single crystal diffraction data collection. The pressure was determined by applying the ruby reference scale for quasi-hydrostatic conditions Ruby2020 [212].

4.1.3 Single crystal X-ray diffraction

Single crystal XRD experiments were performed at the extreme conditions beamline P02.2 at Petra-III (DESY, Hamburg, Germany) using an X-ray beam with an energy of 25.6 keV ($\lambda \sim$ 0.29 Å) focused down to 2 x 2 μm^2 by a Kirkpatrick-Baez (KB) mirror system [122].
X-ray diffraction patterns were acquired at ambient temperature with Perkin Elmer XRD 1621 flat-panel detector, using an in-house script for collecting step-scan diffraction images. The instrumental model of the experimental geometry (sample to detector distance, offsets of the angles of the goniometer) was calibrated with a standard single crystal of enstatite ($(Mg_{1.93}Fe_{0.06})(Si_{1.93}Al_{0.06})O_6$, *Pbca*, $a = 18.2391(3)$ Å, $b = 8.8117(2)$ Å, $c = 5.1832(1)$ Å). The images were then converted with an in-house software script to conform to the standard format of the program CrysAlis PRO (Rigaku Oxford Diffraction, [53]). The intensities of the reflections were measured in omega step scans. The experimental details are reported in Table 4.1. The data processing (unit cell determination and integration of the reflections' intensities) was performed with the CrysAlis PRO software. The indexing of the unit cell was carried out on reflections manually selected in the reciprocal space viewer (Ewald explorer, implemented in the CrysAlis PRO software). The crystal structures were solved by direct method implemented in SHELXT [211], and refined using the JANA software package [181]. For data collection at pressures lower than 5 GPa, the displacement parameters of all atoms were refined anisotropically. At higher pressures, the displacement parameters were refined anisotropically only for Sr and Ca. The software VESTA [161] was used for structure visualization.

4.1.4 TEM analysis

Three samples were studied by Transmission Electron Microscopy (TEM). The sample preparation was performed with focused Ga-ion beam (FIB) milling at GFZ Potsdam using a HELIOS system operated at an accelerating voltage of 30 kV and a current of 2.2 nA. Details of TEM sample preparation using FIB milling can be found elsewhere [256]. High-resolution TEM (HRTEM) images were acquired using a FEI Tecnai G2 F20-X-Twin microscope, at the German Research Centre for Geosciences (GFZ), Potsdam. The TEM was operated at 200 kV acceleration voltages and a field emission gun was used as electron source. The TEM is equipped with a high-angle annular dark field detector HADDF, a Gatan imaging filter Tridiem and EDAX X-ray analyzer.

4.2 Experimental results

4.2.1 Crystal structure of Sr-CC-II and micro-structural analysis at ambient conditions

The structure determination carried out on XRD datasets obtained at ambient conditions revealed a monoclinic structure, space group $P2_1/c$ and $Z = 4$. This structure is referred to as Sr-calcite-II (Sr-CC-II) because of its similarities with the calcite-II structure [156, 145]. The unit cell parameters of Sr-CC-II, at ambient conditions, are $a = 6.4237(7)$ Å, $b = 5.0176(1)$ Å, $c = 8.1129(1)$ Å, $\beta = 108.064(1)°$ and $V = 248.60(1)$ Å^3. The density of Sr-CC-II is $\rho = 2.982(1)$ g/cm^3, approximately 10 % higher than calcite at ambient conditions. The Sr and Ca cations in the Sr-CC-II coordinate six oxygens, forming octahedra. The structure of Sr-CC-II is shown in Fig. 4.1.

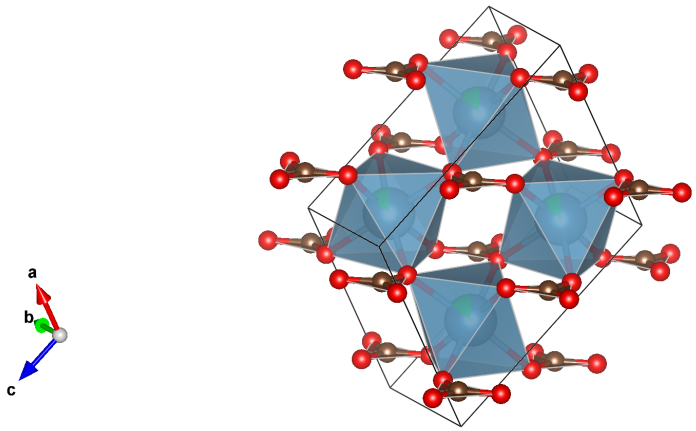

Figure 4.1: Perspective view of the structure of Sr-CC-II, visualizatized using VESTA [161]. The cations (Sr,Ca) are represented by the blue octahedra, while the CO_3 planar groups are in brown: the brown atoms are C and the red ones are O.

Similar to calcite-II, Sr-CC-II is a modified calcite structure and exhibits a rotation of the CO_3 groups around the calcite three-fold axis, and a displacement of the cations is observed in Sr-CC-II. Sr and Ca are completely disordered in the cationic site. The details of the structure refinement for the Sr-CC-II phase are shown in Table B.3. Table B.1 and B.2 show the atomic positions the isotropic displacement factors, the atomic bond distances.
Some additional reflections were observed on the diffraction patterns, which motivated a further microstructural analysis of the Sr-calcite samples by TEM. Three thin films from different grains were studied with TEM and the

electron diffraction patterns of the studied samples were refined with the Sr-CC-II structure model. The main phase was indexed based on a monoclinic structure with $a = 6.4237$ Å, $b = 5.0175$ Å, $c = 8.1129$ Å, and $\beta = 108.064°$ (Fig. 4.2(a)).
The samples are overall homogeneous, as shown in Fig. 4.2(b) (high-angle annular dark-field (HAADF) image), but present a high density of dislocations in bright field imaging and a lamellar texture with clear interfaces caused by complex twinning (Fig. 4.2(c)). Furthermore, TEM bright-field imaging study revealed the presence of antiphase domains (APDs) separated by antiphase boundaries (Fig. 4.2(d)).

4.2.2 Crystal structure of Sr-CC-III and its equation of state

P (GPa)	a (Å)	b (Å)	c (Å)	β	V (Å^3)	Phase
0	6.4237(7)	5.0176(1)	8.1129(1)	108.064(1)	248.60(1)	Sr-CC-II
0.31(5)	6.418(6)	5.0059(6)	8.102(2)	107.88(6)	247.7(3)	Sr-CC-II
0.53(5)	6.406(7)	5.0063(6)	8.087(2)	107.93(7)	246.8(3)	Sr-CC-II
1.72(5)	6.2683(2)	9.922(5)	7.6574(6)	103.856(6)	462.39(5)	Sr-CC-III
2.61(5)	6.2467(2)	9.9009(5)	7.6052(6)	104.005(9)	456.38(5)	Sr-CC-III
4.71(5)	6.2181(4)	9.8667(6)	7.521(8)	104.091(9)	447.55(6)	Sr-CC-III
6.68(5)	6.178(5)	9.816(7)	7.4222(9)	104.298(7)	436.16(7)	Sr-CC-III
7.44(5)	6.1685(3)	9.7906(8)	7.4051(8)	104.34(1)	433.23(6)	Sr-CC-III
8.97(5)	6.1445(6)	9.7852(8)	7.329(1)	104.53(1)	426.55(9)	Sr-CC-III
2.0(1)	6.2596(4)	9.9224(5)	7.640(1)	103.749(9)	460.95(7)	Sr-CC-III

Table 4.2: Lattice parameters and unit-cell volumes of Sr-calcite polymorphs at different pressures determined by single crystal X-ray diffraction.

Upon pressure increase Sr-CC-II transforms into a new phase, Sr-calcite-III (Sr-CC-III). Table 4.2 shows the lattice parameters and unit cell volumes obtained from the single crystal XRD experiments. This observation is consistent with the findings of Martirosyan et al. (2021) [145] in their vibrational spectroscopy study of a sample from the same synthesis batch as the crystals

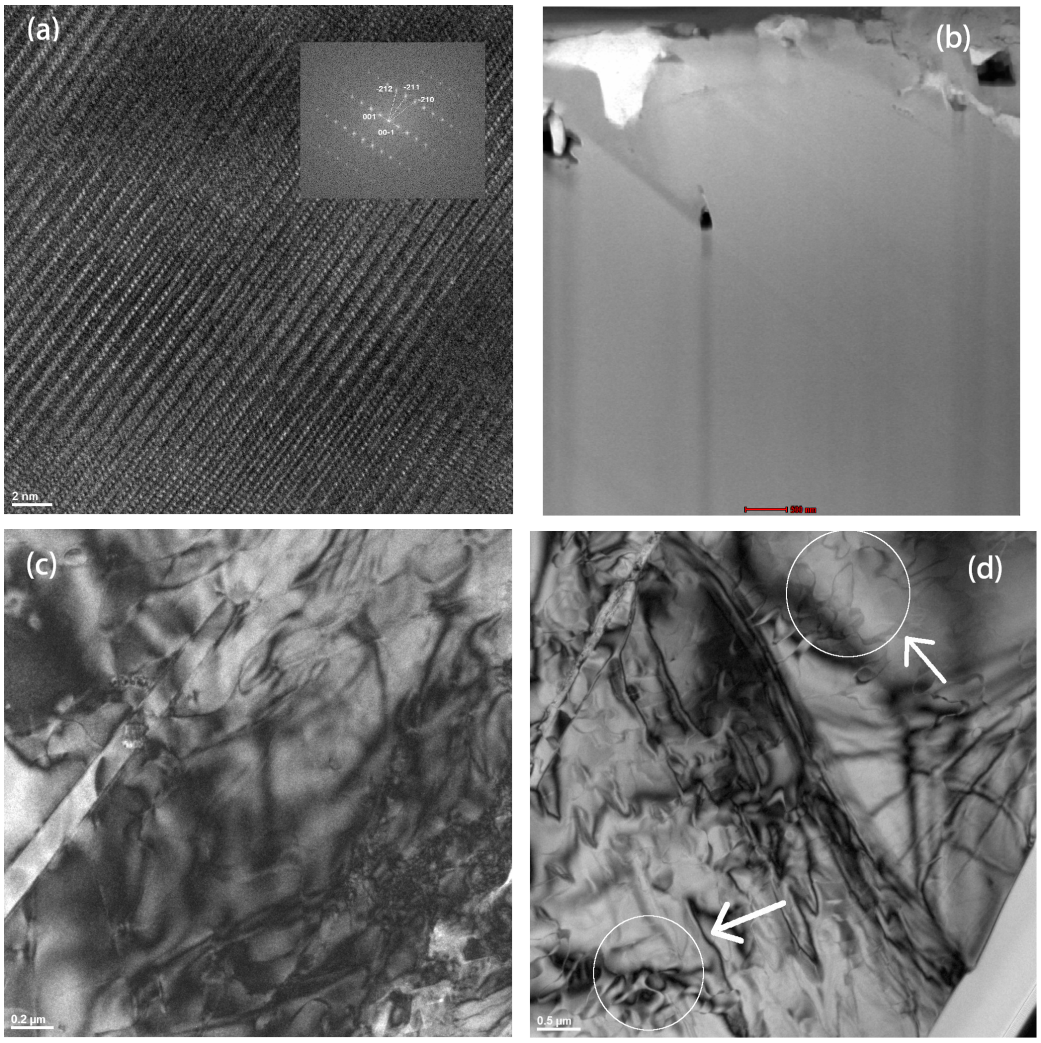

Figure 4.2: (a) Energy filtered TEM lattice fringe image of $Ca_{0.82}Sr_{0.18}CO_3$ and in the inset the calculated diffraction pattern from the Fast Fourier Transform (FFT) of the lattice fringe image indexed based on a monoclinic lattice (sample 6401). The scale bar in the image is 2 nm. (b) TEM HAADF image (sample 6401). The vertical black stripes are due to a curtaining effect from FIB milling. Dark areas are holes. The bar scale is 500 nm. (c) Bright-field (BF) image of one of the Sr-calcite samples. The lamella on the left side of the image is a twin lamella. The scale bar in the image is 0.2 μm. (d) Antiphase domains in Sr-calcite (sample 6402). The scale bar is 0.5 μm. The white arrows are a guide to the eye.

described here. Our single crystal XRD experiments confirmed a structural phase transition from Sr-CC-II to Sr-CC-III occurring at 1.73(5) GPa. Ac-

cording to [145], further compression of Sr-CC-III revealed some additional features in the Raman spectra, and two high-pressure modifications were reported: Sr-CC-IIIb at 4 GPa and Sr-CC-IIIc around 7 GPa. Our XRD experiments did not detect any structural changes in the pressure ranges at which the Raman spectroscopy study observed Sr-CC-IIIb and Sr-CC-IIIc. Sr-CC-III crystallizes in a monoclinic structure, space group $P2_1/m$ and $Z = 8$. The lattice parameters are $a = 6.2683(2)$ Å, $b = 9.9220(5)$ Å, $c = 7.6574(6)$ Å, $\beta = 103.856(6)^\circ$ and $V = 462.39(5)$ Å^3 at 1.73(5) GPa. The structure refinement details for Sr-CC-III are shown in Table B.4. The structure of Sr-CC-III is disordered, as the Sr and Ca cations occupy crystallographically equivalent positions. Sr-CC-III has two features in common with the structure of pure calcite-III such as the planar CO_3 groups, which are no longer coplanar to one another [150], and the presence of non-equivalent cation sites with different coordination number (8 and 7) (green and blue octahedra in Fig. 4.3). Table B.5, B.6 show the refined atomic coordinates and isotropic displacement factors and the bond distances for Sr-CC-III at 1.72(5) GPa. However, Sr-CC-III has monoclinic symmetry rather than triclinic as in the case of calcite-III and the two structures are topologically different. The compression of *a, b* and *c* lattice parameters of Sr-CC-III (here expressed as the value normalized to the initial one at 1.73(5) GPa) is depicted in Fig. 4.4.

It is evident that the compression of Sr-CC-III is strongly anisotropic, as the relative contraction along the c-axis between 1.73(5) and 8.97(5) GPa is almost two times larger compared to that of the *a*-axis and *b*-axis. A second order Birch-Murnaghan EoS was applied to the cubes of the *a,b* and *c* lattice parameters [79] giving $K_{0a} = 102(3)$ GPa, $K_{0b} = 148(8)$ GPa and $K_{0c} = 37(2)$ GPa. Confirming that Sr-CC-III is more compressible along the *c*-axis. The volume compression data were analyzed using the Birch-Murnaghan finite-strain equation of state (EoS), as shown in Fig. 4.5. The unit cell volume V_0 and bulk modulus K_0 ($K_0 = (\partial P/\partial V)_{T0}$) were obtained by performing a least-square fit of the second-order Birch-Murnaghan equation of state to the experimental data:

$$P = 1.5K_0((V_0/V)^{7/3} - (V_0/V)^{5/3}) \tag{4.1}$$

The refinement of the EoS parameters (simultaneously weighted by the uncertainties in both P and V) yielded the parameters of $V_0 = 474(1)$ Å^3 and $K_0 = 69(2)$ GPa.

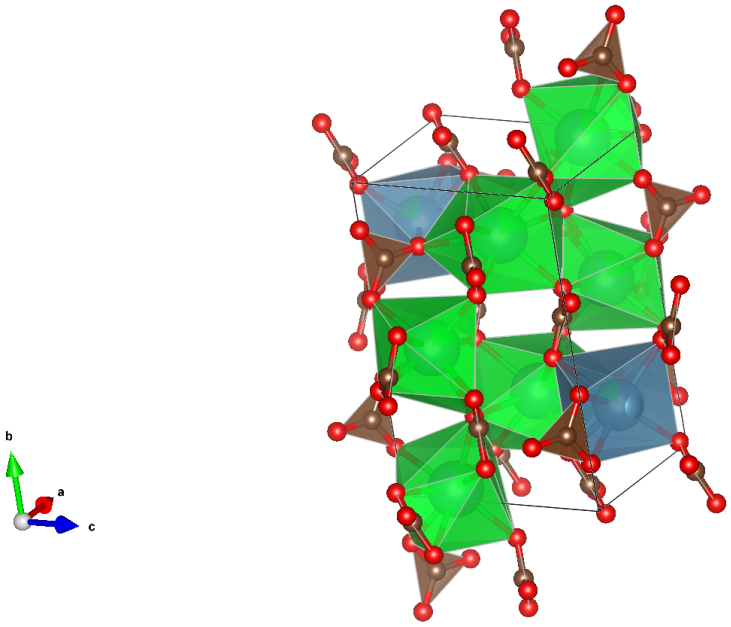

Figure 4.3: Perspective view of the structure of Sr-CC-III, visualizatized using VESTA [161]. The cations (Ca, Sr) are represented by the distorted octahedra. The different colors help distinguish the two coordination sites: in blue the site with coordination number of 7, while the green site has coordination number 8. The CO_3 groups are in brown. The brown atoms are C and the red ones are O.

4.3 Discussion

The synthesis conditions of the samples used in this study (2 GPa, 1273 K) [145] lie on the boundary between the calcite-IV and calcite-V stability field in the pure $CaCO_3$ phase diagram [10, 97, 96, 13]. The crystal structures of these polymorphs of $CaCO_3$ are closely related to that of calcite, and are characterized by orientational disordering of the CO_3 groups due to the rotation of the anionic groups around the threefold axis [160, 190, 232]. Chang (1965) [41] and Carlson (1980) [32] extensively studied the $CaCO_3$-$SrCO_3$ system at high pressures (up to 2.5 GPa) and temperatures (up to 1000 K) by performing quench-experiments and checking the resulting phases by means of X-ray diffraction of the high pressure (and high temperature) synthesis product and at high temperatures with a high-temperature X-ray diffraction device. Their studies reported the presence of a disordered rhombohedral structure at high temperatures (T>1000 K), suggested by the abrupt change in slope and offset of the Ca-rich limb of the miscibility gap. The disordered

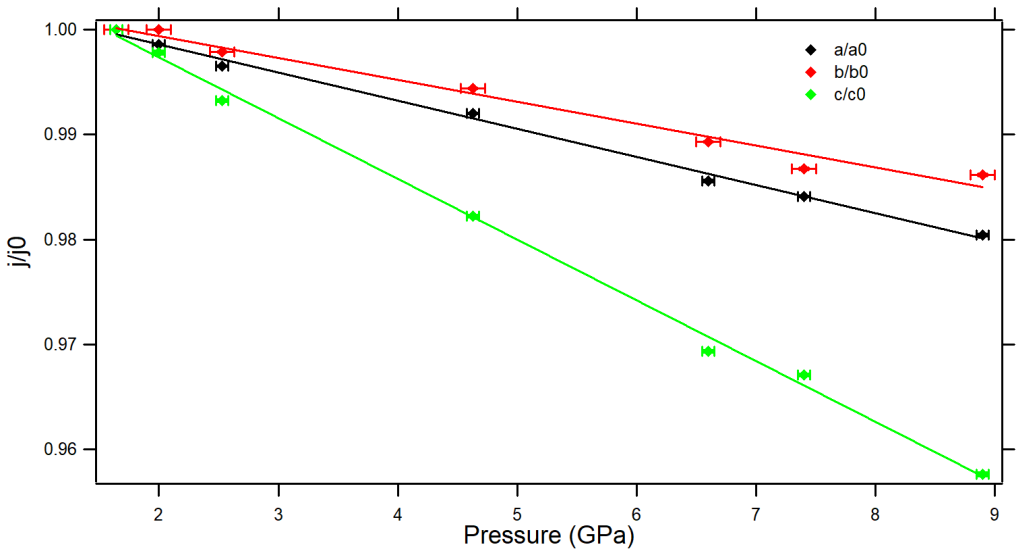

Figure 4.4: Relative variation of unit cell parameters and volume with pressure at room temperature for the Sr-CC-III phase. Error bars of the relative cell parameter values are smaller than the size of the symbols. The solid lines are a guide to the eye.

character of this second rhombohedral phase is explained by the gradual disappearance of the 113 reflection (present in calcite) in the powder diffraction patterns [41]. The 113 reflection is the most intense among a class of reflections whose presence implies orientational ordering of the CO_3 groups in the calcite structure [41, 32, 97, 96]. The complete disappearance of the 113 reflection above 1000 K corresponds to a structural transition from the space group $R\bar{3}c$ to $R\bar{3}m$ [41]. Carlson (1980)[32], combining his new results with those of the previous studies presents a full high pressure/high temperature phase diagram for the subsolidus $CaCO_3$-$SrCO_3$ system. The phase diagram shows the presence of an extended miscibility gap between an orthorhombic Sr-rich phase and a trigonal Ca-rich phase, with an increase in the maximum content of Sr in the trigonal phase with increasing temperature. The boundary between the ordered and disordered phase was also observed to be dependent on the Sr content. Furthermore, it was shown that Sr preferentially fractionates into the disordered structure [32]. Unfortunately, the high pressure disordered phase was not preserved on quenching, therefore its structure could only be guessed. Initially, calcite-II was considered as a possible structure to describe the high-temperature high-pressure phase as, despite the small cell volume, calcite-II has a greater Ca - O average bond length than calcite, and as such it's expected to accommodate larger Sr ion more easily than calcite [32]. Eventually, this structural model was discarded

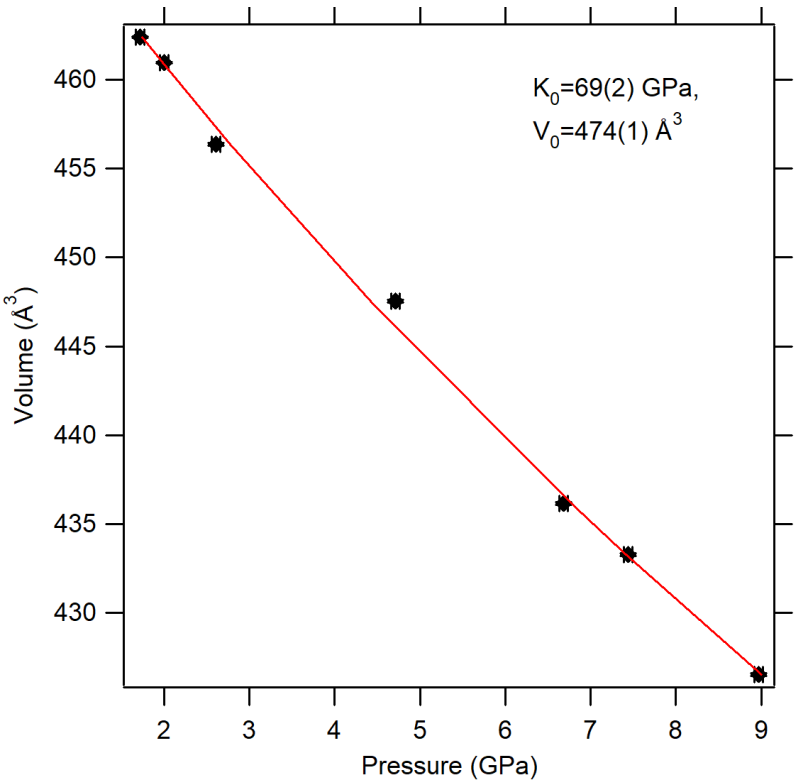

Figure 4.5: Compression curve of Sr-calcite-III in the pressure range between 1.7 and 9 GPa. The red curve is the best fit of the second-order Birch-Murnaghan EoS. Error bars of the relative cell parameter values are smaller than the size of the symbols.

as the XRD patterns did not show any of the reflections characteristic for calcite-II. However, the reasoning that lead Carlson (1980) [32] to consider calcite-II as a possible structural model can be used to understand why we observe a similar structure in the quenched samples in our study. We believe the SrCC-II phase resulting from the rapid quenching and decompression to be related to the disordered phase proposed by Carlson (1980) [32].
The TEM analysis of our samples showed the presence of antiphase domains (APD) in Sr-CC-II. Domains typically form as result of a phase transformation from a structurally or chemically disordered state to an ordered arrangement of atoms, and are particularly common in solid solutions [257, 164]. A rearrangement of atoms from a disordered to an ordered state is often accompanied by a loss in symmetry, which can be either due to a compositional ordering, such as Mg-Ca in dolomite, or positional ordering, such as the orientation of the CO_3 groups in calcite and dolomite [195, 194]. Antiphase domain boundaries separate two domains of the same phase. They

result from symmetry breaking that occurs during an ordering process during cooling or pressure drop, which can start at different locations in the cyrstal in a disordered lattice. Based on our results and previous studies, we propose that the APDs of our samples result from an initially disordered calcite-like phase ($CaCO_3$-IV or $CaCO_3$-V, described by orientational disorder of the CO_3 groups) at the synthesis conditions which ordered during rapid quenching to ambient temperature, transforming into the Sr-calcite-II phase observed in the present study, characterized by ordering of the CO_3 groups, but in which the Sr and Ca cations are disordered (i.e. occupy equivalent positions). The analysis of the powder X-ray diffraction pattern of our samples showed weak intensities (I/I_0) for the calcite-II reflections, confirming the similarities with the calcite-II phase. We conclude that the synthesis conditions lead to a Sr fractionation in the disordered calcite structure, which then ordered during quenching. In the ordering process from a disordered calcite phase to the ambient conditions structure, the presence of Sr, in the amount of 18 mol% leads to a distortion of the calcite structure to better accommodate this larger ion.

The density of Sr-CC-II obtained from single crystal XRD experiments ($\rho = 2.982(1)$ g/cm^3) is higher than pure calcite and is in good agreement with the values reported in a previous powder XRD study [200] for a solid solution with a similar composition. In their study, Saito et al. (2020)[200] synthesized $SrCO_3$-$CaCO_3$ solid solutions with different Sr content using amorphous calcium carbonate as a starting material. They report the structure of their solid solution to be trigonal calcite. However, the results of our study, in combination with the study by Martirosyan et al. (2021) [145] showed that the powder XRD pattern of the distorted calcite phase (Sr-CC-II) differs from that of trigonal calcite only by the splitting of the $(10\bar{2})$, $(10\bar{8})$, (110) and (116) peaks [145]. The two phases cannot be distinguished by powder XRD techniques when the grain-size is small and the crystallinity is poor, therefore the samples produced in the previous studies [41, 32, 200] could indeed have been monoclinic (Sr-CC-II structured) rather than trigonal. Our experiments show that 18 mol% of Sr in the synthesized solid solution, leads to significant changes in the phase behavior of calcium carbonate. End-member calcite-II is a metastable phase detected in a narrow pressure range, between 1.7 and 2.5 GPa, and not quenchable to atmospheric pressure [184]. The incorporation of Sr leads to the occurrence of a calcite-II-like structure (Sr-CC-II) at ambient conditions. Furthermore, Sr-CC-III is a new high pressure polymorph which is different from the previously described pure $CaCO_3$ polymorphs. Despite the similarities between Sr-CC-III and calcite-III polymorph, namely, the non-coplanar CO_3 groups and non-equivalent Ca coordination polyhedral, those structures have major differences. Sr-CC-III has a

higher monoclinic symmetry, the coordination numbers of the cations are 8 and 7 versus the triclinic structure of calcite-III, where the calcium cations coordinate 7 or 9 oxygens [150]. The results of the single crystal XRD experiments also allowed us to make a statement on the elastic properties of the studied samples. The data collected at low pressures in the Sr-CC-II stability field were not sufficient to be studied using the Birch-Murnaghan equation of state. A rough estimate of the value of the bulk modulus at ambient conditions for Sr-CC-II, obtained as a linear extrapolation to $P_0 = 0$ GPa, is $K_{0SrCC-II} = 50(10)$ GPa. For Sr-CC-II phase a direct comparison of the bulk modulus with the isostructural calcite-II at ambient conditions was impossible due to the scarcity of available data. Furthermore, despite the numerous studies on calcite-II [156, 150, 184, 266], the existent published data on calcite-II are mutually inconsistent and insufficient to obtain an accurate value for the bulk modulus, a rough estimate would result in a bulk modulus of 50(15) GPa, but the large uncertainty makes a comparison with Sr-CC-II structure inconclusive. The high-pressure phase, Sr-CC-III is experimentally observed in a wider pressures range, and it was possible to collect enough data to perform a fitting of the second-order Birch-Murnaghan equation of state to our data. The bulk modulus at ambient conditions of Sr-CC-III is 69(2) GPa, about 20% lower than that of end member calcite-III (87(5) GPa), (see Table 2). The lower value of the bulk modulus is most likely caused by the significant difference between the structures of Sr-CC-III and calcite-III. Generally, Sr-incorporation produces a softening with respect to the Ca end-member material ([16, 14]). Table 4.3 shows the values of the bulk modulus at ambient conditions for pure $CaCO_3$ (calcite, aragonite and calcite-III), the $CaCO_3$-$SrCO_3$ solid solution (this work) and pure $SrCO_3$.

Carbonate	Z	V_0 (Å^3)	K_0 (GPa)	dK/dP_0	References
Calcite	6	367.789(4)	73.5(3)	4	[191]
Calcite-III	10	570(1)	87(5)	4	[184]
Aragonite	4	227.11(3)	65.7(8)	5.1(1)	[126]
Strontianite	4	259.8(3)	62.7(6)	3.2(1)	[14]
Sr-CC-III	8	474(1)	69(2)	4	This work

Table 4.3: Comparison of the literature data at ambient conditions for carbonates in the system $CaCO_3$-$SrCO_3$.

Experimental [222] and theoretical studies [63] of aragonite-structured

$Ca_xSr_{1-x}CO_3$ solid solutions described the effect of Sr substitution on the bulk modulus of these solid solutions with x ranging from 0 to 1. Both studies observed a significant lowering of the bulk moduli compared to a simple linear decrease between aragonite and strontianite. Unfortunately, a thorough comparison between the elastic properties of Sr-aragonite and Sr-calcite systems is difficult due to a lack of data and the difference in structures between Sr-CC-III and calcite-III.
Summarizing our results, it can be concluded that the substitution of Ca^{2+} with a larger cation Sr^{2+} in the amount of 18 mol%, causes a distortion of the calcite structure at ambient conditions and the crystallization of new structures at high pressures different from the ones observed in pure $CaCO_3$. Sr-CC-II, is closely related to calcite-II structure, while Sr-CC-III which is structurally distinct from calcite-III, is 20% softer than calcite-III.

4.4 Implications

The rich mineralogy and diversity of carbonate compositions found in diamond inclusions and other mantle minerals point to the importance of extending the study of carbonates to more complicated systems other than the end-member compositions. The results presented here, in combination with previous studies show how composition strongly affects the phase diagram and the physical properties the calcium carbonate-based solid solutions. Our structural and micro-textural observations suggest the possibility that high temperature and relatively low-pressure conditions can represent pathways, even in natural systems, for anomalous incorporation of Sr in calcite-related calcium carbonate phases. This could help explain the origin of Sr-enriched calcites found in carbonatites. The highest Sr content in calcite from carbonatites is in general around 2 mol% [40]. However, there are few occurrences of calcite carbonatites with higher Sr-contents [241, 69, 196]. One study, in particular, reports a Sr-enriched calcite with a Sr content up to 9 mol% [241]. Carbonatites in those localities contain primary Sr-rich calcite with SrO content 3-9 mol% and Ca-rich strontianite (<30 mol% $CaCO_3$) that form exsolution textures. Typical exsolution textures consist of Sr-rich calcite in a core, and the subsolvus mineral assemblage confined to marginal parts of the crystal [196]. Due to the major similarities in the powder XRD patterns [143], calcite and Sr-calcite-II cannot be accurately distinguished in the multiphase assemblages, such as those observed in carbonatites. Therefore, the occurrence of Sr-calcite-II rather than calcite cannot be ruled out and should be checked in the future studies. The findings of Sr-calcites in carbonatites confirm the increasing miscibility of Sr in calcite-like structures

(either calcite-IV, Sr-calcite-II or calcite) at high pressures and temperatures. According to previous works [241, 196], the formation of Sr-calcite in carbonatites occurs above 923 K and 2 kbar. The compositions of the Sr-calcites found at room temperature and pressures may not correspond to the initial magmatic "protocarbonates" [40]). Owing to the limited miscibility in the calcite-strontianite system at ambient conditions, early magmatic carbonates became enriched in Sr unmix upon cooling. The unmixing is evident from the observed exsolution textures of Sr-calcite and Ca- strontianite or carbocenaite [241, 40].

4.5 Conclusions

This study reports the crystal structures of two high pressure polymorphs of Sr-bearing calcium carbonate. Several studies reported the present of Sr-rich calcium carbonate in carbonatites and diamond inclusions. We performed single-crystal X-ray diffraction studies on a synthetic solid solution with composition $Sr_{0.18}Ca_{82}CO_3$ up to 9 GPa. The samples used in this experimental work are from the same batch as the ones used in a previous high pressure Raman spectroscopy study (Martirosyan et al. [145]). The results of this study showed that 18% of Sr leads to strucural modifications compared to pure $CaCO_3$. At ambient conditions the $CaCO_3$-$SrCO_3$ solid solution is isostructural to the high pressure polymorph of $CaCO_3$, calcite-II. At 1.73(5) GPa a structural phase transition is observed to a new monoclinic structure $P2_1/m$, Sr-CC-III. This structure is different from any pure $CaCO_3$ polymorph, but shares some common features with calcite-III such as the non-coplanar CO_3 groups and the presence of different coordination sites with coordination number of 7 and 8 respectively. No additional structural modifications were observed in the pressure range between 1.7 and 9 GPa.
The combination of structural and microstructural (TEM) measurements, provide possible pathways for Sr-incorporation in calcite-like $CaCO_3$ phases at high temperature and relatively low pressure conditions, which may have relevance for processes in natural carbonatite-related systems. The effect of cationic substitution on the structure and phase diagram of $CaCO_3$ shows the importance of extending the study to more complex carbonate systems than the pure end-member compositions.

Chapter 5

Mechanical properties of amorphous calcium carbonate at high pressures

Calcium carbonate is a material of great interest due to its technological applications and for its importance in the formation of biogenic minerals [1]. At ambient conditions, in addition to the anhydrous polymorphs (calcite, vaterite, aragonite) hydrous forms are observed: amorphous calcium carbonate (ACC), calcium carbonate monohydrate (monohydrocalcite, $CaCO_3{\cdot}H_2O$), and calcium carbonate hexahydrate (Ikaite, $CaCO_3{\cdot}6\,H_2O$) [31]. ACC is the least stable non-crystalline polymorph, and is often a precursor in the formation of the more stable crystalline polymorphs, functioning as temporary calcium storage or as a metastable precursor in biological mineralized structural materials [248]. Inspired by magnesium incorporation in carbonatic biomineralization, where many organisms form magnesium-rich calcite skeletons, ACC has also recently been used for doping incompatible elements into calcite [148, 200, 250, 251, 208, 252].
Furthermore, it has been demonstrated that ACC is a compound that possesses more than one amorphous state, a phenomenon known as polyamorphism, where each polyamorphic form has a distinct short-range order (observed in both natural and synthetic samples) [33]. Previous studies showed that it is possible to produce synthetic ACC samples with different local structures by varying the pH of the starting solutions. Syntheses of ACC performed at pH$\sim$8.75 and pH$>$9.80 produce local structures related to calcite and vaterite, respectively [33, 77].
Water also plays a key role in ACC formation, stability and crystallization mechanisms [188]. A previous study by Schmidt et al. (2014)[205] investigated the effect of hydration and synthesis procedure on the structure and

physical properties of amorphous calcium carbonate samples. Their X-ray absorption fine structure spectroscopy (XAFS) and synchrotron X-ray total scattering measurements on ACC samples revealed little differences in the structures of the synthetic samples produced via different synthesis procedures [114, 68]. Despite the short-range structural similarities between the samples (obtained from the different synthesis procedures), simultaneous thermo-gravimetric analysis and differential scanning calorimetry (TGA-DSC) measurements revealed differences in crystallization and dehydration temperatures [205], providing insights into the role of water in the ACC structure at the different length scales (mid- to long-range).

Amorphous calcium carbonate is not only interesting as a precursor for the crystalline calcium carbonate polymorphs present at the Earth's surface, but may also have implications for the study of the deep Earth. The phase diagram of calcium carbonate has been extensively studied at high pressures and high temperatures [230, 171, 126, 13, 92]. A recent article by Hou et al. (2019) [92] focused on the region of the phase diagram of $CaCO_3$ above 3 GPa and 1000 K, which has long been controversial: Suito et al. (2001)[230] described the stable phase at these P-T conditions to be a disordered crystalline phase, while Litasov et al. (2017) [126] suggested it might be a different new phase. However, neither study provided detailed structural information on this high P-T phase. A recent *ab initio* study by Gavryushkin et al. (2020) [76] described this phase as a disordered aragonite with dynamically disordered, freely rotating CO_3 groups, similar to the trigonal $CaCO_3$-V structure [97, 96]. Hou et al. (2019) [92] reported a reversible temperature-induced transition from aragonite to an amorphous calcium carbonate phase at pressures of 3.9-7.5 GPa and a temperature above 1000 K. If crystalline $CaCO_3$ progressively disorders, and eventually amorphizes, in the pressure range from 4 to 8 GPa and at high temperatures, knowing the elastic properties and seismic velocities of ACC and comparing them to the high pressure crystalline $CaCO_3$ polymorphs in this pressure range allows us to determine whether the presence of ACC in the upper mantle may cause a seismically detectable signature.

In a previous study on the high pressure behavior of a synthetic ACC in a diamond anvil cell (DAC) up to 20 GPa, Fernandez-Martinez et al. (2013) [70] compressed a synthetic 'vaterite-like' ACC sample in diamond anvil cell (DAC) up to 20 GPa and measured X-ray diffraction and Raman scattering. This study revealed the presence of a pressure-induced polyamorphic transition from "vaterite-like" ACC to "aragonite-like" ACC, at a pressure of $\sim$ 10 GPa.

A second study on amorphous calcium carbonate at high pressures was performed by Fruhner et al. (2018) [73], who studied Eu doped calcite and

aragonite samples by time-resolved optical fluorescence spectroscopy and total X-ray scattering combined with pair distribution function analysis up to 20 GPa. They observed that, below 1.7 GPa, crystalline calcite:Eu transforms into an amorphous phase with a calcite-like local structure which then transforms to an amorphous phase with an aragonite-like local structure at about 10 GPa [73].
Here, we present a high pressure study on the acoustic velocities and elastic properties of both hydrous and anhydrous synthetic samples ACC, obtained from different synthesis procedures [114, 68] studied up to 20 GPa.

5.1 Experimental

5.1.1 Sample synthesis and characterization

Two different synthesis methods were employed to produce the ACC samples. The synthesis of the sample was performed by Rita Luchitskaia at the Goethe University, Frankfurt am Main. The procedure of Faatz et al. (2004) [68] was adopted for the synthesis of the first sample, ACC-I: 294 mg (0.002 mol) of calcium chloride solution $CaCl_2 \cdot 2H_2O$ and 900 mg (0.01 mol) of dimethyl carbonate were dissolved in 160 ml water in a vessel that was placed in an ice water bath at 278 K. The precipitation of ACC was initiated by adding drop-by-drop 40 ml of 0.5 N sodium hydroxide under stirring to the reaction solution. The precipitation occurred slowly, after a delay of about 5 minutes. The precipitate was vacuum filtered, rinsed with aceton and dried. The sample was then heated at 423 K for 12 hours. The sample was checked by X-ray diffraction before being loaded in a diamond anvil cell (DAC) (Fig. 5.1). The samples ACC-II and ACC-III were prepared according to the procedure of Koga et al. (1998) [114], 100 ml of 0.02 M sodium carbonate and 25 ml of 0.5 N sodium hydroxide were mixed under stirring in a vessel, while 100 ml of 0.02 M calcium chloride solution was prepared in a different vessel. Both solutions were kept in an ice water bath at 278 K for about 30 minutes. Then, the calcium chloride solution was added rapidly to the mixed solution of carbonates under stirring. The precipitated colloidal phase was vacuum filtered, rinsed with aceton and dried.
Sample ACC-II was heated at 520 K for 20 hours. The heated sample was checked by X-ray diffraction before being loaded in the DAC (Fig. S1). Sample ACC-III was loaded into a diamond-anvil cell without being subjected to any dehydration treatment. The pH of the starting solutions used in the samples preparation produced samples with a 'vaterite-like' local structure [31, 77].

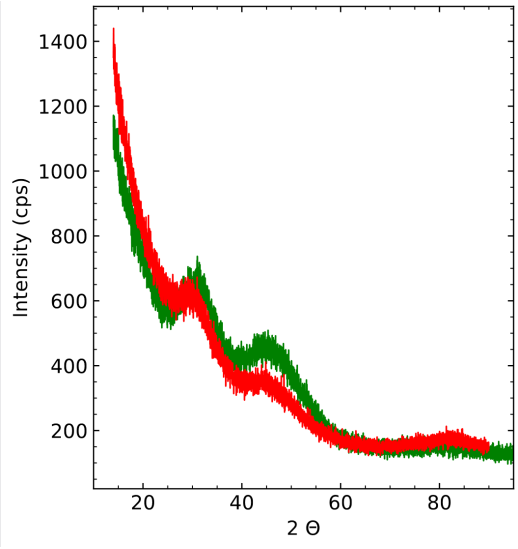

Figure 5.1: X-ray diffraction patterns of samples obtained by the two synthesis procedures. The green curve refers to sample ACC-I [68], while the red curve refers to sample ACC-II [114]. The absence of sharp peaks in the diffractogram proves the amorphous nature of the samples.

Both synthesis methods produce nanospheres of ACC [68, 114]. Before loading in the DAC, the samples were compressed between two diamonds (culets 500 μm) to an unknown pressure in order to obtain transparent platelets of about $100 \times 100 \times 30$ μm^3 (ACC-I and ACC-II) and $50 \times 80 \times 15$ μm^3 (ACC-III) which were then loaded in the DAC.

5.1.2 Thermogravimetric analysis

The evolution of the samples under heat treatment was characterized by simultaneous thermogravimetric and differential thermal analysis (TGA-DTA). The thermogravimetric analysis was performed on a Linseis STA 1600PT (Linseis, Selb, Germany). The measurements were performed on fresh samples obtained following the same synthesis procedures as the samples loaded in the DACs. Sample A1 (analog for ACC-I) was heated at 10 K/min up to 423 K, then kept at constant temperature for 12 hours and finally heated to 1500 K at 10 K/min. Sample A2 (analog for ACC-II) was heated at 10 K/min up to 521 K, kept at constant temperature for 20 hours and finally heated to 1500 K at 10 K/min. The TGA-DTA measurements were carried out by Matthias Schneider from the University of Potsdam, Institute of Chemistry, Potsdam, Germany.

5.1.3 High-pressure measurements

High pressure measurements at ambient temperature were carried out using a Boehler Almax diamond anvil cell (DAC)[21]. Diamonds with 300 μm culets were used for both samples. Sample chambers of 150 μm in diameter were laser drilled in rhenium gaskets, which had been pre-indented to a final thickness of 40-48 μm. The cells were loaded with Ne as pressure transmitting medium. A ruby (Al_2O_3:Cr^{3+}) fragment was placed inside the sample chamber as pressure calibrant. The pressure was measured using the shift of the R1 fluorescence line of ruby, relative to a standard ruby at room pressure. The pressure was determined before and after each set of Brillouin measurements using the ruby reference scales for quasi-hydrostatic conditions (referred to as Ruby2020) [212].

5.1.4 Brillouin spectroscopy

Brillouin scattering is the inelastic scattering of light by acoustic phonons. Brillouin scattering measurements were performed in the Brillouin laboratory at the German Research Centre for Geosciences, GFZ, Potsdam.
At low pressures, in addition to the Brillouin shifts due to the forward scattering of both the sample $\Delta\nu_{60}^{ACC}$ and the pressure transmitting medium (Ne) $\Delta\nu_{60}^{Ne}$, it was possible to measure the Brillouin shift due to the backscattering of Ne $\Delta\nu_{B}^{Ne}$, because the laser beam reflected from the downstream diamond (defined as the DAC diamond on the side of the detector) serves as an incident beam. The wavevector q of the acoustic phonon, in forward scattering geometry, is parallel (60°) to the interfaces of the diamonds crossed by the laser beam, while the backscattering wavevector is in the same direction of the beam reflected by the culet of the downstream diamond (Fig. 5.2).
The measured acoustic velocities for Ne are reported in the Supplementary material and are in complete agreement with the results reported by Shimizu et al. (2005) [214] and Wei et al. (2019) [246]. The reproducibility of the data of Ne provides an additional control on the compression conditions and the pressure determination in our experiments.
ACC-I was studied by Brillouin scattering while increasing pressure from 2.0(1) GPa up to 17.0(2) GPa and on pressure release down to 3.4(1) GPa. ACC-II was measured in compression from 2.68(3) up to 19.9(1) GPa and decompression to 3.3(3) GPa. ACC-III was studied in compression from 0 to 18.8(2) GPa and decompression down to 0.6(1) GPa.
The Brillouin spectra features were fitted using pseudo-Voigt functions and a linear background using the Peakfit software (Systat Software, California).

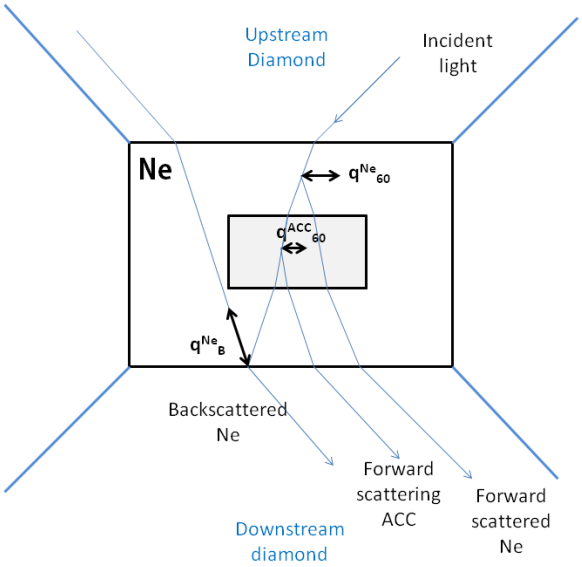

Figure 5.2: Sketch of the forward and backscattering from ACC and Ne. **q** is the scattering wavevector. The grey rectangle represents the sample. The white rectangle is the sample chamber in the DAC.

5.2 Results

5.2.1 TGA

The results of simultanous TGA-DTA allowed us to constrain the water content depending on the synthesis and heat-treatment of the samples. Fig. 5.3 shows the results of the TGA measurements on samples ACC-I and ACC-II. As observed by Schmidt et al. (2014) [205], three regimes were defined on the basis of the distinct mass-loss slopes, separated by vertical grey lines in Fig. 5.3. The first regime is indicative of the bulk H_2O mass loss and is the same for the two samples; regime 2 is dependent on the treatment of the samples; regime 3 is insensitive to the treatement temperatures, and is unaffected by dehydration. It is evident, from Fig.5.3, that the two synthesis methods produce samples with different water contents. The total water content of sample ACC-I is of 22%. The mass-loss after the heat-treatment (12h at 423 K) is 16%, resulting in ∼6 wt% residual water. The total water content of samples ACC-II and ACC-III (produced with the same synthesis procedure as ACC-II) is 18%. The heat-treatment of ACC-II (20h at 518 K) leads to the loss of all the bulk water in the sample. A water uptake

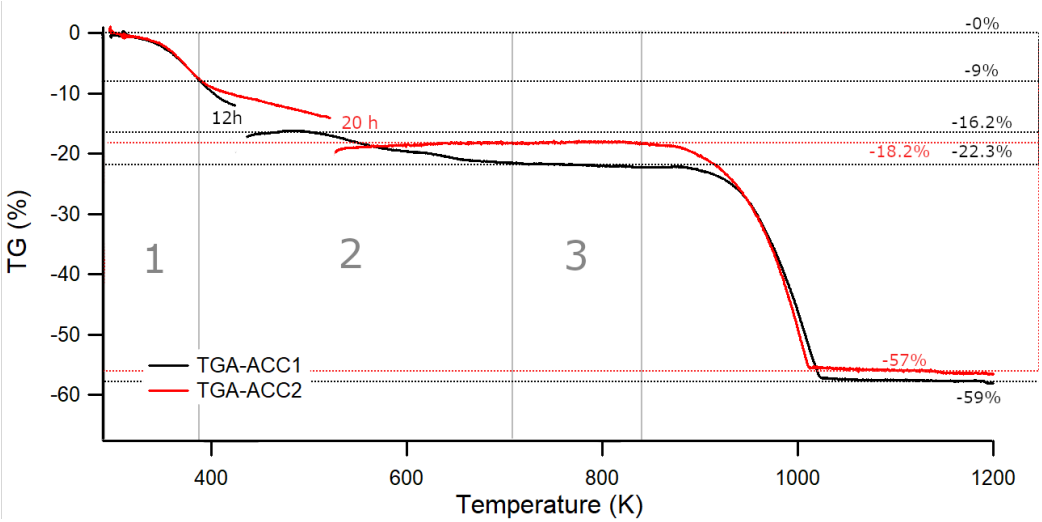

Figure 5.3: TGA results. The black solid line refers to sample ACC-I, the red solid line refers to sample ACC-II. The blank spaces in the curves are due to a technical malfunctioning of the temperature reading. The grey vertical lines separate the three mass-loss regimes for ACC-I.

of ∼1% was estimated for both samples at the end of heat treatment and before sample preparation for the high pressure experiments, resulting in a water content of 7(1) wt% for sample ACC-I and 1 wt% for sample ACC-II. Sample ACC-III was not subjected to any dehydration/heating treatment. The water content of ACC-III was estimated to be 18(1) wt%, based on the total water content of sample ACC-II which was produced according to the same synthesis method.

5.2.2 Brillouin spectroscopy

At each pressure, we collected at least one Brillouin spectrum from the center of the sample and from the pressure medium. The majority of the samples' spectra contain spectral features corresponding to the acoustic longitudinal phonon mode (LA) and the acoustic transverse phonon mode (TA) of the ACC (Fig. 5.4). For each sample, the ACC spectra was collected in different spots to check for homogeneity of the sample and to verify the reproducitility of the measurements. At pressures below 7 GPa, it was possible to observe, in addition to the Brillouin shifts of the acoustic modes of the sample $\Delta\nu_{60}^{ACC}$, Brillouin frequency shifts of the forward scattering and backscattering of the Ne LA mode, $\Delta\nu_{60}^{Ne}$ and $\Delta\nu_{B}^{Ne}$. At higher pressures only the peak corresponding to the LA mode of Ne was observed in addition to the sample peaks.

The analysis of the Brillouin spectra gives us access to different informa-

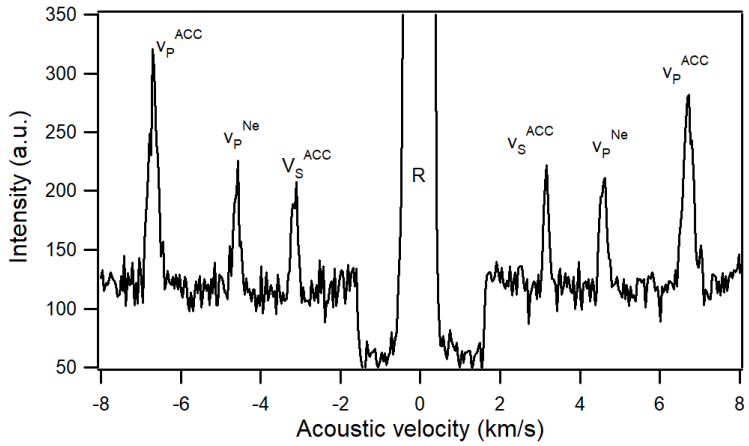

Figure 5.4: Brillouin spectrum of ACC-II at $P_3 = 7.7$ GPa. The Brillouin frequency shift is converted to acoustic velocities (see main text). The central part of the spectrum is attenuated by a factor of 10^2.

tion, such as (a) the velocity of the acoustic waves that propagate through the sample (v_p is the velocity corresponding to the LA mode and v_s is the velocity of the TA mode), which can be calculated using Eq. **??**Eg:BSvel, and (b) the Poisson's ratio σ; (c) if the density of the material is known it is possible to determine aggregate elastic properties such as the isentropic bulk modulus K_S and the isentropic shear modulus G_S from the acoustic velocities.

Acoustic velocities

Fig. 5.5 shows the pressure dependence of the acoustic velocities of the three ACC samples in compression and decompression experiments and the velocities measured by Faatz et al. (2005) [67] by Brillouin spectroscopy at ambient conditions for a sample synthesized with the same procedure as ACC-I [68]. The longitudinal velocity v_p appears to be more sensitive to pressure compared to the transverse velocity v_s. Both the v_p and the v_s values increase monotonically with pressure. As shown in Fig. 5.5, the acoustic velocities of the two heat-treated samples (ACC-I and ACC-II) are the same within the experimental error. The acoustic velocities for both the longitudinal and the transverse mode are reproducible in compression and decompression. Unfortunately, it was impossible to measure the v_S at pressures lower than 6 GPa for sample ACC-III in the DAC, but a second platelet, obtained from the

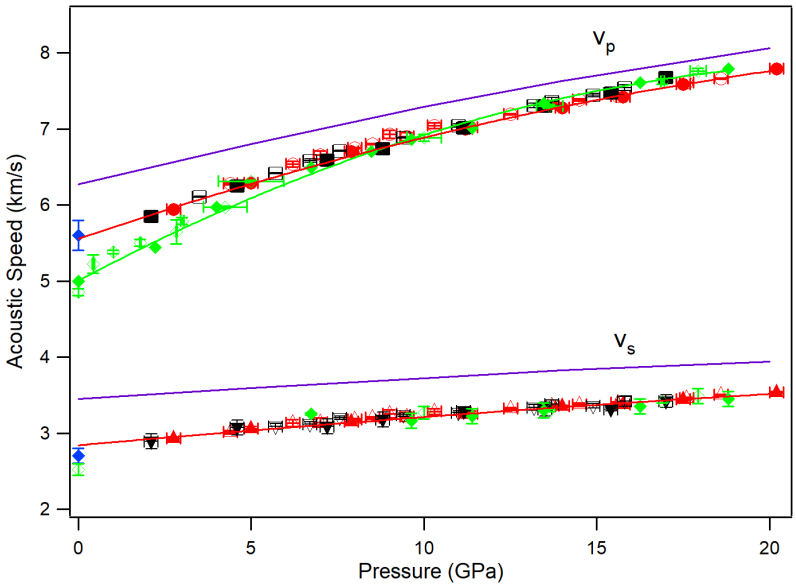

Figure 5.5: Acoustic velocities of ACC-I (black), ACC-II (red) and ACC-III (green) in compression and decompression experiments. The filled symbols represent compression data, while open symbols represent the velocities measured upon pressure release. In blue are the acoustic longitudinal and transverse velocities of ACC from Faatz et al. (2005) [67] at ambient conditions. The purple curves represent the acoustic wave velocities for aragonite from Huang et al. (2017) [94]. The red and green curves follow the acoustic velocities data as a function of pressure for the heat treated ACC-II (red curve) and the hydrous sample ACC-III (green curve).

same synthesis batch as ACC-III, was measured at ambient conditions to obtain the acoustic velocities of hydrous ACC.

Poisson's ratio

Amorphous calcium carbonate is an isotropic material. Poisson's ratio σ for isotropic materials can be obtained directly from the measured velocities as:

$$\sigma = \frac{(v_p^2 - 2v_s^2)}{2(v_p^2 - v_s^2)}$$

Most materials have a Poisson ratio close to 1/3, and a much smaller shear velocity v_S compared to their longitudinal velocity v_P [2]. Here, the Poisson's ratio was obtained for the three ACC samples for each pressure point where both the v_p and the v_s peaks were measured (see Fig. 5.6). The value of the Poisson's ratio increases with pressure up to 15 GPa, above this pressure

point σ becomes independent of pressure, as shown in Fig. 5.6. Due to the lower v_p detected in ACC-II the values for the Poisson's ratio $\sigma_{\text{ACC-II}}$ at high pressures are lower than $\sigma_{\text{ACC-I}}$ and $\sigma_{\text{ACC-III}}$, however they overlap within their uncertainties. Our results show that the Poisson's ratio of ACC is higher compared to that of aragonite (Fig. 5.6).

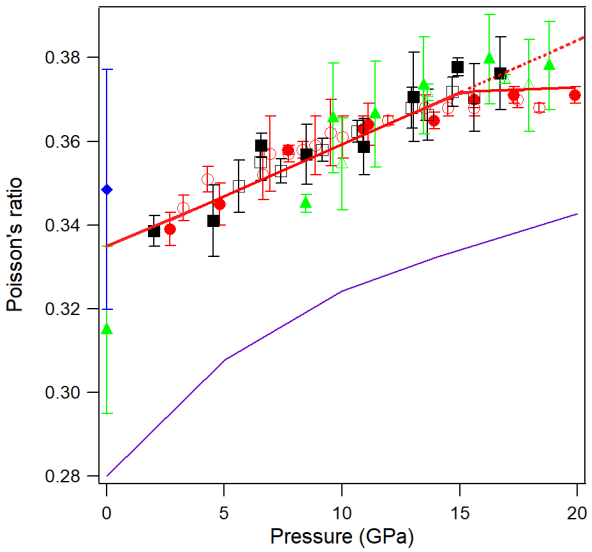

Figure 5.6: Poisson's ratio σ as a function of pressure. Black squares: ACC-I; red circles: ACC-II; green triangles: ACC-III, blue diamond: value of the Poisson's ratio at ambient conditions from Faatz et al. (2005) [67], purple curve: Poisson's ratio of aragonite from Huang et al. (2017) [94]. Filled symbols: compression data; open symbols: decompression data. Solid red curve: σ behaviour of ACC as a function of pressure, the dashed line shows the extrapolation of the low-pressure dependence of the Poisson's ratio to high pressures.

Elastic Moduli

Once the density ρ of the material is known, it is possible to obtain the isentropic shear modulus G_S and the isentropic bulk modulus K_S. In this study we used the density values measured by Fernandez-Martinez et al. (2013) [70] for a hydrous ACC sample, which is similar to sample ACC-III as they were both synthesized using the same procedure and have the same water content. A more thorough discussion on the density can be found in the Supplementary material. It is important to mention that the different water content of the samples has an effect on the density of the material [199]. In particular, we expect the heat-treated samples to have a higher density compared

to the pristine hydrous one. A previous molecular dynamics study on the effect on water on the properties of ACC at ambient conditions reports a lowering (-4.43 %) of the density of hydrous ($CaCO_3$·1 H_2O) compared to anhydrous ACC [199]. However, the density values reported in the modelling study are much higher (∼16 % higher) compared to the densities measured by Fernandez-Martinez et al. (2013) [70] for a hydrous ACC sample at ambient conditions. Due to the inability to directly measure the density of the ACC samples used in this study, the effect of water on the density of the water-poor samples was not considered and the densities measured by Fernandez-Martinez et al. (2013) [70] were used for the determination of the elastic moduli of all the three samples.
The elastic moduli are directly proportional to the density of the material and to the combination of the squared values of the acoustic velocities, as shown in the following description. Therefore, the values reported here have to be considered as a lower bound for the shear modulus G_S and bulk modulus K_S of the heat-treated ACC samples, ACC-I and ACC-II. The values of the elastic moduli for samples ACC-I and ACC-II at ambient conditions were extrapolated from the high pressure data. ACC-III was studied both at ambient conditions and high pressures. Sample ACC-III deserves special attention as it is the best characterized sample: it was synthesized with the same method as the sample used by Fernandez-Martinez et al. (2013) [70] and, as such, the pressure-density curve is known for hydrous ACC. Furthermore, the data collected at ambient conditions allows for a more complete understanding of the behaviour of the sample. Therefore, a more thorough analysis of the high-pressure behaviour of the aggregate moduli K and G was carried out for sample ACC-III using the finite strain formalism [229].
The isentropic shear modulus G_S and the isentropic bulk modulus K_S at high pressure are obtained using the equations:

$$G_S = v_s^2 \rho$$

$$K_S = v_p^2 \rho - \frac{4}{3} G_S$$

Fig. 5.7 shows the dependence of the shear modulus (a) and bulk modulus (b) on pressure, respectively. The pressure dependence of the bulk and shear moduli of sample ACC-III was studied using the finite strain formalism [229]:

$$K_{\mathrm{III}} = (1+2f)^{5/2} \left(K_0 + (3K_{T0}K_0' - 5K_0)f + \left(6K_{T0}K_0' - 40K_{T0} - 14K_0 + \frac{15}{2} K_{T0}K_{T0}' \right) f^2 \right)$$

$$G_{\mathrm{III}} = (1+2f)^{5/2} \left(G_0 + (3K_{0T}G_0' - 5G_0)f + \left(6K_{0T}G_0' - 24K_{0T} - 14G_0 + \frac{9}{2} K_{0T}K_{0T}' \right) f^2 \right)$$

where, f is the Eulerian strain (Eq: 2.38), K_0 and K'_0 are the isentropic bulk modulus and its pressure derivative, G_0 and G'_0 are the isentropic shear modulus and its pressure derivative and K_{0T} and K'_{0T} are the isothermal bulk modulus and its pressure derivative. The isothermal values, K_{T0} and K'_{T0} were obtained from Fernandez-Martinez et al. (2013) [70] and kept as fixed parameters.
The bulk and shear moduli of samples ACC-I and ACC-II, as previously mentioned represent a lower bound on the values, due to the unknown densities for water-poor samples at high pressures. A linear dependence of the elastic moduli on pressure was assumed:

$$G(P) = G_0 + G' \cdot P$$

$$K(P) = K_0 + K' \cdot P$$

Tab. 5.1 shows a comparison between the bulk and shear moduli of ACC and

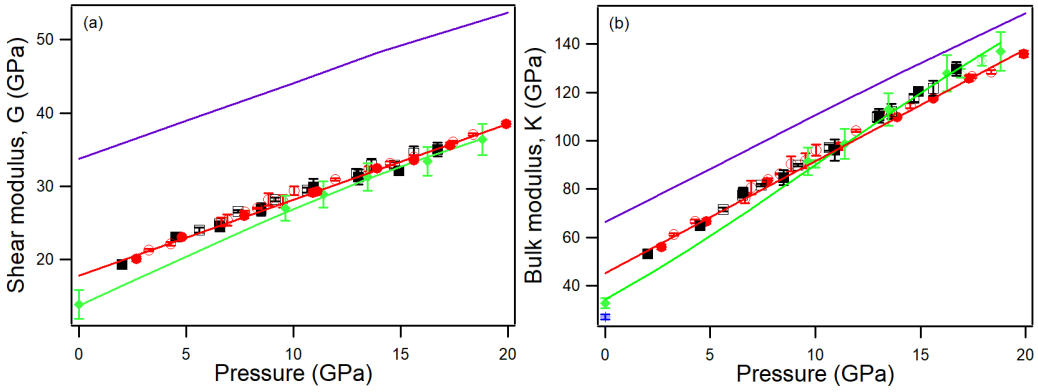

Figure 5.7: Pressure dependence of (a) the shear modulus, G, and (b) the bulk modulus, K, of ACC. Black squares: ACC-I; red circles: ACC-II, green diamond: ACC-III; blue cross: isothermal bulk modulus [70]. Filled symbols: compression data; open symbols: decompression data. Purple lines: pressure dependence of G and K for aragonite [94]; Red lines: linear fit of the elastic moduli as function of pressure for ACC-II; green lines: finite strain fit of the high pressure values for sample ACC-III.

their derivatives at ambient conditions determined in this study, compared to literature data [70, 67]. In addition to the values for amorphous calcium carbonate, the values of bulk and shear moduli for crystalline calcite [123, 191], aragonite [176, 126], vaterite [207, 147], monohydrocalcite [38] and ikaite [38] are reported in Tab. 5.1.

Dataset	ρ_0 (g/cm^3)	G_0 (GPa)	G'_0	K_0 (GPa)	K'_0	Method
ACC-Ic		18.0(5)	1.02(5)	42(1)	5.2(1)	BS
ACC-Id		18.6(4)	1.02(4)	44.3(7)	4.99(6)	BS
ACC-IIc		17.8(2)	1.04(2)	45.0(1)	4.65(8)	BS
ACC-IId		18.3(3)	1.03(2)	49(1)	4.5(1)	BS
ACC-IIIm		13.7(3)	-	32.7(5)	-	BS
ACC-IIIc		13.7(2)	1.63(1)	34(1)	6.2(1)	BS
ACC-FM-c [70]	2.17 [70]	-	-	27(1)	4	EoS
ACC-FM-d [70]	2.24 [70]	-	-	32.4(6)	4	EoS
ACC-F [67]	1.9 [67]	14(1)	-	41(3)		
Calcite [123]	2.71 [123]	32.1(2)	-	78.6(4)	-	BS
Calcite [191]		-	-	73.4(3)	4	EoS
Aragonite (Ch. 3)	2.93	37(2)	-	71(3)	-	BS
Aragonite [126]			-	65.7(8)	5.1(1)	EoS
Vaterite [207]	2.54 [81]	18.8	-	69.1	-	AS
Vaterite [147]			-	63.8(6)	4	EoS
Monohydrocalcite [38]	2.4 [70]	27.28	-	44.28	-	DFT-PBE
Ikaite [38]	1.8 [81]	16.40		31.08		DFT-PBE

Table 5.1: Elastic bulk (K_0) and shear moduli (G_0) at ambient pressure and temperature of the measured ACC samples, together with the values of K_0 and G_0 obtained from the acoustic velocities measured by Brillouin spectroscopy by Faatz et al. (2005) [67], ACC-F, the values of the isothermal bulk modulus at ambient conditions measured by Fernandez-Martinez et al. (2013) [70], ACC-FM, and the bulk and shear moduli for the different crystalline $CaCO_3$ polymorphs. The elastic moduli for calcite [123, 191] and aragonite (Ch. 3, [126]) from Brillouin spectroscopy (BS) and from X-ray diffraction experiments (EoS) are also reported. The elastic moduli for vaterite result from atomistic simulations (AS) [207] and synchrotron X-ray diffraction experiments (EoS) [147]. The elastic moduli for monohydrocalcite and ikaite result from DFT-PBE calculations (DFT) [38]. K' and G' are the pressure derivatives of the elastic moduli. $-c$ compression data; $-d$ decompression data.

5.3 Discussion

The experiments performed in this study allow us to discuss the effect on the elastic properties of a pressure-induced phase transition from vaterite-like ACC to aragonite-like ACC, reported by Fernandez-Martinez et al. (2013)[70]. Fernandez-Martinez t al. (2013) [70] studied a hydrous ACC sample and observed a discontinuous change in the position of the main diffraction peak

and some changes in the in the CO_3^{-2} v_1 and v_4 Raman modes as a function of pressure at approximately 10 GPa. Reverse Monte-Carlo modeling of the diffraction data allowed the authors to interpret these features as a phase transition from vaterite-like to aragonite-like amorphous calcium carbonate. In addition to that, the study by Fernandez-Martinez et al. (2013) [70] reports the first values for the bulk modulus at ambient conditions of ACC and the density as a function of pressure. They observed an irreversible densification of the material upon compression, but the measured density values showed no discontinuities across the transition at 10 GPa. It is important to note that the experiments described in their study were performed using methanol-ethanol as pressure transmitting medium, which is known to be significantly non-hydrostatic above 10 GPa [112].
The samples used in this study, ACC-I, ACC-II and ACC-III, differ in synthesis method and hydration state. In our Brillouin spectroscopy experiments, performed with Ne as pressure transmitting medium, we did not observe, independently on the hydration state and synthesis procedure of the samples, any discontinuities in the acoustic velocities' trend in the pressure range from 0 to ∼20 GPa. Our results suggest that, if indeed a phase transition takes place in amorphous calcium carbonate at 10 GPa, it does not have a noticeable effect on the acoustic velocities and elastic parameters of ACC.
Tab. 5.1 reports the elastic moduli of hydrous and anhydrous ACC and $CaCO_3$ polymorphs at ambient conditions. It is evident from Tab. 5.1 that there is a substatial difference in the isothermal and isentropic bulk moduli (∼20%) and their pressure derivatives (∼30%) at ambient conditions. The higher value of K'_S, compared to K'_T leads to a divergence of the bulk moduli at high pressures (see Fig. 5.8). In crystalline materials, the isothermal and isentropic bulk moduli tend to coverge at high pressures, as shown for $MgCO_3$ in Fig. 5.8.

The relationship between isothermal and isentropic bulk modulus is given by:

$$K_S = K_T(1 + \alpha\gamma_{th}T) \tag{5.1}$$

where α is the thermal expansion coefficient, γ_{th} is the thermodynamic Grüneisen parameter and T is the temperature. The pressure derivatives of isothermal and isentropic elastic moduli are related by:

$$K'_S = K'_T(1 + \alpha\gamma_{th}T) + K_T\gamma_{th}\alpha' + K_T\alpha\gamma'_{th} \tag{5.2}$$

For crystalline phases, the thermal expansion α and thermal Grüneisen parameter γ_{th} normally decrease with increasing pressure, leading to higher value of K'_T than K'_S [229]. The unusual behaviour of the pressure derivatives of ACC can be explained by an increase of the Grüneisen parameter

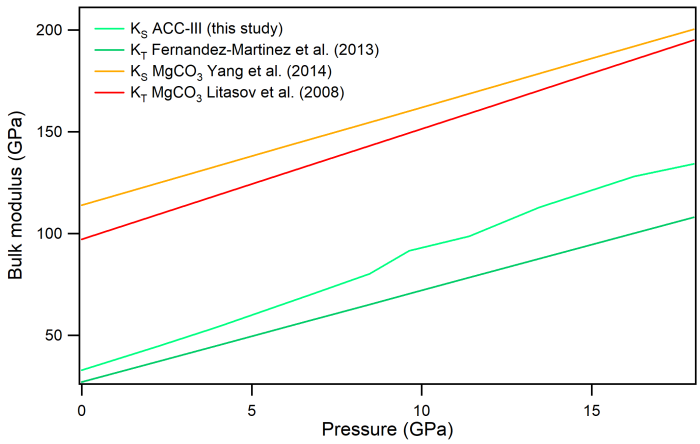

Figure 5.8: Isothermal bulk modulus from Fernandez-Martinez et al. [70] and isentropic bulk modulus of ACC-III as a function of pressure, together with the isothermal [125] and isentropic [261] bulk moduli of crystalline $MgCO_3$.

γ_{th} with pressure, which could be indicative of pressure-induced changes in the structure of ACC. A similar behaviour was reported in a computational study for liquid $MgSiO_3$ [228], where the continuous pressure-induced increase of the average Si-O coordination to a higher coordinated phase was shown to produce an increase in the γ_{th} of the liquid, qualitatively comparable to the increase of γ_{th} due to the effect of pressure. If indeed the originally vaterite structured ACC undergoes a continuous evolution of the local structure towards that of an aragonite-like ACC, a phase where Ca has a higher coordinated number, it would lead to an increase in the value of γ_{th} which results in the unusual behaviour of the elastic bulk moduli for this material. Our measurements and results allow us to quantify the effect of hydration on the elastic properties of amorphous calcium carbonate. The present study shows that, at pressures lower than 5 GPa, the longitudinal acoustic velocities of the hydrous sample are lower than those of the dehydrated ones (-13% at ambient conditions), as shown in Fig. 5.5. At pressures higher than 5 GPa the effect of water on the stiffness of the material is remarkably reduced, with the acoustic velocities of the three samples almost overlapping at the maximum experimental pressure (Fig. 5.5). However, further studies are necessary to study the behaviour of water in the hydrous samples as pressure is increased. Fernandez-Martinez et al. (2013) [70] in their Raman spectroscopy study, observed the loss of loosely bound water around 5 GPa. The softening of the ACC as a function of its water content is confirmed by the values of the elastic moduli at ambient conditions. Fig. 5.9 shows

the bulk and shear moduli for ACC (Fig. 5.9(a-b)) and $CaCO_3$ polymorphs (Fig. 5.9(c)) as a function of the water content. The values of bulk and shear moduli at ambient conditions were corrected to account for the effect of the water content on the density of the samples, a 4.43 % increase on the density for the dry sample as observed by Saharay et al. (2013) [199]. The simplest model to describe the behaviour of the moduli as a function of the water content (in wt %, x) up to the maximum H_2O content in the hydrous samples studied here (18(1) wt %) is a linear dependence of the data obtained from the BS experiments, using both compression and decompression data as data points:

$$K_a(x) = -1.1(1)x + 53(1) \tag{5.3}$$

$$G_a(x) = -0.37(6)x + 21.3(8) \tag{5.4}$$

The values for the bulk modulus and shear modulus for anhydrous ACC at ambient conditions obtained by the linear extrapolation (blue data Fig. 5.9a-b) are $K_a = 53(1)$ GPa and $G_a = 21.3(8)$ GPa. The values of the bulk and shear moduli obtained from linear extrapolation of the data, without accounting for the density correction due to the water content (grey data Fig. 5.9) are $K_a = 48(1)$ GPa and $G_a = 19.0(6)$ GPa. According to our results, the elastic moduli decrease, as a function of the H_2O content of the samples, up to 38 % for the bulk modulus and 36 % for the shear modulus.

Finally, by comparing the results of this study on ACC with crystalline and molten $CaCO_3$ it is possible to obtain information of geophysical interest. If indeed pressure has an effect on the local structure of ACC, as observed by Fernandez-Martinez et al. (2013) [70] and Fruhner et al. (2018) [73], the initially vaterite-like ACC should transform to aragonitic-like ACC with pressure. Therefore, we expect the elastic properties of fully hydrous and dehydrated ACC measured at high pressures in this study to be related to an aragonitic-like ACC. According to a study by Hou et al. (2019) [92], in the pressure range between 4.8 and 8 GPa and at temperatures higher than 1000 K, aragonite undergoes a temperature induced phase transition to an amorphous phase. For this reason, we will focus on the comparison between ACC and crystalline aragonite. In particular, we are interested in the comparison between water-poor ACC and aragonite, as the amorphous calcium carbonate resulting from amorphization of aragonite is expected to be anhydrous. ACC is more compressible than aragonite over the pressure range from 0 to 20 GPa, as shown in Fig. 5.7. If indeed an amorphization process is taking place in the P-T range between 4.8 and 8 GPa and temperatures higher than 1000 K, it would be associated with a softening of the material, different mechanical properties of the material (ACC is isotropic, while aragonite is strongly anisotropic) and a change in the acoustic velocities. Studies on the

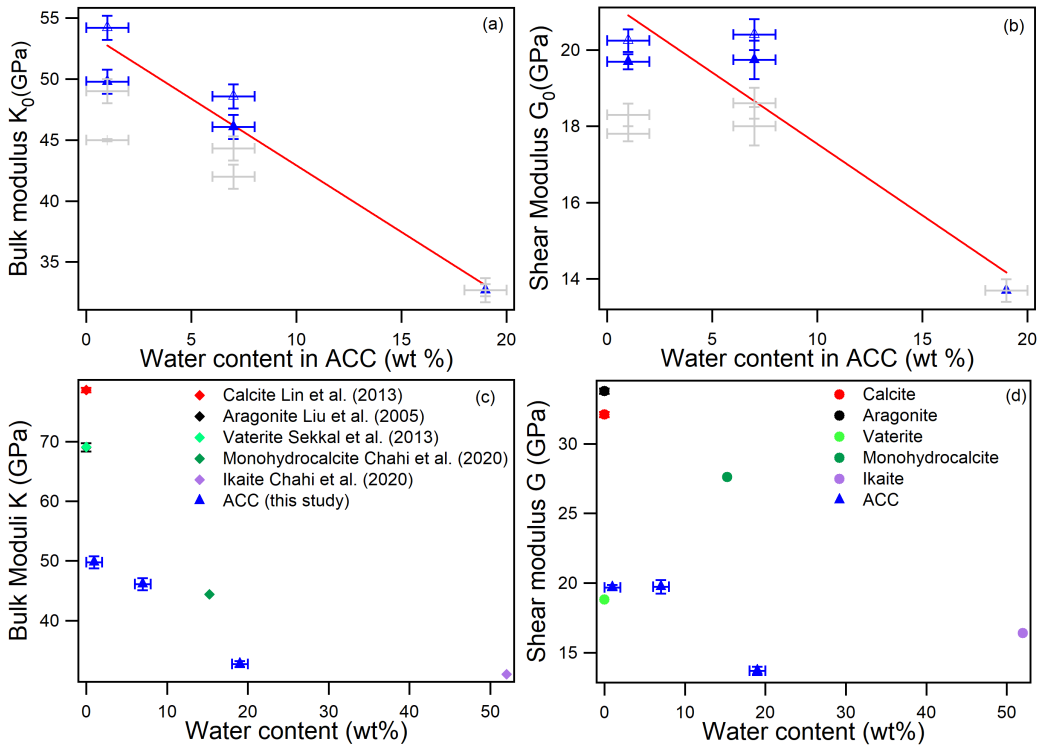

Figure 5.9: (a) Isentropic bulk modulus of ACC as a function of the H_2O content, (b) isentropic shear modulus as a function of the H_2O content. The grey symbols are the values without the density correction for the water content. The blue symbols are the elastic moduli corrected for the water effect on the density of ACC. The red line is the linear fit of the data corrected for the effect of water on the density of ACC. Dependence of the bulk modulus (c) and shear modulus (d) on the water content for crystalline [207, 123, 38, 133] and amorphous $CaCO_3$.

thermal behavior of crystalline aragonite and calcite polymorphs prove that the effect of temperature on the elastic properties of $CaCO_3$ is much smaller than the effect of pressure (e.g. for aragonite, an increase in temperature to 1000 K would lead to a lowering of the bulk modulus of ∼16% [126], while an increase in pressure of 10 GPa would lead to an increase on the bulk modulus of ∼33% [123]). Therefore, assuming the temperature effect on the density and elastic moduli of ACC and aragonite to be comparable, we focus on the pressure dependence of the acoustic velocities and elastic parameters. At 4.8 GPa a phase transition from aragonite to amorphous calcium carbonate would produce a lowering in the longitudinal (-7.3 %) and transverse (-15 %) acoustic velocities (Fig. 5.5). The bulk carbon content in the Earth is poorly

constrained, but previous studies estimate the amount of carbon to be in the order of $\sim$ 120(60) ppm [72, 260]. Due to this small abundance in the mantle, it is doubtful that the velocity jump related to the phase transition from aragonite to ACC could be detected based on seismic data. However, knowledge on the elastic properties of ACC at high pressures might have important implications for the full characterization of processes associated with the decarbonation of the subducting slabs and the recycling of carbon in the subduction zones. Our results show that ACC is softer than aragonite, with the bulk and shear moduli of ACC at 4.8 GPa being lower ($\sim$25% for the bulk modulus and $\sim$40% for the shear modulus) than that of aragonite [94]. Hou et al. (2019) [92] proposed that the presence of a soft, bouyant amorphous phase could facilitate the dissolution mechanisms through percolation of the ACC from the subducting slab to the mantle wedge.
High pressure-temperature measurements of the acoustic velocities and elastic properties of $CaCO_3$, using calcite as a starting material, and their comparison with the results from our study could provide a way to verify if amorphous calcium carbonate is indeed a candidate phase in subducted slab materials in the pressure range between 4-10 GPa and temperatures higher than 1000 K, which is of great importance for understanding the mechanisms of carbon migration.

5.4 Conclusions

The acoustic velocities of synthetic ACC samples with different water contents have been measured at high pressures by Brillouin spectroscopy. The smooth behavior of the acoustic velocities with pressure does not provide a direct confirmation of the polyamorphic phase transition observed at 10 GPa by Fernandez-Martinez et al. (2013) [70], however the anomalous behaviour of the isothermal and isentropic bulk moduli are indicative of a continous evolution of the local structure of the studied samples. The presence of up to 18 wt% H_2O in the samples leads to a softening of ACC, causing a 38 % decrease of the bulk modulus and a 36 % decrease of the shear modulus. Further measurements on the densities of anhydrous ACC are necessary to better constrain the high pressure elastic moduli. The phase transition from aragonite to ACC [92], assuming the temperature effect on the density and elastic moduli of ACC and aragonite to be comparable, would lead to a lowering in the acoustic velocities (v_P $\sim$-7.3 %, $v_S \sim -15$ %).

Chapter 6

Elastic properties of Fe-dolomite as a function of the Fe content

Most of the studies available on the elastic properties of dolomite and ankerite are based on XRD experiments [198, 141, 273, 153, 273, 151, 18, 48], which only provide information on the isothermal bulk modulus, K_T. The results of these studies show that composition has little effect on the compressibility of dolomite and ankerite, reporting bulk moduli ranging from 91.7(10) GPa up to 95(1) GPa [198, 151] for the Dol-I phase.
The complete elastic tensor of dolomite was reported in only two experimental studies [95, 46]. Humbert and Plicque (1972) [95] and Chen et al. (2006) [46] performed ultrasound pulse measurements and Brillouin spectroscopy experiments, respectively, and obtained the complete elastic tensor of dolomite, however, no chemical characterization of the samples was reported in these studies and the results show clear discrepancies (i.e. 14% in the C_{33}, 25% in the C_{13}, 14% in the C_{14} and 48% in the C_{15} coefficients). To help resolve this disagreement, an additional Brillouin spectroscopy study on a natural, well characterized, sample was performed by Speziale et al. [223] who investigated the effect of ordering on the elastic properties of dolomite. A natural (ordered) dolomite sample from the Eugui metamorphic complex (fragment of the sample studied by Zucchini et al. (2012) [272]) was studied by Brillouin spectroscopy. A second fragment, from the same Egui dolomite, was heated at 3 GPa to 1473 K and then quenched, this second (disordered) dolomite was also studied by Brilloiun spectroscopy to determine the effect of ordering on the elasticity of $CaMg(CO_3)_2$. However, the data has not yet been published.
The elastic tensor of dolomite has also been obtained from computational studies: Bakri et and Zaoui (2011) [12] performed density functional theory (DFT) calculations, while Titiloye et al. (1998) [233] performed an atom-

istic simulation study based on the Born model of solids [22]. The elastic tensor coefficients obtained from the atomistic simulation from Titiloye et al. (1998) [233] are in perfect agreement with the results from Humbert and Plicque (1972) [95], but show a clear discrepancy with the results from Bakri and Zaoui (2011) [12] (92% in the C_{15} coefficient, 10% in the C_{12} coefficient). No elastic tensor has been provided theoretically or experimentally, to this date, for ankerite.
Here, we studied the elastic properties of Fe-dolomite and ankerite samples with different compositions by synchrotron PXRD up to 40 GPa and ambient conditions Brillouin spectroscopy.

6.1 Samples and methodology

Natural samples of Fe-dolomite from Hospental, Switzerland (named Ank-1), Wittmannsgereuth, Thüringer Wald, Germany (sample 2008-15895, named Ank-2), Leogang, Salzburg, Austria (sample 1998-2093, named Ank-4), and a natural ankerite sample from Vordernberg, Steiermark, Austria (sample 1998-2098, named Ank-5) were used in the current study. Samples Ank-2, Ank-4 and Ank-5 were provided by the Museum für Naturkunde of Berlin.
The chemical composition of the samples was determined by electron microprobe analysis at GFZ (Helmholtz Center Potsdam, Germany). EMPA results indicate a stoichiometry of $Ca_{0.96}(Mg_{0.99},Fe_{0.05})(CO_3)_2$ for sample Ank-1, $Ca_{0.99}(Mg_{0.55},Fe_{0.40}Mn_{0.06})(CO_3)_2$ for sample Ank-2, $Ca_{0.89}(Mg_{0.78},Fe_{0.29}Mn_{0.03})(CO_3)_2$ for sample Ank-4 and $Ca_{0.99}(Mg_{0.33},Fe_{0.63}Mn_{0.05})(CO_3)_2$ for sample Ank-5 (details in the Appendix).
The unit cell parameters of each sample were determined by PXRD at ambient conditions, using a Bragg-Brentano STOE Stadi-P diffractometer at GFZ, Potsdam. The data were processed with the GSAS software package (Larson and Von Dreele, 1994)[117] (details in the Appendix Tab. D.1).

Table 6.1: Lattice parameters a, b, c, unit cell volume, V, and density ρ obtained from Rietfeld refinement of ambient conditions PXRD of the samples used in this study.

Sample	a (Å)	b (Å)	c (Å)	V (Å^3)	ρ (g/cm^3)
Ank-1	4.8076(5)	4.8076(5)	16.012(1)	320.50(5)	2.88(3)
Ank-2	4.8264(5)	4.8264(5)	16.138(1)	325.55(5)	3.04(2)
Ank-4	4.8083(2)	4.8083(2)	16.080(2)	321.35(1)	2.98(1)
Ank-5	4.8364(5)	4.8364(5)	16.200(2)	328.10(5)	3.12(5)

The unit cell parameters for the samples obtained from Rietveld analysis are shown in Tab. 6.1.

6.1.1 Brillouin spectroscopy experiments

Single crystals of samples Ank-1, Ank-2 and Ank-5 were studied by Brillouin spectroscopy at the Brillouin Spectroscopy laboratory in GFZ (Helmoltz Centre, Potsdam). A solid state laser (Nd:YVO4) (λ = 532 nm) and six-pass tandem Fabry-Perot interferometer (JRS Scientific Instruments) were used for the experiments. The experiments were performed in a symmetric forward scattering configuration with $\theta = 60°$. Orthogonal platelets were cut and finely polished for each sample in order to obtain parallel faces. Three orthogonal platelets were studied for sample Ank-1, one platelet was studied for sample Ank-2 and two orthogonal platelets were studied for sample Ank-5. The normal vector of the platelets was determined by single crystal X-ray diffraction using a Xcalibur single crystal diffractometer in Goethe University, Frankfurt am Main.

6.1.2 DFT

First principle calculations were used to obtain the elastic stiffness tensor at ambient conditions for end-member dolomite, $CaMg(CO_3)_2$, and ankerite, $CaFe(CO_3)_2$. Unfortunately, the determination of the elastic tensor coefficients for end-member ankerite, $CaFe(CO_3)_2$, was unsuccesful due to limitations of DFT in handling Fe-bearing compounds.
The elastic stiffness coefficients of dolomite were obtained from stress-strain relations. Two strain patterns were employed along the xx and $zz + yz$ directions, using six amplitudes for each direction with an amplitude maximum strain of 0.003. Pseudopotentials generated using the descriptors in the CASTEP data base were employed in conjunction with plane waves up to a maximum cutoff energy of 630 eV. A Monkhorst-Pack grid [162] of 8×8×8 was employed (k-point separation of less than 0.031 $Å^{-1}$). The calculations were considered to converge once the maximal residual force acting on an atom was < 0.01 eV/Å, the residual stress was <0.02 GPa, and the maximal energy change was $< 5 \cdot 10^{-6}$ eV/atom.

6.1.3 High pressure experiments

Samples Ank-2, Ank-4 and Ank-5 were studied at high pressures by means of PXRD. The samples were ground into a fine powder and loaded in symmetric DAC, with diamond culets of 300 μm in diameter. A sample chamber

of 150 μm in diameter was obtained by pre-indenting the central part of a 250 μm-thick Re-foil to 35 μm and drilling a hole in it with an electric discharge machine (EDM). Neon was used as pressure transmitting medium (Klotz et al. 2009)[112] and a ruby sphere as pressure calibrant. The ruby's fluorescence was measured immediately after each data collection. The high pressure experiments were performed at the extreme conditions beamline P02.2 at Petra-III (DESY, Hamburg, Germany) using an X-ray beam of wavelength $\lambda = 0.2906$ Å [122]. The samples were studied up to a maximum pressure of $\sim$40 GPa in steps of 1-2 GPa. We obtained the lattice parameters and unit cell volumes by Pawley refinement using the GSAS software package [235]. The unit cell volumes were fitted to a second order Birch-Murnaghan equation of State (EOS) [19, 5] using the EoSFit program [7, 79]. The BM-EoS parameters were simultaneously refined using the data weighted by uncertainties in both P and V.

6.2 Results and discussion

6.2.1 Brillouin spectroscopy

Fig. 6.1 shows a representative spectrum collected in the BS experiments for samples Ank-1 (a) and Ank-5 (b). The peaks are sharp and exhibit an excellent signal to noise ratio for both the longitudinal and transverse modes. The

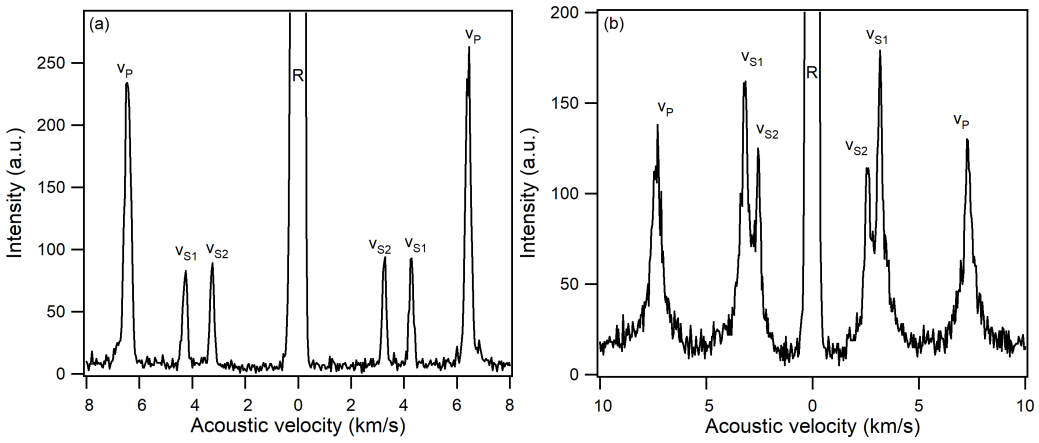

Figure 6.1: Brillouin spectrum of: (a) Ank-1, orientation (-0.17, 0.02, 1); (b) Ank-5, orientation (0.6, 0.6, -1).

normal vectors of the platelets used in this study, determined from SC-XRD are: (-0.14, 1, -0.2), (1, -0.64, -0.02) and (-0.17, 0.02, 1) for sample Ank-1, (0, 1, 0.7) for sample Ank-2 and (0.06, 0.06, -1) and (0.5, -1, 0.7) for sample

Ank-5. Using these normal vectors and the elastic coefficients from Chen et al. (2006) [46] as initial set of values, it was possible to obtain the elastic stiffness tensor for the studied samples, by a least-square fit of the full set of the Christoffel equations (Eq. 2.21). Fig. 6.2 shows the acoustic velocities measured in the BS experiments as a function of the rotational angle for the two samples Ank-1, Ank-2 and Ank-5 and the results of the fit. Due to the fact that only one platelet of Ank-2 was studied, it was not possible to determine all the elastic tensor coefficients for this sample.
Tab. D.2 lists the elastic tensor coefficients and elastic moduli obtained in this work from BS experiments and DFT calculations, together with literature values on dolomite (Speziale et al. (*unpublished material*) [223], Chen et al. (2006), Humbert and Plicque (1972), Bakri and Zaoui (2011) and Titiloye et al. (1998) [46, 95, 12, 233]. The elastic tensor coefficients obtained in our

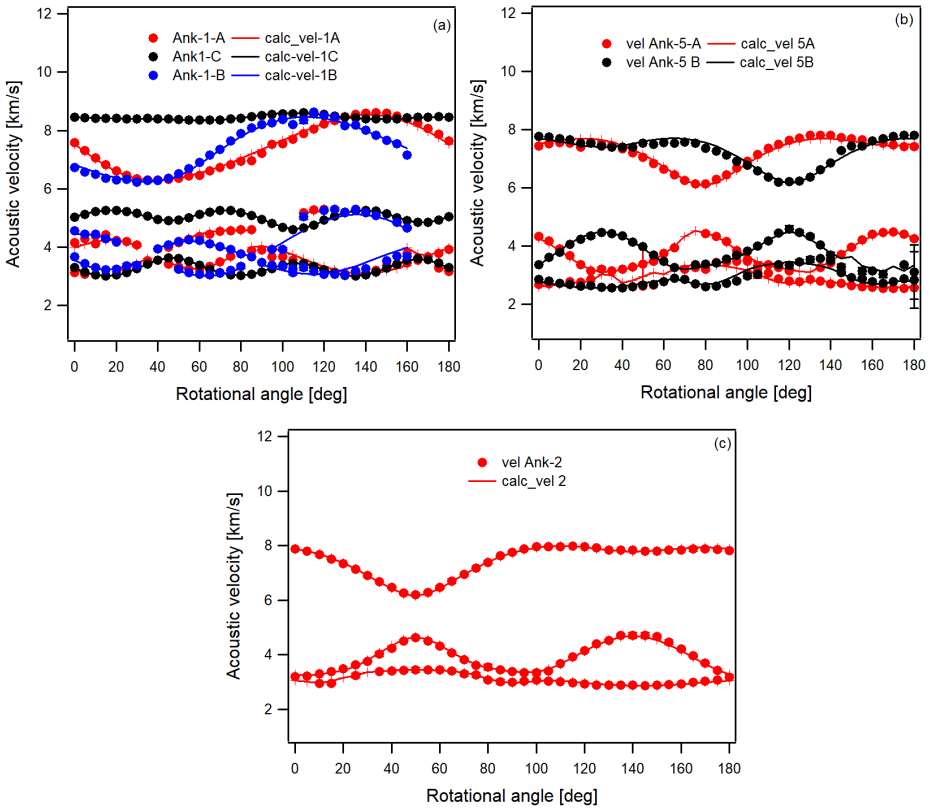

Figure 6.2: Distribution of the acoustic velocities as a function of the rotational angle for the different platelets (red, black and blue) of samples Ank-1 (a), Ank-5 (b) and Ank-2 (c).

study for sample Ank-1 are in good agreement with the results on ordered

dolomite reported by Speziale et al. [223], as shown in Fig. 6.3. The sign of the C_{14} and C_{15} coefficients (Tab. D.2) is related to the coordinate system selected for the description of the orientation of the samples (a and b are rotated clockwise by 60 degrees about the c axis). Therefore, Fig. 6.3 shows the value of $|C_{14}|$ and $|C_{15}|$ for a better comparison with the literature data. The experimental results obtained in this study show discrepancies with the elastic tensor coefficients from DFT calculations, in particular for the C_{14} and C_{15} coefficients (10% in the C_{12}, 25% in the C_{14}, 11% in the C_{33} coefficients).

The presence of Fe in samples Ank-2 and Ank-5 has a remarkable effect

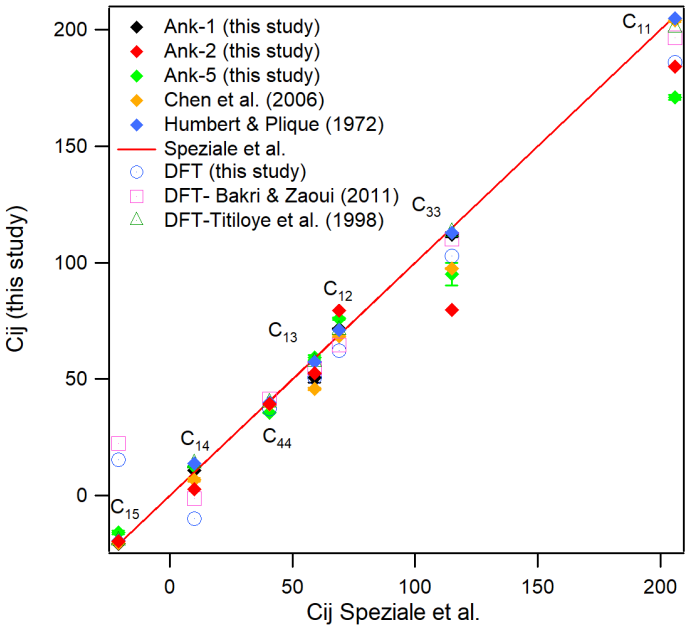

Figure 6.3: Comparison between the Cij obtained in this study for sample Ank-1 and Ank-5, the DFT values computed for dolomite and the literature data (Chen et al. (2006), Humbert and Plicque (1972), Bakri and Zaoui (2011), Titiloye et al. (1998) [46, 95, 12, 233]). The red line is a guide to the eye representing perfect correspondence between the data obtained for dolomite from Speziale et al. (unpublished data) and the other datasets.

on the elastic tensor coefficients compared to the Fe-free sample Ank-1: C_{11}, C_{33} and C_{44} decrease with increasing Fe (-17% for C_{11} and C_{33} and -13% for C_{44} comparing sample Ank-1 and Ank-5); C_{12} and C_{15} show an increase (9% and 20% respectively with 63% Fe, Ank-5); while C_{13} and C_{14} do not appear to be sensitive to compositional changes. Fig. 6.4 shows the variation of the elastic tensor coefficients C_{ij} as a function of the composition of the studied

samples, together with the results from Speziale et al. [223].
The increase in the off-diagonal components and lowering of the diagonal components of the elastic tensor is similar to what observed in megnesiosiderite in previous experimental studies, where the effect of composition on the elasticity of a $Mg_{1-x}Fe_xCO_3$ solid solution was investigated [227, 74, 124, 202]. Tab. D.2 lists the isentropic bulk and shear moduli in the Voigt-Reuss-Hill

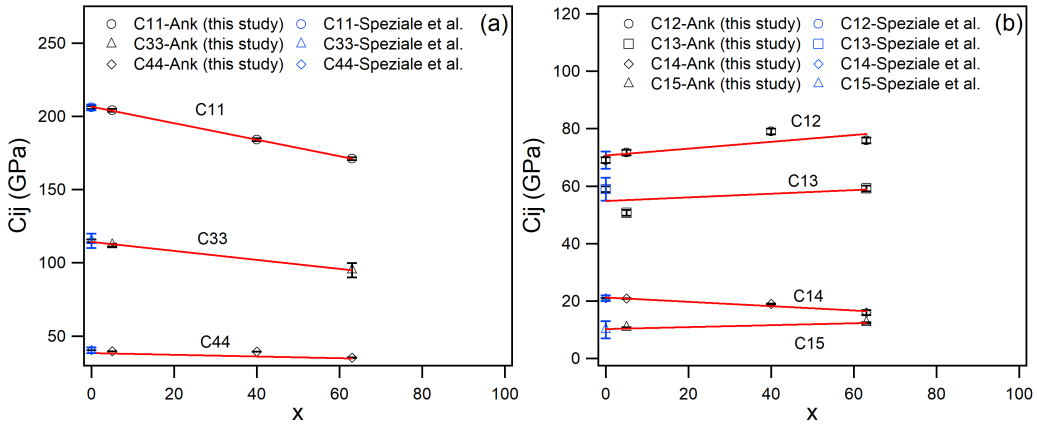

Figure 6.4: Elastic tensor coefficients, C_{ij}, as a function of the $CaFe(CO_3)_2$ content, x, in the dolomite-ankerite solid solutions $CaMg_{1-x}Fe_x(CO_3)_2$ (Ank-this study, Speziale et al. [223]). The solid lines represent the fit of the C_{ij} as a function of the Fe content.

bound, K_S and G_S, the acoustic velocities v_P and v_S, and the values of the universal anisotropy index, A^u [189]. Fig. 6.5 shows the aggregate elastic properties (VHR bound) of dolomite (from Speziale et al. [223]) and ankerite as a function of the Fe content. The presence of Fe leads to a lowering of the aggregate elastic properties, differently from what was observed for $MgCO_3$-$FeCO_3$ solid solutions, where the presence of Fe showed no effect on the bulk modulus, K, but caused a drastic lowering of the shear modulus (33 %) and acoustic velocities (20 % for v_P and 30 % for v_S) [202].

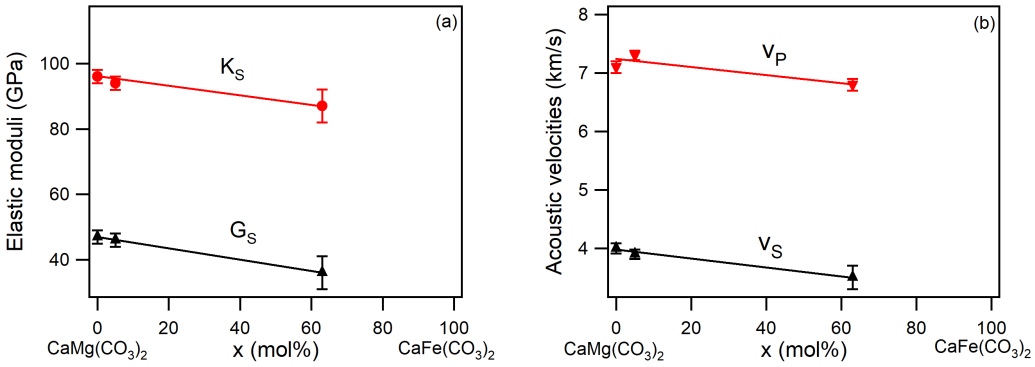

Figure 6.5: Aggregate properties at ambient conditions of dolomite (Speziale, [223]) and ankerite (Ank-1 and Ank-5) as a function of the $CaFe(CO_3)_2$ content x of the samples.

6.2.2 High pressure powder diffraction experiments

Samples Ank-2, Ank-4 and Ank-5 were studied by PXRD up to $\sim$ 40 GPa in steps of $\sim$ 1 GPa. In this pressure range dolomite and ankerite are known to undergo two well defined phase transitions [153, 151, 18]. The Pawley refinement of the high pressure diffractograms was carried out in collaboration with Dr. Naira Martirosyan (GFZ, Potsdam).

Ankerite-2 Upon compression of sample Ank-2 (Fe=40 at%), we observed a change in the PXRD pattern at about 17 GPa, related to the second-order Dol-I to Dol-II phase transition. A second order Birch-Murnaghan equation of state (EOS) (Birch 1947 [19], Angel 2000 [6]) was fitted to the unit cell volumes, using the EoSFit program [7, 79]

$$P = \frac{3K_{0T}}{2}\left[\left(\frac{V_0}{V}\right)^{7/3} - \left(\frac{V_0}{V}\right)^{5/3}\right] \tag{6.1}$$

where K_{0T} is the isothermal bulk modulus, V_0 is the volume at ambient pressure and V is the volume at pressure P. The second order was selected for the fitting as the F vs f plots (Eq. 2.40) show a constant trend up to the transition pressure. The fitting of the Dol-I phase data yielded $K_0 = 84(2)$ GPa and $V_0 = 325.8(5)$Å^3. The value of bulk modulus at ambient conditions for the Dol-I phase obtained in this study is lower compared to literature data on ankerite samples with similar compositions [153, 151] (Tab. 6.2, Fig. 6.6). A second-order BM was fitted to the Dol-II data, yielding a bulk modulus and volume at ambient conditions of $K_0 = 60(3)$ GPa and $V_0 = 225(2)$Å^3. Dol-II is observed up to 36 GPa. At pressures higher than 36 GPa a new

polymorph was observed. Merlini et al. (2012, 2017) [153, 151] performed SC-XRD studies on Fe-dolomite samples with similar compositions reporting either a triclinic (Dol-III) or a trigonal (Dol-IIIb) structure. The trigonal Dol-IIIb structure matches better the XRD pattern of Ank-2 phase at 41 GPa.

Ank-4 Upon compression of Ank-4 (Fe = 29 at%), the phase transition from Dol-I to Dol-II was observed at about 13 GPa. Fitting of the Dol-I phase with a second order BM yielded values of K_0 = 86(1) GPa and V_0 = 321.35(3) Å^3. At 32-34 GPa a first-order transition from Dol-II to a new polymorph was observed. The monoclinic Dol-IIIc phase indexes the XRD pattern at 44 GPa.

Ank-5 The XRD patterns of Ank-5 (Fe = 63 at%) reveal the presence of a secondary phase, however no reaction occurred between this secondary phase and the sample in the pressure range investigated. The phase transition from Dol-I to Dol-II phase in Ank-5 was observed at about 10 GPa. Dol-II was observed up to 35-37 GPa. At 38 GPa the XRD patterns could be indexed with the trigonal Dol-IIIb structure, although the XRD pattern still contained peaks corresponding to the Dol-II phase.

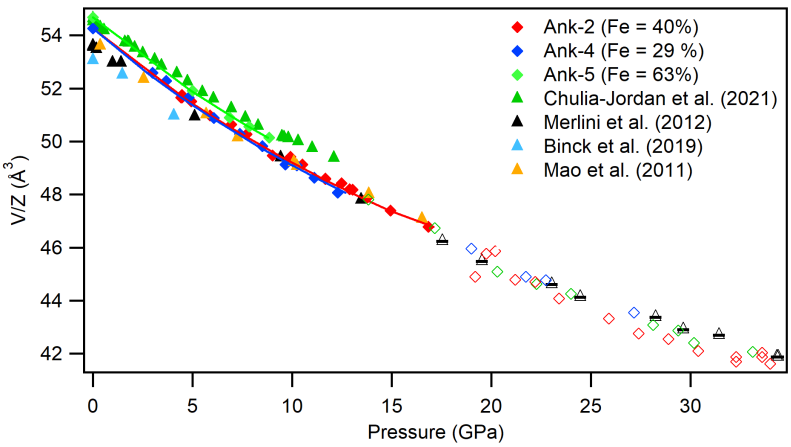

Figure 6.6: Unit cell volumes V/Z as a function of pressure for Ank-2, Ank-4 and Ank-5 together with literature data from Mao et al. (2011) [141], Merlini et al. (2012) [153], Binck et al. (2019) [18], Chulia-Jordan et al. (2021) [48]. Filled symbols: Dol-I phase; Open symbols: Dol-II phase.

The P-XRD measurements conducted in this study, combined with Raman scattering measurements reported in Martirosyan et al. *in prepara-*

tion [144] showed a clear dependence on the chemical composition of the pressures at which the Dol-I to Dol-II phase transition occurs, as already observed in the study by Mao et al. (2011) and Merlini et al. (2017) [141, 151]. This is consistent with what observed in previous carbonate studies where the cationic substitution with a bigger ions leads to a lowering in the transition pressures [15, 14]. The collected data are in good agreement with the literature data [141, 153, 48, 18], as shown in Fig. 6.6 for the Dol-I and Dol-II phases.
Furthermore, from the analysis of the high pressure phases it appears that the triclinic Dol-IIIc phase is favoured for pure Fe-poor dolomites up to 29 mol% Fe, while the trigonal Dol-IIIb is adopted for higher Fe concentrations, from 40 mol% Fe [144]. Martirosyan et al. [144] suggested that the different structural behaviour of the high pressure phases of dolomite with the pressure induced Fe-spin transition, observed around 45 GPa. Higher contents of Fe lead to a more significant structural change due to the Fe-spin transition leading to larger tilting of the CO_3 atoms and consequently different structures [144].

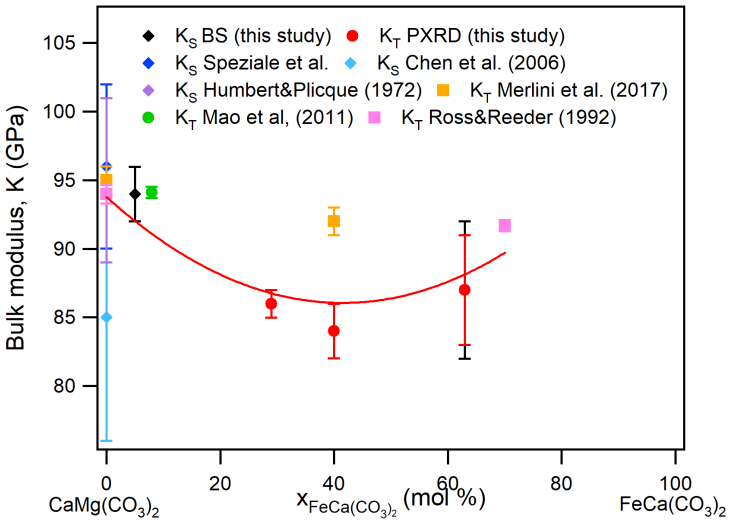

Figure 6.7: Experimental bulk moduli of dolomite and ankerite as function of the $CaFe(CO_3)_2$ content x. Diamonds: isentropic bulk moduli from Brillouin spectroscopy experiments (this study, Speziale et al. [223], Chen et al. (2006) [46], Humbert and Plicque (1972) [95]). Circles: isothermal bulk moduli from high pressure PXRD experiments (this study, Mao et al. (2011) [141]). Squares: isothermal bulk moduli from high pressure SC-XRD experiments (Merlini et al. (2017) [151], Ross and Reeder (1992) [198]). The red curve represents a polynomial fit to the data on dolomite.

Fig. 6.7 shows the values of the isothermal and isentropic bulk moduli for dolomite and ankerite samples from this study and from literature [151, 48, 198, 46, 95, 12, 233] for the Dol-I phase. The experimental bulk moduli obtained in this work are lower compared to the ones reported in literature as shown in Fig. 6.7. In particular there seem to be a discrepancy in the data related to compositions with 40% Fe.

Table 6.2: Elastic data obtained from X-ray diffraction experiments for ankerite and dolomite samples with different compositions. (2^{nd} order BM EoS were fitted to the data, $K' = 4$.)

Fe content	**Phase**	V_0(Å^3)	K_0 (GPa)	**Reference**
0	dolomite-I	320.7(9)	95(1)	Merlini et al. (2017) [151]
0	dolomite-I	320.22(8)	94.1(7)	Ross & Reeder (1992) [198]
8	dolomite-I	321.77(6)	94.1(4)	Mao et al. (2011) [141]
29	dolomite-I	321.35(3)	86(1)	this study-Ank4
40	dolomite-I	325.8(5)	84(2)	this study-Ank2
40	dolomite-I	323.1(9)	92(1)	Merlini et al. (2017) [151]
63	dolomite-I	328(1)	87(4)	this study-Ank5
68	dolomite-I	328.0(2)	95(1)	Chulia-Jordan et al. (2021) [48]
70	dolomite-I	327.8(1)	91.7(4)	Ross&Reeder (1992) [198]

6.3 Conclusions

We experimentally measured the elastic properties of ankerite samples with different Fe content via Brillouin spectroscopy and PXRD. Ambient conditions BS measurements of samples Ank-1 (Fe = 0.05%), Ank-2 (Fe = 40%) and Ank-5 (Fe = 63%) show a clear dependence of the elastic tensor coefficients and of the aggregate elastic properties with Fe content. The values of the elastic tensor coefficients C_{11} and C_{33} decrease with increasing Fe content, while the off diagonal coefficients C_{12}, C_{13}, C_{15} show an increase with increasing Fe. C_{44} and C_{14} are not sensitive to compositional changes. The aggregate elastic properties K_S, G_S, v_P and v_S show a decrease with increasing Fe content. Unfortunately, further BS measurements, along different crystallographic directions are needed to constrain the complete elastic tensor of Ank-2. Having measured only one platelet, it was possible to constrain only C_{11}, C_{12}, C_{14}, C_{44} and C_{66} for this sample. The values of bulk moduli for the ankerite and Fe-dolomite samples Ank-2, Ank-4 and Ank-5 where also measured by high pressure synchrotron PXRD.

Chapter 7

Elasticity of dense metal-organic framework compounds

In addition to the study of the elastic properties of carbonates, the effect of cationic substitution on the elasticity of a material was also investigated by performing elasticity measurements on dense metal organic framework compounds. Metal-organic frameworks (MOFs), are an emerging class of very promising crystalline microporous materials. They are hybrid materials consisting of organic and inorganic components, characterized by metal ions coordinated by organic linkers forming structures with ultrahigh porosity (up to 90% free volume) and incredibly high internal surface areas extending beyond 6000 m^2/g [270]. These structural features are crucial in functional applications, typically in storage and separation, sensing, proton conduction and drug delivery [270]. It is possible to design MOFs according to targeted properties by controlling the geometries of the organic linkers and coordination modes of the inorganic metal ions or clusters of metal ions [270]. The organic linkers connecting the metal cations often allow magnetic interactions, leading to weak ferromagnetic materials whose magnetic properties are of great importance for a large number of applications [243, 52]. Due to their potential for different compositions and great promise in photovoltaic applications [262, 104], hybrid perovskite-structured materials (ABX_3) have gained increasing attention [183].
Perovskite materials are characterized by B cations linked by anions X in a pseudo-cubic network where A cations occupy the cubic interstices. In this study, the elastic behavior of the metal-guanidinium formates (MGF), where M= Mn, Co, Zn, Cu, Cd and Ca was investigated. MGFs are perovskite-like MOFs $ABX_3 = C(NH_2)_3M^{II}(HCOO)_3$, where $A = C(NH_2)_3{}^+$ is guanidinium, $B = M^{II}$ is a divalent metal ion (Mn, Fe, Co, Ni, Cu, or Zn) and $X = (HCOO)^-$ is anion formate, a large polyatomic linker. The guanidinium

Figure 7.1: Structures of (a) ZnGF (isostructural to MnGF and CoGF) and (b) CuGF. Grey polyhedra: Zn; dark blue polyhedra: Cu. Red spheres represent O atoms; brown spheres represent C atoms, light blue spheres represent N atoms; pink spheres represent H atoms. Structural models drawn using VESTA [161].

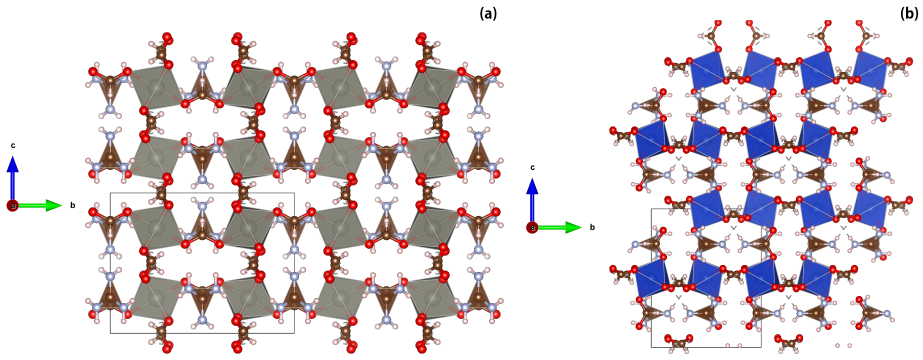

cation $C(NH_2)_3^+$ is a unique hydrogen bonding cationic component that possesses powerful structure directing capability in constructing predictable organic architectures [93]. In the structures presented here, the metal cations (M) are octahedrally coordinated with formate anions $HCOO^-$, while the guadininium cation resides within the nanoporous cavities of the structure and is bound to the surrounding framework by hydrogen bridge bonds [93]. As a result of the strong hydrogen bonding the guanidinium ions are crystallographically ordered [231]. Substitution of the divalent metal cation in $C(NH_2)_3M^{II}(HCOO)_3$ results in different structures: MGFs with M^{II} = Mn, Fe, Co, Ni, Cu and Zn are structurally close to each other, crystallizing in the orthorhombic symmetry. In this study we will focus on orthorhombic structured MGFs with M^{II} = Mn, Co, Cu and Zn. MnGF, ZnGF and CoGF are isostructural with space group $Pnna$, in which the pseudocubic perovskite cell is distorted slightly along the face diagonal. The structure of ZnGF is shown in Fig. 7.1a. CuGF has a similar crystal structure as ZnGF, however, being Cu^{2+} is a Jahn-Teller (JT) ion, a higher distortion of the octahedra is observed for this compound, leading to a symmetry reduction from $Pnna$ to $Pn2_1a$ [80] (Fig. 7.1). A more detaied description of the structures of the metal organic frameworks studied here can be found in Hu et al. (2009) [93]. The unit cell parameters, densities and structural information for the MGF mentioned above are listed in Tab. 7.1.

MGFs have attracted a lot of attention as they exhibit interesting effects such as temperature induced phase transformations, polar properties, ferroelectric phases and almost zero axial compressibilities [262, 93, 50]. Collings

et al. (2016) [50] studied the thermal behaviur of perovskite-like MOFs of composition $[A^I][M^{II}HCOO_3]$, with different A^I cations (i.e $[CH_3CH_2NH_3]$, $[(CH_3)_2NH_2]$, $[(CH_2)_3NH_2]$ and $[C(NH_2)_3]$), and found an essential relationship between the radius of the divalent metal cation M^{II} and the flexibility of the framework and determined the thermal expansion of these compounds using PXRD. The larger the cation, the more flexible the metal formate structures formed are. Additionally, Collings et al. (2016) [50] correlated the shape of the complex cation, A^I, residing in the cavities of the framework with the framework hingeing: prolate cations cause all framework angles to converge towards 90°, forming more cubic-like frameworks, while oblate cations are associated with diverging angles, leading to distortions of the pseudo-cubic framework. Furthermore, the thermal behaviour of the different MOFs compositions was studied, in particular, it was observed that MnGF, ZnGF and CoGF show an expansion in the *a*- and *b*-axes with rising temperature but a contraction in the *c*-axis, while in CuGF, the *a*- and *c*-axes expand with increasing temperature and the *b*-axis exhibits a crossover from contraction to expansion [50]. A more thorough study on the thermomechanical behviour of CuGF is reported by Viswanathan (2018) [238], who performed temperature dependent neutron diffraction measurements on deutered MnGF, CuGF and CoGF. In their study they observed that, MGFs show wider hydrogen bond lengths in the case of CuGF, a Jahn Teller ion, with a consequent influence on the framework flexibility.
In this study several different methods were employed, such as Brillouin spectroscopy, plane parallel plate ultrasonic technique (measurements performed by Dr. Eiken Haussühl), resonant ultrasound spectroscopy (measurements performed by Dr. Eiken Haussühl), thermal diffuse scattering analysis (data analysis performed by Julia Büscher) and DFT calculations (performed by Prof. Björn Winkler) in order to accurately determine of the elastic stiffness coefficients of bulk single crystals.

7.1 Samples description and characterization

Samples of Cu-, Zn-, Mn-, Co-guanidinum formate were grown from aqueous solution via evaporation at room temperature. The phases were characterized by powder or single crystal XRD. The evaporation solution was prepared by dissolving all educts in bidistilled water. The synthesis of the samples was performed by Julia Büscher. Metal sulfate, guanidinium carbonate and formic acid in a molar ratio corresponding to the stoichiometric composition of the crystals were used. To ensure that the educts dissolve properly, the metal sulfate and the guanidinium carbonate were added to the bidistilled

water separately. After combining the solutions, the formic acid was added. The pH value of the solution was initally between 3.3 and 3.8. It was left to evaporate at room temperature in a fume hood. The first crystals formed after seven to fourteen days. ZnGF (transparent) and CuGF (bright blue) crystals grew up to an edge length of 1 cm, while most of the crystals had edge lengths of 3-5 mm. The MnGF crystals showed pale pink and yellowish colour. The biggest crystals had edge lengths of ≈7 mm, but typically, the edges were 2-4 mm long. The CoGF solution produced crystals in an intense purple colour. The largest crystals reached edge lengths of ≈4 mm, most of them were 0.5-2 mm long.

7.2 Methods

In this study the elastic properties of ZnGF, MnGF, CoGF and CuGF were investigated by means of several techniques: plane parallel plate ultrasonic technique, resonant ultrasound spectroscopy, Brillouin spectroscopy, density functional theory, and thermal diffuse scattering analysis. The MGF samples studied here are orthorhombic therefore the elastc stiffness tensor is completely described by 9 independent elastic tensor coefficients: C_{11}, C_{12}, C_{13}, C_{22}, C_{23}, C_{33}, C_{44}, C_{55} and C_{66} in Voigt notation.

7.2.1 Powder X-ray diffraction

Powder X-ray diffraction measurements were performed on the samples to check the phase purity and determine the lattice parameters and the density of the samples. The experiments were performed at Goethe University, using a X'Pert Pro diffractometer from PANalytical in Bragg-Brentano geometry equipped with a PIXcel detector and Cu-$K_{\alpha 1}$ radiation. Rietveld refinements were performed using the GSAS software package [235]. The obtained lattice parameters and densities are shown in Tab. 7.1.

Table 7.1: Crystallographic data for Mn, Zn, Co, Cu-GFs from PXRD.

	MnGF	CoGF	ZnGF	CuGF
space group	$Pnna$	$Pnna$	$Pnna$	$Pna2_1$
a (Å)	8.5211(3)	8.3343(2)	8.3493(3)	8.5212(3)
b (Å)	11.9779(4)	11.7530(4)	11.7276(5)	9.0321(3)
c (Å)	9.0593(3)	8.9111(3)	8.9089(4)	11.3497(4)
V (Å^3)	924.64(5)	872.87(5)	872.34(6)	873.52(5)
ρ (g/cm^3)	1.796	1.933	1.984	1.967

7.2.2 Plane parallel plate ultrasound technique

A preliminary determination of the elastic tensor coefficients, later used as a set of initial parameters for the resonant ultrasound spectroscopy measurements, was obtained by the plane parallel plate ultrasonic technique for CuGF and ZnGF. The plane parallel plate ultrasound measurements and data analysis were performed by Dr. Haussühl at Goethe University. In the case of CuGF, the complete elasticity tensor of the samples was solved for 295 K using the corresponding Christoffel determinants and a computer programm developed by Siegert [217].

7.2.3 Resonant ultrasound spectroscopy

The elastic properties of ZnGF and CuGF samples were studied experimentally by Dr. Haussühl with the aid of an ambient-temperature in-house Resonant ultrasound spectroscopy device [84]. The dimensions of the samples are $\sim$5.351(2)$\times$5.091(2)$\times$4.252(2) mm^3 for ZnGF and $\sim$5.961(2)$\times$3.578(2)$\times$4.376(2) mm^3 for CuGF. The samples were clamped between an ultrasound generator and detector. The force acting on the opposite corners of the sample was kept below 0.05 N to ensure the conditions of a nearly freely vibrating body. For signal generation and detection, network analyzers (4394A and 4194A from Keysight) were employed. On each sample at least 10 resonance spectra in the frequency range between 100 kHz and 1400 kHz with a resolution of 0.01 kHz were collected at 295 K for different sample positions (Fig. 7.2).
234 RUS eigen-frequencies for CuGuFormate and 89 for ZnGuFormate, respectively, which were recorded at room temperature.

Figure 7.2: Photograph of a ZnGF single crystal mounted in the RUS set-up. The sample size is of $\sim$5.351(2)$\times$5.091(2)$\times$4.252(2) mm^2.

7.2.4 Brillouin Spectroscopy

Single crystals of samples ZnGF and MnGF were studied by Brillouin spectroscopy at ambient conditions. The experiments were carried out in the

Figure 7.3: Single crystal of Mn-guanidinium formate ($\approx$ 800 $\times$ 1180 $\times$ 500 μm^3) used for the TDS experiments, mounted on a carbon fiber.

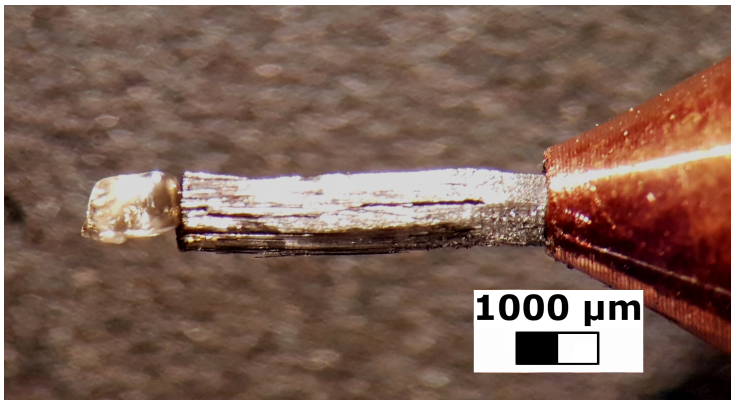

Brillouin Spectroscopy laboratory at the GFZ (Helmoltz center, Potsdam), using a Fabry-Perot interferometer (JRS Scientific Instruments) and a solid state laser (Nd:YVO_4) ($\lambda = 532$ nm) as excitation source. The measurements were performed in a symmetric scattering configuration with a scattering angle between the external incident beam and scattered beam path of $\theta = 60°$. Measurements were conducted on two different platelets for each composition. The platelets were obtained by polishing samples along their natural faces, obtaining plates with parallel faces. The orientation of the platelets was determined from the dispersion curves of the acoustic velocities, using an intial set of elastic tensor coefficients obtained from DFT calculations. The orientation was then refined in combination with the C_{ij} with a least square fitting procedure of the full set of Christoffel equations, as described in the subsequent section. The platelets orientations, thus determined, are: (0, 1, 0.13) and (1, 0, 1) for MnGF and (1, 0.08, 0.88) and (1, 0.11, 0.99) for ZnGF.

7.2.5 TDS

Thermal diffuse scattering analysis was performed on a Mn-guanidinium formate (MnGF) sample of about 800 $\times$ 1180 $\times$ 500 μm^3. The crystal was glued with heat conducting glue (VE GARNISH) on a $\approx$4 mm long carbon fiber with $\approx$1.5 mm diameter which was attached to a copper sample holder to ensure heat conduction to the cooling system (cold finger) from the sample (Fig. 7.3). The diffraction experiments were performed in a closed cycle cryostat using a vacuum of $\approx 4 \times 10^{-3}$ mbar at beamline P21.1 of DESY, using a beam with energy of 100 keV. For better temperature control, the sample was shielded by a mylar foil tube during the experiments. The TDS of MnGF

was measured at 295 K and 265 K with a PILATUS CdTe 2M detector with a pixel size of 172×172 μm^2 which provides a high dynamic range and allows near noiseless measurements. The distance between the detector and the sample was about 1020 mm. The scattered X-rays are directly converted into charge pulses in the CdTe sensor, so that nearly no intensity is spread between neighbouring pixels, and hence the point spread function of this detector is smaller than the pixel size. This allows the detection of weak TDS close to strong Bragg reflections. At 100 keV, the detector has a quantum efficiency of 56%.
At each temperature, we performed four 200° ϕ-scans where each frame was exposed for 1 s, covering a ϕ rotation of 0.1°. The four separate measurements were added together in one data set with an exposure time of 4 s per frame. This strategy was adopted to avoid overexposure of the detector.

7.2.6 DFT

First-principles calculations were carried out by Prof. Bjoern Winkler within the framework of density functional theory employing the Perdew-Burke-Ernzerhof exchange-correlation function [177] with a Tkatchenko-Scheffler correction for dispersion forces [234] and the plane wave/pseudopotential approach implemented in the CASTEP [49] simulation package. "On the fly" norm-conserving pseudopotentials generated using the descriptors in the CASTEP data base were employed in conjunction with plane waves up to a kinetic energy cutoff of 990 eV. A Monkhorst-Pack [162] grid was used for Brillouin-zone integrations with a distance of <0.03 $Å^{-1}$ between grid points. Convergence criteria included an energy change of $<5 \times 10^{-6}$ eV $atom^{-1}$, a maximal force of <0.008 eV $Å^{-1}$, and a maximal component of the stress tensor <0.02 GPa. Phonon frequencies were obtained from density functional perturbation theory (DFPT) calculations.

7.3 Data Analysis

7.3.1 Plane parallel plate ultrasound technique

The elastic stiffness tensor coefficients C_{ij} can be determined from the Christoffel equations (Eq. 2.21). The resonance frequencies are detected by measuring the phase angle between the current and the voltage. The acoustic velocities are calculated from the impedence spectra using the highest and lowest frequency modes. An example of the spectrum is shown in Fig. 7.4. The evolution of the frequencies from the resonance modes taken from the spec-

trum of the (111) plate of CuGF are shown in Fig. 7.5. The complete elastic tensor was obtained for CuGF, while the elastic tensor coefficients C_{11}, C_{22}, C_{33}, C_{44}, C_{55} and C_{66} were obtained for sample ZnGF. The results are shown in Tab. E.2.

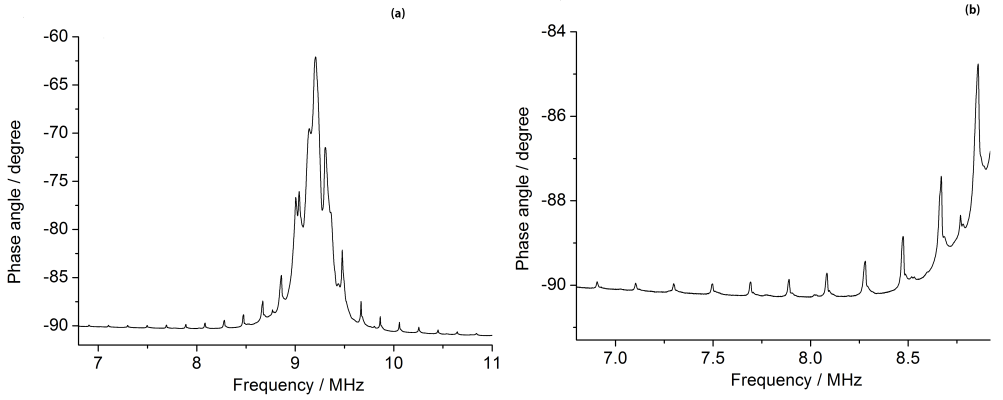

Figure 7.4: Ultrasound resonance spectrum of a plane parallel plate of CuGF with orientation (111) (a). (b) Showns an enlargement of the full spectrum displayed in (a), where the frequency regions in the range dominated by the transducer is excluded. Figures provided by Dr. Eiken Haussühl.

7.3.2 RUS

Fig. 7.6 shows a part of an experimental RUS spectrum collected for ZnGF at ambient conditions. The evaluation of the elastic coefficients, C_{ij}, from the measured resonance frequencies was carried out by a non-linear least-squares procedure in which the observed resonance frequencies were compared to those calculated from the dimensions of the sample, the density and an initial set of elastic coefficients which were derived from ultrasound plane wave technique. In order to minimize errors due to truncation effects, up to 10962 normalized Legendre polynomials were used in the expansion of the displacement vector. The results of the RUS measurements are reported in Tab. E.2

7.3.3 Brillouin spectroscopy

Fig. 7.7 shows representative spectra collected in the BS experiments for samples ZnGF (a) and MnGF (b). The peaks are sharp and exhibit a strong signal to noise ratio for both the longitudinal and transverse modes. The elastic tensor coefficients of ZnGF and MnGF were obtained from an initial set of

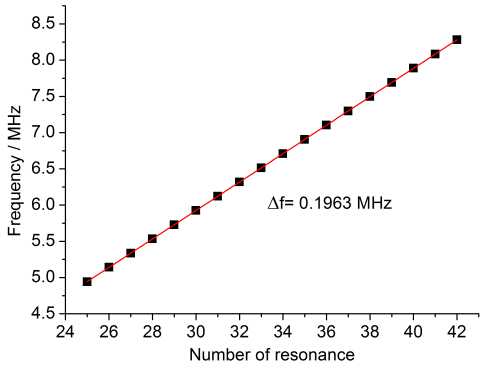

Figure 7.5: Number of resonance modes of the plane parallel plate of CuGF with orientation (111) plotted against frequency. Figure provided by Dr. Eiken Haussühl.

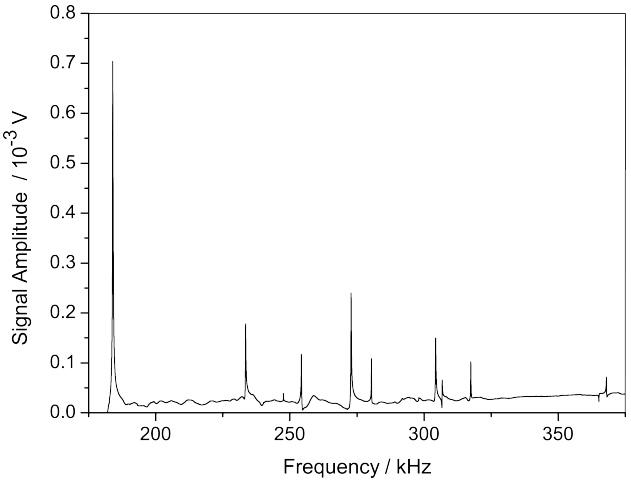

Figure 7.6: Part of an experimental RUS spectrum of ZnGF at ambient conditions. Figure provided by Dr. Eiken Haussühl.

estimated elastic constants using least-square algorithm to fit the Christoffel equations (Eq. 2.21) to the measured acoustic velocities as a function of the azimuthal angle [66]. The initial set of estimated elastic coefficients used are the C_{ij} obtained by DFT calculations. The fitting of the acoustic velocities was performed using the IGOR PRO software (Wavemetrics, Lake Oswego, OR, USA). Fig. 7.8 shows the acoustic velocities measured in the BS experiments as a function of the azimuthal angle for the two samples ZnGF and MnGF. The results of the BS measurements are listed in Tab. E.2.

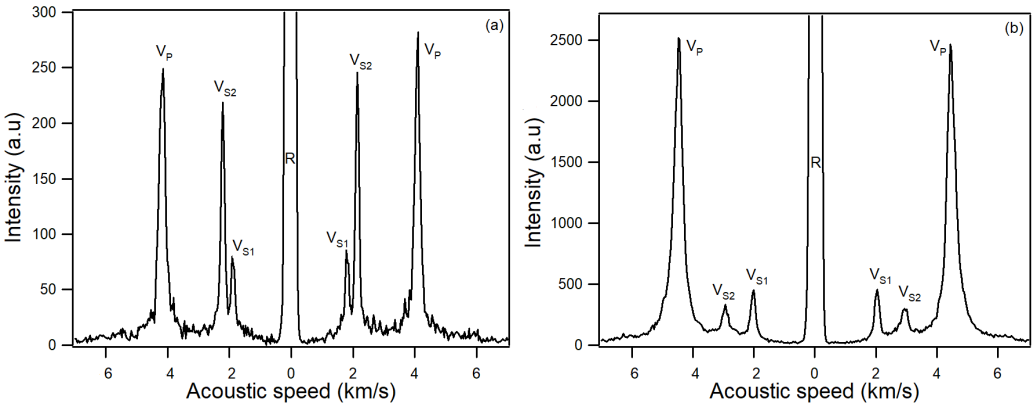

Figure 7.7: Brillouin spectrum of ZnGF (a) and MnGF (b).

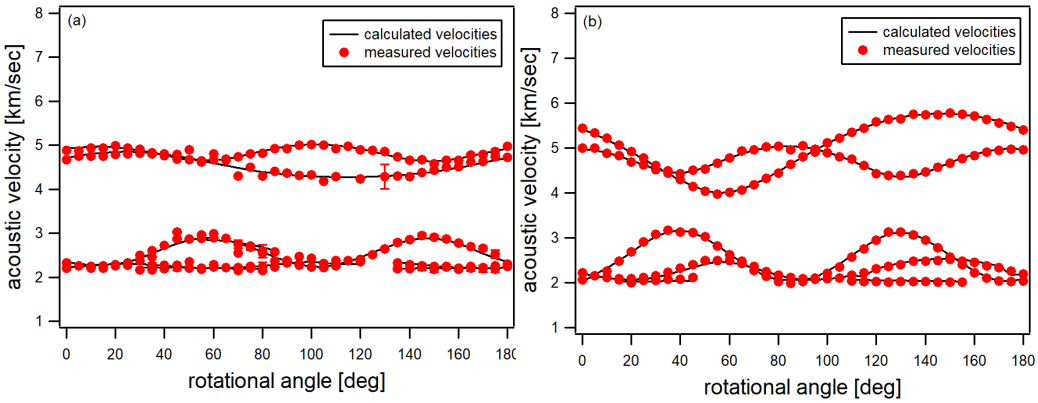

Figure 7.8: Distribution of the acoustic velocities as a function of the rotational angle for sample ZnGF (a) and MnGF (b).

7.3.4 TDS

The elastic stiffness coefficients C_{ij} of MnGF were obtained using the open-source package TDS2EL2 [159] with the multi-temperature approach [245], collecting data sets at 265 K and 295 K. The analysis of the TDS data was performed by Julia Büscher. ROI between $q = 0.05$ Å^{-1} and $q = 0.09$ Å^{-1} were chosen, based on the phonon dispersion curve of MnGF and on empirical testing with TDS2EL2. The data was imported and prepared following the procedure described by Mirone and Wehinger (2017) [159]. The C_{ij} obtained from DFT were used as starting values. The collected scattering intensity was too weak to refine all nine C_{ij} at once, therefore, we first refined our starting values individually for each coefficient to determine starting values tailored to our data set. Then, we refined the coefficients in groups ordered

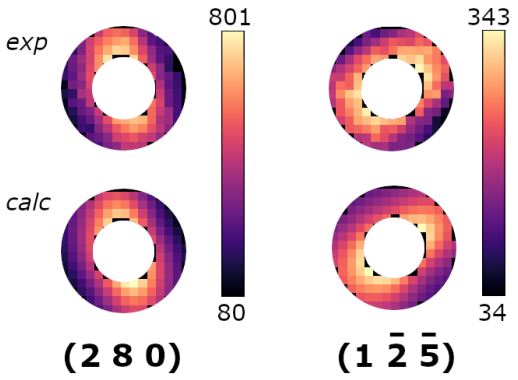

Figure 7.9: Comparison between experimental TDS (top) and calculated TDS (bottom) of the (2 8 0) and (1 $\bar{2}$ $\bar{5}$) Bragg reflections using c_{ij} fitted to our experimental data (Table E.2) with an ROI between $q = 0.05$ Å^{-1} and $q = 0.09$ Å^{-1}. The intensity scale is logarithmic. Figure from Julia Büscher.

by stability of the C_{ij}, in order to achieve the most accurate result without making the fit unstable. The C_{ij} values obtained from our TDS analysis are reported in Tab. E.2.

7.4 Results

The elastic tensor coefficients obtained in this study, via PPPU, RUS, BS TGA and DFT are reported in Tab. E.2. For sample ZnGF, only the elastic tensor coefficients C_{11}, C_{22}, C_{33}, C_{44}, C_{55} and C_{66} were obtained using PPPU. Fig. 7.10 shows a comparison between the experimentally obtained C_{ij} and the DFT-computed C_{ij}. The results from PPPW, RUS, BS and DFT show perfect agreement between the elastic tensor coefficients, except for C_{33}, where the value determined by DFT is 15% larger (Fig. 7.10a).
The experimental results (TDS and BS) for MnGF are in good agreement, however, here too, C_{33} is an exception because the experimental results are about 15% (BS) smaller than the DFT calculated value (Fig. 7.10b).
The C_{ij}s determined for CuGF are shown in Fig. 7.10c. The DFT calculations for this compound were performed both with and without dispersion correction (Tab.E.1). C_{12}, C_{13} and C_{23} from the corrected calculation are in better agreement with the experiments, while C_{11}, C_{22} from the uncorrected calculation are in better agreement with the experimentally obtained values.

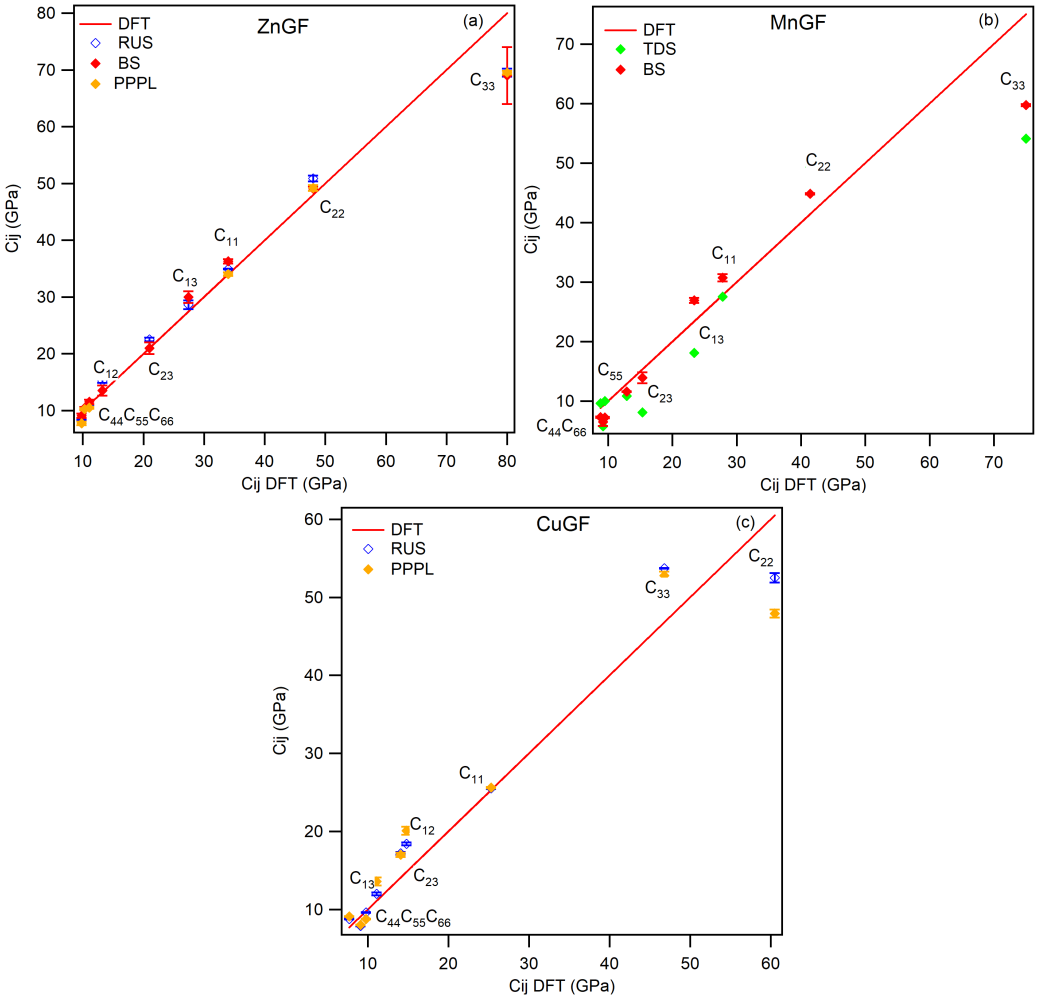

Figure 7.10: Comparison between the data obtained by DFT with and the data collected with the different experimental methods for MnGF (a), ZnGF (b) and CuGF (c). The straight line represents perfect correspondence between the DFT data and the other datasets.

7.5 Discussion

Table 7.2 shows the best estimate for the elastic tensor coefficients and elastic moduli. The values reported in the table were obtained by averaging among the values obtained from the different methods. Some values were discarded as clearly not representative for the studied compounds: C_{33} for ZnGF and MnGF obtained by DFT calculations is 15% larger compared to the measured (with both RUS and BS) elastic tensor coefficients, and as such was not considered in the averaging process. For CuGF the DFT values for C_{22}

were discarded and the dispersion corrected values were considered as the most representative values to describe the elasticity of CuGF. For CoGF, we report only the DFT-calculated values of C_{ij}.

The discrepancy between the experimental results and the ones obtained

Table 7.2: Preferred elastic tensor coefficients, C_{ij}, elastic bulk K_S and shear G_S moduli and acoustic velocities for the studied orthorhombic MoFs.

Compound	**ZnGF**	**MnGF**	**CuGF**	**CoGF**
C_{11} (GPa)	34.9(8)	29(2)	25.6(3)	39.0(8)
C_{12} (GPa)	14(1)	7(1)	19(1)	12.7(3)
C_{13} (GPa)	29(1)	25(2)	12(1)	29.6(4)
C_{22} (GPa)	49(1)	43(2)	50(3)	56.2(3)
C_{23} (GPa)	21.5(9)	13(4)	16(2)	17.1(6)
C_{33} (GPa)	69.3(3)	58(2)	51(3)	86.1(4)
C_{44} (GPa)	8.8(9)	9(2)	8.3(7)	10.9(5)
C_{55} (GPa)	11.0(8)	12.1(7)	9.5(6)	15.2(3)
C_{66} (GPa)	10.3(4)	9(2)	8.5(7)	9.8(8)
K_V (GPa)	31.3(8)	24(1)	24.6(8)	33.3(2)
G_V (GPa)	12.0(5)	11.6(7)	10.6(4)	15.3(2)
K_R (GPa)	27.13(7)	20.9(2)	21.75(7)(8)	28.82(2)
G_R (GPa)	10.9(2)	9.4(2)	10.0(5)	13.2(1)
K_S (GPa)	29.2(5)	23(1)	23.2(8)	31.1(2)
G_S (GPa)	11.4(3)	10.8(7)	10.0(5)	14.2(2)
v_P (km/s)	4.7(2)	4.5(4)	4.3(2)	5.09(8)
v_S (km/s)	2.39(8)	2.44(3)	2.25(2)	2.714(8)
A^u	0.64	0.99	0.73	0.96

from DFT can be associated to temperature issues. The experiments were conducted at ambient conditions, while the calculations were performed at 0 K (athermal limit).

Having studied MGF with different compositions, it is possible to see the effect of cationic substitution on the elastic properties of MGFs.

The differences in elasticity between the different MOFS can be illustrated using a graphical representation of longitudinal effects [11]. Fig. 7.11 shows the representation surfaces of the longitudinal elastic stiffness $F = x_i x_j x_k x_l C_{ijkl}$, where x_i are the components of the radius vector that points from the origin of the tensor to the surface, of the orthorhombic ZnGF, MnGF, CuGF and CoGF MOFs. The differences between the representation surfaces for the different MGFs are substential, showing a strong dependence of the elastic

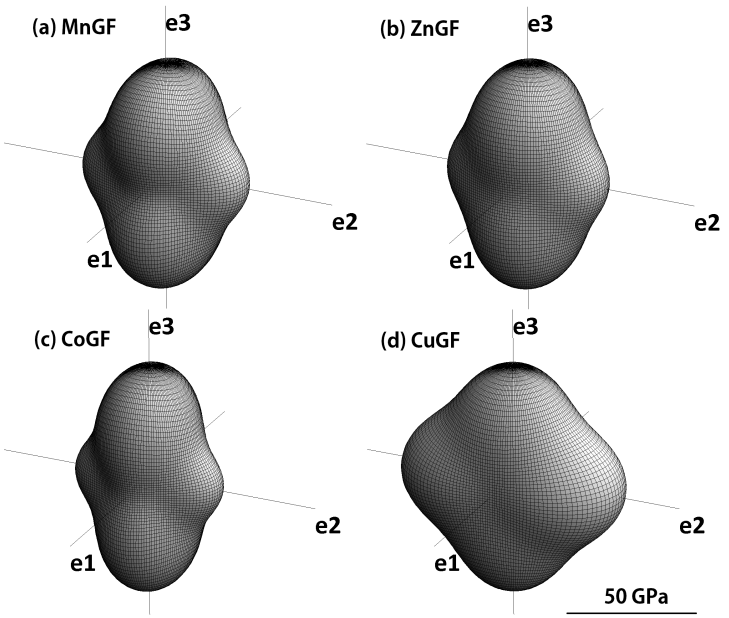

Figure 7.11: Representation surfaces of the longitudinal elastic stiffness for orthorhombic MGFs.

properties on the cationic substitution in these structures.
The studied MGFs exhibit a strong anisotropic behavior due to their crystal structure (Fig. 7.1). Along the c-axis the longitudinal elastic stiffness for Mn-, Zn- and CoGF is the largest and is the smallest along the a-axis (Fig. 7.11). In the direction of c-axis, the guanidinium cations that sit in the framework cavities are oriented with one N-O bond aligning exactly along the axis, and although the metal formate chains do not run along the axis but at an angle of 45° from c, the chains bend less than the those running along b, making them stronger against uniaxial pressure. The b-axis aligns with metal formate chains that bend significantly due to the distorted octaedra. Since none of the N-O bonds are exactly aligned with the axis, it is weaker against uniaxial stress than c. The a-axis is weakest because the metal formate chains run diagonal to the axis and none of the N-O bonds of the guanidinium cation align with the axis. CuGF has a similar behaviour, however due to the octahedra deformation caused by the fact that the $Cu_2{}^+$ cation is a JT ion, the N-O bonds are aligned along the b-axis, causing the b-axis to be substantially stiffer to uniaxial compression.
Additionally, the effect of cationic substitution on the elasticity of MOFs can be studied by considering the dependence of the aggregate elastic properties of these materials. Fig. 7.12 shows the dependence of the bulk (K_S)

and shear (G_S) moduli in the Voigt-Reuss-Hill formalism and of the acoustic velocities (v_P, v_S) of the studied MGFs, obtained from the preferred elastic tensor coefficients reported in Tab. 7.2, as a function of the unit cell volume. CoGF, ZnGF and MnGF are isostructural with space group $Pnna$. Zn and

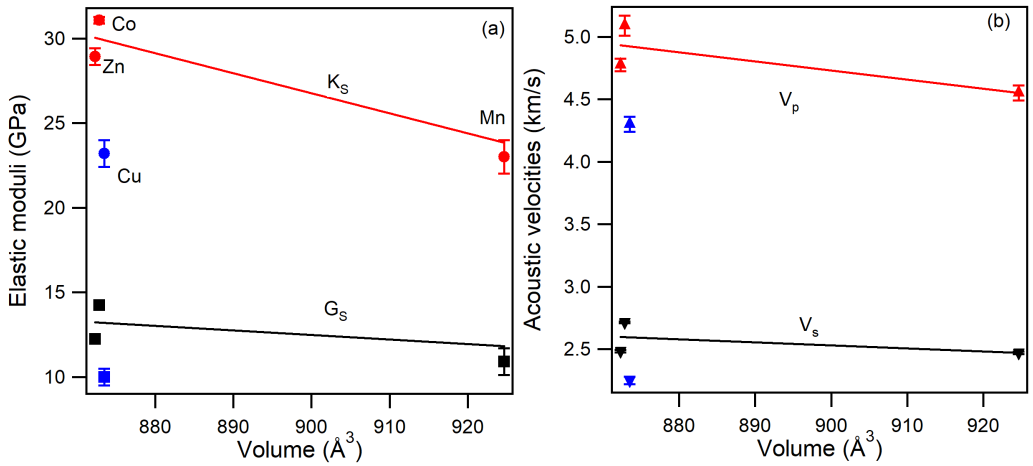

Figure 7.12: Bulk modulus in the VHR formalism, K_S, as a function of the unit cell volume. In blue are the data for CuGF.

Co have a similar cation size (the atomic radii of Zn and Co only differ by 1%) and have similar elastic moduli. MnGF is characterized by a larger volume but a much smaller density compared to ZnGF and CoGF. This results in a lower (-20%) value of the bulk modulus for MnGF compared to isostructural CoGF. CuGF has orthorhombic symmetry, but Cu^{2+} is a JT ion, and as such it causes a structural distortion of the ochtahedra, leading to a lower symmetry, space group $Pna2_1$. Due to this distortion, CuGF is more compressible compared to the other MOFs studied, with a bulk modulus 24% lower compared to that of ZnGF, but similar to that of MnGF.
Table 7.2 also reports the values of the universal anisotropy index A^u[189]. MGFs exhibit anisotropic behaviour, with A^u values in the range between 0.64 (ZnGF) and 0.96 (CoGF). The octahedra distortion in the CuGF does not have a great effect on the elastic anisotropy of the material.
In addition to the effect of composition on the aggregate moduli of metal guandinium formates it is interesting to study the linear axial compressibilities β_i of these compounds. A previous study by Yang et al. (2019) [262] studied the behaviour of MnGF, CoGF and CdGF at high pressured by DFT, single crystal XRD and powder neutron diffraction. The values obtained in their study for the axial compressibilities and bulk moduli are in agreement with our study (see Tab. 7.3). The four MGFs show substantial differences

Table 7.3: Axial compressibilities of the studied MOFs from DFT obtained in this study compared with the results of Yang et al. (2019) [262].

Compound	**ZnGF**	**MnGF**		**CuGF**	**CoGF**	
Reference	This work	This work	Yang [262]	This work	This work	Yang [262]
β_a (TPa^{-1})	22(4)	30(1)	26.7(4)	30(5)	20(1)	19.5(3)
β_b (TPa^{-1})	13(2)	17.3(5)	15.2(2)	5(4)	12.61(4)	11.4(2)
β_c (TPa^{-1})	1(4)	0.5(7)	0.03(2)	11(3)	2.3(5)	1.10(8)

in the linear compressibilitis along the crystallographic axes. In particular, MnGF shows a large compressibility along the a-axis while it is within the experimental error of zero along c-axis. This behaviour can be easily explained by considering the orientation of the guanidinium (Gua^+) ions, which keep the framework rigid within their plane, acting like struts, while preserving void spaces above and below this plane. In the orthorhombic MnGF structure, the c-axis is parallel to the plane of the Gua^+ ion, while a- and b-axes are angled away from the Gua^+ planes. This leads to a far greater linear compression along the a- and b-axes than along the c-axis [262].

7.6 Conclusions

In this chapter the elastic properties of orthorhombic MGFs ZnGF, MnGF, CoGF and CuGF are reported. The elastic tensor of MGFs obtained from different experimental and computational (DFT) methods are in good agreement, with the exception for the values of the C_{33} coefficient obtained from DFT calculations, which is (15%) larger compared to the experimental values. The results of this study provide the most complete determination of the elastic properties of MGFs at ambient conditions. The cationic substitution has a strong effect on the individual elastic tensor coefficients, C_{ij}, and on the aggregate elastic properties of MGFs. Larger M^{II} cations lead to a softening of the material in isostructural compounds. The cationic substitution with $M^{II} = Cu^{2+}$, a JT ion, causes a structural distortion which leads to a softer compound. Our results also confirm the almost-zero axial compressibility along the c-axis of MnGF, ZnGF observed in previous single crystal diffraction and neutron diffraction experimental study.

Summary and outlook

Within the overarching scope of my PhD work, I investigated the effect of chemical composition on the elastic properties of carbonates. The measurements were performed on both crystalline (natural and synthetic) and amorphous materials.

Well-characterized natural aragonite samples, covering the range of natural compositions, with Sr contents ranging from 0.3 to 1.5 mol% were investigated by Brillouin spectroscopy. My results, combined with the values obtained in a previous Brillouin study on a natural aragonite with 2.5 wt% [133], show a compositional trend in qualitative agreement with what observed in a high-pressure XRD study on synthetic $CaCO_3$-$SrCO_3$ solid solutions [222].

The elastic properties of Fe-dolomite and ankerite were first determined in this study. The combination of Brillouin spectroscopy and high pressure PXRD show a clear dependence of the elastic properties of Fe-dolomite and ankerite on composition, showing a non-linear behaviour of the bulk modulus with the Fe content, with a minimum ($\sim$-10%) around 40 mol% in the $CaFe(CO_3)_2$ component. The new high quality results set the reference for elasticity of these carbonate minerals.

The effect of cationic substitution of Ca with Sr in a calcite-structured $CaCO_3$ was studied by synchrotron SC-XRD on a sample synthesized at 2 GPa and 1300 K. The presence of 18% of Sr leads to structural modifications compared to pure calcite and at ambient conditions $Sr_{0.18}Ca_{0.82}CO_3$ adopts a calcite-II structure (monoclinic, space group $P2_1/c$), Sr-CC-II. The samples were studied at ambient conditions and at high pressures up to 9 GPa. At 1.7 GPa, a phase transformation from Sr-CC-II to a new polymorph, Sr-CC-III (monoclinic, space group $P2_1/m$) was observed. Sr-CC-III is different from any other pure $CaCO_3$ polymorph but shares some common features with the metastable $CaCO_3$-III polymorph, such as the non-coplanar CO_3 groups

and the presence of different coordination sites.

The elastic properties of amorphous calcium carbonate were investigated upon compression up to 20 GPa as a function of the water content. Three synthetic ACC samples, with different H_2O contents up to 18 wt%, were studied by Brillouin spectroscopy. No discontinuities were observed in the elastic properties of the samples independently on the water content, however the difference between the isothermal and isentropic bulk moduli, which increases with increasing pressure, seems to be indicative of a continuous evolution of the local structure upon compression. Our results also show that the addition of 18 wt% H_2O leads to a softening of -38% in the bulk modulus and -36% in the shear modulus of ACC.

The effect of composition on the elasticity of metal guanidinium formates, $C(NH_2)_3M^{II}(HCOO)_3$, with M^{II}=Mn, Co, Zn and Cu, was investigatedby combining the methods used for the study of the elasticity of carbonates with additional probes. The results obtained with the different techniques are in good agreement and show that cationic substitution has a strong effect on the individual elastic tensor coefficients, C_{ij}, and on the aggregate elastic properties of MGFs due to cationic substitution. Larger M^{II} cations lead to a softening of the material in isostructural compounds. In particular, the introduction of $M^{II} = Cu^{2+}$, a JT ion, causes a structural distortion which leads to a softer compound.

Appendix A

Aragonite

Electron microprobe image and results of the electron microprobe analysis EMPA performed on the aragonite samples used in this study.

Sample	CaO	FeO	SrO	BaO	Total
Arag-T	56.51(8)	-	0.12(6)	-	56.65(7)
Arag-NT	55.9(8)	-	0.4(1)	-	56.3(7)
Arag-S	53.51(7)	-	1.44(6)	-	55.0(1)

Table A.1: EMPA results for aragonite Arag-T, Arag-NT and Arag-S samples.

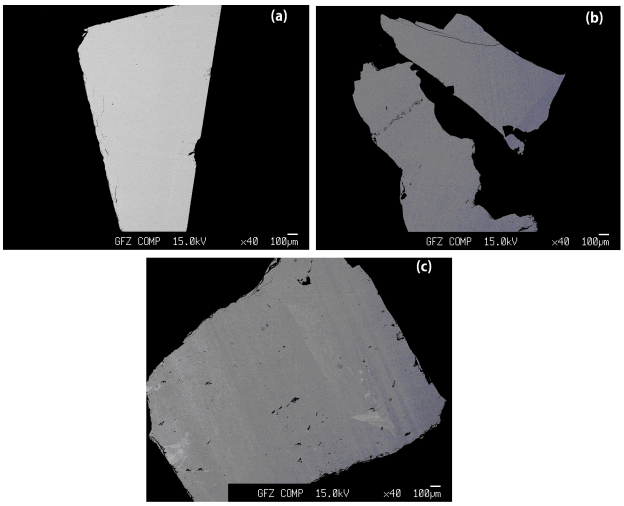

Figure A.1: EDX images for the aragonite samples studied: (a) Arag-T, (b) Arag-NT and (c) Arag-S.

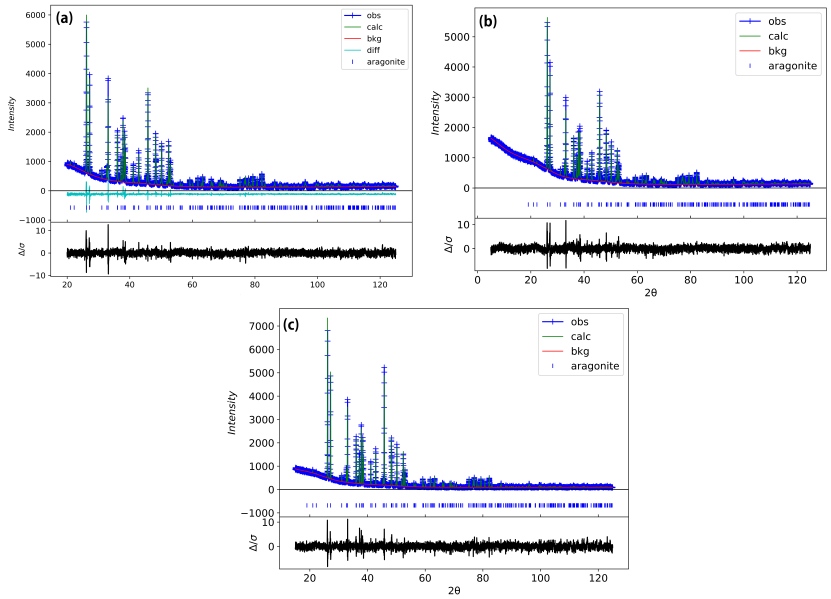

Figure A.2: Rietveld refinement of the powder sample of (a) Arag-T ($wR = 6.53$ %), (b) Arag-NT ($wR = 5.44\%$) and (c) Arag-S ($wR = 6.99\%$). Reflection positions are shown by blue tick marks and the residuals are shown in black.

Appendix B

SrCC

Table B.1: Refined atomic coordinates and isotropic displacement factors for Sr-CC-II at ambient conditions.

Atom	Element	x	y	z	$U_{eq/iso}$
Sr01	Sr	0.23963(4)	0.24700(6)	0.22746(5)	0.0186(2)
Ca01	Ca	0.23963(4)	0.24700(6)	0.22746(5)	0.0186(2)
O001	O	0.3856(2)	0.6470(5)	0.6353(2)	0.0350(8)
O002	O	0.1312(2)	0.5926(5)	0.3839(2)	0.0353(9)
O003	O	0.2357(3)	0.9984(5)	0.4792(2)	0.0353(9)
C001	C	0.2527(2)	0.7476(4)	0.4992(2)	0.0154(7)

Table B.2: Atomic distances for Sr-CC-II at ambient conditions.

Bond	Distance (Å)
Ca01-O001	2.384(1)
Ca01-O001	2.383(1)
Ca01-O002	2.375(1)
Ca01-O002	2.377(1)
Ca01-O003	2.384(3)
Ca01-O003	2.383(3)
<Ca-O>	2.381(5)
C-O001	1.260(3)
C-O002	1.283(3)
C-O003	1.269(2)
<C-O>	1.270(5)

Table B.3: Crystallographic information and details of the crystal structure refinement for the Sr-CC-II structure.

Phase	**Monoclinic**
Crystal system	Monoclinic
Space group	$P2_1/c$
a (Å)	6.4237(7)
b (Å)	5.0176(1)
c (Å)	8.1129(1)
α (°)	90
β (°)	108.064(1)
γ (°)	90
V (Å^3)	248.60(1)
ρ (g/cm^3)	3.007(1)
Z	4
F(000)	218
Theta range for data collection (°)	$1.97 - 17.69$
Index ranges	$-12 < h < 12$
	$-6 < k < 8$
	$-14 < l < 14$
Reflections collected	709
Goodness of fit on F^2	1.39
Num. parameters	48
Final R indices ($I > 3\sigma(I)$)	R_1 =0.0286, wR_2 =0.0594
Final R indices (all data)	R_1 =0.029, wR_2 =0.059
R_{int}	0.0676
Completeness to d = 0.8 Å	49.65

$R_{int} = \frac{\sum |F^2_{obs} - (F^2_{obs})_{mean}|}{\sum F^2_{obs}}$; $R_1 = \frac{\sum ||F_{obs}| - F_{calc}||}{\sum |F_{obs}|}$; $wR_2 = \left[\frac{\sum w\left(F^2_{obs} - F^2_{calc}\right)^2}{\sum wF^2_{obs}}\right]^{1/2}$,
$w = 1/\left[\sigma^2(F^2_{obs}) + (0.01 * P)^2\right]$, $P = (Max(F^2_{obs}, 0) + 2 * F^2_{calc})/3$

Table B.4: Crystallographic information and details of the crystal structure refinement for Sr-CC-III

Phase	**Sr-CC-III**
Pressure (GPa)	1.7(3)
Crystal system	Monoclinic
Space group	$P2_1/m$
a (Å)	6.2683(2)
b (Å)	9.922(5)
c (Å)	7.6574(6)
β (°)	103.856(6)
V (Å^3)	462.39(5)
ρ (g/cm^3)	3.217(3)
Z	8
F(000)	429
Theta range for data collection (°)	1.6-17.92
Index ranges	$-13 < h < 12$
	$-17 < k < 20$
	$-9 < l < 15$
Reflections collected	2164
Goodness of Fit on F^2	1.49
Num. parameters	100
R_1/wR_2 ($I > 3\sigma(I)$)	0.025/0.053
R_1/wR_2 (all)	0.033/0.057
R_{int}	0.0527
Completeness to d = 0.8 Å	67.06

$R_{int} = \frac{\sum |F^2_{obs} - (F^2_{obs})_{mean}|}{\sum F^2_{obs}}$; $R_1 = \frac{\sum ||F_{obs}| - F_{calc}||}{\sum |F_{obs}|}$; $wR_2 = \left[\frac{\sum w\left(F^2_{obs} - F^2_{calc}\right)^2}{\sum wF^2_{obs}}\right]^{1/2}$,
$w = 1/\left[\sigma^2(F^2_{obs}) + (0.01 * P)^2\right]$, $P = (Max(F^2_{obs}, 0) + 2 * F^2_{calc})/3$

Table B.5: Refined atomic coordinates and isotropic displacement factors for Sr-CC-III at P=1.72(5) GPa.

Atom	Element	x	y	z	$U_{eq/iso}$
Sr01	Sr	0.03975(3)	0.47602(2)	0.25445(3)	0.01470(7)
Ca01	Ca	0.03975(3)	0.47602(2)	0.25445(3)	0.01470(7)
Sr02	Sr	0.49006(4)	0.75	0.47063(5)	0.01475(9)
Ca02	Ca	0.49006(4)	0.75	0.47063(5)	0.01475(9)
Sr03	Sr	0.41737(4)	0.25	-0.01886(5)	0.01651(9)
Ca03	Ca	0.41737(4)	0.25	-0.01886(5)	0.01651(9)
O001	O	0.2539(2)	0.75	0.1609(4)	0.0368(8)
O002	O	-0.1028(2)	0.75	0.6166(2)	0.0159(4)
O003	O	0.6632(2)	0.4130(1)	0.1369(2)	0.0284(4)
O004	O	0.1265(1)	0.86168(9)	0.4865(2)	0.0165(3)
O005	O	0.6473(2)	0.5994(1)	0.2859(2)	0.0240(3)
O006	O	-0.0514(2)	0.6398(1)	0.0264(2)	0.0218(3)
O007	O	0.4170(2)	0.4257(2)	0.2957(3)	0.0345(5)
C001	C	0.0559(2)	0.75	0.0730(3)	0.0150(4)
C002	C	0.0466(2)	0.75	0.5281(3)	0.0119(4)
C003	C	0.5735(2)	0.4816(1)	0.2415(2)	0.0123(3)

Table B.6: Atomic distances for Sr-CC-III at 1.72(5) GPa.

Bond	Distance [Å]	Bond	Distance [Å]		
Sr01-O002	2.441(6)	Sr02-O001	2.477(3)	Ca03-O001	2.550(3)
Sr01-O003	2.390(1)	Sr02-O002	2.441(6)	Ca03-O003	2.352(1)
Sr01-O004	2.363(1)	Sr02-O004	2.563(1)	Ca03-O005	2.486(1)
Sr01-O004	2.701(1)	Sr02-O004	2.563(1)	Ca03-O005	2.486(1)
Sr01-O005	2.810(1)	Sr02-O005	2.423(1)	Ca03-O006	2.529(1)
Sr01-O006	2.353(1)	Sr02-O005	2.423(1)	Ca03-O006	2.529(1)
Sr01-O006	2.455(1)	Sr02-O007	2.466(1)	Ca03-O007	2.974(3)
Sr01-O007	2.363(1)	Sr02-O007	2.466(1)		
<Sr1-O>	2.486(7)	<Sr2-O>	2.491(3)	<Ca3-O>	2.558(5)
C01-O006	1.289(1)	C02-O002	1.281(2)	C03-O003	1.279(2)
C01-O006	1.289(1)	C02-O004	1.287(1)	C03-O005	1.274(2)
C01-O001	1.262(2)	C02-O004	1.287(1)	C03-O007	1.280(2)
		<C-O>	1.281(5)		

Appendix C

ACC

The structure of crystalline Ne is cubic FCC. The longitudinal and backscattered velocities of Ne were measured as a function of pressure up to ~ 5 GPa, as they are related to the Brillouin shifts $\Delta\nu^{Ne}$:

$$v_p^{Ne} = \Delta\nu_{60}^{Ne}\lambda \tag{C.1}$$

$$v_B^{Ne} = \frac{\Delta\nu_B^{Ne}\lambda}{2n} \tag{C.2}$$

where λ is the wavelength of the laser, n is the refractive index of the medium. At pressures lower than 4.6 GPa, because the liquid is acoustically isotropic, the sound velocity is the same for all directions. Fig. C.1, shows the measured longitudinal acoustic velocity as a function of pressure for Ne, with the literature data from a previous Brillouin study on Ne by Shimizu *et al.* [214].

From the measured v_p and v_B it is possible to determine the refractive index dependence on pressure. Fig. C.1 shows the values of the refractive index up to 4.6 GPa. The measured values are in good agreement with literature values from the Brillouin study by Shimizu *et al.* [214], as shown in Fig. C.1.

The density of amorphous calcium carbonate during compression can be estimated from the measured acoustic velocities by:

$$\rho(P) = \rho_0 + \int_{P_0}^{P} \frac{c}{v_B^2} dP \tag{C.3}$$

where, where $\rho(P)$ and ρ_0 are the density of the sample at pressure P and at the ambient pressure P_0 respectively, $c = C_P/C_V$ is the ratio of specific heats a constant pressure and volume and v_B is the bulk velocity.

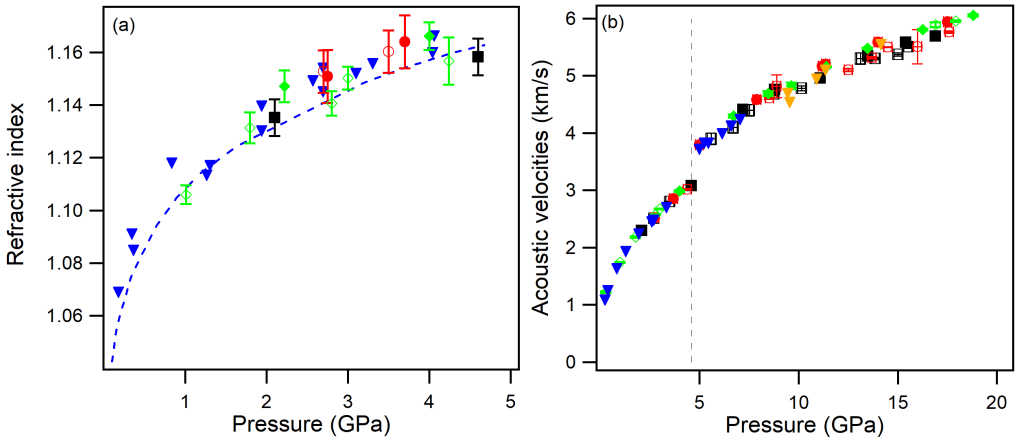

Figure C.1: Pressure dependence of the (a) the refractive index and (b) acoustic longitudinal velocities v_p for Ne. Black squares: ACC-I; Red circles: ACC-II; green diamonds: ACC-III; triangles: literature data from Shimizu et al. (2005) [214] (blue) and Wei et al. (2019) [246] (orange); dashed blue line in (a): literature data from Dewale et al. [61]; vertical dashed line (b) indicates the liquid solid phase transition at $P = 4.6$ GPa. Filled symbols: compression data; Open symbols: decompression data.

For elastically isotropic materials the bulk velocity v_B is given by:

$$v_B^2 = v_p^2 - \frac{4}{3}v_s^2 \tag{C.4}$$

where v_p and v_s are the longitudinal and transverse acoustic velocities, respectively.

The density of ACC at ambient pressure used in this study is the value measured for an hydrous ACC sample by Fernandez-Martinez *et al.* [70] at ambient conditions, $\rho_0 = 2.17$ g/cm^3.
The ratio of specific heats follows:

$$\frac{C_P}{C_V} = \frac{K_S}{K_T} = 1 + \gamma_{th}\alpha T \tag{C.5}$$

where K_S is the isentropic (adiabatic) bulk modulus, K_T is the isothermal bulk modulus, α is the thermal expansion coefficient, γ_{th} is the Grüneisen parameter and T is the temperature. For values of γ_{th} and α typical of a wide range of minerals, the difference between K_S and K_T is in the order of 1% and the value of the ratio c is close to 1 [186]. For crystalline aragonite, the values of the Grüneisen paramenter and thermal expansion coefficient at ambient

conditions are $\gamma_{th} = 1.39$ and $\alpha = 5.8(2) \times 10^{-5}$ K^{-1} [126], corresponding to a value of $c = 1.02$.

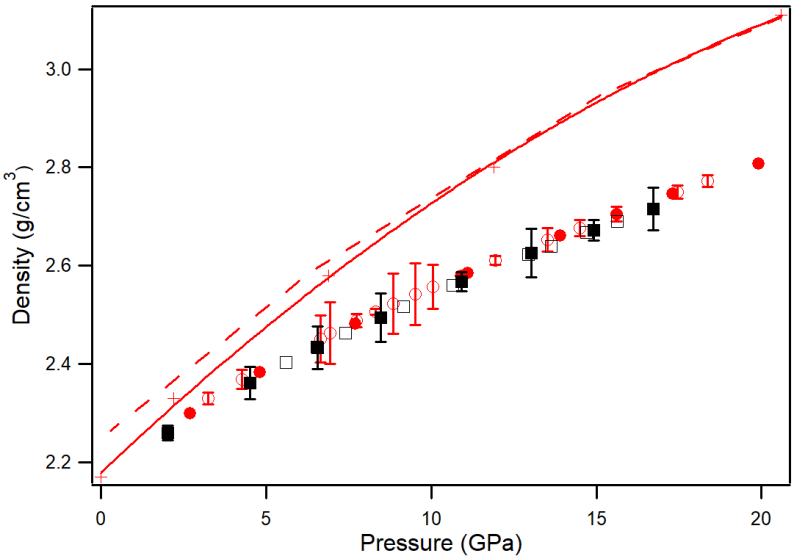

Figure C.2: Density of ACC-I (black) and ACC-II (red) from the Brillouin spectroscopy acoustic velocities measured during compression (filled symbols) and decompression (open symbols) using the ambient pressure of ACC measured by Fernandez-Martinez *et al.* [70]. The red curve represents the density data measured by Fernandez-Martinez *et al.* [70] in compression (red line) and decompression (dashed line).

Fig. C.2 shows the values of density at high pressures estimated for samples ACC-I and ACC-II in this Brillouin spectroscopy study. The red line represents the density values measured by Fernandez-Martinez *et al.* [70] using a combination of X-ray diffraction and absorption measurements. Unfortunately, it was not possible to obtain the density as a function of pressure for sample ACC-III because of the missing signal for the transverse velocity for this sample at ambient conditions. It is evident from Fig. C.2 that the density values from Fernandez-Martinez *et al.* [70] are considerably higher compared to the ones obtained from our Brillouin spectroscopy measurements (9 % higher for ACC-I at 16.7 GPa). Petitgirard *et al.* [180] observed a similar inconsistency between the densities of amorphous $MgSiO_3$ at high pressures from X-ray absorption measurements and those estimated from Brillouin spectroscopy [201] using the same approach as the one used for samples ACC-I and ACC-II in this study. The contrast between X-ray and Brillouin measurements is due to the fact that the values for isothermal

and isentropic bulk moduli of ACC are different and diverge with increasing pressure, as discussed in the main text.

This results in the densities' values of the material obtained from the measured acoustic velocities to be underestimated.

Appendix D

Ankerite

Electron microprobe image and results of the electron microprobe analysis EMPA performed on the ankerite samples used in this study. Dolomite (Dol), siderite (Sid) and calcite (Cal) where used as standards. The compositions reported in Tab. D.1 are the result of an average of 6 to 12 measurements for each phase.

Sample		MgO	FeO	CaO	MnO	Total
Ank-1		21.9(3)	2.1(2)	29.59(5)	0.12(3)	53.84(5)
Ank-2		11.3(4)	14.7(4)	28.2(2)	2.2(2)	56.36
Ank-4		16.6(9)	9(1)	29.0(3)	1.1(1)	55.50
Ank-5		6(2)	22(2)	26.9(5)	1.7(1)	56.95
Standards	Dol	22.20	0.11	30.53	0.04	52.87
	Sid	0.12	59.06	-	2.80	61.98
	Cal	-	0.04	54.84	0.11	54.99

Table D.1: EMPA results of the ankerite Ank-1, Ank-2, Ank4 and Ank-5 samples.

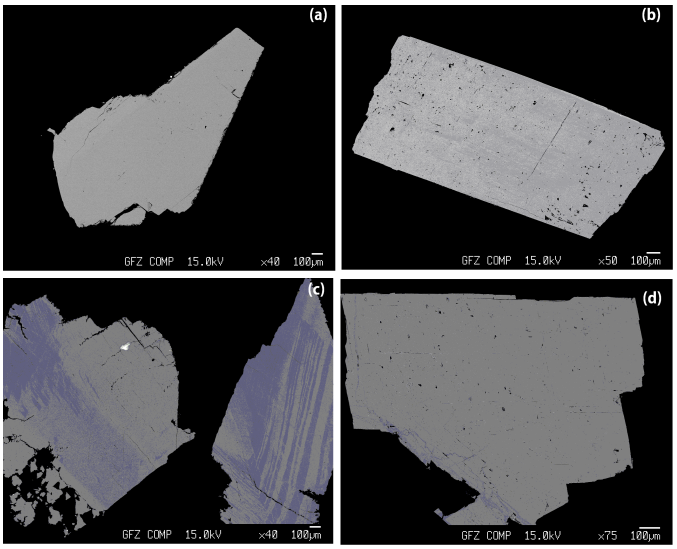

Figure D.1: EDX images for the ankerite samples studied: (a) Ank-1, (b) Ank-2, (c) Ank-4 and (d) Ank-5.

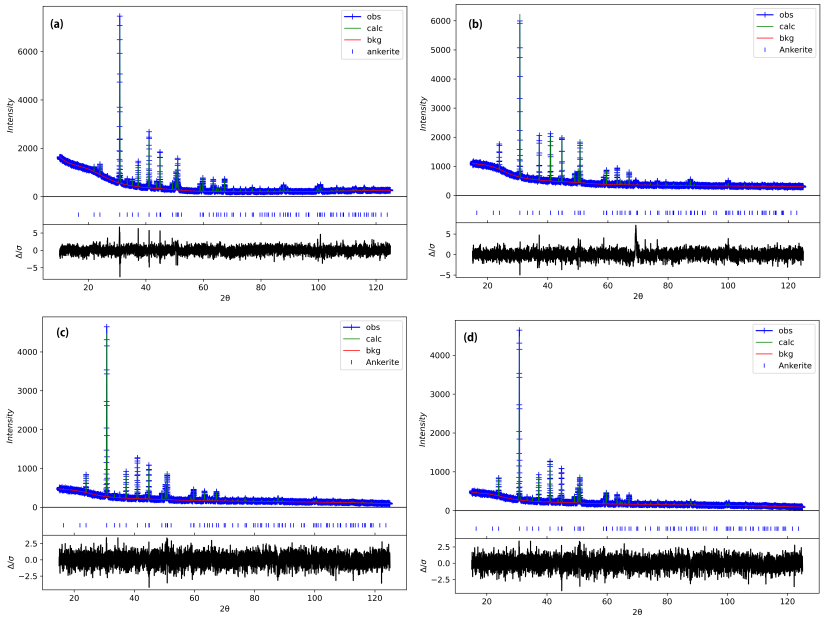

Figure D.2: Rietveld refinement of ankerite Ank-1 ($wR = 4.463\%$) (a), Ank-2 ($wR = 4.33\%$) (b), Ank-4 ($wR = 5.99\%$) (c) and Ank-5 ($wR = 4.93\%$) (d). Reflection positions are shown by the blue tick marks and the residuals are shown in black.

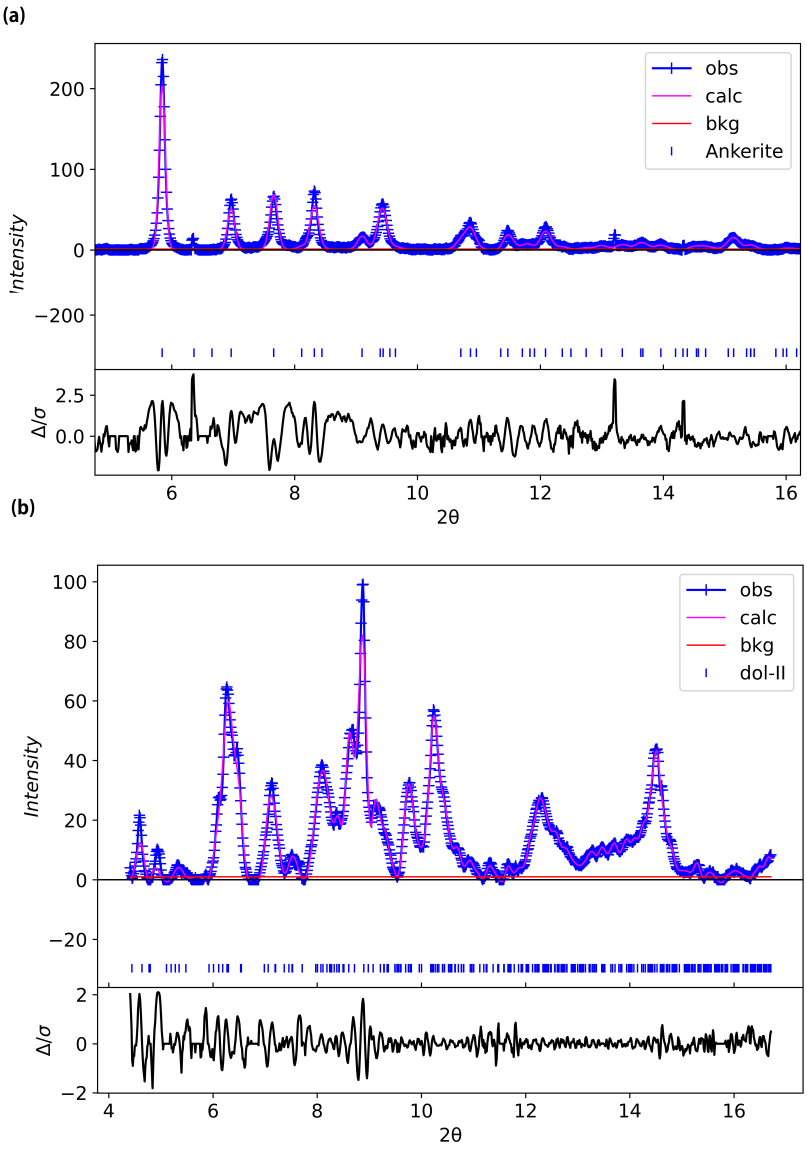

Figure D.3: Pawley refinement of (a) Ank-2 (Dol-I) at 4.6 GPa ($wR = 16\%$); (b) Ank-4 (Dol-II) phase at 33.3 GPa ($wR = 12.6\%$).

Table D.2: Elastic tensor coefficients for Ank-1, Ank-2 and Ank-5 and experimental data from Speziale et al. (*unpublished material*), Chen et al. (2006) [46] and Humbert et al. (1972) [95], together with calculations for dolomite samples (DFT, this work), Bakri et al. (2011) [12] and Titiloye et al. (1998) [233].

	Experimental					DFT		
	Spez. [223]	This work			Chen [46]	Humbert [95]	This work	Bakri [12]	Titiloye [233]
		Ank-1	Ank-2	Ank-5					
C_{11} (GPa)	206 (1)	204.2(8)	184.1(7)	171(1)	204(2)	205	186(1)	196.6	201.6
C_{12} (GPa)	69(2)	71.7(6)	79(1)	76.0(6)	69(3)	71	62.3(5)	64.6	71.0
C_{13} (GPa)	59(2)	57.0(6)		59(1)	46(4)	57.4	50.5(5)	54.71	57.4
C_{14} (GPa)	-21(2)	-20.8(4)	-20(78)	-16(9)	20(1)	-19.5	15.28(7)	22.45	-19.5
C_{15} (GPa)	10(3)	10.7(8)		12.4(2)	7(2)	13.7	-10(3)	-1.35	13.7
C_{33} (GPa)	115 (1)	112.0(3)		95(5)	97(5)	112.8	102.8(3)	110.01	113.0
C_{44} (GPa)	40.5(4)	40.0(5)	39.4(5)	35.4(3)	39(2)	39.8	37.1(3)	41.57	39.8
C_{66}(GPa)	69(2)	66.2(6)	52(1)	47(1)			62(1)		
K_S(GPa)	96(6)	94(2)		87(5)	85(9)	95(6)	85(5)	90(6)	94(6)
G_S(GPa)	47(7)	46(2)		36(5)	46(8)	47(7)	44(5)	46(7)	46(7)
A^u	1.34	1.37		1.2			1.01		

Appendix E

MOFs

Table E.1: Elastic tensor coefficients of CuGF using standard (DFT-) and dispersion corrected (DFT-d) and without dispersion correction (DFT) for CuGF.

	CuGF	
Technique	**DFT**	**DFT-d**
C_{11} (GPa)	25.3(7)	19.3(4)
C_{12} (GPa)	9.0(5)	14.8(6)
C_{13} (GPa)	8.1(5)	11(1)
C_{22} (GPa)	49.8(7)	60.5(1)
C_{23} (GPa)	13.3(8)	14.1(6)
C_{33} (GPa)	49(2)	47(2)
C_{44} (GPa)	9.0(5)	9.1(6)
C_{55} (GPa)	8.4(2)	9.8(5)
C_{66} (GPa)	7.3(5)	7.7(2)

Table E.2: Elastic tensor coefficients, bulk modulus K_S, shear modulus G_S and acoustic velocities for the orthorhombic MOFs studied from DFT and experimental methods.PPPW = plane parallel plate wave ultrasound technique, RUS = resonant ultrasound spectroscopy, BS = Brillouin spectroscopy, DFT = density functional theory.

MGF	**ZnGF**				**MnGF**			**CuGF**			**CoGF**
Method	**DFT**	**PPPW**	**RUS**	**BS**	**DFT**	**BS**	**TDS**	**DFT**	**RUS**	**PPPW**	**DFT**
C_{11} (GPa)	34.5(6)	34.0(3)	34.90(5)	36.3(4)	27.8(5)	30.7(6)	27.5(5)	25.3(7)	25.5(1)	25.6(1)	39.0(8)
C_{12} (GPa)	13.3(5)		15.2(3)	13.5(9)	9.2(2)	6.5(7)	5.8(5)	14.8(6)	18.4(2)	20.1(5)	12.7(3)
C_{13} (GPa)	27.4(6)		28.6(8)	30(1)	23.4(3)	26.9(4)	18.1(5)	11(1)	12.0(2)	13.6(5)	29.6(4)
C_{22} (GPa)	48.6(7)	49.2(5)	50.9(5)	49.1(4)	41.4(6)	44.8(1)	49.3(5)	60.5(1)	52.5(6)	47.9(5)	56.2(3)
C_{23} (GPa)	21.0(5)		22.5(3)	21(1)	15.3(3)	13.9(9)	8.1(5)	14.1(6)	17.2(2)	17.0(3)	17.1(6)
C_{33} (GPa)	81(2)	69.5(3)	69.5(7)	69(5)	75(1)	59.7(2)	54.1(5)	47(2)	53.7(1)	52.8(5)	86.1(4)
C_{44} (GPa)	9.8(4)	7.7(3)	8.42(7)	9.1(4)	8.8(1)	7.3(1)	9.6(5)	9.1(6)	7.88(4)	8.05(6)	10.9(4)
C_{55} (GPa)	11.0(4)	10.5(2)	10.80(5)	11.5(4)	12.9(2)	11.6(1)	10.9(5)	9.8(5)	9.61(4)	8.78(6)	15.2(3)
C_{66} (GPa)	10.4(2)	10.2(2)	10.27(5)	10.4(2)	9.5(1)	7.2(1)	10.0(5)	7.7(2)	8.78(4)	9.12(6)	9.82(8)

Bibliography

[1] Lia Addadi, Sefi Raz, and Steve Weiner. Taking advantage of disorder: amorphous calcium carbonate and its roles in biomineralization. *Advanced Materials*, 15(12):959–970, 2003.

[2] Muhtar Ahart, Jeffery L Yarger, Kristina M Lantzky, Satoshi Nakano, Ho-kwang Mao, and Russell J Hemley. High-pressure Brillouin scattering of amorphous BeH_2. *The Journal of chemical physics*, 124(1):014502, 2006.

[3] MW Anderson, SM Lindsay, and RT Harley. Quasielastic light scattering in silicon. *Journal of Physics C: Solid State Physics*, 17(36):6877, 1984.

[4] Orson L Anderson, Orson L Anderson, et al. *Equations of state of solids for geophysics and ceramic science*. Number 31. Oxford University Press on Demand, 1995.

[5] RJ Angel, RT Downs, and LW Finger. High-pressure and high-temperature crystal chemistry. *Reviews in Mineralogy and Geochemistry*, 41:35–59, 2000.

[6] Ross J Angel. Equations of state. *Reviews in mineralogy and geochemistry*, 41(1):35–59, 2000.

[7] Ross J. Angel, Matteo Alvaro, and Javier Gonzalez-Platas. Eosfit7c and a fortran module (library) for equation of state calculations. *Zeitschrift für Kristallographie - Crystalline Materials*, 229(5):405–419, 2014.

[8] Ross J Angel, Jennifer M Jackson, Hans J Reichmann, and Sergio Speziale. Elasticity measurements on minerals: a review. *European Journal of Mineralogy*, 21(3):525–550, 2009.

[9] Sytle M Antao and Ishmael Hassan. The orthorhombic structure of $CaCO_3$, $SrCO_3$, $PbCO_3$ and $BaCO_3$: Linear structural trends. *The Canadian Mineralogist*, 47(5):1245–1255, 2009.

[10] Sytle M Antao, Ishmael Hassan, Willem H Mulder, Peter L Lee, and Brian H Toby. In situ study of the R-3c to R-3m orientational disorder in calcite. *Physics and Chemistry of Minerals*, 36(3):159–169, 2009.

[11] Dirk Arbeck, Eiken Haussühl, Victor L Vinograd, Bjoern Winkler, Natalia Paulsen, Siegfried Haussuehl, Victor Milman, and Julian D Gale. Elastic stiffness coefficients of thenardite and their pressure and temperature dependence. *Zeitschrift für Kristallographie-Crystalline Materials*, 227(8):503–513, 2012.

[12] Z Bakri and A Zaoui. Structural and mechanical properties of dolomite rock under high pressure conditions: A first-principles study. *physica status solidi (b)*, 248(8):1894–1900, 2011.

[13] L Bayarjargal, C-J Fruhner, N Schrodt, and B Winkler. $CaCO_3$ phase diagram studied with raman spectroscopy at pressures up to 50 GPa and high temperatures and DFT modeling. *Physics of the Earth and Planetary Interiors*, 281:31–45, 2018.

[14] Nicole Biedermann, Elena Bykova, Wolfgang Morgenroth, Ilias Efthimiopoulos, Jan Mueller, Georg Spiekermann, Konstantin Glazyrin, Anna Pakhomova, Karen Appel, and Max Wilke. Equation of state and high-pressure phase behaviour of $SrCO_3$. *European Journal of Mineralogy*, 32(6):575–586, 2020.

[15] Nicole Biedermann, Sergio Speziale, Björn Winkler, Hans Josef Reichmann, Monika Koch-Müller, and Gerhard Heide. High-pressure phase behavior of SrCO 3: an experimental and computational Raman scattering study. *Physics and Chemistry of Minerals*, 44(5):335–343, 2017.

[16] Nicole Biedermann, B Winkler, S Speziale, Hans-Josef Reichmann, and M Koch-Müller. Single-crystal elasticity of $SrCO_3$ by Brillouin spectroscopy. *High Pressure Research*, 37(2):181–192, 2017.

[17] Jannes Binck, Lkhamsuren Bayarjargal, Sergey S Lobanov, Wolfgang Morgenroth, Rita Luchitskaia, Chris J Pickard, Victor Milman, Keith Refson, Dominik B Jochym, Peter Byrne, et al. Phase stabilities of $MgCO_3$ and $MgCO_3$-II studied by raman spectroscopy, x-ray diffraction, and density functional theory calculations. *Physical Review Materials*, 4(5):055001, 2020.

[18] Jannes Binck, Stella Chariton, Michal Stekiel, Lkhamsuren Bayarjargal, Wolfgang Morgenroth, Victor Milman, Leonid Dubrovinsky, and

Björn Winkler. High-pressure, high-temperature phase stability of iron-poor dolomite and the structures of dolomite-IIIc and dolomite-V. *Physics of the Earth and Planetary Interiors*, 299:106403, 2020.

[19] Francis Birch. Finite elastic strain of cubic crystals. *Physical review*, 71(11):809, 1947.

[20] Peter E Blöchl. Projector augmented-wave method. *Physical review B*, 50(24):17953, 1994.

[21] Reinhard Boehler. New diamond cell for single-crystal X-ray diffraction. *Review of Scientific Instruments*, 77(11):115103, 2006.

[22] Max Born, Kun Huang, and M Lax. Dynamical theory of crystal lattices. *American Journal of Physics*, 23(7):474–474, 1955.

[23] E Boulard, N Menguy, Anne-Line Auzende, K Benzerara, H Bureau, D Antonangeli, A Corgne, Guillaume Morard, J Siebert, Jean-Philippe Perrillat, et al. Experimental investigation of the stability of Fe-rich carbonates in the lower mantle. *Journal of Geophysical Research: Solid Earth*, 117(B2), 2012.

[24] Eglantine Boulard, Alexandre Gloter, Alexandre Corgne, Daniele Antonangeli, Anne-Line Auzende, Jean-Philippe Perrillat, François Guyot, and Guillaume Fiquet. New host for carbon in the deep Earth. *Proceedings of the National Academy of Sciences*, 108(13):5184–5187, 2011.

[25] Eglantine Boulard, Alexander F Goncharov, Marc Blanchard, and Wendy L. Mao. Pressure-induced phase transition in $MnCO_3$ and its implications on the deep carbon cycle. *Journal of Geophysical Research: Solid Earth*, 120(6):4069–4079, 2015.

[26] Eglantine Boulard, Ding Pan, Giulia Galli, Zhenxian Liu, and Wendy L Mao. Tetrahedrally coordinated carbonates in Earth's lower mantle. *Nature communications*, 6:6311, 2015.

[27] Frank E Brenker, Christian Vollmer, Laszlo Vincze, Bart Vekemans, Anja Szymanski, Koen Janssens, Imre Szaloki, Lutz Nasdala, Werner Joswig, and Felix Kaminsky. Carbonates from the lower part of transition zone or even the lower mantle. *Earth and Planetary Science Letters*, 260(1-2):1–9, 2007.

[28] Benjamin P Burton and A Van de Walle. First-principles-based calculations of the $CaCO_3$-$MgCO_3$ and $CdCO_3$-$MgCO_3$ subsolidus phase diagrams. *Physics and chemistry of minerals*, 30(2):88–97, 2003.

[29] Julia Büscher, Alessandro Mirone, Michał Stękiel, Dominik Spahr, Wolfgang Morgenroth, Eiken Haussühl, Victor Milman, Alexei Bosak, Oleh Ivashko, M von Zimmermann, et al. Elastic stiffness coefficients of thiourea from thermal diffuse scattering. *Journal of Applied Crystallography*, 54(1):287–294, 2021.

[30] Elena Bykova. *Single-crystal X-ray diffraction at extreme conditions in mineral physics and material sciences*. PhD thesis, 2015.

[31] Bram Cantaert, David Kuo, Shunichi Matsumura, Tatsuya Nishimura, Takeshi Sakamoto, and Takashi Kato. Use of amorphous calcium carbonate for the design of new materials. *ChemPlusChem*, 82(1):107–120, 2017.

[32] William D Carlson. The calcite–aragonite equilibrium: effects of sr substitution and anion orientational disorder. *American Mineralogist*, 65(11-12):1252–1262, 1980.

[33] Julyan HE Cartwright, Antonio G Checa, Julian D Gale, Denis Gebauer, and C Ignacio Sainz-Díaz. Calcium carbonate polyamorphism and its role in biomineralization: how many amorphous calcium carbonates are there? *Angewandte Chemie International Edition*, 51(48):11960–11970, 2012.

[34] William H Casey, Liang Chal, Alexandra Navrotsky, and Peter A Rock. Thermochemistry of mixing strontianite [$SrCO_3$(s)] and aragonite [$CaCO_3$(s)] to form $Ca_xSr_{1-x}CO_3$ (s) solid solutions. *Geochimica et Cosmochimica Acta*, 60(6):933–940, 1996.

[35] B Castagnede, AG Every, and W Sachse. Numerical simulation of the instabilities associated to the recovery of elastic constants of anisotropic solids from quasi-longitudinal velocities alone. *Comptes rendus de l'Académie des sciences. Série 2, Mécanique, Physique, Chimie, Sciences de l'univers, Sciences de la Terre*, 314(9):865–871, 1992.

[36] Valerio Cerantola, Elena Bykova, Ilya Kupenko, Marco Merlini, Leyla Ismailova, Catherine McCammon, Maxim Bykov, Alexandr I Chumakov, Sylvain Petitgirard, Innokenty Kantor, et al. Stability of iron-bearing carbonates in the deep Earth's interior. *Nature Communications*, 8(1):1–9, 2017.

[37] G Chahi, D Bradai, and I Belabbas. Structural and elastic properties of $CaCO_3$ hydrated phases: A dispersion-corrected density functional

theory study. *Journal of Physics and Chemistry of Solids*, 138:109295, 2020.

[38] G. Chahi, D. Bradai, and I. Belabbas. Structural and elastic properties of $CaCO_3$ hydrated phases: A dispersion-corrected density functional theory study. *Journal of Physics and Chemistry of Solids*, 138:109295, 2020.

[39] L Chai and A Navrotsky. Synthesis, characterization, and energetics of solid solution along the dolomite-ankerite join, and implications for the stability of ordered $CaFe(CO_3)_2$. *American Mineralogist*, 81(9-10):1141–1147, 1996.

[40] Anton R Chakhmouradian, Ekaterina P Reguir, and Anatoly N Zaitsev. Calcite and dolomite in intrusive carbonatites. I. Textural variations. *Mineralogy and Petrology*, 110(2-3):333–360, 2016.

[41] Luke LY Chang. Subsolidus phase relations in the systems $BaCO_3$-$SrCO_3$, $SrCO_3$-$CaCO_3$, and $BaCO_3$-$CaCO_3$. *The Journal of Geology*, 73(2):346–368, 1965.

[42] Luke LY Chang. Subsolidus Phase Relations in the Aragonite-Type Carbonates: I. The System $CaCO_3$-$SrCO_3$-$BaCO_3$. *American Mineralogist: Journal of Earth and Planetary Materials*, 56(9-10):1660–1673, 1971.

[43] Stella Chariton, Maxim Bykov, Elena Bykova, Egor Koemets, Timofey Fedotenko, Björn Winkler, Michael Hanfland, Vitali B Prakapenka, Eran Greenberg, Catherine McCammon, et al. The crystal structures of Fe-bearing $MgCO_3$ sp^2-and sp^3-carbonates at 98 GPa from single-crystal X-ray diffraction using synchrotron radiation. *Acta Crystallographica Section E: Crystallographic Communications*, 76(5):715–719, 2020.

[44] Stella Chariton, Catherine McCammon, Denis M Vasiukov, Michal Stekiel, Anastasia Kantor, Valerio Cerantola, Ilya Kupenko, Timofey Fedotenko, Egor Koemets, Michael Hanfland, et al. Seismic detectability of carbonates in the deep earth: A nuclear inelastic scattering study. *American Mineralogist: Journal of Earth and Planetary Materials*, 105(3):325–332, 2020.

[45] Chien-Chih Chen, Chung-Cherng Lin, Lin-Gun Liu, Stanislav V Sinogeikin, and Jay D Bass. Elasticity of single-crystal calcite and

rhodochrosite by brillouin spectroscopy. *American Mineralogist*, 86(11-12):1525–1529, 2001.

[46] Po-Fei Chen, Ling-Yun Chiao, Pao-hsien Huang, Yi-jong Yang, and Lin-gun Liu. Elasticity of magnesite and dolomite from a genetic algorithm for inverting brillouin spectroscopy measurements. *Physics of the Earth and Planetary Interiors*, 155(1-2):73–86, 2006.

[47] Andrew G Christy. A review of the structures of vaterite: the impossible, the possible, and the likely. *Crystal Growth & Design*, 17(6):3567–3578, 2017.

[48] Raquel Chuliá-Jordán, David Santamaria-Perez, Javier Ruiz-Fuertes, Alberto Otero-de-la Roza, and Catalin Popescu. Compressibility and phase stability of iron-rich ankerite. *Minerals*, 11(6):607, 2021.

[49] Stewart J Clark, Matthew D Segall, Chris J Pickard, Phil J Hasnip, Matt IJ Probert, Keith Refson, and Mike C Payne. First principles methods using CASTEP. *Zeitschrift für Kristallographie-Crystalline Materials*, 220(5/6):567–570, 2005.

[50] Ines E Collings, Joshua A Hill, Andrew B Cairns, Richard I Cooper, Amber L Thompson, Julia E Parker, Chiu C Tang, and Andrew L Goodwin. Compositional dependence of anomalous thermal expansion in perovskite-like ABX_3 formates. *Dalton Transactions*, 45(10):4169–4178, 2016.

[51] Nathan C Collins, Gray E Bebout, Samuel Angiboust, Philippe Agard, Marco Scambelluri, Laura Crispini, and Timm John. Subduction zone metamorphic pathway for deep carbon cycling: II. Evidence from HP/UHP metabasaltic rocks and ophicarbonates. *Chemical Geology*, 412:132–150, 2015.

[52] Eugenio Coronado, Jose R Galan-Mascaros, Carlos J Gomez-Garcia, and Vladimir Laukhin. Coexistence of ferromagnetism and metallic conductivity in a molecule-based layered compound. *Nature*, 408(6811):447–449, 2000.

[53] PRO CrysAlis. Rigaku Oxford Diffraction: Yarnton, 2018.

[54] HZ Cummins and PE Schoen. Laser handbook, 1972.

[55] Dattatraya P Dandekar. Elastic constants of calcite. *Journal of Applied Physics*, 39(6):2971–2973, 1968.

[56] Dattatraya P Dandekar. Variation in the elastic constants of calcite with temperature. *Journal of Applied Physics*, 39(8):3694–3699, 1968.

[57] Rajdeep Dasgupta, Antonio Buono, Geoff Whelan, and David Walker. High-pressure melting relations in Fe–C–S systems: Implications for formation, evolution, and structure of metallic cores in planetary bodies. *Geochimica et Cosmochimica Acta*, 73(21):6678–6691, 2009.

[58] Rajdeep Dasgupta and Marc M Hirschmann. Melting in the Earth's deep upper mantle caused by carbon dioxide. *Nature*, 440(7084):659–662, 2006.

[59] Rajdeep Dasgupta and Marc M Hirschmann. The deep carbon cycle and melting in Earth's interior. *Earth and Planetary Science Letters*, 298(1-2):1–13, 2010.

[60] Paula M Davidson, Gregory H Symmes, Barbara A Cohen, Richard J Reeder, and Donald H Lindsley. Synthesis of the new compound cafe (co3) 2 and experimental constraints on the (ca, fe) co3 join. *Geochimica et Cosmochimica Acta*, 57(23-24):5105–5109, 1993.

[61] Agnès Dewaele, Marc Torrent, Paul Loubeyre, and Mohamed Mezouar. Compression curves of transition metals in the Mbar range: Experiments and projector augmented-wave calculations. *Physical Review B*, 78(10):104102, 2008.

[62] Martin T Dove and Martin T Dove. *Introduction to lattice dynamics*. Number 4. Cambridge university press, 1993.

[63] VB Dudnikova, VS Urusov, and NN Eremin. Simulation of the local structure, mixing properties, and stability of $ca_xsr_{1-x}CO_3$ solid solutions by the interatomic potential method. *Physics of the Solid State*, 57(6):1108–1113, 2015.

[64] DJ Dunstan. Theory of the gasket in diamond anvil high-pressure cells. *Review of scientific instruments*, 60(12):3789–3795, 1989.

[65] I Efthimiopoulos, S Jahn, A Kuras, U Schade, and M Koch-Müller. Combined high-pressure and high-temperature vibrational studies of dolomite: Phase diagram and evidence of a new distorted modification. *Physics and Chemistry of Minerals*, 44(7):465–476, 2017.

[66] AG Every. General closed-form expressions for acoustic waves in elastically anisotropic solids. *Physical Review B*, 22(4):1746, 1980.

[67] Michael Faatz, Wei Cheng, Gerhard Wegner, George Fytas, Raluca S Penciu, and Eleftherios N Economou. Mechanical strength of amorphous $CaCO_3$ colloidal spheres. *Langmuir*, 21(15):6666–6668, 2005.

[68] Michael Faatz, Franziska Gröhn, and Gerhard Wegner. Amorphous calcium carbonate: synthesis and potential intermediate in biomineralization. *Advanced Materials*, 16(12):996–1000, 2004.

[69] AR Faiziev, F Sh Iskandarov, and FG Gafurov. Mineralogical and petrogenetic characteristics of carbonatites of the Dunkeldykskii alkalic massif (eastern Pamirs). *Zapiski Vserossiiskogo Mineralogicheskogo Obshchestva*, 127(3):54–57, 1998.

[70] Alejandro Fernandez-Martinez, Bora Kalkan, Simon M Clark, and Glenn A Waychunas. Pressure-induced polyamorphism and formation of 'aragonitic' amorphous calcium carbonate. *Angewandte Chemie*, 125(32):8512–8515, 2013.

[71] Guillaume Fiquet, François Guyot, Martin Kunz, Jan Matas, Denis Andrault, and Michael Hanfland. Structural refinements of magnesite at very high pressure. *American Mineralogist*, 87(8-9):1261–1265, 2002.

[72] Rebecca A Fischer, Elizabeth Cottrell, Erik Hauri, Kanani KM Lee, and Marion Le Voyer. The carbon content of Earth and its core. *Proceedings of the National Academy of Sciences*, 117(16):8743–8749, 2020.

[73] Chris-Julian Fruhner, Lkhamsuren Bayarjargal, Nadine Schrodt, Rita Luchitskaia, Wolfgang Morgenroth, and Björn Winkler. Pressure-induced phase transition from calcite to aragonite detected by fluorescence spectroscopy. *European Journal of Mineralogy*, 30(4):711–720, 2018.

[74] Suyu Fu, Jing Yang, and Jung-Fu Lin. Abnormal elasticity of single-crystal magnesiosiderite across the spin transition in earth's lower mantle. *Physical review letters*, 118(3):036402, 2017.

[75] Pavel N Gavryushkin, Naira S Martirosyan, Talgat M Inerbaev, Zakhar I Popov, Sergey V Rashchenko, Anna Yu Likhacheva, Sergey S Lobanov, Alexander F Goncharov, Vitali B Prakapenka, and Konstantin D Litasov. Aragonite-II and $CaCO_3$-VII: New high-pressure, high-temperature polymorphs of $CaCO_3$. *Crystal Growth & Design*, 17(12):6291–6296, 2017.

[76] Pavel N Gavryushkin, Nursultan Sagatov, Anatoly B Belonoshko, Maksim V Banaev, and Konstantin D Litasov. Disordered aragonite: The new high-pressure, high-temperature phase of $CaCO_3$. *The Journal of Physical Chemistry C*, 124(48):26467–26473, 2020.

[77] Denis Gebauer, Philips N Gunawidjaja, JY Peter Ko, Zoltan Bacsik, Baroz Aziz, Lijia Liu, Yongfeng Hu, Lennart Bergström, Cheuk-Wai Tai, Tsun-Kong Sham, et al. Proto-calcite and proto-vaterite in amorphous calcium carbonates. *Angewandte Chemie International Edition*, 49(47):8889–8891, 2010.

[78] Lucille A Giannuzzi et al. *Introduction to focused ion beams: instrumentation, theory, techniques and practice*. Springer Science & Business Media, 2004.

[79] Javier Gonzalez-Platas, Matteo Alvaro, Fabrizio Nestola, and Ross Angel. EosFit7-GUI: a new graphical user interface for equation of state calculations, analyses and teaching. *Journal of Applied Crystallography*, 49(4):1377–1382, 2016.

[80] Di Gui, Lijun Ji, Azeem Muhammad, Wei Li, Weizhao Cai, Yanchun Li, Xiaodong Li, Xiang Wu, and Peixiang Lu. Jahn-Teller effect on framework flexibility of hybrid organic-inorganic perovskites. *The Journal of Physical Chemistry Letters*, 9(4):751–755, 2018.

[81] Nikolaus Gussone, Gernot Nehrke, and Barbara MA Teichert. Calcium isotope fractionation in ikaite and vaterite. *Chemical Geology*, 285(1-4):194–202, 2011.

[82] Tahar Hammouda and Shantanu Keshav. Melting in the mantle in the presence of carbon: Review of experiments and discussion on the origin of carbonatites. *Chemical Geology*, 418:171–188, 2015.

[83] Dorian M Hatch and Leo Merrill. Landau description of the calcite-$CaCO_3$ (II) phase transition. *Physical Review B*, 23(1):368, 1981.

[84] Eiken Haussühl, Hans Josef Reichmann, Jürgen Schreuer, Alexandra Friedrich, Christian Hirschle, Lkhamsuren Bayarjargal, Björn Winkler, Igor Alencar, Leonore Wiehl, and Steffen Ganschow. Elastic properties of single crystal $Bi_{12}SiO_{20}$ as a function of pressure and temperature and acoustic attenuation effects in $Bi_{12}MO_{20}$ (M= Si, Ge and Ti). *Materials Research Express*, 7(2):025701, 2020.

[85] Eiken Haussühl, Jürgen Schreuer, Björn Winkler, Siegfried Haussühl, Lkhamsuren Bayarjargal, and Victor Milman. Structure–property relations and thermodynamic properties of monoclinic petalite, $LiAlSi_4O_{10}$. *Journal of Physics: Condensed Matter*, 24(34):345402, 2012.

[86] Robert M Hazen, Robert T Downs, Adrian P Jones, and Linda Kah. Carbon mineralogy and crystal chemistry. *Reviews in Mineralogy and Geochemistry*, 75(1):7–46, 2013.

[87] RFS Hearmon. The third-and higher-order elastic constants. *Numerical Data and Functional Relationships in Science and Technology, Landolt-Bornstein*, 11, 1979.

[88] RFS Hearmon. The elastic constants of crystals and other anisotropic materials. *Landolt-Bornstein Tables, III/18*, 1154, 1984.

[89] Richard Hill. The elastic behaviour of a crystalline aggregate. *Proceedings of the Physical Society. Section A*, 65(5):349, 1952.

[90] Marc M Hirschmann. Comparative deep Earth volatile cycles: The case for C recycling from exosphere/mantle fractionation of major (H_2O, C, N) volatiles and from H_2O/Ce, CO_2/Ba, and CO_2/Nb exosphere ratios. *Earth and Planetary Science Letters*, 502:262–273, 2018.

[91] P Hohenberg and WJPR Kohn. Density functional theory (dft). *Phys. Rev*, 136:B864, 1964.

[92] Mingqiang Hou, Qian Zhang, Renbiao Tao, Hong Liu, Yoshio Kono, Ho-kwang Mao, Wenge Yang, Bin Chen, and Yingwei Fei. Temperature-induced amorphization in $CaCO_3$ at high pressure and implications for recycled $CaCO_3$ in subduction zones. *Nature communications*, 10(1):1–8, 2019.

[93] Ke-Li Hu, Mohamedally Kurmoo, Zheming Wang, and Song Gao. Metal–organic perovskites: synthesis, structures, and magnetic properties of $[C(NH_2)_3][M^{II}(HCOO)_3]$(M= Mn, Fe, Co, Ni, Cu, and Zn; $C(NH_2)_3$= guanidinium). *Chemistry–A European Journal*, 15(44):12050–12064, 2009.

[94] Dan Huang, Hong Liu, Ming-Qiang Hou, Meng-Yu Xie, Ya-Fei Lu, Lei Liu, Li Yi, Yue-Ju Cui, Ying Li, Li-Wei Deng, et al. Elastic properties of $CaCO_3$ high pressure phases from first principles. *Chinese Physics B*, 26(8):089101, 2017.

[95] Pierre Humbert and F. Plicque. Proprietés élastiques de carbonates rhomboédriques monocristallins: calcite, magnésite, dolomie. *Comptes Rendus de l'Académie des Sciences de Paris*, (275):391–394, 1972.

[96] Nobuo Ishizawa. Calcite V: a hundred-year-old mystery has been solved. *Powder Diffraction*, 29(S1):S19–S23, 2014.

[97] Nobuo Ishizawa, Hayato Setoguchi, and Kazumichi Yanagisawa. Structural evolution of calcite at high temperatures: Phase V unveiled. *Scientific Reports*, 3:2832, 2013.

[98] Maiko Isshiki, Tetsuo Irifune, Kei Hirose, Shigeaki Ono, Yasuo Ohishi, Tetsu Watanuki, Eiji Nishibori, Masaki Takata, and Makoto Sakata. Stability of magnesite and its high-pressure form in the lowermost mantle. *Nature*, 427(6969):60, 2004.

[99] Pierre Jacquinot. New developments in interference spectroscopy. *Reports on progress in physics*, 23(1):267, 1960.

[100] Lee Kabalah-Amitai, Boaz Mayzel, Yaron Kauffmann, Andrew N Fitch, Leonid Bloch, Pupa UPA Gilbert, and Boaz Pokroy. Vaterite crystals contain two interspersed crystal structures. *science*, 340(6131):454–457, 2013.

[101] F Kaminsky, Richard Wirth, S Matsyuk, Anja Schreiber, and Rainer Thomas. Nyerereite and nahcolite inclusions in diamond: evidence for lower-mantle carbonatitic magmas. *Mineralogical Magazine*, 73(5):797–816, 2009.

[102] Felix Kaminsky. Mineralogy of the lower mantle: A review of 'super-deep' mineral inclusions in diamond. *Earth-Science Reviews*, 110(1-4):127–147, 2012.

[103] Felix V Kaminsky, Igor D Ryabchikov, and Richard Wirth. A primary natrocarbonatitic association in the Deep Earth. *Mineralogy and Petrology*, 110(2-3):387–398, 2016.

[104] Yoshihiko Kanemitsu and Taketo Handa. Photophysics of metal halide perovskites: From materials to devices. *Japanese Journal of Applied Physics*, 57(9):090101, 2018.

[105] Innokenty Kantor, V Prakapenka, Anastasia Kantor, P Dera, Alexander Kurnosov, S Sinogeikin, Natalia Dubrovinskaia, and Leonid Dubrovinsky. *BX90*: *A* new diamond anvil cell design for *X*-ray

diffraction and optical measurements. *Review of Scientific Instruments*, 83(12):125102, 2012.

[106] Bijaya B Karki, Lars Stixrude, and Renata M Wentzcovitch. High-pressure elastic properties of major materials of Earth's mantle from first principles. *Reviews of Geophysics*, 39(4):507–534, 2001.

[107] T Katsura and E Ito. Melting and subsolidus phase relations in the $MgSiO_3$–$MgCO_3$ system at high pressures: implications to evolution of the Earth's atmosphere. *Earth and Planetary Science Letters*, 99(1-2):110–117, 1990.

[108] Peter B Kelemen and Craig E Manning. Reevaluating carbon fluxes in subduction zones, what goes down, mostly comes up. *Proceedings of the National Academy of Sciences*, 112(30):E3997–E4006, 2015.

[109] Hans Keppler, Michael Wiedenbeck, and Svyatoslav S Shcheka. Carbon solubility in olivine and the mode of carbon storage in the Earth's mantle. *Nature*, 424(6947):414, 2003.

[110] Ekaterina S Kiseeva, Gregory M Yaxley, Jörg Hermann, Konstantin D Litasov, Anja Rosenthal, and Vadim S Kamenetsky. An experimental study of carbonated eclogite at 3.5–5.5 GPa—implications for silicate and carbonate metasomatism in the cratonic mantle. *Journal of Petrology*, 53(4):727–759, 2012.

[111] Charles Kittel. Introduction to solid state physics. 1976.

[112] S Klotz, JC Chervin, P Munsch, and Gilles Le Marchand. Hydrostatic limits of 11 pressure transmitting media. *Journal of Physics D: Applied Physics*, 42(7):075413, 2009.

[113] Monika Koch-Müller, Sandro Jahn, Natalie Birkholz, Eglof Ritter, and Ulrich Schade. Phase transitions in the system $CaCO_3$ at high P and T determined by in situ vibrational spectroscopy in diamond anvil cells and first-principles simulations. *Physics and Chemistry of Minerals*, 43(8):545–561, 2016.

[114] Nobuyoshi Koga, Yuzou Nakagoe, and Haruhiko Tanaka. Crystallization of amorphous calcium carbonate. *Thermochimica Acta*, 318(1-2):239–244, 1998.

[115] Walter Kohn and Lu Jeu Sham. Self-consistent equations including exchange and correlation effects. *Physical review*, 140(4A):A1133, 1965.

[116] Georg Kresse and Jürgen Furthmüller. Efficient iterative schemes for ab initio total-energy calculations using a plane-wave basis set. *Physical review B*, 54(16):11169, 1996.

[117] Allen C Larson and Robert B Von Dreele. Gsas. *Report lAUR*, pages 86–748, 1994.

[118] Barbara Lavina, Przemyslaw Dera, Eunja Kim, Yue Meng, Robert T Downs, Philippe F Weck, Stephen R Sutton, and Yusheng Zhao. Discovery of the recoverable high-pressure iron oxide Fe_4O_5. *Proceedings of the National Academy of Sciences*, 108(42):17281–17285, 2011.

[119] Cin-Ty Lee, Roberta L Rudnick, William F McDonough, and Ingo Horn. Petrologic and geochemical investigation of carbonates in peridotite xenoliths from northeastern Tanzania. *Contributions to Mineralogy and Petrology*, 139(4):470–484, 2000.

[120] Xinyang Li, Zhigang Zhang, Jung-Fu Lin, Huaiwei Ni, Vitali B Prakapenka, and Zhu Mao. New high-pressure phase of $CaCO_3$ at the topmost lower mantle: Implication for the deep-mantle carbon transportation. *Geophysical Research Letters*, 45(3):1355–1360, 2018.

[121] Zeyu Li, Jie Li, Rebecca Lange, Jiachao Liu, and Burkhard Militzer. Determination of calcium carbonate and sodium carbonate melting curves up to Earth's transition zone pressures with implications for the deep carbon cycle. *Earth and Planetary Science Letters*, 457:395–402, 2017.

[122] H-P Liermann, Z Konôpková, W Morgenroth, K Glazyrin, J Bednarčik, EE McBride, S Petitgirard, JT Delitz, M Wendt, Y Bican, et al. The extreme conditions beamline P02.2 and the extreme conditions science infrastructure at PETRA III. *Journal of synchrotron radiation*, 22(4):908–924, 2015.

[123] Chung-Cherng Lin. Elasticity of calcite: thermal evolution. *Physics and Chemistry of Minerals*, 40(2):157–166, 2013.

[124] Jung-Fu Lin, Jin Liu, Caleb Jacobs, and Vitali B Prakapenka. Vibrational and elastic properties of ferromagnesite across the electronic spin-pairing transition of iron. *American Mineralogist*, 97(4):583–591, 2012.

[125] Konstantin D Litasov, Yingwei Fei, Eiji Ohtani, Takahiro Kuribayashi, and Kenichi Funakoshi. Thermal equation of state of magnesite to

32 GPa and 2073 K. *Physics of the Earth and Planetary Interiors*, 168(3-4):191–203, 2008.

[126] Konstantin D Litasov, Anton Shatskiy, Pavel N Gavryushkin, Altyna E Bekhtenova, Peter I Dorogokupets, Boris S Danilov, Yuji Higo, Abdirash T Akilbekov, and Talgat M Inerbaev. PVT equation of state of $CaCO_3$ aragonite to 29 GPa and 1673 K: In situ X-ray diffraction study. *Physics of the Earth and Planetary Interiors*, 265:82–91, 2017.

[127] Konstantin D Litasov, Anton Shatskiy, Pavel N Gavryushkin, Igor S Sharygin, Peter I Dorogokupets, Anna M Dymshits, Eiji Ohtani, Yuji Higo, and Kenichi Funakoshi. P-V-T equation of state of siderite to 33 GPa and 1673 K. *Physics of the Earth and Planetary Interiors*, 224:83–87, 2013.

[128] Janice L Littlewood, Samuel Shaw, Caroline L Peacock, Pieter Bots, Divyesh Trivedi, and Ian T Burke. Mechanism of enhanced strontium uptake into calcite via an amorphous calcium carbonate crystallization pathway. *Crystal Growth & Design*, 17(3):1214–1223, 2017.

[129] Yuriy Litvin, Anna Spivak, Natalia Solopova, and Leonid Dubrovinsky. On origin of lower-mantle diamonds and their primary inclusions. *Physics of the Earth and Planetary Interiors*, 228:176–185, 2014.

[130] Jin Liu, Razvan Caracas, Dawei Fan, Ema Bobocioiu, Dongzhou Zhang, and Wendy L Mao. High-pressure compressibility and vibrational properties of $(Ca, Mn)CO_3$. *American Mineralogist*, 101(12):2723–2730, 2016.

[131] Jin Liu, Jung-Fu Lin, Zhu Mao, and Vitali B Prakapenka. Thermal equation of state and spin transition of magnesiosiderite at high pressure and temperature. *American Mineralogist*, 99(1):84–93, 2014.

[132] Jin Liu, Jung-Fu Lin, and Vitali B Prakapenka. High-pressure orthorhombic ferromagnesite as a potential deep-mantle carbon carrier. *Scientific Reports*, 5(1):1–6, 2015.

[133] Lin-gun Liu, Chien-chih Chen, Chung-Cherng Lin, and Yi-jong Yang. Elasticity of single-crystal aragonite by Brillouin spectroscopy. *Physics and Chemistry of Minerals*, 32(2):97–102, 2005.

[134] Yongsheng Liu, Detao He, Changgui Gao, Stephen Foley, Shan Gao, Zhaochu Hu, Keqing Zong, and Haihong Chen. First direct evidence of

sedimentary carbonate recycling in subduction-related xenoliths. *Scientific reports*, 5(1):1–11, 2015.

[135] Alla M Logvinova, Anton Shatskiy, Richard Wirth, Anatoly A Tomilenko, Sargylana S Ugap'eva, and Nikolay V Sobolev. Carbonatite melt in type Ia gem diamond. *Lithos*, 342:463–467, 2019.

[136] Alla M Logvinova, Richard Wirth, Ekaterina N Fedorova, and Nikolai V Sobolev. Nanometre-sized mineral and fluid inclusions in cloudy siberian diamonds: new insights on diamond formation. *European Journal of Mineralogy*, 20(3):317–331, 2008.

[137] AM Logvinova, Richard Wirth, AA Tomilenko, VP Afanas'Ev, and NV Sobolev. The phase composition of crystal-fluid nanoinclusions in alluvial diamonds in the northeastern siberian platform. *Russian Geology and Geophysics*, 52(11):1286–1297, 2011.

[138] Anita Lucas-Girot, Olivier Hernandez, and Hassane Oudadesse. Re-examination of the structural properties of solid solutions $Sr_xCa_{1-x}CO_3$. *Materials research bulletin*, 42(6):1061–1068, 2007.

[139] Fumiya Maeda, Eiji Ohtani, Seiji Kamada, Tatsuya Sakamaki, Naohisa Hirao, and Yasuo Ohishi. Diamond formation in the deep lower mantle: A high-pressure reaction of $MgCO_3$ and SiO_2. *Scientific reports*, 7:40602, 2017.

[140] D Mainprice, Guilhem Barruol, and Walid Ben Ismaïl. The seismic anisotropy of the earth's mantle: from single crystal to polycrystal, 2000.

[141] Zhu Mao, Matt Armentrout, Emma Rainey, Craig E Manning, Przemyslaw Dera, Vitali B Prakapenka, and Abby Kavner. Dolomite III: A new candidate lower mantle carbonate. *Geophysical Research Letters*, 38(22), 2011.

[142] Hauke Marquardt and Andrew R Thomson. Experimental elasticity of Earth's deep mantle. *Nature Reviews Earth & Environment*, 1(9):455–469, 2020.

[143] Naira Martirosyan, Ilias Efthimiopoulos, Lea Pennacchioni, Richard Wirth, Sandro Jahn, and Monika Koch-Müller. Effect of cationic substitution on the pressure-induced phase transitions in calcium carbonate. *American Mineralogist*, 2020.

[144] Naira Martirosyan, Lea Pennacchioni, Richard Wirth, Sergey Lobanov, Sandro Jahn, Ilias Efthimiopoulos, Hans-Josef Reichmann, Björn Winkler, and Monika Koch-Müller. Dolomite-ankerite solid solution at high pressure, *In preparation.* 2022.

[145] Naira S Martirosyan, Ilias Efthimiopoulos, Lea Pennacchioni, Richard Wirth, Sandro Jahn, and Monika Koch-Müller. Effect of cationic substitution on the pressure-induced phase transitions in calcium carbonate. *American Mineralogist: Journal of Earth and Planetary Materials*, 106(4):549–558, 2021.

[146] Bernard Marty, Conel M O'D Alexander, and Sean N Raymond. Primordial origins of Earth's carbon. *Reviews in Mineralogy and Geochemistry*, 75(1):149–181, 2013.

[147] Koji Maruyama, Hiroyuki Kagi, Kazuki Komatsu, Toru Yoshino, and Satoshi Nakano. Pressure-induced phase transitions of vaterite, a metastable phase of $CaCO_3$. *Journal of Raman Spectroscopy*, 48(11):1449–1453, 2017.

[148] Satoshi Matsunuma, Hiroyuki Kagi, Kazuki Komatsu, Koji Maruyama, and Toru Yoshino. Doping incompatible elements into calcite through amorphous calcium carbonate. *Crystal growth & design*, 14(11):5344–5348, 2014.

[149] M Menadakis, G Maroulis, and PG Koutsoukos. A quantum chemical study of doped $CaCO_3$ (calcite). *Computational materials science*, 38(3):522–525, 2007.

[150] M Merlini, M Hanfland, and WA Crichton. $CaCO_3$-III and $CaCO_3$-VI, high-pressure polymorphs of calcite: Possible host structures for carbon in the Earth's mantle. *Earth and Planetary Science Letters*, 333:265–271, 2012.

[151] Marco Merlini, Valerio Cerantola, G. Diego Gatta, Mauro Gemmi, Michael Hanfland, Ilya Kupenko, Paolo Lotti, Harald Müller, and Li Zhang. Dolomite-IV: Candidate structure for a carbonate in the Earth's lower mantle. *American Mineralogist*, 102(8):1763–1766, 2017.

[152] Marco Merlini, WA Crichton, Julien Chantel, Jeremy Guignard, and Stefano Poli. Evidence of interspersed co-existing $CaCO_3$-III and $CaCO_3$-IIIb structures in polycrystalline $CaCO_3$ at high pressure. *Mineralogical Magazine*, 78(2):225–233, 2014.

[153] Marco Merlini, Wilson A Crichton, Michael Hanfland, Mauro Gemmi, Harald Müller, Ilya Kupenko, and Leonid Dubrovinsky. Structures of dolomite at ultrahigh pressure and their influence on the deep carbon cycle. *Proceedings of the National Academy of Sciences*, 109(34):13509–13514, 2012.

[154] Marco Merlini, Michael Hanfland, and Mauro Gemmi. The $MnCO_3$-ii high-pressure polymorph of rhodocrosite. *American Mineralogist*, 100(11-12):2625–2629, 2015.

[155] Marco Merlini, Michael Hanfland, Ashkan Salamat, Sylvain Petitgirard, and Harald Müller. The crystal structures of $Mg_2Fe_2C_4O_{13}$, with tetrahedrally coordinated carbon, and $Fe_{13}O_{19}$, synthesized at deep mantle conditions. *American Mineralogist*, 100(8-9):2001–2004, 2015.

[156] Leo Merrill and William A Bassett. The crystal structure of $CaCO_3$ (II), a high-pressure metastable phase of calcium carbonate. *Acta Crystallographica Section B: Structural Crystallography and Crystal Chemistry*, 31(2):343–349, 1975.

[157] Albert Migliori and JD Maynard. Implementation of a modern resonant ultrasound spectroscopy system for the measurement of the elastic moduli of small solid specimens. *Review of scientific instruments*, 76(12):121301, 2005.

[158] John D Milliman, German Müller, and F Förstner. *Recent sedimentary carbonates: Part 1 marine carbonates*. Springer Science & Business Media, 2012.

[159] Alessandro Mirone and Björn Wehinger. Open source package TDS2EL2, 2017.

[160] Peter W Mirwald. A differential thermal analysis study of the high-temperature polymorphism of calcite at high pressure. *Contributions to Mineralogy and Petrology*, 59(1):33–40, 1976.

[161] Koichi Momma and Fujio Izumi. VESTA 3 for three-dimensional visualization of crystal, volumetric and morphology data. *Journal of applied crystallography*, 44(6):1272–1276, 2011.

[162] Hendrik J Monkhorst and James D Pack. Special points for Brillouin-zone integrations. *Physical review B*, 13(12):5188, 1976.

[163] Jan Müller, Ilias Efthimiopoulos, Sandro Jahn, and Monika Koch-Müller. Effect of temperature on the pressure-induced spin transition in siderite and iron-bearing magnesite: a Raman spectroscopy study. *European Journal of Mineralogy*, 29(5):785–793, 2017.

[164] Wolfgang Friedrich Müller and Gerhard Franz. TEM-microstructures in omphacite and other minerals from eclogite near to a thrust zone; the Eclogite Zone Venediger nappe area, Tauern Window, Austria. *Neues Jahrbuch für Mineralogie-Abhandlungen*, pages 285–298, 2008.

[165] MJP Musgrave. *Crystal acoustics*. Acoustical Society of America New York, 2003.

[166] Tra Nguyen-Thanh, Alexei Bosak, Johannes D Bauer, Rita Luchitskaia, Keith Refson, Victor Milman, and Bjoern Winkler. Lattice dynamics and elasticity of $SrCO_3$. *Journal of Applied Crystallography*, 49(6):1982–1990, 2016.

[167] John Frederick Nye et al. *Physical properties of crystals: their representation by tensors and matrices*. Oxford university press, 1985.

[168] Artem R Oganov, Colin W Glass, and Shigeaki Ono. High-pressure phases of $CaCO_3$: *C*rystal structure prediction and experiment. *Earth and Planetary Science Letters*, 241(1-2):95–103, 2006.

[169] Artem R Oganov, Shigeaki Ono, Yanming Ma, Colin W Glass, and Alberto Garcia. Novel high-pressure structures of $MgCO_3$, $CaCO_3$ and CO_2 and their role in Earth's lower mantle. *Earth and Planetary Science Letters*, 273(1-2):38–47, 2008.

[170] S Ono. High-pressure phase transformation in $MnCO_3$: a synchrotron XRD study. *Mineralogical Magazine*, 71(1):105–111, 2006.

[171] Shigeaki Ono, Takumi Kikegawa, and Yasuo Ohishi. High-pressure transition of $CaCO_3$. *American Mineralogist*, 92(7):1246–1249, 2007.

[172] Beth N Orcutt, Isabelle Daniel, and Rajdeep Dasgupta. *Deep C*arbon: P*ast to* P*resent*. Cambridge University Press, 2019.

[173] Sarah EM Palaich, Robert A Heffern, Michael Hanfland, Andrea Lausi, Abby Kavner, Craig E Manning, and Marco Merlini. High-pressure compressibility and thermal expansion of aragonite. *American Mineralogist*, 101(7):1651–1658, 2016.

[174] Yu N Pal'Yanov, AG Sokol, Yu M Borzdov, AF Khokhryakov, and NV Sobolev. Diamond formation from mantle carbonate fluids. *Nature*, 400(6743):417–418, 1999.

[175] Alessandro Pavese, M Catti, GD Price, and RA Jackson. Interatomic potentials for $CaCO_3$ polymorphs (calcite and aragonite), fitted to elastic and vibrational data. *Physics and chemistry of minerals*, 19(2):80–87, 1992.

[176] L Pennacchioni, S Speziale, and B Winkler. Elastic properties of natural aragonite invistigated by brillouin spectroscopy, *In preparation.* 2021.

[177] John P Perdew, Kieron Burke, and Matthias Ernzerhof. Generalized gradient approximation made simple. *Physical review letters*, 77(18):3865, 1996.

[178] John P Perdew, Adrienn Ruzsinszky, Gabor I Csonka, Oleg A Vydrov, Gustavo E Scuseria, Lucian A Constantin, Xiaolan Zhou, and Kieron Burke. Generalized gradient approximation for solids and their surfaces. *arXiv preprint arXiv:0707.2088*, 2007.

[179] John P Perdew, Adrienn Ruzsinszky, Gábor I Csonka, Oleg A Vydrov, Gustavo E Scuseria, Lucian A Constantin, Xiaolan Zhou, and Kieron Burke. Restoring the density-gradient expansion for exchange in solids and surfaces. *Physical review letters*, 100(13):136406, 2008.

[180] Sylvain Petitgirard, Wim J Malfait, Ryosuke Sinmyo, Ilya Kupenko, Louis Hennet, Dennis Harries, Thomas Dane, Manfred Burghammer, and Dave C Rubie. Fate of $MgSiO_3$ melts at core–mantle boundary conditions. *Proceedings of the National Academy of Sciences*, 112(46):14186–14190, 2015.

[181] Václav Petříček, Michal Dušek, and Lukáš Palatinus. Crystallographic computing system JANA2006: General features. *Zeitschrift für Kristallographie-Crystalline Materials*, 229(5):345–352, 2014.

[182] Chris J Pickard and Richard J Needs. Structures and stability of calcium and magnesium carbonates at mantle pressures. *Physical Review B*, 91(10):104101, 2015.

[183] Ben Pilgrim and Neil R Champness. Metal-organic frameworks and metal-organic cages–A perspective. *ChemPlusChem*, 85(8), 2020.

[184] T Pippinger, R Miletich, M Merlini, P Lotti, P Schouwink, T Yagi, WA Crichton, and M Hanfland. Puzzling calcite-III dimorphism: crystallography, high-pressure behavior, and pathway of single-crystal transitions. *Physics and Chemistry of Minerals*, 42(1):29–43, 2015.

[185] Terry Plank and Craig E Manning. Subducting carbon. *Nature*, 574(7778):343–352, 2019.

[186] Jean-Paul Poirier. *Introduction to the Physics of the Earth's Interior*. Cambridge University Press, 2000.

[187] Clemens Prescher and Vitali B Prakapenka. Dioptas: a program for reduction of two-dimensional x-ray diffraction data and data exploration. *High Pressure Research*, 35(3):223–230, 2015.

[188] Paolo Raiteri and Julian D Gale. Water is the key to nonclassical nucleation of amorphous calcium carbonate. *Journal of the American Chemical Society*, 132(49):17623–17634, 2010.

[189] Shivakumar I Ranganathan and Martin Ostoja-Starzewski. Universal elastic anisotropy index. *Physical review letters*, 101(5):055504, 2008.

[190] SAT Redfern, E Salje, and A Navrotsky. High-temperature enthalpy at the orientational order-disorder transition in calcite: implications for the calcite/aragonite phase equilibrium. *Contributions to Mineralogy and Petrology*, 101(4):479–484, 1989.

[191] Simon AT Redfern and Ross J Angel. High-pressure behaviour and equation of state of calcite, $CaCO_3$. *Contributions to Mineralogy and Petrology*, 134(1):102–106, 1999.

[192] Stephen Jervis Brent Reed. *Electron microprobe analysis and scanning electron microscopy in geology*. Cambridge university press, 2005.

[193] Richard J Reeder and Wayne A Dollase. Structural variation in the dolomite-ankerite solid-solution series; an X-ray, Moessbauer, and TEM study. *American Mineralogist*, 74(9-10):1159–1167, 1989.

[194] RJ Reeder and Y Nakajima. The nature of ordering and ordering defects in dolomite. *Physics and Chemistry of Minerals*, 8(1):29–35, 1982.

[195] RJ Reeder and Hans-Rudolf Wenk. Structure refinements of some thermally disordered dolomites. *American Mineralogist*, 68(7-8):769–776, 1983.

[196] Ekaterina Reguir. *Aspects of the mineralogy of the Murun alkaline complex, Yakutia, Russia*. Lakehead University Thunder Bay, Ontario, 2001.

[197] A Rosenthal, EH Hauri, and MM Hirschmann. Experimental determination of C, F, and H partitioning between mantle minerals and carbonated basalt, CO_2/Ba and CO_2/Nb systematics of partial melting, and the CO_2 contents of basaltic source regions. *Earth and Planetary Science Letters*, 412:77–87, 2015.

[198] Nancy L Ross and Richard J Reeder. High-pressure structural study of dolomite and ankerite. *American Mineralogist*, 77(3-4):412–421, 1992.

[199] Moumita Saharay, A Ozgur Yazaydin, and R James Kirkpatrick. Dehydration-induced amorphous phases of calcium carbonate. *The Journal of Physical Chemistry B*, 117(12):3328–3336, 2013.

[200] Ayaka Saito, Hiroyuki Kagi, Shiho Marugata, Kazuki Komatsu, Daisuke Enomoto, Koji Maruyama, and Jun Kawano. Incorporation of incompatible Strontium and Barium ions into calcite ($CaCO_3$) through amorphous calcium carbonate. *Minerals*, 10(3):270, 2020.

[201] Carmen Sanchez-Valle and Jay D Bass. Elasticity and pressure-induced structural changes in vitreous $MgSiO_3$-enstatite to lower mantle pressures. *Earth and Planetary Science Letters*, 295(3-4):523–530, 2010.

[202] Carmen Sanchez-Valle, Sujoy Ghosh, and Angelika D Rosa. Sound velocities of ferromagnesian carbonates and the seismic detection of carbonates in eclogites and the mantle. *Geophysical Research Letters*, 38(24), 2011.

[203] JR Sanderocock. Light scattering from surface acoustic phonons in metals and semiconductors. *Solid State Communications*, 26(8):547–551, 1978.

[204] Marco Scambelluri, Gray E Bebout, Donato Belmonte, Mattia Gilio, Nicola Campomenosi, Nathan Collins, and Laura Crispini. Carbonation of subduction-zone serpentinite (high-pressure ophicarbonate; ligurian western alps) and implications for the deep carbon cycling. *Earth and Planetary Science Letters*, 441:155–166, 2016.

[205] Millicent P Schmidt, Andrew J Ilott, Brian L Phillips, and Richard J Reeder. Structural changes upon dehydration of amorphous calcium carbonate. *Crystal Growth & Design*, 14(3):938–951, 2014.

[206] Jürgen Schreuer and Siegfried Haussühl. Elastic and piezoelectric properties of minerals i. principles and experimental approaches. *Mineral Behaviour at Extreme Conditions*, 7:95–116, 2005.

[207] W Sekkal and A Zaoui. Nanoscale analysis of the morphology and surface stability of calcium carbonate polymorphs. *Scientific Reports*, 3:1587, 2013.

[208] Eva Seknazi, Davide Levy, Iryna Polishchuk, Alex Katsman, and Boaz Pokroy. Experimental and Theoretical Insights into the Bioinspired Formation of Disordered Ba-Calcite. *Advanced Functional Materials*, 30(18):1805028, 2020.

[209] Robert D Shannon. Revised effective ionic radii and systematic studies of interatomic distances in halides and chalcogenides. *Acta crystallographica section A: crystal physics, diffraction, theoretical and general crystallography*, 32(5):751–767, 1976.

[210] Svyatoslav S Shcheka, Michael Wiedenbeck, Daniel J Frost, and Hans Keppler. Carbon solubility in mantle minerals. *Earth and Planetary Science Letters*, 245(3-4):730–742, 2006.

[211] George M. Sheldrick. Crystal structure refinement with *SHELXL*. *Acta Crystallographica Section C*, 71(1):3–8, Jan 2015.

[212] Guoyin Shen, Yanbin Wang, Agnes Dewaele, Christine Wu, Dayne E Fratanduono, Jon Eggert, Stefan Klotz, Kamil F Dziubek, Paul Loubeyre, Oleg V Fat'yanov, et al. Toward an international practical pressure scale: A proposal for an IPPS ruby gauge (IPPS-Ruby2020). *High Pressure Research*, 40(3):299–314, 2020.

[213] Weiguang Shi, Michael E Fleet, and Sean R Shieh. High-pressure phase transitions in ca-mn carbonates $(Ca, Mn)CO_3$ studied by raman spectroscopy. *American Mineralogist*, 97(5-6):999–1001, 2012.

[214] Hiroyasu Shimizu, Hiroki Imaeda, Tetsuji Kume, and Shigeo Sasaki. High-pressure elastic properties of liquid and solid neon to 7 gpa. *Physical Review B*, 71(1):014108, 2005.

[215] Miki Shirasaka, Eiichi Takahashi, Yu Nishihara, Kyoko Matsukage, and Takumi Kikegawa. In situ x-ray observation of the reaction dolomite= aragonite+ magnesite at 900–1300 k. *American Mineralogist*, 87(7):922–930, 2002.

[216] Steven B Shirey, Lara S Wagner, Michael J Walter, D Graham Pearson, and Peter E van Keken. Slab transport of fluids to deep focus earthquake depths—Thermal modeling constraints and evidence from diamonds. *AGU Advances*, 2(2):e2020AV000304, 2021.

[217] H Siegert. Selbstkonsistenter algorithmus zur vollständigen bestimmung des elastizitätstensors aus schallgeschwindigkeitsmessungen. *Z. Kristallogr*, 186:274–276, 1989.

[218] Norman H Sleep. Stagnant lid convection and carbonate metasomatism of the deep continental lithosphere. *Geochemistry, Geophysics, Geosystems*, 10(11), 2009.

[219] Norman H Sleep and Kevin Zahnle. Carbon dioxide cycling and implications for climate on ancient Earth. *Journal of Geophysical Research: Planets*, 106(E1):1373–1399, 2001.

[220] Dean Smith, Keith V Lawler, Miguel Martinez-Canales, Austin W Daykin, Zachary Fussell, G Alexander Smith, Christian Childs, Jesse S Smith, Chris J Pickard, and Ashkan Salamat. Postaragonite phases of ´$CaCO_3$ at lower mantle pressures. *Physical Review Materials*, 2(1):013605, 2018.

[221] NA Solopova, L Dubrovinsky, AV Spivak, Yu A Litvin, and N Dubrovinskaia. Melting and decomposition of $MgCO_3$ at pressures up to 84 GPa. *Physics and Chemistry of Minerals*, 42(1):73–81, 2015.

[222] Dominik Spahr, Jannes König, Lkhamsuren Bayarjargal, Victor Milman, Martin P Persson, and Björn Winkler. Structural, physical, and thermodynamic properties of aragonitic $Ca_xSr_{1-x}CO_3$ solid solutions. *The Journal of Physical Chemistry C*, 125(31):17474–17481, 2021.

[223] S Speziale, S Gentili, B Wunder, HJ Reichmann, A Zucchini, and P Comodi. The elastic stiffness tensor of natural dolomite.

[224] Sergio Speziale, Hauke Marquardt, and Thomas S Duffy. Brillouin scattering and its application in geosciences. *Reviews in Mineralogy and Geochemistry*, 78(1):543–603, 2014.

[225] Thomas Stachel and Jeff W Harris. Formation of diamond in the Earth's mantle. *Journal of Physics: Condensed Matter*, 21(36):364206, 2009.

[226] Thomas Stachel, Jeff W Harris, Gerhard P Brey, and Werner Joswig. Kankan diamonds (guinea) ii: lower mantle inclusion parageneses. *Contributions to Mineralogy and Petrology*, 140(1):16–27, 2000.

[227] Michal Stekiel, Tra Nguyen-Thanh, Stella Chariton, Catherine McCammon, Alexei Bosak, Wolfgang Morgenroth, Victor Milman, Keith Refson, and Björn Winkler. High pressure elasticity of $FeCO_3$-$MgCO_3$ carbonates. *Physics of the Earth and Planetary Interiors*, 271:57–63, 2017.

[228] Lars Stixrude and Bijaya Karki. Structure and freezing of $MgSiO_3$ liquid in Earth's lower mantle. *Science*, 310(5746):297–299, 2005.

[229] Lars Stixrude and Carolina Lithgow-Bertelloni. Thermodynamics of mantle minerals—i. physical properties. *Geophysical Journal International*, 162(2):610–632, 2005.

[230] Kaichi Suito, Junpei Namba, Takashi Horikawa, Yozo Taniguchi, Noriko Sakurai, Michihiro Kobayashi, Akifumi Onodera, Osamu Shimomura, and Takumi Kikegawa. Phase relations of $CaCO_3$ at high pressure and high temperature. *American Mineralogist*, 86(9):997–1002, 2001.

[231] Katrine L Svane, Alexander C Forse, Clare P Grey, Gregor Kieslich, Anthony K Cheetham, Aron Walsh, and Keith T Butler. How strong is the hydrogen bond in hybrid perovskites? *The journal of physical chemistry letters*, 8(24):6154–6159, 2017.

[232] JH Ter Heege and J Renner. In situ impedance spectroscopy on pyrophyllite and $CaCO_3$ at high pressure and temperature: phase transformations and kinetics of atomistic transport. *Physics and Chemistry of Minerals*, 34(7):445–465, 2007.

[233] JO Titiloye, NH De Leeuw, and SC Parker. Atomistic simulation of the differences between calcite and dolomite surfaces. *Geochimica et cosmochimica acta*, 62(15):2637–2641, 1998.

[234] Alexandre Tkatchenko and Matthias Scheffler. Accurate molecular van der waals interactions from ground-state electron density and free-atom reference data. *Physical review letters*, 102(7):073005, 2009.

[235] Brian H Toby and Robert B Von Dreele. Gsas-ii: the genesis of a modern open-source all purpose crystallography software package. *Journal of Applied Crystallography*, 46(2):544–549, 2013.

[236] Cara E Vennari and Quentin Williams. A novel carbon bonding environment in deep mantle high-pressure dolomite. *American Mineralogist*, 103(1):171–174, 2018.

[237] Victor L Vinograd, Marcel HF Sluiter, and Björn Winkler. Subsolidus phase relations in the $CaCO_3$-$MgCO_3$ system predicted from the excess enthalpies of supercell structures with single and double defects. *Physical Review B*, 79(10):104201, 2009.

[238] M Viswanathan. Neutron diffraction studies on the thermal expansion and anomalous mechanics in the perovskite-type $[C(ND_2)_3]$ Me^{2+} $(DCOO)_3$ [Me = Cu, Mn, Co]. *Physical Chemistry Chemical Physics*, 20(25):17059–17070, 2018.

[239] D Vo Thanh and A Lacam. Experimental study of the elasticity of single crystalline calcite under high pressure (the calcite I—calcite II transition at 14.6 kbar). *Physics of the Earth and Planetary Interiors*, 34(3):195–203, 1984.

[240] Woldemar Voigt. *Lehrbuch der kristallphysik:(mit ausschluss der kristalloptik)*, volume 34. BG Teubner, 1910.

[241] F Wall, MJ Le Bas, and RK Srivastava. Calcite and carbocernaite exsolution and cotectic textures in a Sr, REE-rich carbonatite dyke from Rajasthan, India. *Mineralogical Magazine*, 57(388):495–513, 1993.

[242] Alian Wang, Jill D Pasteris, Henry OA Meyer, and Marie L Dele-Duboi. Magnesite-bearing inclusion assemblage in natural diamond. *Earth and Planetary Science Letters*, 141(1-4):293–306, 1996.

[243] Xin-Yi Wang, Zhe-Ming Wang, and Song Gao. Constructing magnetic molecular solids by employing three-atom ligands as bridges. *Chemical Communications*, (3):281–294, 2008.

[244] Björn Wehinger. *On the combination of thermal diffuse scattering, inelastic x-ray scattering and ab initio lattice dynamics calculations*. PhD thesis, University of Geneva, 2013.

[245] Björn Wehinger, Alessandro Mirone, Michael Krisch, and Alexeï Bosak. Full elasticity tensor from thermal diffuse scattering. *Physical review letters*, 118(3):035502, 2017.

[246] Wei Wei, Xinyang Li, Ningyu Sun, Sergey N Tkachev, and Zhu Mao. Sound velocity of neon at high pressures and temperatures by Brillouin

scattering. *American Mineralogist: Journal of Earth and Planetary Materials*, 104(11):1650–1655, 2019.

[247] Donald J Weidner, Karl Swyler, and Herbert R Carleton. Elasticity of microcrystals. *Geophysical Research Letters*, 2(5):189–192, 1975.

[248] S. Weiner, I. Sagi, and L. Addadi. Choosing the crystallization path less traveled. *Science*, 309(5737):1027–1028, 2005.

[249] Christopher Weis, Christian Sternemann, Valerio Cerantola, Christoph J Sahle, Georg Spiekermann, Manuel Harder, Yury Forov, Alexander Kononov, Robin Sakrowski, Hasan Yavaş, et al. Pressure driven spin transition in siderite and magnesiosiderite single crystals. *Scientific reports*, 7(1):1–10, 2017.

[250] Michael L Whittaker, Paul JM Smeets, Hasti Asayesh-Ardakani, Reza Shahbazian-Yassar, and Derk Joester. Multi-step crystallization of barium carbonate: Rapid interconversion of amorphous and crystalline precursors. *Angewandte Chemie*, 129(50):16244–16247, 2017.

[251] Michael L Whittaker, Wenhao Sun, Karen A DeRocher, Saivenkataraman Jayaraman, Gerbrand Ceder, and Derk Joester. Structural basis for metastability in amorphous calcium barium carbonate (ACBC). *Advanced Functional Materials*, 28(2):1704202, 2018.

[252] Michael L Whittaker, Wenhao Sun, Danielle O Duggins, Gerbrand Ceder, and Derk Joester. Dynamic Barriers to Crystallization of Calcium Barium Carbonates. *Crystal Growth & Design*, 21(8):4556–4563, 2021.

[253] Douglas A Wiens. Diamonds hold clues about the cause of deep earthquakes. *AGU Advances*, 2(2), 2021.

[254] David B Williams and C Barry Carter. The transmission electron microscope. In *Transmission electron microscopy*, pages 3–17. Springer, 1996.

[255] Bjoern Winkler and Victor Milman. Density functional theory based calculations for high pressure research. *Zeitschrift für Kristallographie–Crystalline Materials*, 229(2):112–122, 2014.

[256] Richard Wirth. Focused Ion Beam (FIB) combined with SEM and TEM: Advanced analytical tools for studies of chemical composition, microstructure and crystal structure in geomaterials on a nanometre scale. *Chemical Geology*, 261(3-4):217–229, 2009.

[257] H Wondratschek and W Jeitschko. Twin domains and antiphase domains. *Acta Crystallographica Section A: Crystal Physics, Diffraction, Theoretical and General Crystallography*, 32(4):664–666, 1976.

[258] William Alfred Wooster. *Diffuse X-ray reflections from crystals*. Courier Corporation, 1997.

[259] Shijun Xiao, Scott A Edwards, and Frauke Gräter. A new transferable forcefield for simulating the mechanics of $CaCO_3$ crystals. *The Journal of Physical Chemistry C*, 115(41):20067–20075, 2011.

[260] Man Xu, Zhicheng Jing, Suraj K Bajgain, Mainak Mookherjee, James A Van Orman, Tony Yu, and Yanbin Wang. High-pressure elastic properties of dolomite melt supporting carbonate-induced melting in deep upper mantle. *Proceedings of the National Academy of Sciences*, 117(31):18285–18291, 2020.

[261] Jing Yang, Zhu Mao, Jung-Fu Lin, and Vitali B Prakapenka. Single-crystal elasticity of the deep-mantle magnesite at high pressure and temperature. *Earth and Planetary Science Letters*, 392:292–299, 2014.

[262] Zhengqiang Yang, Guanqun Cai, Craig L Bull, Matthew G Tucker, Martin T Dove, Alexandra Friedrich, and Anthony E Phillips. Hydrogen-bond-mediated structural variation of metal guanidinium formate hybrid perovskites under pressure. *Philosophical Transactions of the Royal Society A*, 377(2149):20180227, 2019.

[263] Gregory M Yaxley, Anthony J Crawford, and David H Green. Evidence for carbonatite metasomatism in spinel peridotite xenoliths from western Victoria, Australia. *Earth and Planetary Science Letters*, 107(2):305–317, 1991.

[264] Dmitriy A Zedgenizov, Anton Shatskiy, Alexey L Ragozin, Hiroyuki Kagi, and Vladislav S Shatsky. Merwinite in diamond from Sao Luiz, Brazil: A new mineral of the Ca-rich mantle environment. *American Mineralogist*, 99(2-3):547–550, 2014.

[265] Yanfei Zhang, Chao Wang, and Zhenmin Jin. Decarbonation of stagnant slab in the mantle transition zone. *Journal of Geophysical Research: Solid Earth*, 125(7):e2020JB019533, 2020.

[266] Chao-Shuai Zhao, He-Ping Li, Po-Fei Chen, and Jian-Jun Jiang. Sound velocities across calcite phase transitions by brillouin scattering spectroscopy. *American Mineralogist: Journal of Earth and Planetary Materials*, 104(3):418–424, 2019.

[267] Chaoshuai Zhao, Heping Li, Pofei Chen, Jianjun Jiang, and Wen Liang. Single-crystal elasticity of the rhodochrosite at high pressure by Brillouin scattering spectroscopy. *High Pressure Research*, 38(4):396–405, 2018.

[268] Chaoshuai Zhao, Heping Li, Jianjun Jiang, Yu He, and Wen Liang. Phase transition and vibration properties of $MnCO_3$ at high pressure and high-temperature by Raman spectroscopy. *High Pressure Research*, 38(3):212–223, 2018.

[269] Vladimir Naumovich Zharkov and Vladimir Alekseevich Kalinin. *Equations of state for solids at high pressures and temperatures*. Springer, 1971.

[270] Hong-Cai Zhou, Jeffrey R Long, and Omar M Yaghi. Introduction to metal–organic frameworks. *Chemical reviews*, 112(2):673–674, 2012.

[271] Yunxuan Zhou, Qianli Liu, Mingyu Hu, Gengsen Xu, Ruiju Xu, Xiaoyu Chong, and Jing Feng. Investigation on the stability, electronic, optical, and mechanical properties of novel calcium carbonate hydrates via first-principles calculations. *International Journal of Quantum Chemistry*, 120(10):e26219, 2020.

[272] A Zucchini, P Comodi, A Katerinopoulou, T Balic-Zunic, C McCammon, and F Frondini. Order-disorder-reorder process in thermally treated dolomite samples: a combined powder and single-crystal X-ray diffraction study. *Physics and Chemistry of Minerals*, 39(4):319–328, 2012.

[273] Azzurra Zucchini, Paola Comodi, Sabrina Nazzareni, and Michael Hanfland. The effect of cation ordering and temperature on the high-pressure behaviour of dolomite. *Physics and Chemistry of Minerals*, 41(10):783–793, 2014.

Acknowledgements

This Ph.D. was carried out within the scope of the DFG-funded FOR2125 'CarboPaT' (Projects 435 WI1231, SP1216/7-1). I also wish to acknowledge Prof. Winkler and Dr. Speziale for the additional funding.
I am grateful to my supervisors Dr. Sergio Speziale and Bjoern Winkler, for the time they have invested in me, for all our discussions and for teaching me how to stand on my own and grow independent as a scientist.
I also would like to thank all the people that have helped me make this thesis possible, all the professors, researchers, staff and friends from both section 3.6 at GFZ and the crystallography section (Arbeitsgruppe Winkler) at Goethe University (Prof. Monika Koch-Müller, Prof. Maribel Nunez-Valdez, Dr. Bernd Wunder, Hanns-Peter Nabein, Dr. Christian Schmidt, Prof. Matthias Gottschalk, Prof. Richard Wirth, Dr. Hans-Josef Reichmann, Dr. Sergey Lobanov, Beate Hein, Dr. Franziska Wilke, Dr. Eiken Haussühl, Dr. Lkhamsuren Bayarjargal, Dr. Rita Luchitskaia, Anja Neubauer, Sigrid Schickling Herzog) that have helped me through the years.
A special thanks goes to my friend Dr. Naira Martirosyan, for all her help and her will to share her ideas and projects with me. I am also thankful to Jannes König for sharing his knowledge with me and for his help.
I also want to thank all my friends and my family from my adoptive section, Nada A., Lukas S., Jakob R., Yongchao L., Johannes W., Nicole S., Roberta S., Lélia L., Willemjin, Cappo, Katja B., Julia B., Tamara K., Nandine, Dominik S., Julien M., Livia N., Stephan B., Johannes H., Audrey B., Amandine A., Valerian S. and all the other people I had the pleasure of meeting at work and at conferences, who have made me a better person and without whom this Ph.D. would have been so much harder!
Finally, I would like to thank my family for their support. In particular, Andrea, thank you for your love and care, you are my best friend and my partner and I will always be grateful for everything you have done for me.